

Thèse présentée à l'université Aix-Marseille Université pour obtenir le  
grade de docteur en sciences

# Optical Diffraction Tomography Microscopy: Towards 3D Isotropic Super-resolution

**Charankumar Godavarthi**

20 Septembre 2016

## Membres du jury:

Président	<b>Olivier HAEBERLÉ</b>	MIPS, Mulhouse
Rapporteur	<b>Pascal PICART</b>	LAUM, Le Mans
Rapporteur	<b>Sylvain LECLER</b>	ICube, Strasbourg
Examineur	<b>Serge MONNERET</b>	Institut Fresnel
Directeur de thèse	<b>Hugues GIOVANNINI</b>	Institut Fresnel
Codirecteur de thèse	<b>Guillaume MAIRE</b>	Institut Fresnel

Discipline: **Optique, photonique et traitement d'image**  
Laboratoire d'accueil: **Institut Fresnel, équipe S.E.M.O**  
École Doctorale: **352 - Physique et Sciences de la Matière**



---

# Acknowledgement

---

I extend my warmest thanks to my director of the thesis, Prof. Hugues Giovannini. Words fail me to express my gratitude. He always offered me help from any point of view and provided the best possible working conditions. I thank him especially for his many councils, his availability, best quality scientific advice and confidence in me. Thank you for providing the friendly working atmosphere.

I would also express my strongest gratitude to Guillaume Maire, my co-director of thesis. He has been the guiding light throughout this thesis work. He was always there to help me, guide me, and point me in the right direction, I consider myself really lucky to work with him and everyday it was entirely happy experience throughout. With his scientific rigor and foresight I learned a lot, thanks for everything.

I also wish to warmly thank Olivier Haeberlé, Sylvain Lecler, Pascal Picart and Serge Monneret for taking part in my thesis jury committee. I am grateful to Sylvain Lecler and Pascal Picart for reviewing this manuscript and for the comments.

I would also like to thank Anne Sentenac. She is always enthusiastic with lot of scientific ideas and charming personality. Thank you for motivating me and helping me to become a better researcher. I must also thank Patrick Chaumet for his guidance and help with the inversion algorithm code, fruitful discussions and scientific ideas. My sincere thanks to Kamal Belkebir, wonderful person and personality for helping me understand the theoretical concepts of inversion, constant discussions and scientific rigor.

I owe my gratitude to Anne Talneau at LPN, Marcoussis, France for the samples she prepared for us and helping to understand the concepts of fabrication during my stay in LPN, thank you. A big thank you to Julien Savatier and Cendrine Nicoletti for preparing the biological samples for me. A special mention of Daniel Sentenac for the help with the hardware integration on the experimental setup.

I thank Gabriel for the help with theoretical calculation which helped me to quantify the aberration. My warm thanks to Marc Alain, for constant encouragement, fruitful discussions and willing to help with different aspects. I express my gratitude to Nicolas Sandeau for guidance, discussions and financial support towards the end of my thesis.

I have to thank CNRS for the financial support for the three years, the Doctoral School 352 and Aix-Marseille University, and especially the Fresnel Institute that allowed me to do this work.

Ting Zhang deserves a special thanks for sharing the office with me, for discussions on various topics, help with the inversion programs and working to accomplish the scientific goals together.

I also thank all the members of SEMO (called SEMOX for first two years of my PhD). Thanks to Virgine, Patrick, David, Anastasios, Awoke, Simon and Dam-be. My special gratitude to Gerald Tayeb for co-curricular activities and motivation.

I thank all the great people I met at the Institute Fresnel, St-Jérôme campus. Frederic Forestier (merci pour les excursions en bateau) and Jean Cayzac for help with computers and smooth functioning of my scientific work. A special thank you to Marc Traversari, Nelly, Claire, Magali and Emilie, who assured the smooth process of administrative work and especially everyday life.

I also wish to thank Naveen, Nicolas, Luisa, Anar, Hassan, Xavier, Alberto, Siddarth, Paulina, Shishe, Vincent, Charles, etc., for the social and scientific life in the institute.

My gratitude to Abbe School of Photonics, Jena for giving me the opportunity to study my Masters and helping me to realize my potential. Thanks to Toufic Jabbour and Bernd Kleemann for giving me the opportunity to work in Carl Zeiss, I learnt a lot in the short span. I wish to thank all the people I know in Marseille that made my stay memorable and wonderful in this warm city. Thanks to all my friends, colleagues and teachers for influencing my life and for the person I am today.

Finally, I would like to thank my mom and dad for their patience and believing in me and constant support. Thank you for all the foundation you laid, I am standing on top of it today.

“Don’t Stop Believin’ ”

Just a small town girl  
Livin’ in a lonely world  
She took the midnight train  
Goin’ anywhere  
Just a city boy  
Born and raised in South Detroit  
He took the midnight train  
Goin’ anywhere

A singer in a smokey room  
The smell of wine and cheap perfume  
For a smile they can share the night  
It goes on and on, and on, and on

Strangers waiting  
Up and down the boulevard  
Their shadows searching  
In the night  
Streetlight people  
Livin’ just to find emotion  
Hidin’ somewhere in the night

Workin’ hard to get my fill  
Everybody wants a thrill  
Payin’ anything to roll the dice  
Just one more time  
Some will win  
Some will lose  
Some were born to sing the blues  
Oh, the movie never ends  
It goes on and on, and on, and on

Don’t stop believin’  
Hold on to that feelin’  
Streetlight people  
Don’t stop believin’  
Hold on  
Streetlight people  
Don’t stop believin’  
Hold on to that feelin’  
Streetlight people

by **Journey**



---

# Contents

---

<b>Acknowledgement</b>	<b>iii</b>
<b>Lists of the figures</b>	<b>ix</b>
<b>Introduction and outline</b>	<b>1</b>
<b>1 Principles of tomographic diffractive microscopy</b>	<b>5</b>
1.1 Introduction . . . . .	5
1.2 Conventional wide-field optical microscope . . . . .	6
1.2.1 Abbe sine condition for aberration free imaging . . . . .	7
1.2.2 Rayleigh criterion for resolution limit . . . . .	8
1.3 Phase microscopy . . . . .	10
1.4 Towards 3D imaging by phase microscopy . . . . .	11
1.4.1 Volumetric sample . . . . .	11
1.4.2 How to get a 3D quantitative image of an object? . . . . .	13
1.5 Tomography: multiple-illumination angle approach . . . . .	13
1.5.1 Tomographic diffractive microscope . . . . .	14
1.5.2 Electromagnetic diffraction . . . . .	15
1.5.3 Born approximation . . . . .	17
1.5.4 TDM: synthetic numerical aperture . . . . .	19
1.5.5 Rytov approximation . . . . .	28
1.5.6 Improvements to TDM . . . . .	29
1.6 Experimental Set-up . . . . .	31
1.6.1 Experimental methods for phase imaging . . . . .	31
1.6.2 Description of the set-up . . . . .	35
1.6.2.1 Measurement of the full vectorial diffracted field . . . . .	37
1.6.3 Developments to the set-up . . . . .	38
1.7 Conclusion . . . . .	39
<b>2 Imaging with tomographic diffractive microscopy holograms under scalar approximations</b>	<b>41</b>
2.1 Introduction . . . . .	41

2.2	TDM data set . . . . .	42
2.3	Bright-field microscopy . . . . .	43
2.4	Dark-field imaging . . . . .	45
2.5	Phase contrast microscopy . . . . .	49
2.6	Confocal microscopy . . . . .	53
2.7	2D synthetic aperture microscopy . . . . .	58
2.8	3D synthetic aperture microscopy . . . . .	61
2.9	Conclusion . . . . .	63
<b>3</b>	<b>Imaging with tomographic diffractive microscopy holograms using accurate models</b>	<b>65</b>
3.1	Introduction . . . . .	65
3.2	Normalization of TDM data . . . . .	66
3.2.1	Normalization procedure . . . . .	66
3.2.2	Normalization factor . . . . .	67
3.3	Non linear inversion method . . . . .	68
3.3.1	Polarization and transverse isotropic resolution . . . . .	68
3.3.2	Forward problem . . . . .	70
3.3.3	Inverse problem . . . . .	73
3.3.4	Experimental results . . . . .	75
3.4	TDM imaging in noisy environment . . . . .	79
3.4.1	Principle of DORT . . . . .	80
3.4.2	Application of DORT to TDM . . . . .	81
3.4.2.1	Experimental result . . . . .	84
3.4.3	SVD in image space . . . . .	88
3.5	Bounded inversion method for $\lambda/10$ resolution . . . . .	90
3.6	Conclusion . . . . .	94
<b>4</b>	<b>Mirror-assisted tomography: axial resolution improvement</b>	<b>95</b>
4.1	Introduction . . . . .	95
4.2	Problem statement . . . . .	96
4.3	Solution: Mirror assisted tomography using non-linear inversion . . . . .	98
4.4	Validation on synthetic data . . . . .	100
4.5	Sample requirements and fabrication . . . . .	103
4.5.1	Sample requirements and synthetic reconstructions . . . . .	103
4.5.2	Sample fabrication . . . . .	106
4.6	Experimental results . . . . .	108
4.6.1	Data pre-conditioning . . . . .	109
4.6.2	Mirror-assisted tomography using non-linear inversion: results . . . . .	110
4.7	Future perspectives . . . . .	118
4.8	Conclusion . . . . .	120
	<b>Conclusion</b>	<b>121</b>

---



---

# List of Figures

---

1.1	Wide-field microscope - a general representation . . . . .	6
1.2	Airy disk formation in a microscope for a point source . . . . .	9
1.3	In Fig. <b>A</b> , the Airy disk formation from a single point source is seen. In Fig. <b>B</b> when two points are closer than the Rayleigh criterion, the two points cannot be resolved and an overlapping intensities is observed. In Fig. <b>C</b> when the first minimum of one of the Airy disk overlaps with the maximum of other Airy disk, the two point sources can be resolved, this is at the Rayleigh criterion limit. . . . .	9
1.4	Paraxial approximation of the perturbation of incident wavefront due to the volume object. . . . .	12
1.5	Principle of Tomographic Diffractive Microscopy (TDM): illuminating the sample with varied illumination angles, light emerges out of sample for each varied angle of incidence. Interferometric optical imaging system magnifies the light for varied illumination angles and holograms are recorded. Phase and amplitude information are retrieved for reconstruction of the 3D refractive index map corresponding to varied illumination angles . . . . .	14
1.6	The sample of volume $\mathbf{V}$ is illuminated with plane wave $\mathbf{E}_{inc}$ of direction $\mathbf{k}_{inc}$ . The diffracted field $\mathbf{E}_d$ for all the possible directions of $\mathbf{k}_d$ is measured. The goal is to reconstruct the $\varepsilon(\mathbf{r})$ (relative permittivity) inside the object of volume $\mathbf{V}$ . . . . .	15
1.7	Projection of 2D diffracted field of radius $k_0 NA$ on to a sphere of radius $k_0$ to form a cap of sphere. . . . .	20
1.8	Center cut along the 3D synthetic aperture (optical transfer function) for transmission configuration, which is a torus located at the center of the synthetic sphere in 3D. The white region represents the detectable spatial frequency region of the OTF for a given numerical aperture of $NA=0.95$ . . . . .	22
1.9	The real part of 3D PSF (3D Fourier transform of optical transfer function) for transmission configuration. Fig. <b>A</b> : Center cut (for x-z at $y=0$ ). Fig. <b>B</b> : Center cut (for x-y at $z=0$ ). . . . .	22

- 1.10 Synthetic numerical aperture formation in transmission configuration of TDM. In Fig.**A**, object is illuminated in normal incidence, the diffracted field is shown in Fourier domain with red dot being the specular focus of the incident field. The diffracted field is projected to form a cap of sphere and positioned on the synthetic Ewald's sphere satisfying the condition  $\mathbf{K} = \mathbf{k} - \mathbf{k}_{inc}$ . Similarly for Fig.**B**, object is illuminated with extreme angle along positive  $r_{\parallel}$  direction and cap of sphere is positioned according to  $\mathbf{K} = \mathbf{k} - \mathbf{k}_{inc}$ . It can be noted that the specular focus of incident field is located at the center of the Ewald's sphere or synthetic 3D aperture. For Fig.**C**, object is illuminated with extreme angle along negative  $r_{\parallel}$  direction and the cap of sphere is positioned. . . . . 23
- 1.11 Synthetic numerical aperture formation in reflection configuration of TDM. In Fig.**A**, object is illuminated in normal incidence and detected in the same direction, the diffracted field is shown in Fourier domain with red dot being the reflected specular focus of the incident field. The diffracted field is projected to form a cap of sphere and positioned on the synthetic Ewald's sphere satisfying the condition  $\mathbf{K} = \mathbf{k} - \mathbf{k}_{inc}$ . Similarly for Fig.**B**, object is illuminated with extreme angle along positive  $r_{\parallel}$  direction and cap of sphere is positioned according to  $\mathbf{K} = \mathbf{k} - \mathbf{k}_{inc}$ . It can be noted that the specular focus of incident field is located along the  $\mathbf{k}_z$  axis of the Ewald's sphere or synthetic 3D aperture. For Fig.**C**, object is illuminated with extreme angle along negative  $r_{\parallel}$  direction and the cap of sphere is positioned. . . . . 25
- 1.12 Center cut along the 3D synthetic aperture (optical transfer function) for reflection configuration with NA=0.95, which is a spherical solid incomplete sphere located at the polar end of the synthetic sphere in 3D. The white region represents the detectable spatial frequency region of the OTF for a given numerical aperture. . . . . 26
- 1.13 The 3D PSF (Fourier transform of 3D optical transfer function) of reflection configuration. It is complex in nature. Fig.**A**: Center cut (x-z at y=0) of real part of 3D PSF . Fig.**B**: Center cut of imaginary part of the 3D PSF (x-z at y=0). . . . . 26
- 1.14 Optical transfer function corresponding to a complete configuration of a TDM provided the illumination and the detection are performed in all possible directions. . . . . 27

1.15	In Fig. <b>A</b> , object is illuminated by $\lambda = 632.8nm$ , wavelength of light at normal incidence, the diffracted fields 2D Fourier components are measured with a NA (i.e. of $\lambda = 632.8nm$ ) and projected to form a cap of sphere. Similarly, in Fig. <b>B</b> , object is illuminated by $\lambda = 475nm$ wavelength light at normal incidence, the diffracted fields 2D Fourier components are measured with a NA (i.e. of $\lambda = 475nm$ ) and projected to form a cap of sphere. Note that the radius of 3D synthetic aperture varies from $2k_0$ to $2k'_0$ due to wavelength. These two measurements can be combined in a synthetic aperture provided there is no dispersion, since they belong to the same object at different wavelengths. Optical transfer function corresponding to two wavelengths when combined and averaged at overlapping points fills additional points in the 3D synthetic aperture sphere compared to a single wavelength configuration. This can be performed in all possible directions and combined together to fill the additional spatial frequency information about the object compared to single wavelength measurement. . . . .	30
1.16	Mach-Zehnder interferometer: M1, M2, mirrors; BS1, BS2, beam splitters. The interferometer consists of two arms: reference arm and object arm. The beam passing through the object encodes the information about the object. The reference beam is interfered with the object beam from off-axis. The interference pattern is recorded on the CCD. . . . .	33
1.17	Sketch of the experimental set-up: M, rotating mirror; D, diaphragm; OL, objective lens; L, tube lens; $L_{1,\dots,7}$ , lenses; $BS_{1,\dots,3}$ , beam splitters; $HW_{1,2}$ , half wave plates; P, pinhole. . . . .	36
1.18	Measurement of full vectorial field is performed along two bases. The illumination polarization is either along $\hat{x}$ or $\hat{y}$ . The detection polarization is either along $\hat{D}_1$ or $\hat{D}_2$ . This illumination and detection schema form an orthogonal basis. With $\alpha = 45^\circ$ . . . . .	37
2.1	Scanning Electron Microscopy image of the fabricated sample used for demonstration of different numerical simulated imaging techniques in this chapter. . . . .	42
2.2	The TDM bright-field image of the sample at $\lambda = 475nm$ . Scale bar represents the intensity. . . . .	45
2.3	Dark field microscopy principle . . . . .	46
2.4	Dark field microscopy using TDM, only normal incidence illumination case is demonstrated here. . . . .	47
2.5	Suppression of the specular reflection in the Fourier space on the scattered field data. Fig. <b>A</b> : Total field in log10 scale inside the NA in the Fourier domain for normal incidence case. The bright spot corresponds to the non-diffracted field. Fig. <b>B</b> : The non-diffracted field is substituted by zeros numerically (black region), giving only the diffracted field ( $\mathbf{E}_d(\mathbf{r})$ ). . . . .	48
2.6	Dark field image of the sample Fig. 2.1 at $\lambda = 475nm$ . . . . .	48

2.7	Phase contrast microscopy principle. . . . .	50
2.8	Phase contrast microscopy with TDM . . . . .	51
2.9	Phase contrast TDM results of sample Fig. 2.2.A: Fig.A: Positive phase contrast TDM image. Fig.B: Negative phase contrast TDM image. . . . .	52
2.10	Confocal microscopy principle. . . . .	54
2.11	For a focused point $(x_0, y_0)$ on the sample, the detected intensity on a camera in the image space without a pinhole. . . . .	56
2.12	The confocal TDM image of the sample Fig. 2.1 generated numerically by utilizing the TDM hologram data and scanning digitally. Fig.A: The size of the confocal pinhole is 25nm. Fig.B: Size of the confocal pinhole is 425 nm, the size of central spot. . . . .	57
2.13	Formation of 2D synthetic aperture in TDM. . . . .	59
2.14	Final 2D synthetic aperture in TDM if all the possible angles of illumination are used compared to only 4 angles shown in Fig. 2.13.D. . . . .	60
2.15	Fig.A: The modulus of 2D synthetic aperture in the Fourier domain shown in log scale for eight directions of incidences. The 8 incidences were defined by a fixed polar angle of $60^\circ$ and an azimuthal angle regularly spaced within $2\pi$ . Specular region (illumination modulus) is masked. Fig.B: 2D synthetic aperture reconstruction of sample (see Fig. 2.1 for the sample). Fourier transform of A would yield B. The Fig.B here displays the modulus of the complex reconstruction. . . . .	61
2.16	Fig.A: Modulus of 3D synthetic aperture reconstruction of sample Fig. 2.2.A in xy plane, a cut along z=0 plane. Fig.B: Modulus of reconstruction along the xz plane, a cut along the y=0 plane. Same scale in x, y and z. . . . .	62
3.1	Dark field images corresponding to, Fig.A: $\hat{x}\hat{D}_1$ , Fig.B: $\hat{x}\hat{D}_2$ , Fig.C: $\hat{y}\hat{D}_1$ , and Fig.D: $\hat{y}\hat{D}_2$ . . . . .	69
3.2	Unpolarized dark-field image of the sample at $\lambda = 475nm$ , resulting from the summation of Figs. 3.1.A, B, C, and D, in the transverse direction (xy). . . . .	69
3.3	The coupled dipole method discretization of arbitrary 3D object into N cubical units. The $\mathbf{E}_{inc}$ is the incident field and $\mathbf{E}_d$ scattered field. . . . .	70
3.4	Geometry of the inverse problem: the investigation domain in inversion procedure $\Omega$ . $\Gamma$ is the measurement data. The unknown object is reconstructed from the measured data within an inversion box discretized by cubic units of desired size. . . . .	73
3.5	Reference sample: Fig.A: Full-polarized dark-field image. Fig.B: Transverse cut along the center of the full-polarized 3D-FFT reconstruction. Fig.C: Reconstructed permittivity averaged over the sample's height using $\hat{x}\hat{x} + \hat{y}\hat{y}$ TDM. Fig.D: Reconstructed permittivity averaged over the sample's height using the full-polarized TDM. . . . .	76

3.6	Reference sample. Fig. <b>A</b> : Axial cut along the center of the full-polarized 3D-FFT reconstruction. Fig. <b>B</b> : Reconstructed permittivity along the center of yz-plane using $\hat{x}\hat{x} + \hat{y}\hat{y}$ TDM. Fig. <b>C</b> : Reconstructed permittivity along the center yz-plane using the full-polarized TDM at $\lambda = 475nm$ . . . . .	77
3.7	SEM image of sample with one missing branch compared to the sample shown in Fig. 3.6. . . . .	78
3.8	Results of star sample with one missing branch. Fig. <b>A</b> : Full-polarized dark-field image. Fig. <b>B</b> : Transverse cut along the center of the full-polarized 3D-FFT reconstruction. Fig. <b>C</b> : Reconstructed permittivity averaged over the sample's height using $\hat{x}\hat{x} + \hat{y}\hat{y}$ TDM. Fig. <b>D</b> : Reconstructed permittivity averaged over the sample's height using the full-polarized TDM at $\lambda = 475nm$ . . . . .	78
3.9	(SEM image of sample with one branch misaligned compared to sample Fig. 3.6. . . . .	79
3.10	Results of star sample with misaligned branches. Fig. <b>A</b> : Full-polarized dark-field image. Fig. <b>B</b> : Transverse cut along the center of the full-polarized 3D-FFT reconstruction. Fig. <b>C</b> : Reconstructed permittivity averaged over the sample's height using $\hat{x}\hat{x} + \hat{y}\hat{y}$ TDM. Fig. <b>D</b> : Reconstructed permittivity averaged over the sample's height using the full-polarized TDM at $\lambda = 475nm$ . . . . .	79
3.11	Sample geometry in the transverse cut plane. It is composed of four resin cylinders with permittivity 2, height 170 nm and different radii deposited on a silicon substrate with permittivity $15.07+0.148i$ at the illumination wavelength 632.8 nm. . . . .	84
3.12	Noise free configuration. Fig. <b>A–B</b> : Qualitative images of the sample in the (x, y) plane. Fig. <b>A</b> : Bright field conventional microscope image generated by summing the experimental intensity recorded at the image plane of the TDM for the $2L = 50$ illuminations. Fig. <b>B</b> : DORT image obtained by summing the intensities of the fields generated by all the singular vectors $v_j=1,\dots,2L$ of the scattering matrix at $z = 100$ nm above the substrate. Fig. <b>C–F</b> : Selective quantitative reconstructions of the four cylinders. The quantitative inversion procedure is run on the scattered fields $u_j=1\dots 2L$ obtained for the agile illuminations $v_j=1\dots 2L$ . The investigation domain is restricted to a $2 \times 2 \times 0.25\mu m^3$ box surrounding one scatterer at a time. The reconstructed permittivity map is displayed in the (x, y) plane at $z = 100$ nm. Figs.G-H: Image of the sample in the (x, z) plane along the line passing through the middle of the largest cylinder indicated in subplot Fig.B. Fig. <b>G</b> : qualitative DORT image [as in subplot Fig.B]. The bright torse observed above the cylinder reflects the complexity of the DORT focusing behavior when the scatterer size is comparable to the wavelength. Fig. <b>H</b> : Selective quantitative reconstruction of the largest cylinder. The scatterer shape is significantly improved compared to Fig.G. . . . .	86

3.13	Same as Fig. 3.12 but in the noisy configuration. . . . .	87
3.14	DORT inversion in the image space. A. The dark-field image of the noisy data with cylinders being distorted. B. The SVD focusing property at the location of the cylinders, obtained by summing the singular vectors. . . . .	88
3.15	Images of a resin star-sample of 97 nm wide rods of length 520 nm on a Si substrate. Fig.A: Scanning electronic microscope image. Fig.B: Dark field microscopy with NA=0.95. Fig.C: Reconstruction obtained with non-linear inversion method from Tomographic Diffraction Microscopy data with NA=0.95. Fig.D: Permittivity reconstruction obtained with BIM using the knowledge of the resin permittivity from the same data as Fig.C. Fig.E: Permittivity distribution in the axial z direction versus the curvilinear abscissa of the dashed circle in Fig.D. The mesh size taken for all the reconstructions is 20 nm. BIM is able to distinguish the rods down to an inter spacing about 50 nm. The width of the rods is estimated to 117 nm in average (between 5 and 6 pixels). The color code indicates the level of relative permittivity in Figs.C and D at $\lambda = 632.8nm$ . . . . .	92
3.16	Same as Fig. 3.15, but the rods width is 76 nm and their length is 490 nm. Similarly to Fig. 3.15, BIM is able to distinguish the rods down to an inter spacing about 50 nm. The rods width is estimated to 87 nm in average (between 4 and 5 pixels) at $\lambda = 632.8nm$ . . . . .	93
4.1	Different possible configurations used for imaging in microscopy. Fig.A: Isotropic or complete configuration (hypothetical configuration). Fig.B: Transmission configuration. Fig.C: Reflection configuration. Fig.D: Mirror-assisted configuration . . . . .	97
4.2	Combination of transmission configuration and reflection configuration OTF, which is Fig. 1.8 + Fig. 1.12 for NA= 0.95. This yields better axial OTF support. . . . .	98
4.3	Fig.A: General microscopy configurations, <b>first transmission measurement</b> : illuminated along 1 and detected along 4, <b>second transmission measurement</b> : illuminated along 2 and detected along 3, <b>first reflection measurement</b> : illuminated along 1 and detected along 3 and <b>second reflection measurement</b> : illuminated along 2 and detected along 4. Fig.B: Mirror-assisted tomography: this configuration includes <b>two transmission measurements</b> (illuminated along 1, mirror with its reflection helps in detecting transmission components 4 and illumination along 2 with detection along 3) and <b>two reflection measurements</b> (illuminated along 1, detection of reflection components along 3 and mirror illuminates the sample 2 with detection along 4). Note that all these components are mixed. . . . .	99
4.4	Mirror-assisted tomography OTF and PSF. Fig.A: axial cut ( $\mathbf{K}_x \mathbf{K}_z$ ) of the 3D synthetic aperture along the center of the $\mathbf{K}_y$ axis in the Fig. 4.5.C. Fig.B: Intensity of the PSF along the axial direction. . . . .	100

- 4.5 Synthetic numerical aperture formation in mirror-assisted TDM configuration. In Fig.A, object is illuminated by normal incidence, the diffracted field is shown in Fourier domain with red dot being the specular focus of the incident field. This is decomposed into two transmission and two reflection measurements. They are projected to form a cap of spheres and positioned on the synthetic Ewald's sphere satisfying the condition  $\mathbf{K} = \mathbf{k} - \mathbf{k}_{inc}$ . There are 4 cap of spheres corresponding to transmission ( $A_{T1}$  &  $A_{T2}$ ) and reflection ( $A_{R3}$  &  $A_{R4}$ ) respectively. Similarly for Fig.B, object is illuminated with extreme angle along positive  $r_{\parallel}$  direction and cap of spheres is positioned according to  $\mathbf{K} = \mathbf{k} - \mathbf{k}_{inc}$ . For Fig.C, object is illuminated with many varying angles in  $r_{\parallel}$  direction and diffracted field is collected. Then they are positioned in the 3D synthetic aperture, transmission components form a torus at the center, and the reflection components form hemispheres at the bottom and top of the 3D synthetic aperture. 101
- 4.6 Numerical Validation of the mirror-assisted tomography on a test object in transmission and mirror-assisted tomography configurations [3].  
**Transmission:** Fig.A: Sphere (diameter =  $2\lambda$ ) of dielectric permittivity  $\varepsilon = 1.01$  containing two absorbent spherical inclusions (diameter =  $\lambda/4$ ) of *permittivity*,  $\varepsilon = 1.01 + 0.02i$ . The distance between the two absorbent spherical objects was  $0.6\lambda$ . Fig.B: Reconstruction of Fig.A, real part. Fig.C: Reconstruction of Fig.A, imaginary part.  
**Mirror-assisted tomography:** Fig.D: Same as Fig.A with a mirror positioned along the  $\mathbf{x}$  axis. Reconstruction of Fig.D, real part shown in Fig.E, imaginary part shown in Fig.F [3]. . . . . 102
- 4.7 Test samples. Fig.A: General specifications of the test samples, with  $s$  being the separation distance between the two  $\text{TiO}_2$  cylinders and  $d$  being the distance between the Al mirror layer and the first  $\text{TiO}_2$  cylinder. Fig.B: Specifications of the sample used for the numerical experiment of the mirror-assisted tomography presented in this section. Fig.C: Top view of  $\text{TiO}_2$  cylinder, it shows the diameter of 300 nm. . . . . 104
- 4.8 Illumination schema used for mirror-assisted tomography. The NA of the objective is shown in Fourier space with illumination angles (red dots). The samples were illuminated with 24 angles of incidence, 12 each along the  $\mathbf{K}_x$  and  $\mathbf{K}_y$  directions within the NA of the objective. 105
- 4.9 Result of numerical experimental reconstruction. Fig.A: Transverse cut (xy direction) along center of the bottom of the  $\text{TiO}_2$  shown in Fig.B. Fig.B: Axial cut (xz direction) along  $y=0$  in (A). . . . . 105
- 4.10 SEM image of the layers deposited on the Si substrate of  $100\mu\text{m}$ . The layers and their thickness shown are Al (112nm),  $\text{SiO}_2$  (215nm),  $\text{TiO}_2$  (103nm),  $\text{SiO}_2$  (321nm) and  $\text{TiO}_2$  (96nm) respectively. . . . . 106

- 4.11 Lift-off procedure: I. Preparation of the substrate (1) with layers deposited on it. II. Deposition of the PMMA stencil layer (2). III. Patterning the PMMA layer using e-beam lithography, creating an inverse pattern. IV. Deposition of the target material, Al (3). V. Washing out the PMMA layer together with the Al material on its surface VI. Final pattern Layers: (1) substrate with different layers and (3) Al pattern. . . . . 107
- 4.12 Fabricated sample under SEM. Fig.**A**: Top view of the cylinder. Fig.**B**: The axial view of the cylinder. . . . . 108
- 4.13 Aberration profile of the experimental setup obtained using a calibrated sample for NA=1.49, CFI Apo TIRF 100×: Nikon. . . . . 110
- 4.14 Mirror-assisted tomography experimental result. Fig.**A**: Fabrication schema of the sample, TiO<sub>2</sub> (refractive index = 2.32) cylinders of 300nm in diameter separated by 100nm side-by-side axial distance filled with SiO<sub>2</sub> (refractive index = 1.5). The mirror and the first cylinder are separated by a distance of 200nm with SiO<sub>2</sub>. The sample is covered by a resin layer(refractive index = 1.5). Fig.**B**: The experimental non-linear reconstruction of the sample shown in Fig.A. TiO<sub>2</sub> cylinders are well resolved along the axial direction (z). Fig.**C**: Transverse cut (xy) along the center of the first cylinder from the mirror, diameter of 300nm is well reconstructed at  $\lambda = 632.8nm$  and 1.49 NA objective. . . . . 112
- 4.15 Mirror-assisted tomography experimental result. Fig.**A**: Fabrication schema of the sample: similar to Fig. 4.14.A, except the distance between the two TiO<sub>2</sub> cylinders is 200nm. Fig.**B**: The experimental non-linear reconstruction of the sample shown in Fig.A. TiO<sub>2</sub> cylinders are well resolved along the axial direction z. . . . . 112
- 4.16 Mirror-assisted tomography experimental result. Fig.**A**: Fabrication schema of the sample: similar to Fig. 4.14.A, except the distance between the two TiO<sub>2</sub> cylinders is 300nm and Al mirror layer to first cylinder is 600nm. Fig.**B**: The experimental non-linear reconstruction of the sample shown in Fig.A along xz direction. . . . . 114
- 4.17 Mirror-assisted tomography inversion result applied on theoretical data. Fabrication schema of the sample shown in Fig. 4.16.A. The numerical non-linear reconstruction, the cylinders are well resolved along the axial direction xz separated by 300nm side-by-side. . . . . 115
- 4.18 Reconstruction of sample with configuration shown in Fig. 4.16.A with the scattered field data corresponding to the angles of incidence close to the normal incidence suppressed and the phase at the edge of the NA in Fourier replaced by numerically calculated phase. This is better than the experimental result presented in Fig. 4.16.B, this gives insights into the importance of noise and aberrations. . . . . 116

- 4.19 Sample schema to demonstrate both axial and transverse resolution: the schema is similar to the schema shown in Fig. 4.15.A, additional to that, two more TiO<sub>2</sub> cylinders are positioned along the x-axis separated by 100nm. This forms four TiO<sub>2</sub> cylinders to be resolved in both transverse and axial direction. . . . . 117
- 4.20 Result to demonstrate both axial and transverse resolution using mirror-assisted tomography on sample shown in Fig. 4.19. Fig.A: The axial-cut (xz direction) showing four TiO<sub>2</sub> cylinders along with few rebounds. Fig.B: The transverse-cut (xy direction) along the center of TiO<sub>2</sub> cylinders located close to the mirror, each cylinder is of diameter 300nm. The two cylinders are transversely separated by 100nm side-by-side. Fig.C: Axial-cut (yz direction) along the center of x-axis with faint rebound. . . . . 118
- 4.21 Illumination in mirror-assisted tomography: Fig.A: A sample positioned on top of a mirror is illuminated with an objective, we observe real object and the mirror-image. Fig.A: The sum of the illuminations forms a interference pattern due to the illuminated and the reflected beams. . . . . 119



---

# Introduction and outline

---

“That’s one small step for man, one giant leap for mankind.”  
-Neil Armstrong, Astronaut

## Introduction

Microscope magnifies small objects to observe a magnified image. Magnified image of the objects enables us to see finer details which are invisible to the human eyes. Various fields (microelectronics, biology, material science, medicine etc.) require microscopy tools to observe objects with micron, sub-micron and nanometric resolution on wide range of samples for better understanding. Though there are varying forms of microscopes, optical microscopy has an unique advantage with its non-destructive and contact-free probing nature in the optical regime. Optical microscope was invented around 16th century, it has been revolutionized since then. This is evident from the Nobel Prize for Chemistry 2014 being awarded for the development of super-resolution microscopy [1].

Classical optical microscopy is limited in resolution by the wavelength of light (diffraction limit) restricting lateral resolution to about  $\lambda/2$ , and axial resolution to about  $\lambda$  (the wavelength) [2]. The Nobel Prize for Chemistry 2014 winning microscopes depend on the fluorescent markers to achieve super-resolution. It can be detrimental to introduce fluorescent markers in to the probed sample, these markers are non-permanent, they introduce artifacts into the sample, the resolution depends on the labeling density etc. On the other hand, the invention of computers and increase in the computational power coupled with the accurate understanding of the light is pushing the horizons of the optical microscopy further beyond the diffraction limit.

This PhD thesis is devoted to the optical tomographic diffractive microscopy (TDM) for improving the three-dimensional isotropic resolution to observe label-free objects beyond diffraction limit by only optical means. The TDM is one of the techniques in the recent years that has seen a tremendous development in high and super-resolution imaging, pushing the spatial resolution beyond its diffraction limit with help of optics and computational algorithms. The principle is to illuminate the sample successively with various angles of coherent light, collect the complex (amplitude and phase) diffracted field and reconstruct the sample 3D permittivity map through an inversion algorithm.

## Motivation

The motivation to pursue this thesis is to break the optical diffraction limit and resolve nano-scale objects in the optical regime. Fluorescence Super-resolution microscope techniques (Stimulated emission depletion microscopy [STED], Stochastic optical reconstruction microscopy [STORM] and Photo-activated localization microscopy [PALM]) resolve beyond the diffraction limit but with the limitations discussed earlier. One of the microscopy application field namely microelectronics does not have the opportunity to take advantage of the fluorescent markers to perform the required super-resolution microscopy. On the other hand, Transmission electron microscopy (TEM) and scanning electron microscopy (SEM) need rigorous sample preparation, measurements have to be performed in the vacuum, and the interaction of the electron beam with the sample are some of the disadvantages of these microscope techniques. Most of the research groups working on TDM utilize transmission configuration because of its simplicity, objects located on reflective surface cannot be resolved with transmission TDM. These disadvantages motivates us to develop a global microscopy tool to obtain a three-dimensional reconstruction of the object with its constitutive material properties (e.g. permittivity etc.) using an optical microscope; namely TDM.

## Objective

The objective of the PhD thesis was to improve the transverse resolution beyond  $\lambda/2$ , and axial resolution beyond  $\lambda$  by using optical tomographic diffraction microscopy (TDM) coupled with non-linear inversion algorithms. Improve the TDM experimental setup with the state-of-art instruments for ameliorating the measured diffracted field data which we believed would help in improving the resolution. Probe the role of polarization on the resolution. To image the objects measured in noisy environment using TDM was also an objective. To experimentally validate the mirror-assisted tomography for axial-resolution improvement, which was theoretically proposed by Mudry et al., [3]. Further explore various horizons in improving the overall performance of the TDM and simplification of the sample fabrication, experimental setup, data processing and non-linear inversion algorithm.

## Outline of the thesis

This PhD thesis contains four chapters:

- In the first chapter, the principles of optical microscopy will be introduced and the optical diffraction limit will be described in detail. With help of phase microscopy I explain the principle to obtain a 3D quantitative reconstruction of the object, which is tomography approach. The basic principles of optical tomographic diffractive microscopy will be explained using rigorous electromagnetic diffraction. The approximations to this diffraction such as Born

and Rytov are explored in detail to understand the transmission and reflection configuration of the TDM microscope. The last part of the first chapter deals with experimental setup, the process involved in obtaining full-vectorial complex diffracted field data.

- In the second chapter, I will present the numerical imaging of various microscopy techniques such as bright-field microscopy, dark-field microscopy, phase contrast microscopy, confocal microscopy, 2D synthetic aperture microscopy and 3D synthetic aperture microscopy from the measured TDM complex diffracted field data under scalar approximations. These numerical modalities are possible to realize from a single TDM measurement, thanks to the complete measurement one obtains from TDM. Each of the above stated microscopy techniques will be explained with underlying basic principle, numerical realization with TDM, advantages and disadvantages of their experimental realizations against the numerical realization from TDM data.
- In the third chapter, I will firstly explain the meaning and importance of normalization of measured data. Then, the role of polarization to obtain the isotropic transverse resolution will be demonstrated on an experimental sample. The brief understanding of rigorous non-linear inversion algorithm will be explained with help of forward problem and inverse problem theory. The experimental results corresponding to the coupling of TDM measurement with non-linear inversion algorithm are detailed to achieve  $\lambda/4$  transverse resolution. It will be shown that this coupling is efficient in reconstructing any defects in the sample too. Further, the imaging of objects in the noisy environment with help of singular value decomposition (SVD) will be presented with experimental data. Finally, SVD noise reduction will be applied on the experimental data and the non-linear inversion algorithm will be provided with a priori information about the sample, this will help in achieving  $\lambda/10$  transverse resolution.
- In the last chapter, I will present the experimental demonstration of the axial resolution improvement by mirror-assisted tomography. First steps will be to validate on numerical data, fabricate the samples on top of a mirror and perform TDM measurement. The final step will be to perform non-linear inversion on the measured complex scattered field data accounting for the presence of mirror. The challenges facing the mirror-assisted tomography and perspectives to solve them will be detailed.



---

# Principles of tomographic diffractive microscopy

---

“Seeing Is Believing”

-Manfred von Heimendahl, Materials scientist

## 1.1 Introduction

Tomographic Diffractive Microscopy (TDM) is a developing advanced digital imaging technique. The technique was first proposed by E. Wolf in 1969 [4], it had to wait until recently for the experimental realization by V. Lauer [5]. This convinced experts and made them realize of a new imaging technique which can image beyond the optical diffraction limit.

In the last 7 years it has seen a growth in the number of publications over the world. This microscopy is also known as synthetic aperture microscopy, tomographic phase microscopy, optical diffraction tomography, digital holographic microscopy, scanning holography microscopy etc. The TDM is a label free imaging tool, it has the ability to reconstruct the 3D refractive index of the sample [6] reconstruction of biological samples [7]; it can probe the profile of a surface [8], etc.

To understand the TDM and its working principle, we start with understanding the wide-field general optical microscope. In wide-field microscope we understand the general principles governing the microscopy, method to obtain a good quality image and the resolution limit in the general optical microscopes. Wide-field microscope does not provide 3D reconstruction of the sample, since TDM is a 3D phase microscope, we briefly explore the phase microscope and the information the phase microscope can provide to obtain the 3D reconstruction of the sample and the permittivity map.

Later in this chapter, the basic principles and classical approaches to Tomographic Diffractive Microscopy are explained in detail. Then, models (eg., Born approximation) for reconstruction of TDM data and the role of polarization, wavelength, environment are discussed. Finally, experimental methods to obtain the quantitative phase, the experimental setup I developed are presented.

## 1.2 Conventional wide-field optical microscope

Light propagation and interaction with matter can be understood by Maxwell equations and classical electrodynamics. This section will explain light and sample interaction that would lead to magnify intensity image starting from the wide-field conventional optical microscope and progress towards understanding of the Tomographic Diffractive Microscopy via phase microscopy.

It is not very clear about who invented the first optical microscope but the technique has evolved enormously. Optical microscopy itself is a general term, present day has seen several astonishing optical microscopy techniques such as bright field [9], dark field [10], phase contrast [11], differential interference contrast [12], fluorescence [13], confocal [14], light sheet [15], structured illumination [16], single photon and multiphoton microscopy [17, 18] etc.

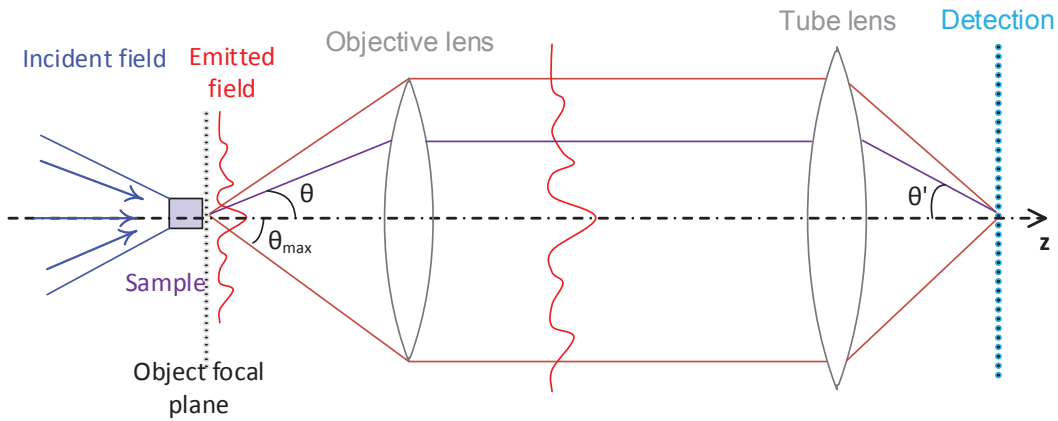


**Figure 1.1 :** *Wide-field microscope - a general representation*

To understand the optical microscopy principle we will consider transmission optical microscope. In the transmission optical microscope Fig. 1.1, the light from a source is illuminated on the sample. Usually, the light is passed through a lens called condenser lens to focus it on the sample to get maximum illumination uniformly. The light passing through the sample is collected by a lens called objective lens. The tube lens then provides a magnified image of the sample on the detector. The magnified image is detected by a detector usually a CCD (Charge Coupled Device) camera. Later, the captured images can be analyzed. It has to be noted that wide-field microscopy does not provide quantitative information about the sample, it provides intensity variation image of the field in the vicinity of the sample.

The electromagnetic field can be defined as,

$$\mathbf{E}(\mathbf{r}) = E_a(\mathbf{r})e^{i\phi(\mathbf{r})} \quad (1.1)$$

where  $\mathbf{r}$  is the position vector,  $E_a$  is the amplitude and  $\phi$  is the phase. The image on a detector is recorded as intensity,

$$\mathbf{I}(\mathbf{r}) = |\mathbf{E}(\mathbf{r})|^2 \quad (1.2)$$

the variations in the intensity is recorded on the detector.

Conventional wide-field optical microscope consists of simultaneous illumination of the whole sample. The simultaneous illumination of whole sample is illumination of a sum of plane waves simultaneously with each plane wave propagating in different directions [19]. As the light propagates through the sample, not all the light is collected, light scattering in the sample may also changes the direction of propagation of light. The direction of propagation of light is described by the wave vector  $\mathbf{k} = k_x\mathbf{x} + k_y\mathbf{y} + k_z\mathbf{z}$ . We can define,  $\mathbf{k}_{\parallel} = k_x\mathbf{x} + k_y\mathbf{y}$  being  $\mathbf{k}$  projected on (x,y) sample plane. The  $\mathbf{k}$  is the wave vector, being  $\|\mathbf{k}\| = k_0 = 2\pi/\lambda$ . When  $\|\mathbf{k}_{\parallel}\| \geq k_0$ ,  $k_z$  is given by,

$$k_z = i\sqrt{\|\mathbf{k}_{\parallel}\|^2 - k_0^2} \quad (1.3)$$

Microscope can be considered as a filter which magnifies and collects some of the plane waves (some of  $\mathbf{k}$  for detection) which are propagating in the z direction away from the sample for detection. The detection of the light would depend on the numerical aperture (NA) of the collecting lens, which collects the light emerging out of the sample. Numerical aperture,  $NA = n_i \sin \theta_{max}$ , where  $\theta_{max}$  (shown in Fig. 1.1) is the maximum polar angle of the plane wave that can be collected by the objective lens and  $n_i$  is the refractive index of the medium in which the object is placed. The collecting lens is called objective lens. The objective lens is combined with tube lens to magnify the light and to image on the detector to form a wide field image.

Wide-field microscopy provides an intensity variation image of the object, it does not provide a quantitative link between the object and the detected image. The intensity image is obtained due to the intensity variation caused by the constitutive material properties and the geometrical properties of the sample. But it is difficult to link the intensity image to the geometrical shape or the material properties of the sample. It is important to have access to this quantitative information about the object, because it would provide insights into the sample and its behavior in optical domain. For example, knowing the permittivity of the object under observation will help in understanding the behavior of the object to polarization, to electric field, to know its material composition etc. It also provides understanding about the reflection, transmission and absorption properties of the object.

The goal of a microscope is to achieve a good quality magnified image of the object. To achieve this there are certain optical limitations and conditions. By understanding these, we will be better able to understand the image obtained using a microscope.

### 1.2.1 Abbe sine condition for aberration free imaging

Abbe sine condition helps in designing a microscope to have a good quality image of the sample. The actual image of the sample is magnified by the microscope, the amount of magnification is defined by the Magnification factor (MF). Magnification is defined as the ratio between the image formed on the detector and the initial

sample size.

$$MF = \frac{\text{Size of the image formed on the detector}}{\text{Initial size of the sample}} \quad (1.4)$$

In microscope all the light emerging out of a point P (let us say a point P on the object focal plane shown in Fig. 1.1) on the sample should be imaged on the detector at point a P' (a point P' on the image plane shown in Fig. 1.1), in this case a sharper image of the sample will be formed on the detector. P' is called conjugate point of P. Such a microscope is called aberration free microscope or stigmatic optical imaging system. In practical cases, imaging is performed with least possible aberrations. The phase of the light emerging out of a point P on the sample varies from the phase detected on the image plane point P', though they are conjugate points. This can be due to the imperfections in the optical components, optical alignment etc.

For each point of P on object focal plane to have a point P' on the image plane imposes a condition proposed by Ernest Abbe called Abbe sine condition. A plane wave emerging out of object focal plane makes an angle  $\theta$  (shown in Fig. 1.1) with the optical axis. The wave travels through the tube lens and detected on the detector in the image plane with an angle  $\theta'$  with the optical axis [20] as shown in Fig. 1.1. Such that,

$$n_i \sin \theta = MF n_d \sin \theta' \quad (1.5)$$

where,  $n_i$  is the refractive index of the medium surrounding the sample and  $n_d$  is the refractive index of the detection medium. When the above condition is satisfied we obtain an aberration free image on the detector from an imaging system. We established a condition to obtain sharp image, the following criterion define the resolution we can reach with a microscope.

### 1.2.2 Rayleigh criterion for resolution limit

Let us consider two point sources which are separated by a distance  $\Delta r$  observed through a microscope. When  $\Delta r$  is significantly large, the two point sources can be distinguishable with the microscope. On the other hand, as we bring the two point sources closer, the smallest distance  $\Delta r$  that is possible to distinguish the two point sources is the resolution of a microscope. There have been several definitions of resolution [21], we will understand few of them here.

Diffraction limit imposes a limit on the resolution. Resolution is limited by the size of the numerical aperture used in the microscope. The plane waves emerging out of a sample with  $\mathbf{k}$  having an angle greater then the angle  $\theta_{max}$  (shown in Fig. 1.1) cannot be collected by the microscope objective. So, plane wave with  $\|\mathbf{k}_{\parallel}\| > k_0 \text{NA}$  cannot be detected. Where,  $\text{NA} = n_i \sin \theta_{max}$  being the numerical aperture.

The interest has been to increase the NA by some means and bring new information to improve the resolution of the microscope. In this direction, water immersion and oil immersion objectives have been designed to have a numerical aperture close to 1.5 with the sample being placed in the water or oil medium. Due to the immersion medium the NA is enhanced to an extent. It is challenging to design a high numerical objective and be aberration free.

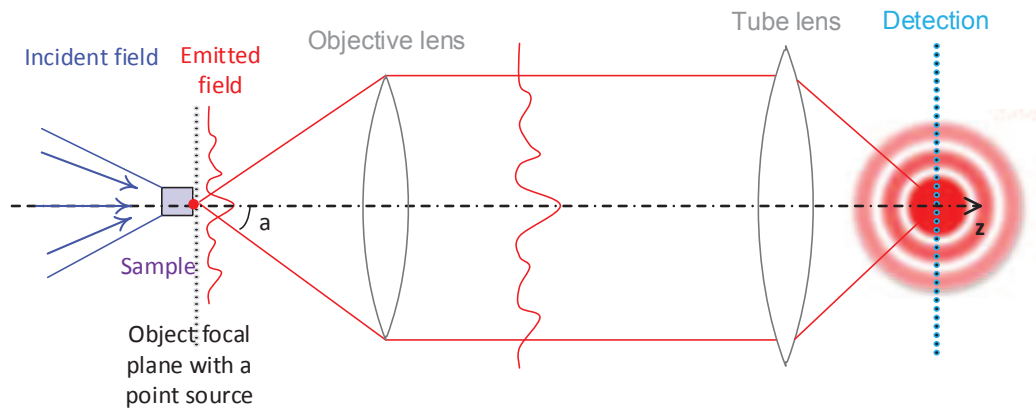


**Figure 1.2 :** *Airy disk formation in a microscope for a point source*

In Fig. 1.2, the objective lens forms a Fourier transform of the object and the tube lens an inverse Fourier transforms to obtain the magnified image of the sample. If the detector is placed between the objective lens and tube lens we will detect the Fourier spatial frequencies ( $\mathbf{k}_d$ ) corresponding to the sample.

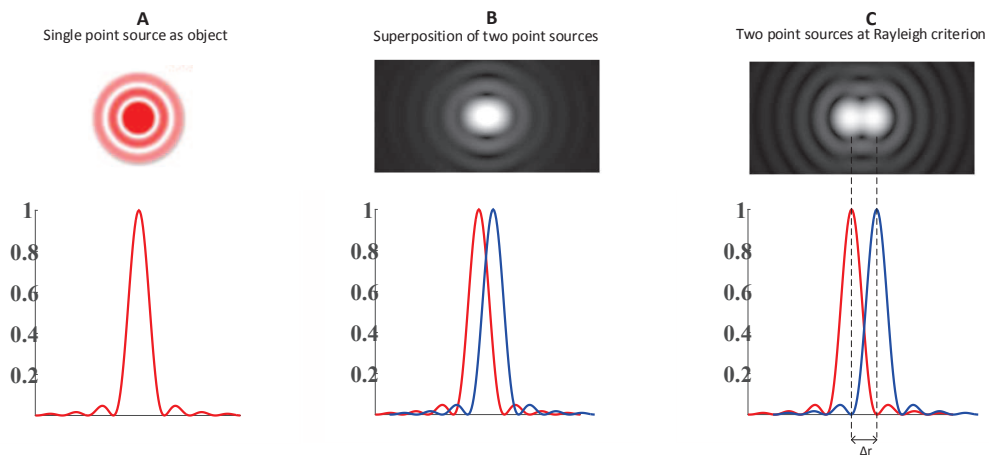


**Figure 1.3 :** *In Fig. A, the Airy disk formation from a single point source is seen. In Fig. B when two points are closer than the Rayleigh criterion, the two points cannot be resolved and an overlapping intensities is observed. In Fig. C when the first minimum of one of the Airy disk overlaps with the maximum of other Airy disk, the two point sources can be resolved, this is at the Rayleigh criterion limit.*

Resolution is generally different in transverse direction (in the  $(x,y)$  plane) and axial direction ( $z$  or optical axis plane) for a given microscope. Usually, the axial resolution is worse than the transverse resolution. The reason being the range of accessible spatial frequencies being different in axial and transverse direction, which can be understood from Sec. 1.5.3. The axial resolution is discussed in detail later. Here we will focus on transverse resolution. One of the possible definition of the

transverse resolution of a microscope is given by Rayleigh criterion. The Rayleigh criterion defines the transverse resolution as:

$$\Delta r = \frac{0.61 \lambda}{NA} = \frac{0.61 \lambda}{n_i \sin \theta_{max}} \quad (1.6)$$

where,  $\Delta r$  is the minimum separation distance between two distinguishable point sources in the transverse direction of observation under a microscope,  $\lambda$  being the wavelength, NA being the numerical aperture.

The limit in resolution is mainly due to the wave nature of light interaction with microscope objective, in particular diffraction and scattering. Let us consider a single point source at the detection as show in Fig. 1.2. The image formed at the detection plane is an airy disk, which is bright spot which contained 84% of energy surrounded by the diffraction rings. The airy disk formed is shown in Fig. 1.3.A.

The objective lens performs a Fourier transform of the point source and the tube lens an inverse Fourier transforms to form the image on the detector, shown in Fig. 1.2. Each point source forms a Airy disk in the image space, Fig. 1.3.A. Now, let us consider two point sources separated by a distance  $\Delta r$ , the image formed is shown in the Fig. 1.3.B or Fig. 1.3.C. The intensity pattern detected on the detector is a superposition of two airy disks formed by two different point sources. When the two point sources are close to each other, the superposition of two point sources does not allow to resolve them, shown in Fig. 1.3.B. As we increase the separation distance  $\Delta r$  the two point sources can be distinguished individually. Thus defining the resolution for a particular microscope with given a NA and observing wavelength. The Rayleigh criterion is obtained when the radial position of the first zero of the two Airy disks is equal to the  $\Delta r$ . Which means that the first minimum of the one of the Airy disk superpositions with the maximum of the other Airy disk and vice verse.

The wide-field microscopy is the fundamental microscope, it records only the intensity variations (Eq. (1.2)). We do not have access to the 3D geometrical information of the sample or the material properties of the sample. The resolution is also limited by the diffraction. To go a step further we will explore the phase microscope which brings in the geometrical information of the sample by exploiting the phase information  $\phi(\mathbf{r})$  in Eq.(1.1).

## 1.3 Phase microscopy

Detectors in general are built to detect the intensity variations (Eq. (1.2)), phase ( $\phi(\mathbf{r})$ ) cannot be detected directly. The ability to measure phase information in the last decades has opened up new possibilities. This led to exploit this phase information to obtain quantitative information on the axial dimensions (along the optical axis of the microscope) of the object, and thus provide a 3D reconstruction. The phase of the light propagating through or reflected by an object is affected by its 3D refractive index. Such that, these changes are encoded in the phase information. So, the phase information becomes important in obtaining the 3D

quantitative information about the sample and to reconstruct the relevant material properties of the sample.

Before we further understand the phase microscopy, I would like to introduce few definitions. If a sample is illuminated by a field  $\mathbf{E}_{inc}(\mathbf{r})$ , it would diffract the field  $\mathbf{E}_d(\mathbf{r})$ . Then the total field detected on the camera is given by  $\mathbf{E}(\mathbf{r}) = \mathbf{E}_0(\mathbf{r}) + \mathbf{E}_d(\mathbf{r})$ , where  $\mathbf{E}_0(\mathbf{r})$  is the field that would be present in the absence of the object, called reference field.

There had been vast interest in the phase imaging since the invention of Zernike phase contrast microscopy (PCM) in 1942 [11] for which Zernike was awarded Nobel prize (physics) in 1953. The principle behind PCM is explained briefly. As the light propagates through the objects the amplitude and phase of the light change depending on the object under observation. Amplitude variation is due to the scattering and absorption of light by the object. Zernike understood that scattered field and the incident field have a  $\pi/2$  phase shift as they are detected on the detector, so they can undergo interference. This led to poorly contrasted image of the object. Zernike introduced a supplementary phase shift of  $\pi/2$  between the diffracted and the non-diffracted (incident) light from the object. By introduction of this phase shift Zernike was able to enhance the contrast of the image recorded. Phase contrast microscope provides only qualitative phase information of the phase object. In 1948, Gabor demonstrated using holography as a tool to extract the phase information [22]. This led to the establishment of phase imaging field.

As explained earlier the phase information cannot be recorded directly, it is usually recovered by some means (e.g. off-axis interference holography [23], phase-shifting methods [24], wavefront sensor [25] etc.). These methods are discussed in detail later in this chapter. The phase ( $\phi(\mathbf{r})$ ) information and the amplitude information of the sample provide complete information and describe the electromagnetic total field diffracted by the sample. But we still have not been able to establish a link between the 3D geometrical properties of the sample or the material properties of the sample and the detected total field. The next section explore this link.

## 1.4 Towards 3D imaging by phase microscopy

The most direct way to exploit phase is to adopt a geometric approach of linear propagation of light. The usual configuration is to illuminate the object of interest with a collimated laser beam at normal incidence. The incident wavefront on the object is a plane wave. At the output of the object, the wavefront is distorted by the optical path variations caused by the presence of the object as shown in Fig. 1.4.

### 1.4.1 Volumetric sample

Take for example a volume object such as a biological cell (see Fig. 1.4). The wavefront distorted by the object is accessed by detecting the phase of the field;

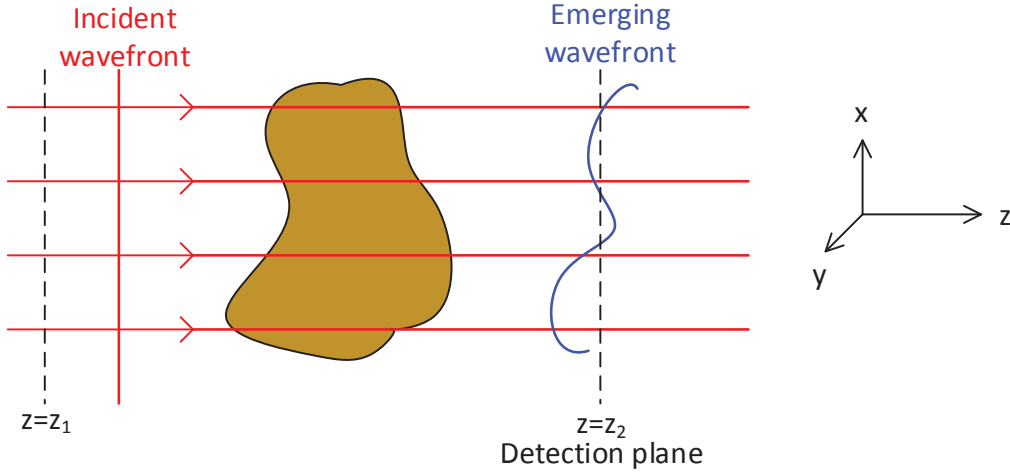


**Figure 1.4 :** *Paraxial approximation of the perturbation of incident wavefront due to the volume object.*

in practice immediately after the object (detection plane in Fig. 1.4). This object plane is thus conjugated with the image plane of the microscope.

The phase  $\varphi(x, y)$  field will then be understood by considering the object being crossed by undeflected parallel rays, with each propagate a different optical path depending on their positions in the object. In the paraxial approximation, this gives the optical phase delay:

$$\varphi(x, y) = k_0 \int_{z_1}^{z_2} n(x, y, z) dz (2\pi), \quad (1.7)$$

where  $z_1$  is the position of a plane before the object,  $z_2$  is that of the detection plane,  $n$  the refractive index in space and  $k_0 = \frac{2\pi}{\lambda}$ , the wave number with  $\lambda$  the illumination wavelength in vacuum. The variations in the phase in the object plane are proportional to the variations of the optical thickness of the object along the  $z$  axis, close to modulo  $2\pi$ , which is optical path integrated over the sample thickness. A sensitivity of the order of several nanometers of thickness has been detected successfully [26]. It goes without saying that this approach ignores the phenomena of refraction and diffraction inside the object, and is therefore limited to low refractive index contrasts. Though this provides more than just 2D information about the object but we still do not have access to the 3D object information or the material properties of the object.

### Geometric approach to retrieve object information

The most direct method is to extend the previous phase microscopy approach to different angles of illumination through the object. For each angle, the measured phase is analyzed with the Eq.( 1.7). From each such data set, an algorithm known as "filtered back projection", based on a Radon transform allows to decorrelate the refractive index of the object from the thickness of the object [27]. The principle is

the same as in X-ray tomography, where the intensity corresponds to the integration of the absorption coefficient of the object along straight rays. However, this method retains limitations as to not take into account either the refraction or diffraction generated by the object. It is therefore limited to very low contrast (as for certain biological samples) and the resolution being of several wavelengths [28–30].

### 1.4.2 How to get a 3D quantitative image of an object?

In 1969, E. Wolf published a paper to reconstruct 3D semi-transparent object from the hologram data [4]. Though the phase microscopy yields only 2D images, the hologram recorded will hold the information of the 3D object under observation. These holograms has to be processed computationally to retrieve the 3D object information or 3D refractive index map. E. Wolf described the determination of the complex refractive index in two steps as:

1. Calculation of the amplitude and the phase of the scattered field of the object from the holograms recorded in transmission.
2. Computational reconstruction of complex refractive index distribution of the 3D object.

Solution to first step, determination of phase and amplitude from the interference hologram data is presented in section ( 1.6.1). Here, solution to second step is to illuminate the object under observation with different directions of illuminations successively and record several holograms for each illumination direction. Recover the amplitude and phase corresponding to each of the illumination direction from the holograms. From this information 3D sample permittivity can be reconstructed [31, 32]. So, the idea of Tomographic Diffractive Microscopy (TDM) was born. The next section presents the detailed theory for obtaining the 3D permittivity map inside the sample using TDM.

## 1.5 Tomography: multiple-illumination angle approach

In digital holography a sample is illuminated by a collimated coherent plane wave, a hologram of the sample is recorded. From the hologram, the phase and amplitude information is recovered. Tomography is an extension of digital holography approach. In tomography several angles of illumination with different angles are used and the complex field is recovered from each hologram. Then the 3D permittivity of sample is reconstructed. This section will present the relation between the relative 3D permittivity of sample and the field diffracted by the 3D sample using electromagnetic theory of light. Later, approximations to the diffraction processes yielding approximate quantitative information about the sample is presented.

### 1.5.1 Tomographic diffractive microscope

As we understood earlier, to reconstruct the sample's 3D permittivity map, it is required to measure the amplitude and phase of the scattered field of the object [4]. The scattered fields are uniquely related to the structure of the object, which will be demonstrated theoretically later in this section.

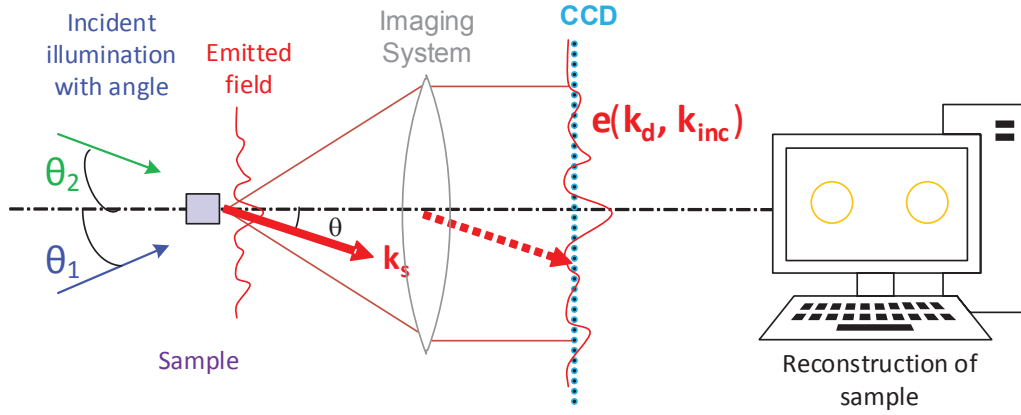


**Figure 1.5 :** *Principle of Tomographic Diffractive Microscopy (TDM): illuminating the sample with varied illumination angles, light emerges out of sample for each varied angle of incidence. Interferometric optical imaging system magnifies the light for varied illumination angles and holograms are recorded. Phase and amplitude information are retrieved for reconstruction of the 3D refractive index map corresponding to varied illumination angles*

Progressing towards the reconstruction of the 3D permittivity map of the sample, Tomographic Diffractive Microscopy (Fig. 1.5) has emerged as a solution. TDM consists of illuminating coherently with collimated light the sample with varied illumination angles from the condenser lens. Later, objective lens helps in collecting and magnifying the complex scattered field from the sample for each illuminated angle. It can be noted in Fig. 1.5, the measurement is performed in Fourier domain compared to the wide-field microscopy (Fig. 1.1) where the measurement is performed in the image space. The image space and Fourier space are linked by a simple 2D Fourier transform. To detect the phase and amplitude information (complex scattered field), usually an interferometric technique is employed, such as off-axis interferometry [33].

It has to be noted that once the complex scattered field data is recorded for varied illumination angles, several imaging techniques such as dark field imaging, bright field imaging, phase imaging, confocal imaging etc., can be realized. This is possible due to the availability of scattered field's amplitude and phase for several illumination angles, which describes the scattered field completely in the electromagnetic domain. Numerically the available information can be processed to obtain the different imaging techniques. The means to realize the above mentioned methods are presented in the next chapter in detail.

## 1.5.2 Electromagnetic diffraction

To understand the link between the recorded holograms (amplitude and phase information) and the 3D reconstruction of the sample (3D permittivity map) we need scattering and the electromagnetic theory of light. So far in the wide-field and in the phase microscopy the link was trivial, but to establish a 3D link taking into account diffraction and scattering we need to understand the electromagnetic diffraction process. Let us consider a sample as show in in Fig. 1.6. The object has a finite volume  $\mathbf{V}$  and relative permittivity  $\varepsilon(\mathbf{r})$ , i.e. the square of the refractive index of the sample; for  $\mathbf{r} \in \mathbf{V}$ ; outside the object i.e.  $\mathbf{r} \notin \mathbf{V}$ ,  $\varepsilon(\mathbf{r}) = 1$ . The goal is to reconstruct the  $\varepsilon(\mathbf{r})$  (relative permittivity) inside the object of volume  $\mathbf{V}$ .

Now, let us illuminate the sample with electromagnetic plane wave with electric field  $\mathbf{E}_{inc}(\mathbf{r})$ . This incident field interacts with the sample. It is well known that the electromagnetic wave satisfies the Maxwell equations. We consider the illumination is a plane wave and sample is non magnetic ( $\mu_r = 1$ ).

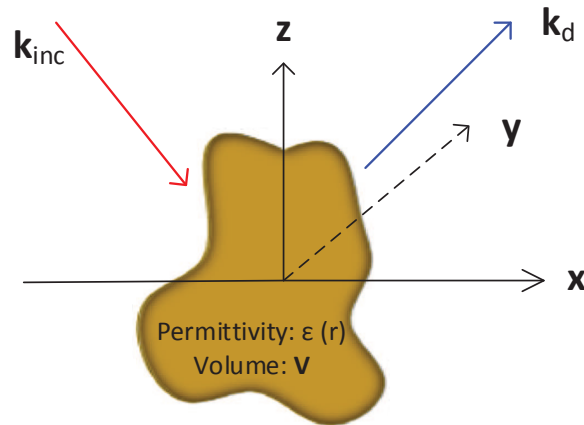


**Figure 1.6 :** *The sample of volume  $\mathbf{V}$  is illuminated with plane wave  $\mathbf{E}_{inc}$  of direction  $\mathbf{k}_{inc}$ . The diffracted field  $\mathbf{E}_d$  for all the possible directions of  $\mathbf{k}_d$  is measured. The goal is to reconstruct the  $\varepsilon(\mathbf{r})$  (relative permittivity) inside the object of volume  $\mathbf{V}$ .*

In the absence of the sample, and in the isotropic linear media, in free space ( $n=1$ ), it can be shown that by combining the Maxwell equations one can obtain the following propagation equation for the incident field [19],

$$\nabla \times \nabla \times \mathbf{E}_0(\mathbf{r}) - k_0^2 \mathbf{E}_0(\mathbf{r}) = i\omega\mu_0 \mathbf{J}(\mathbf{r}). \quad (1.8)$$

The Eq. 1.8 represents the field that would be present in the absence of the object called the reference field  $\mathbf{E}_0(\mathbf{r})$  (not to be confused with the reference beam  $\mathbf{E}_R$ ). With,  $k_0 = \frac{\omega}{c} = \frac{2\pi}{\lambda}$  is the wave number,  $\omega$  being the frequency,  $c$  light velocity in vacuum and  $\lambda$  is the wavelength of the illuminated light in vacuum.  $\mathbf{J}(\mathbf{r})$  is the potential electric current density.

It has to be noted that  $\mathbf{E}_{inc}(\mathbf{r}) \neq \mathbf{E}_0(\mathbf{r})$ <sup>i</sup> because it would depend on the medium of illumination and the configuration (whether transmission or reflection). In case of reflection, sample is usually positioned on a substrate. In this case,  $\mathbf{E}_0(\mathbf{r})$  is the field present with the substrate and the absence of the sample on top of it.

Similarly, the total field  $\mathbf{E}(\mathbf{r})$  which is the field in the presence of the object and illuminated by  $\mathbf{E}_{inc}(\mathbf{r})$  is given by,

$$\nabla \times \nabla \times \mathbf{E}(\mathbf{r}) - k_0^2 \mathbf{E}(\mathbf{r}) = i\omega\mu_0 \mathbf{J}(\mathbf{r}) + k_0^2 [\varepsilon(\mathbf{r}) - 1] \mathbf{E}(\mathbf{r}) \quad (1.9)$$

Such that we can define the diffracted field by the sample with volume  $\mathbf{V}$  as,  $\mathbf{E}_d(\mathbf{r}) = \mathbf{E}(\mathbf{r}) - \mathbf{E}_0(\mathbf{r})$ . Which is the difference between Eq.1.9 and Eq.1.8 given by,

$$\nabla \times \nabla \times \mathbf{E}_d(\mathbf{r}) - k_0^2 \mathbf{E}_d(\mathbf{r}) = k_0^2 [\varepsilon(\mathbf{r}) - 1] \mathbf{E}(\mathbf{r}) \quad (1.10)$$

The Eq. 1.10 is inhomogeneous differential equation with constant coefficients. As the Eq. 1.10 is linear in nature it can be solved using Green's function.

If we place an infinitely small dipole emitter  $\mathbf{p}$  at  $\mathbf{r}$ , then the field created at a distance  $\mathbf{r}'$  is given by  $\bar{\mathbf{G}}(\mathbf{r}, \mathbf{r}')\mathbf{p}$ , where  $\bar{\mathbf{G}}(\mathbf{r}, \mathbf{r}')$  is the Green's tensor. The  $\bar{\mathbf{G}}(\mathbf{r}, \mathbf{r}')\mathbf{p}$  being the solution of the following equation,

$$\nabla \times \nabla \times \bar{\mathbf{G}}(\mathbf{r}, \mathbf{r}')\mathbf{p} - k_0^2 \bar{\mathbf{G}}(\mathbf{r}, \mathbf{r}')\mathbf{p} = \delta(\mathbf{r} - \mathbf{r}')\mathbf{p}. \quad (1.11)$$

The solution of Eq. 1.10 can be shown as,

$$\begin{aligned} \mathbf{E}_d(\mathbf{r}) &= k_0^2 \int_{\mathbf{V}} \bar{\mathbf{G}}(\mathbf{r}, \mathbf{r}') [\varepsilon(\mathbf{r}') - 1] \mathbf{E}(\mathbf{r}') d\mathbf{r}', \\ or \\ &= k_0^2 \int_{\mathbf{V}} \bar{\mathbf{G}}(\mathbf{r}, \mathbf{r}') \chi(\mathbf{r}') \mathbf{E}(\mathbf{r}') d\mathbf{r}', \end{aligned} \quad (1.12)$$

with  $\chi(\mathbf{r}') = [\varepsilon(\mathbf{r}') - 1]$ . Where,  $\chi(\mathbf{r})$  is the linear susceptibility of the object or the permittivity contrast as  $[\varepsilon(\mathbf{r}) - 1]$ . The Eqn. 1.12 represents the diffracted field in the far field. This equation can be solved by using outgoing solution to Green's function in far field [19] and obtain the following equation,

$$\mathbf{E}_d(\mathbf{k}) = k_0 \mathbf{k} \times \left[ \mathbf{k} \times \tilde{\chi}(\mathbf{k}) \tilde{\mathbf{E}}(\mathbf{k}) \right]. \quad (1.13)$$

where  $\tilde{\chi}$  and  $\tilde{\mathbf{E}}$  stands for the Fourier transform of  $\chi$  and  $\mathbf{E}$  respectively.

The above equation can be expressed in Fourier transform as,

$$\mathbf{E}_d(\mathbf{k}) = k_0 \mathbf{k} \times \left[ \mathbf{k} \times \int_{\mathbf{V}} \exp(-i\mathbf{k} \cdot \mathbf{r}) \chi(\mathbf{r}) \mathbf{E}(\mathbf{r}) d\mathbf{r} \right] \quad (1.14)$$

which is product  $\chi\mathbf{E}$ , linear susceptibility and total field inside the sample.

The calculations performed in this section were performed without approximations, Eq.(1.14) can be solved numerically, but the calculations are time and resources consuming.

---

<sup>i</sup> $\mathbf{E}_{inc}(\mathbf{r}) \neq \mathbf{E}_0(\mathbf{r})$

### Retrieval of susceptibility in diffraction microscopy

The diffracted field contains the information about the object. By measuring the diffracted field for a particular illumination, we have access to the Fourier transform of  $\chi \mathbf{E}$ . The measurements are performed on a 2D detector surface for a 3D volume object. But the 3D diffracted field information of the object is encoded in 2D. For a given illumination angle ( $\mathbf{k}_{inc}$ ) the diffracted field measured in the far-field with a microscope objective will only be the accessible field spatial frequencies, being  $\mathbf{k}_{\parallel} \leq k_0 NA$ . The spatial frequencies beyond  $k_0 NA$  cannot be recorded for a given microscope objective with given NA.

Though I claim that spatial frequencies beyond  $k_0 NA$  cannot be recorded, it will be shown later that the accessible spatial frequencies are not limited by the condition  $\mathbf{k}_{\parallel} \leq k_0 NA$  because of the frequency mixing between the  $\chi$  and  $\mathbf{E}$ .

The Eq.(1.14) helps us in determining the quantitative linear susceptibility, which provides the relative permittivity of the object  $\varepsilon(\mathbf{r})$  in three-dimensions. For this the measured diffracted field has to be computed in the Eq.(1.14) taking in to account the polarization, and the vectorial nature of the field. The rigorous computation to reconstruct the permittivity map of the sample is explained in detail in next chapter.

### 1.5.3 Born approximation

A common approximation that is most prevalent in the tomographic diffractive microscopy (TDM) is the Born approximation [19, 34]. To understand the Born approximation it is important to understand the optical transfer function (OTF).

#### Optical transfer function

The optical transfer function (OTF) can be well explained with the understanding of the point-spread-function (PSF) of a microscope. As shown in Fig. 1.3, consider a tiny point object as sample which is much smaller than the diffraction limit specified by the Rayleigh criterion. The object will be visible on the microscope but it would appear larger than the real size of the object under observation. This is due to the diffraction as described in the previous section. Thus PSF can be defined as a 3D image of the point like object. Usually, 3D PSF is sharper in  $x$  and  $y$  plane compared to the  $z$  plane. In general, optical microscopes have better lateral resolution than the axial resolution. The PSF is dependent on the wavelength of light used for observation in microscope and the objective used. The degree to which the PSF spreads defines the quality of the microscope.

If there exists a linear relationship between object  $O$  and the image formed by the microscope it is quantified by the optical transfer function. This provides a quantitative criterion to describe quality of a microscope. The image  $G$  formed on the microscope can be defined as:

$$\begin{aligned} Image &= Object * PSF, \\ G &= O * h, \end{aligned} \tag{1.15}$$

which is a convolution of object  $O$  with PSF  $h$ .

Optical transfer function is the Fourier transform of PSF which is  $\tilde{h}$ . The Fourier transform of Equation (1.15) yields,

$$\tilde{G} = \tilde{O}\tilde{h}. \quad (1.16)$$

As explained earlier, not all the light emerging out of sample is collected by the microscope, only plane waves with  $\|\mathbf{k}_{\parallel}\| < k_0 \text{ NA}$  are detected. The  $\tilde{h}$  defines the accessible frequencies corresponding to a particular objective in the Fourier transform domain. The  $\tilde{h}$  is a low pass filter, frequencies above a certain cut-off frequency cannot be detected for a particular NA. The size of the cut-off frequency defines the NA in Fourier domain. Later, the link between the OTF and to obtain the permittivity of the object is discussed. The accessible frequencies of OTF are different for transmission and reflection configuration optical microscope. These configurations and their corresponding OTF's are discussed in detail later in this chapter.

### Linear link between diffracted field and 3D relative permittivity

Born approximation utilizes the diffracted field's amplitude and phase, and considers diffraction as a phenomenon of simple diffusion, neglecting contribution due to the multiple scattering. That is in the single scattering regime, when the samples are well separated there will be no electromagnetic coupling. This leads us to only interference between the fields scattered by different scatterers in the sample and diffraction [35].

Born approximation is valid if the field diffracted by the object  $\mathbf{E}_d$  is very small compared to the reference field  $\mathbf{E}_0$ , which is the field observed without the presence of the object. This is typical when the object is of low contrast, for typical values of lower refractive index contrasts implying weaker scattering. For weak-scattering the convergence of the Born series and sets the validity of the Born approximation, is known in the literature [36–42] as

$$ka\Delta n \ll 1 \quad (1.17)$$

where,  $\Delta n$  is the refractive index contrast and  $a$  being the radius of the sphere or the radius of an infinite cylinder shape. This theoretical common bound of the validity of the Born approximation provides insights into the objects that can be imaged under born approximation case.

From the previous section it can be seen that, total field ( $\mathbf{E}(\mathbf{r})$ ) can be expressed as,

$$\mathbf{E}(\mathbf{r}) = \mathbf{E}_0(\mathbf{r}) + \mathbf{E}_d(\mathbf{r}) \quad (1.18)$$

Under the Born approximation the Eq.(1.18) can be considered as  $\mathbf{E}(\mathbf{r}) \approx \mathbf{E}_0(\mathbf{r})$ , with the field inside the object is approximately equal to the reference field.

In practice, this approximation is used in TDM with two additional simplifications [5, 7, 43–55]. Firstly, any polarization effect is neglected and the field is considered as scalar quantity. Secondly, the object is considered to be in a homogeneous medium, i.e.  $\mathbf{E}_0$  becomes equal to the illumination field  $\mathbf{E}_{inc}$  (incident field),

namely a plane wave. So, the Eq.(1.12) becomes,

$$E_d(\mathbf{r}) = k_0^2 \int_{\Omega} \bar{G}(\mathbf{r}, \mathbf{r}') \chi(\mathbf{r}') E_{inc}(\mathbf{r}') d\mathbf{r}'. \quad (1.19)$$

To solve the above equation we have to calculate the corresponding Green's function. Since the Eq.(1.19) is scalar in nature, for a position  $\mathbf{r}$ , which is sufficiently far away from the object i.e. in the far-field for a given wave vector of direction  $\mathbf{k}$ , the scalar Green's function can be approximated as,

$$\bar{G}(\mathbf{r}, \mathbf{r}') = \frac{e^{ik_0 r}}{4\pi r} e^{-i\mathbf{k} \cdot \mathbf{r}'}, \quad (1.20)$$

with  $\mathbf{k} = k_0 \frac{\mathbf{r}}{r}$  and  $r = |\mathbf{r}|$ . Using Eq.(1.20) in Eq.(1.19), we obtain:

$$E_d(\mathbf{r}) = k_0^2 \frac{e^{ik_0 r}}{4\pi r} \int_{\Omega} \chi(\mathbf{r}') e^{-i(\mathbf{k} - \mathbf{k}_{inc}) \cdot \mathbf{r}'} d\mathbf{r}'. \quad (1.21)$$

The above equation can be rewritten with Fourier transform as follows:

$$\begin{aligned} E_d(\mathbf{k}, \mathbf{k}_{inc}) &\propto \tilde{\chi}(\mathbf{k} - \mathbf{k}_{inc}) \\ &\propto FT_{3D} [\chi(\mathbf{k} - \mathbf{k}_{inc})] \end{aligned} \quad (1.22)$$

Thus, in the far field, the diffracted field with a wave vector  $\mathbf{k}$  for a wave vector of illumination  $\mathbf{k}_{inc}$  is linearly related to 3D relative permittivity contrast of the object [19].

The object is illuminated with varying angles of incidence ( $\mathbf{k}_{inc}$ ), the amplitude and phase of diffracted field corresponding to varying angle of incidence is retrieved. The object is then reconstructed by a numerical inversion process, using a simple 3D inverse Fourier transform of the spatial frequency map obtained by synthetic aperture (explained in the next section). With this approach, experimental 3D reconstructions along transverse resolution are almost two times better than the Rayleigh criterion predictions [5, 7, 52].

#### 1.5.4 TDM: synthetic numerical aperture

From the holograms, 2D complex diffracted field is extracted. The diffracted field's spatial frequencies will be confined to a radius of  $k_{\parallel} \leq k_0 NA$  in the Fourier domain. This data can be projected on to a sphere of radius  $k_0$  as shown in Fig. 1.7 to form a cap of sphere. As we vary the  $k_{inc}$ , the angle of incidence of the incident field ( $\mathbf{E}_{inc}$ ), we measure complex diffracted field ( $\mathbf{E}_d$ ) for each such incidence. Each of the measured 2D diffracted field ( $\mathbf{E}_d$ ) will be projected on a sphere to form a individual cap of sphere. This provides 3D Fourier components of the diffracted field for a particular incidence in the form of a cap of sphere.

Each such individual cap of sphere can be placed in a single Ewald's sphere called synthetic aperture satisfying the condition  $\mathbf{k} - \mathbf{k}_{inc}$ . The formation of the synthetic aperture in transmission and reflection cases are explained in detail later

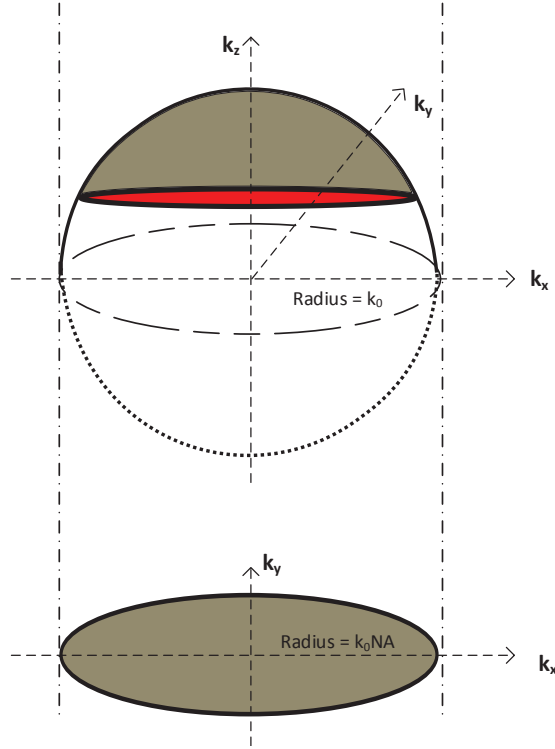


**Figure 1.7 :** Projection of 2D diffracted field of radius  $k_0NA$  on to a sphere of radius  $k_0$  to form a cap of sphere.

in this section. From the Born approximation we understood that this 3D Fourier components are related to the 3D object properties and its reconstruction through Eqn. 1.22.

It was noted in the previous section that due to the frequency mixing between the  $\chi$  and  $\mathbf{E}$  in the diffracted field Eq. 1.14, the accessible spatial frequencies of  $\chi$  would depend on the spatial frequencies of  $\mathbf{E}$ . This means that it is possible to find the diffracted field beyond the  $k_0NA$ . As already stated in the TDM, sample is illuminated with varying angle of incidence ( $\mathbf{E}_{inc}, \mathbf{k}_{inc}$ ), the field inside the sample changes with each illumination, each diffracted field measurement ( $\mathbf{E}_d, \mathbf{k}_d$ ) yields different accessible spatial frequencies. These several different spatial frequencies ( $\chi$ ) corresponding to varying ( $\mathbf{E}_{inc}$ ) incident field are combined together to form a synthetic aperture which has a radius of  $2k_0NA$ [56].

It has to be noted that to perform the tomography, either sample can be rotated [28, 57] or illumination can be varied [5, 30, 58–60]. S. Kou and C. Sheppard showed that when high NA apertures are used for TDM measurements [61, 62] there is no significant difference between these two methods. For practical reasons, change of angle is preferred coupled with high NA objectives.

Using the data collected by either rotating the sample or rotating the illumination 3D synthetic aperture is formed. In this thesis, the illumination is rotated [33]. This 3D synthetic aperture in the Fourier space is called the optical transfer function as

defined in the section. 1.5.3. The OTF is approximated to one at the points that are detectable under a given microscope and zero elsewhere.

The general Eq.(1.21) can be written as,

$$\begin{aligned} E_d(\mathbf{k}, \mathbf{k}_{inc}) &\propto \tilde{\chi}(\mathbf{k} - \mathbf{k}_{inc}) \\ &\propto \tilde{\chi}(\mathbf{K}) \end{aligned} \quad (1.23)$$

where,  $\mathbf{K} = \mathbf{k} - \mathbf{k}_{inc}$  is the object spatial frequency.

Then the reconstruction of the permittivity map can be written as,

$$\begin{aligned} \tilde{\chi}_{rec}(\mathbf{r}) &= \int \tilde{\chi}(\mathbf{K}) \times OTF(\mathbf{K}) e^{i\mathbf{K}\cdot\mathbf{r}} d\mathbf{k} \\ &= \chi(\mathbf{r}) * FT^{-1}[OTF] \\ &= \chi(\mathbf{r}) * PSF(\mathbf{r}) \end{aligned} \quad (1.24)$$

where,  $*$  is the convolution operator, PSF is the synthetic point spread function. One can determine the PSF by inverse Fourier transforming the optical transfer function (OTF). Depending on the illumination and detection schema implemented in TDM, the accessible spatial frequencies and the position of access in the OTF varies. The formation of synthetic aperture OTF is explained with an example schema of transmission as follows.

### Transmission TDM configuration

For the transmission configuration of TDM, let us assume that both the condenser used for illumination and objective used for detection have the same numerical aperture (NA). As shown in Fig. 1.10, a sample is illuminated and the light transmits through the sample and the detection is performed on the opposite side of the illumination.

Let us build the synthetic numerical aperture for transmission configuration of TDM step by step. Consider the sample is illuminated with normal incidence (NI) as shown in Fig. 1.10.A. The Fourier frequency components corresponding to illumination are detected in 2D and they are transformed to form a cap of sphere. This cap of sphere has to be positioned in the Fourier domain depending on the  $\mathbf{k}_{inc}$  and  $\mathbf{k}$  for each detection point on the detector. The position of each detection point is calculated from  $\mathbf{k} - \mathbf{k}_{inc}$ . In the case of normal incidence the illumination angle is equal to zero. The diffracted field is detected on the pixels inside NA in Fourier space which form an angle with the optical axis. Each pixel is shifted to match its spatial frequency component which is determined from  $\mathbf{k} - \mathbf{k}_{inc}$ , which was already in the form of cap of sphere and to be positioned. Now, the final step is to position the cap of sphere in a global synthetic sphere satisfying the condition  $\mathbf{K} = \mathbf{k} - \mathbf{k}_{inc}$  for each pixel. It has to be noted that red spot show in Fig. 1.10.A is the specular transmission component, which corresponds to the illumination field. The specular transmission component for the transmission configuration hides the zero spatial frequency component.

Consider a second case, the sample is illuminated with an angle close to the numerical aperture from  $-\mathbf{r}_{\parallel}$  direction as shown in Fig. 1.10.B. The corresponding

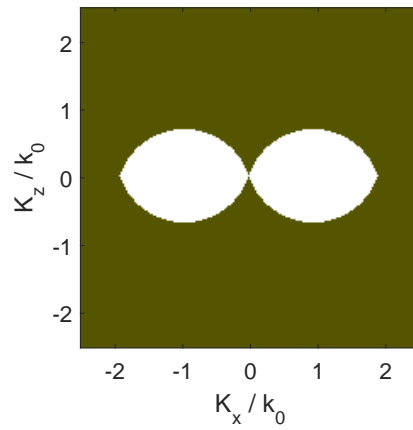


**Figure 1.8 :** Center cut along the 3D synthetic aperture (optical transfer function) for transmission configuration, which is a torus located at the center of the synthetic sphere in 3D. The white region represents the detectable spatial frequency region of the OTF for a given numerical aperture of  $NA=0.95$ .

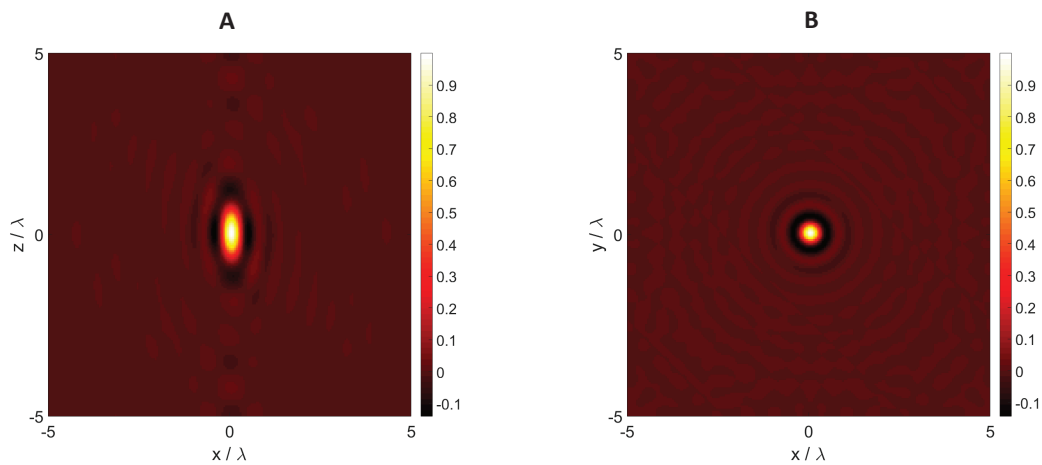


**Figure 1.9 :** The real part of 3D PSF (3D Fourier transform of optical transfer function) for transmission configuration. Fig.A: Center cut (for  $x$ - $z$  at  $y=0$ ). Fig.B: Center cut (for  $x$ - $y$  at  $z=0$ ).

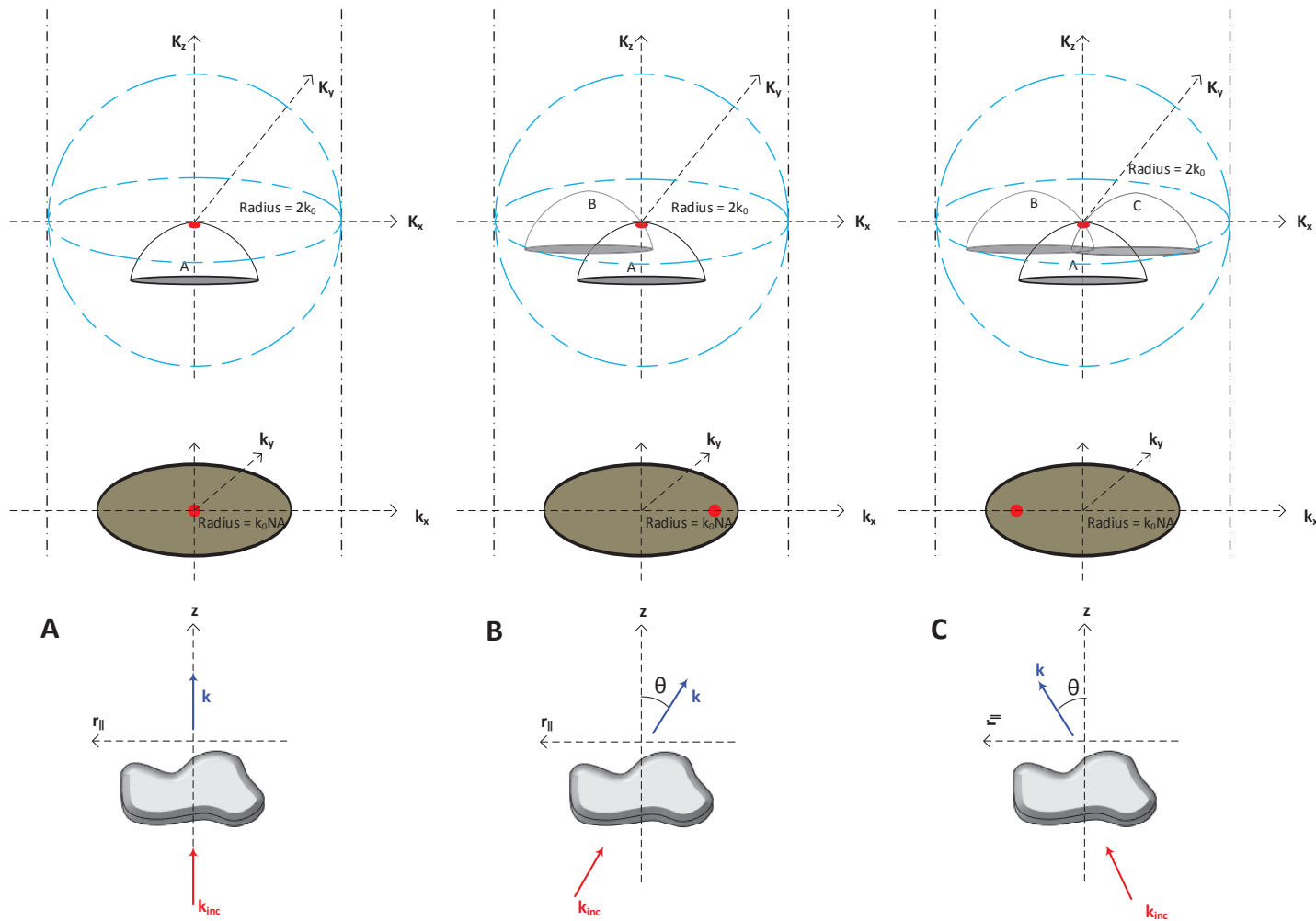


**Figure 1.10 :** Synthetic numerical aperture formation in transmission configuration of TDM. In Fig.A, object is illuminated in normal incidence, the diffracted field is shown in Fourier domain with red dot being the specular focus of the incident field. The diffracted field is projected to form a cap of sphere and positioned on the synthetic Ewald's sphere satisfying the condition  $\mathbf{K} = \mathbf{k} - \mathbf{k}_{inc}$ . Similarly for Fig.B, object is illuminated with extreme angle along positive  $r_{\parallel}$  direction and cap of sphere is positioned according to  $\mathbf{K} = \mathbf{k} - \mathbf{k}_{inc}$ . It can be noted that the specular focus of incident field is located at the center of the Ewald's sphere or synthetic 3D aperture. For Fig.C, object is illuminated with extreme angle along negative  $r_{\parallel}$  direction and the cap of sphere is positioned.

2D spatial frequency components and the transformation into a 3D cap of sphere is performed. The positioning of this 3D cap of sphere in the synthetic 3D sphere again performed using the condition  $\mathbf{K} = \mathbf{k} - \mathbf{k}_{inc}$ . This 3D cap of sphere is positioned along with the normal incidence cap of sphere which was already positioned, the overlapping pixels are averaged out.

Consider a third case, the sample is illuminated with an angle close to the numerical aperture from  $\mathbf{r}_{\parallel}$  direction as shown in Fig. 1.10.C, the direction is exact opposite to the direction used in the second case. Similar process as stated in the second case is employed and the 3D cap of sphere is positioned in the synthetic 3D aperture and the overlapping pixels are averaged. Because we position cap of sphere inside Ewald's sphere, cap of spheres does not overlap through out. Particularly at the edges of the sphere there is no overlap. Nevertheless, at the location of overlap it will have an effect on the noise reduction but not over the whole 3D OTF [46, 62].

One can continue with many such illumination angles, collecting the diffracted field and the positioning of the each cap of sphere in the 3D synthetic aperture. If all the possible illumination angles were used and detected, the resulting synthetic aperture sphere is a torus positioned in the center [62]. A cut along the center of such a 3D synthetic aperture is shown in Fig. 1.8. It has to be noted that the radius of the synthetic aperture is  $2k_0NA$  compared to the radius of the diffracted field data for one illumination which is  $k_0NA$ .

It is important to note the extension of the PSF along the  $z$  direction as shown in Fig. 1.9.A in comparison to  $x$  or  $y$  direction shown in Fig. 1.9.B. The PSF is longer in  $z$  direction. This is due to the range of frequencies that are accessible along the  $z$  direction of the transmission OTF being smaller compared to the transverse direction  $x$  or  $y$  seen in Fig. 1.8. As matter of fact, the axial resolution in transmission configuration is three time worse than the transverse resolution.

### Reflection TDM configuration

In the reflection configuration of the TDM the  $k_{inc}$  is reversed compared to the transmission configuration. This means that the illumination and the detection are performed with the same objective from the same side. Construction of 3D synthetic aperture for reflection configuration is similar to transmission configuration. It is explained in steps as follows.

Firstly, the sample is illuminated as shown in Fig. 1.11 with an incident field  $\mathbf{E}_{inc}$  with incident wave vector  $\mathbf{k}_{inc}$ . The detection of the reflected diffracted field  $\mathbf{E}_d$  having wave vector  $\mathbf{k}$ . Consider the normal incidence case, the corresponding diffracted field and the projection to obtain the 3D cap of sphere were obtained. This cap of sphere is positioned in the synthetic aperture sphere satisfying the condition  $\mathbf{K} = \mathbf{k} - \mathbf{k}_{inc}$  as shown in Fig. 1.11.A. Due to the illumination and detection being performed on the same side, the cap of sphere is positioned at one of the polar edge of the synthetic aperture.

Let us illuminate the sample with an angle close to the numerical aperture from  $-\mathbf{r}_{\parallel}$  direction as shown in Fig. 1.11.B. The corresponding cap of sphere is positioned at location satisfying  $\mathbf{K} = \mathbf{k} - \mathbf{k}_{inc}$  and averaged out. Similarly, if we illuminate with

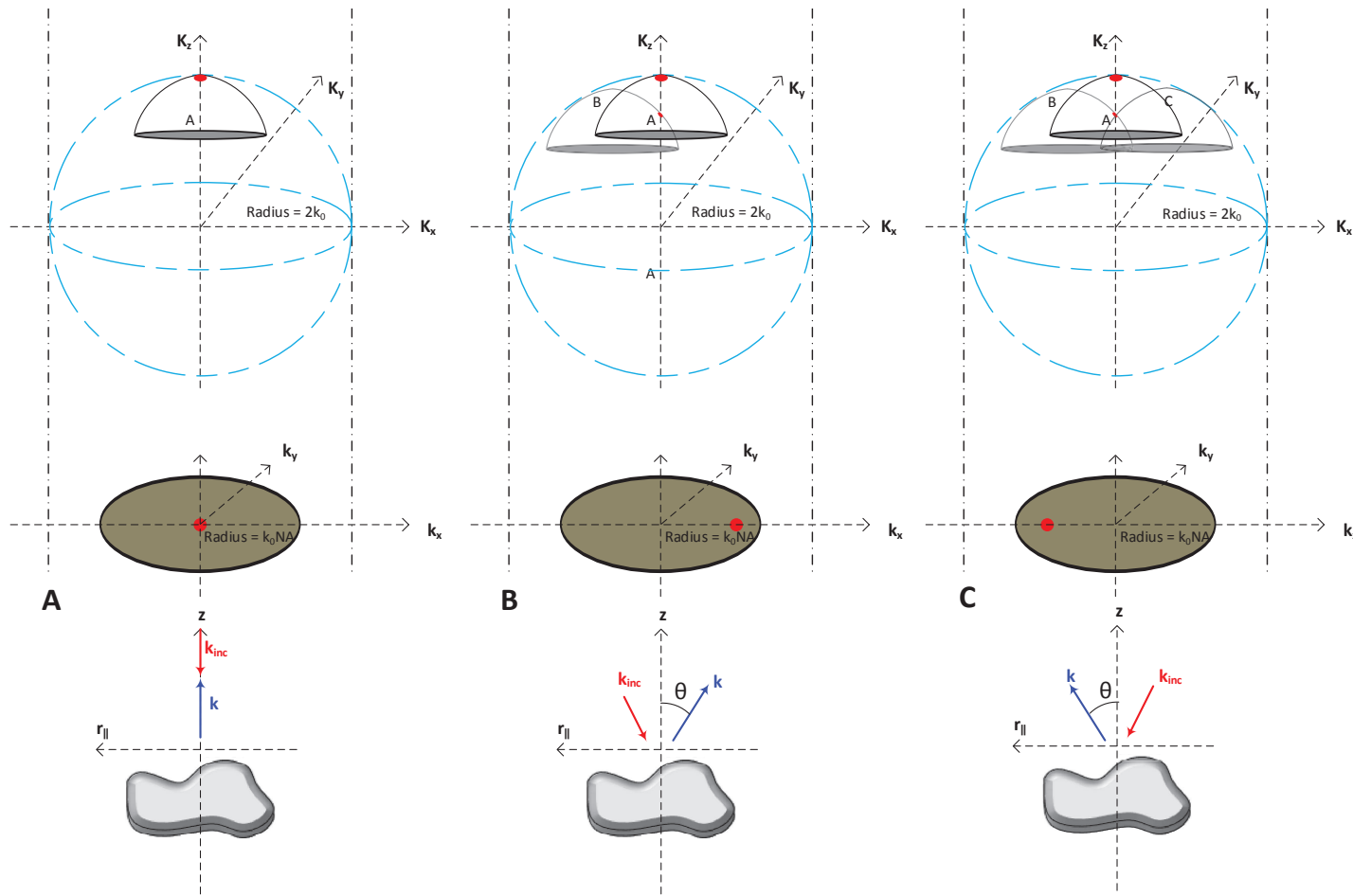


**Figure 1.11 :** Synthetic numerical aperture formation in reflection configuration of TDM. In Fig.A, object is illuminated in normal incidence and detected in the same direction, the diffracted field is shown in Fourier domain with red dot being the reflected specular focus of the incident field. The diffracted field is projected to form a cap of sphere and positioned on the synthetic Ewald's sphere satisfying the condition  $\mathbf{K} = \mathbf{k} - \mathbf{k}_{inc}$ . Similarly for Fig.B, object is illuminated with extreme angle along positive  $r_{\parallel}$  direction and cap of sphere is positioned according to  $\mathbf{K} = \mathbf{k} - \mathbf{k}_{inc}$ . It can be noted that the specular focus of incident field is located along the  $\mathbf{k}_z$  axis of the Ewald's sphere or synthetic 3D aperture. For Fig.C, object is illuminated with extreme angle along negative  $r_{\parallel}$  direction and the cap of sphere is positioned.

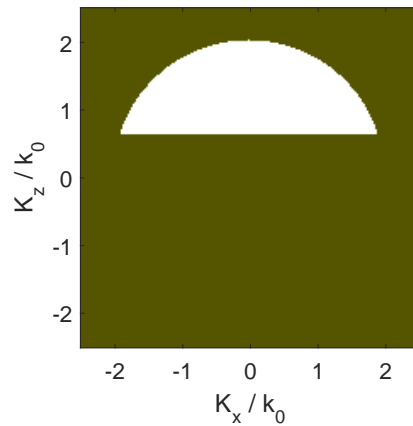


**Figure 1.12 :** Center cut along the 3D synthetic aperture (optical transfer function) for reflection configuration with  $NA=0.95$ , which is a spherical solid incomplete sphere located at the polar end of the synthetic sphere in 3D. The white region represents the detectable spatial frequency region of the OTF for a given numerical aperture.

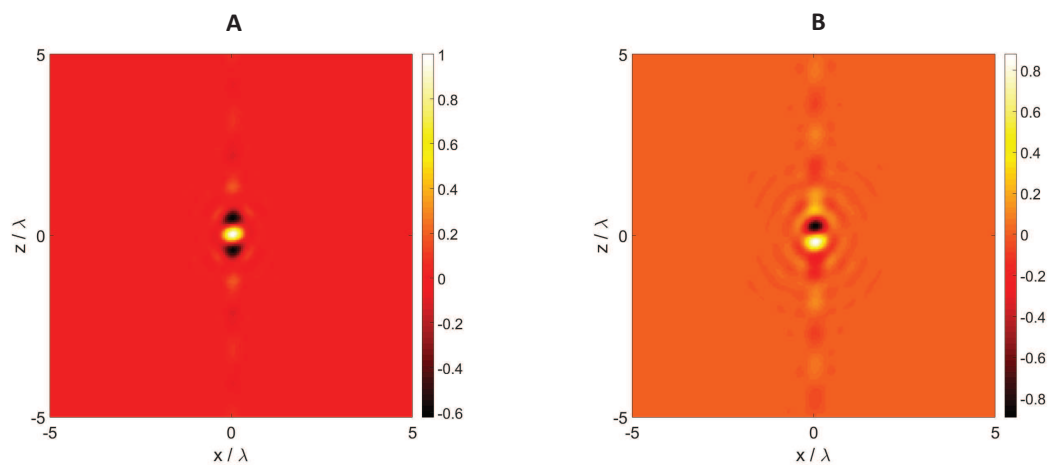


**Figure 1.13 :** The 3D PSF (Fourier transform of 3D optical transfer function) of reflection configuration. It is complex in nature. Fig. **A**: Center cut ( $x$ - $z$  at  $y=0$ ) of real part of 3D PSF . Fig. **B**: Center cut of imaginary part of the 3D PSF ( $x$ - $z$  at  $y=0$ ).

an angle close to the numerical aperture from  $\mathbf{r}_{\parallel}$  direction as shown in Fig. 1.11.C, we can position the corresponding cap of sphere in the synthetic aperture sphere.

By continuing with several such illuminations in the reflection configuration, it is possible to build a synthetic aperture corresponding to reflection TDM as shown in Fig. 1.12. It can be seen that the OTF in Fig. 1.12 is not symmetrical about zero, the inverse Fourier transform of such an OTF will yield a complex point spread function. The real part shown in Fig. 1.13.A shows a PSF with negative rebounds which will corrupt the reconstruction of the object. Whereas, the imaginary part is asymmetric. If the object under observation has complex permittivity, then the complex PSF will mix with the  $\varepsilon'$  and  $\varepsilon''$  in the reconstruction.

### Complete TDM configuration

This is an ideal case in which the object is illuminated under all possible directions ( $4\pi$  radians) with  $\mathbf{E}_{inc}$  and detected under all possible directions ( $4\pi$  radians) the diffracted field  $\mathbf{E}_d$ . In such a case we would obtain a perfect solid sphere with radius  $2k_0NA$  as shown in Fig. 1.14. The OTF for such a configuration is also constructed using the same condition being  $\mathbf{k} - \mathbf{k}_{inc}$  as explained in transmission or reflection configuration. The corresponding PSF will be like as shown in Fig. 1.9.B, but isotropic in all directions.

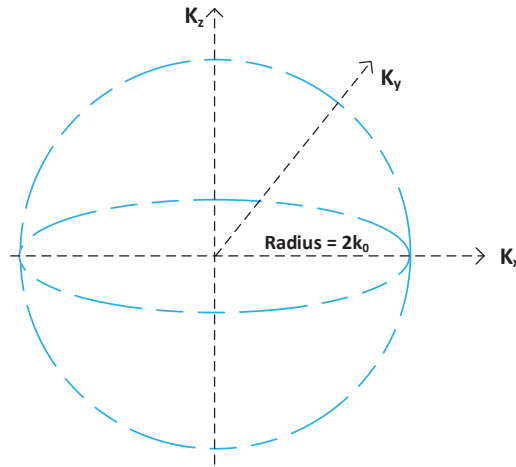


**Figure 1.14 :** *Optical transfer function corresponding to a complete configuration of a TDM provided the illumination and the detection are performed in all possible directions.*

### Resolution of synthetic aperture TDM

In summary, the Rayleigh criterion defined the transverse resolution for the classical wide field microscope, i.e. the smallest distance center to center  $\Delta r$  between two point objects that can be resolved:

$$\Delta r = \frac{0.61 \lambda}{NA} = \frac{0.61 \lambda}{n_i \sin \theta_{max}} \quad (1.25)$$

where NA is the numerical aperture of the objective. Generally the Born approximation synthetic aperture reconstructed using tomographic microscopy achieves an improved theoretical transverse resolution  $\Delta r$  [63]:

$$\Delta r = \frac{0.61\lambda}{\text{NA} + \text{NA}_{\text{inc}}}, \quad (1.26)$$

where  $\text{NA}_{\text{inc}}$  is the numerical aperture of the objective used for illumination.

So, synthetic aperture TDM provides twice better transverse resolution as classical wide-field microscopy, provided the illumination and detection are performed with same numerical aperture objective. The axial resolution is better in case of the reflection configuration compared to the classical wide-field microscopy. The best recipe would be to combine both transmission and reflection spatial frequency components or to have access to the  $4\pi$  steradians scattered field data in all possible directions. In this context, E. Mudry et.al proposed the deposition of a sample on a mirror and measure the diffracted field in the reflection configuration [3]. On the other hand the sample can be rotated to detect all the possible frequencies [64].

### 1.5.5 Rytov approximation

Another linear approximation of the diffracted field to obtain permittivity of object is the Rytov approximation [27, 65, 66]. We have seen in section. 1.5.3 that the Born approximation takes into considering that the total field within the object can be approximated by the incident field, which is usually valid when the index contrast is low. However, even low contrast can lead to a significant phase difference between the two fields if the object is large enough. It is usually considered that the Born approximation may remain valid as long as the phase shift induced by object remains below  $\pi$  [27]. The Rytov approximation is meanwhile no longer dependent on the size of the object. It is however sensitive to the gradient of the refractive index. It has to be noted that this approximation uses the same simplifications as that of Born approximation, namely a scalar approach and homogeneous space.

Under this approximation, the fields are usually expressed with complex phases, which leads to the following expressions for the total field  $E$  and reference field  $E_0$ :

$$E(\mathbf{r}) = e^{\phi(\mathbf{r})} \text{ and } E_0(\mathbf{r}) = e^{\phi_{\text{inc}}(\mathbf{r})}. \quad (1.27)$$

The validity condition for Rytov approximation is given as,

$$\|\nabla(\phi(\mathbf{r}) - \phi_{\text{inc}}(\mathbf{r}))\|^2 \ll k_0^2 |\chi(\mathbf{r})|. \quad (1.28)$$

We can then show that in far field, the diffracted field  $E_d(\mathbf{k}, \mathbf{k}_{\text{inc}})$ , the incident field  $E_0(\mathbf{k}, \mathbf{k}_{\text{inc}})$  and  $\chi$  are connected by the relation [67]:

$$E_0(\mathbf{k}, \mathbf{k}_{\text{inc}}) \ln \left[ 1 + \frac{E_d(\mathbf{k}, \mathbf{k}_{\text{inc}})}{E_{\text{inc}}(\mathbf{k}, \mathbf{k}_0)} \right] \propto \tilde{\chi}(\mathbf{k} - \mathbf{k}_{\text{inc}}). \quad (1.29)$$

The above equation is valid for objects which are weakly absorbing and diffracting with low refractive index contrast  $\Delta n$ ,  $\nabla[\phi(\mathbf{r}) - \phi_{\text{inc}}(\mathbf{r})] \simeq k_0 \Delta n(\mathbf{r})$  and  $\chi \simeq 2\Delta n$ .

The validity condition therefore simplifies  $\Delta n(\mathbf{r}) \ll 1$  in this case. In practice, when  $\Delta n$  exceeds about  $10^{-2}$ , the approximation deteriorates rapidly, even on small objects [27]. The approximation of Rytov is not necessarily always better than the Born approximation, but it is more suited to large low-contrast objects. It is thus in particular possible to provide 3D reconstructions without distortion of biological cells near the sizes of  $10\mu m$ , unlike the Born approximation [67, 68]. One of the drawbacks is that the phase obtained from the reconstruction has to be unwrapped to have practical understanding about the object.

### 1.5.6 Improvements to TDM

Approximations presented above provides a simple means of retrieving the quantitative information about the object under observation. As the goal is to strive for super-resolution with better quality and precision it is important to consider other parameters such as polarization of light, measurement environment, wavelength etc.. In reality, the Eq.( 1.14) has to be solved rigorously without approximations. That would provide a closer estimation to the electromagnetic behavior of light. This means that electromagnetic fields are treated as vectorial fields. Light polarized in a single direction (e.g. x-direction) provides well resolved images in that particular direction. The true link between the scattered field and the object is through full-vectorial field taking into consideration the polarization. The diffracted field measured full-vectorial with light polarized in all directions provide isotropic resolution in all the directions [33]. Later, in the thesis it is explained how to implement a full-vectorial TDM to obtain isotropic resolution images in the transverse direction.

Approximations does not take into account multiple scattering between the sample-sample, sample-substrate etc., taking multiple scattering into account is also expected to improve the imaging overall [69–73].

#### Our specificity

Object deposited on a opaque substrate presents challenge to obtain the 3D permittivity map. Scanning electron microscope (SEM), Atomic force microscope (AFM) are surface probing techniques [74]. TDM on the other hand can work in reflection to obtain the 3D permittivity map for samples of reflecting nature with. By taking into account the substrate and considering it in the calculations can provide quality 3D reconstructions (shown later). These calculations require specific algorithms which are developed in our Team SEMO, Institute Fresnel. The details about the multiple scattering and algorithms are presented in the third chapter.

Measurements can be performed with multiple wavelengths using TDM as shown in Fig. 1.15. An object illuminated by, let us say  $\lambda = 632.8nm$  will have a shorter spatial frequency cut-off compared to  $\lambda = 475nm$ . Provided there is no dispersion, by combining the shorter and longer wavelength measurements ( $\lambda = 632.8nm + \lambda = 475nm$ ) in the synthetic aperture sphere or OTF and averaging fills more spatial frequency points compared to a single wavelength measurement. This would provide a better PSF compared to single wavelength measurement reconstruction of

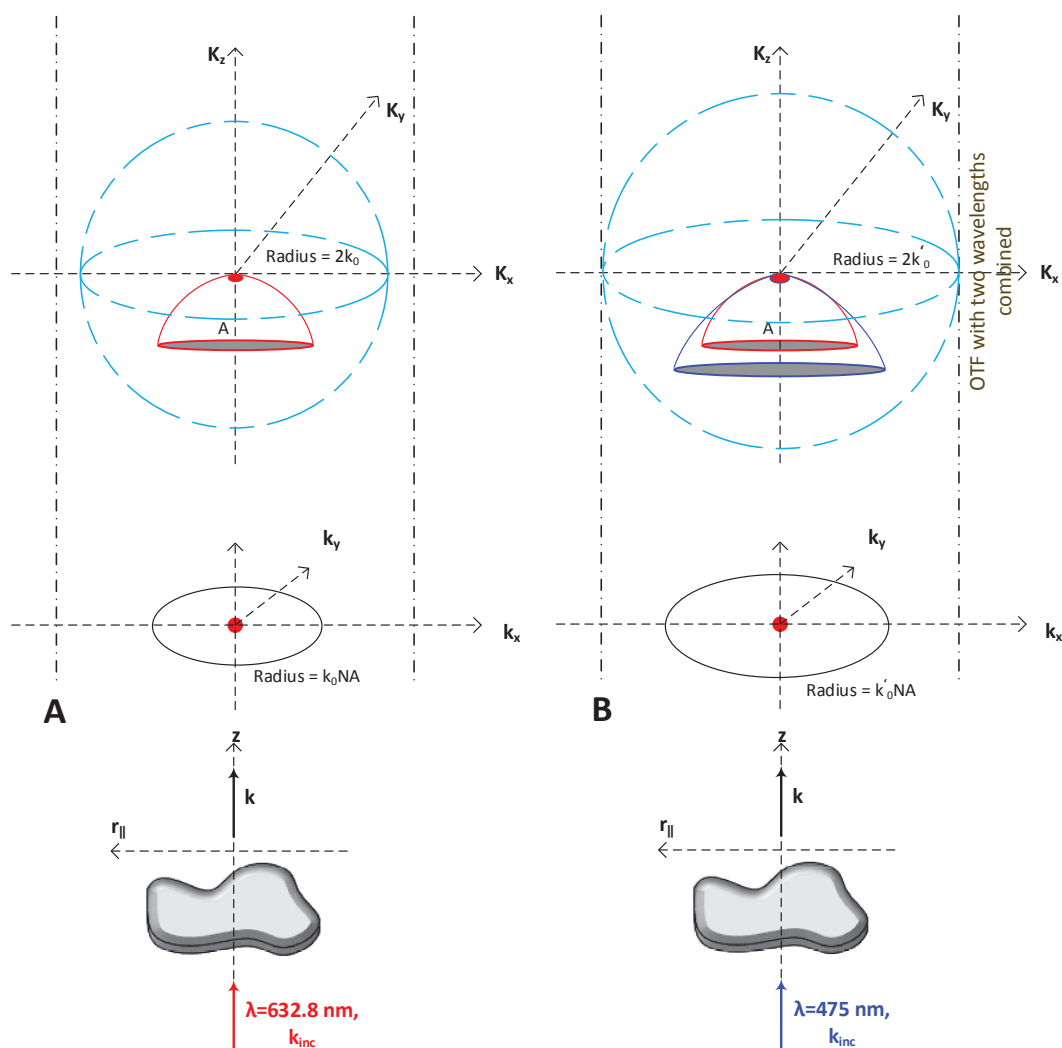


**Figure 1.15 :** In Fig.A, object is illuminated by  $\lambda = 632.8\text{nm}$ , wavelength of light at normal incidence, the diffracted fields 2D Fourier components are measured with a NA (i.e. of  $\lambda = 632.8\text{nm}$ ) and projected to form a cap of sphere. Similarly, in Fig.B, object is illuminated by  $\lambda = 475\text{nm}$  wavelength light at normal incidence, the diffracted fields 2D Fourier components are measured with a NA (i.e. of  $\lambda = 475\text{nm}$ ) and projected to form a cap of sphere. Note that the radius of 3D synthetic aperture varies from  $2k_0$  to  $2k'_0$  due to wavelength. These two measurements can be combined in a synthetic aperture provided there is no dispersion, since they belong to the same object at different wavelengths. Optical transfer function corresponding to two wavelengths when combined and averaged at overlapping points fills additional points in the 3D synthetic aperture sphere compared to a single wavelength configuration. This can be performed in all possible directions and combined together to fill the additional spatial frequency information about the object compared to single wavelength measurement.

sample. J. Jung et.al., present the results obtained with different wavelengths on a sample [75], but we would like to go a step further and combine the multi-wavelength data to better fill the OTF.

This section presented the diffraction theory to understand the TDM and it was compared with classical wide field microscope. Some approximations employed to compute the quantitative image of the object and the possible improvements to the TDM were briefly presented. The following section will present the experimental implementation of the TDM which permits us to realize the above mentioned improvements.

## 1.6 Experimental Set-up

The tomographic diffractive microscope can be implemented in either transmission configuration or reflection configuration as explained in previous section. The measurements performed in this thesis employed a reflection configuration TDM due to its advantages. To summarize the advantages of the reflection configuration: it provides higher Fourier spatial frequency data along the optical-axis of the microscope in comparison to the transmission configuration, reflective samples can be imaged, it requires taking into account the substrate etc. We have recently addressed the specific features of such a configuration [76], not many research groups are involved in such research activity addressing the need of reflective samples which cannot be measured in transmission using TDM. The interest is also to probe the samples that are reflective in nature or that are deposited on a opaque substrate. Note that most of the TDM set-ups can only work in transmission configuration. So, the preferred configuration is reflection configuration for our research group.

Before the experimental implementation of the setup is presented, I present you the experimental retrieval of the phase information.

### 1.6.1 Experimental methods for phase imaging

Quantitative phase imaging is obtaining the phase image of an object quantitatively. The quantitative phase information cannot be recorded directly because phase varies fast. Present cameras are not fast enough to record phase. The frequency of the visible light is between 405 THz and 700 THz. Camera at best can record 500 MHz or little more. But cameras are capable of recording the intensity information of light. By using the intensity image, the phase information can be obtained in two steps indirectly.

1. First step is to record the phase variation by recording the intensity information. The phase information of the object is encoded in the intensity image by means of e.g. interference [56], ptychography [77], Shack-Hartmann sensor[78] etc.
2. From this intensity information the phase is extracted. The second step is to recover the quantitative phase information from the intensity image digitally by processing the holograms or the recorded intensity information.

It has been noted that the phase microscopy detects only the 2D phase for a given volume object as shown in Fig. 1.4 for a particular plane wave incident on the object. It does not directly provide the quantitative information about the sample. Nevertheless, the quantitative information about the sample is coded in the 2D phase information. In the previous section, the link between the phase information and the quantitative 3D object is established.

The first step as explained earlier is an experimental method for encoding the phase in the intensity image. Different experimental methods are presented in this section. The incident field can be expressed in space domain as follows:

$$\mathbf{E}_{inc}(\mathbf{r}) = E_a(\mathbf{r})e^{i\phi(\mathbf{r})} \quad (1.30)$$

where  $\mathbf{r}$  is the position vector,  $E_0$  is the amplitude, and  $\phi$  is the field phase. The image on a detector is recorded as intensity if one observes the  $\mathbf{E}_{inc}(\mathbf{r})$ ,

$$\mathbf{I}_{inc}(\mathbf{r}) = |\mathbf{E}_{inc}(\mathbf{r})|^2 \quad (1.31)$$

as such the phase information cannot be recovered.

When the  $\mathbf{E}_{inc}(\mathbf{r})$  is incident on an object, the object scatters the incident field, this is called scattered field  $\mathbf{E}_d(\mathbf{r})$ . Then the total field is given by  $\mathbf{E}(\mathbf{r}) = \mathbf{E}_{inc}(\mathbf{r}) + \mathbf{E}_d(\mathbf{r})$ .

If the total field  $\mathbf{E}(\mathbf{r})$  is interfered with another field called reference field  $E_R$  whose phase is known, the field detected  $\mathbf{E}_{intf}$  (interference) will be as follows,

$$\mathbf{E}_{intf}(\mathbf{r}) = \mathbf{E}(\mathbf{r}) + \mathbf{E}_R(\mathbf{r}) \quad (1.32)$$

Then the resulting intensity from the above equation has the desired phase term  $\phi(\mathbf{r})$  as shown below,

$$\mathbf{I}_{intf}(\mathbf{r}) = |\mathbf{E}(\mathbf{r})|^2 + |\mathbf{E}_R(\mathbf{r})|^2 + 2|\mathbf{E}(\mathbf{r})| \cdot |\mathbf{E}_R(\mathbf{r})| \cdot \cos[\Delta\phi(\mathbf{r})] \quad (1.33)$$

where,  $\Delta\phi(\mathbf{r})$  represents the phase difference. As the phase of the  $\mathbf{E}_R(\mathbf{r})$  is known (usually a plane wavefront), it is possible to recover the  $\Delta\phi(\mathbf{r})$  term, which is of interest.

Equation 1.33 represents the interference method used to recover phase. Several such methods are presented briefly below that can be used to recover the  $\phi(\mathbf{r})$ .

### Off-axis or shear methods for phase imaging

**Principle:** A reference beam  $\mathbf{E}_R(\mathbf{r})$  is interfered with the total field  $\mathbf{E}(\mathbf{r})$  from an off-axis as shown in the fig. 1.16. Mach-Zehnder interferometer is one such off-axis method used in the optical testing [79]. Mach-Zehnder interferometer consists of two arms object arm and reference arm. The object whose phase has to be reconstructed is positioned in the object arm. The light passes through the object in transmission and carries the phase information of the object. Reference beam whose phase is known (usually a plane wavefront) propagates along the reference beam path. Reference beam and the object beam are interfered with the help of a beam splitter (BS2

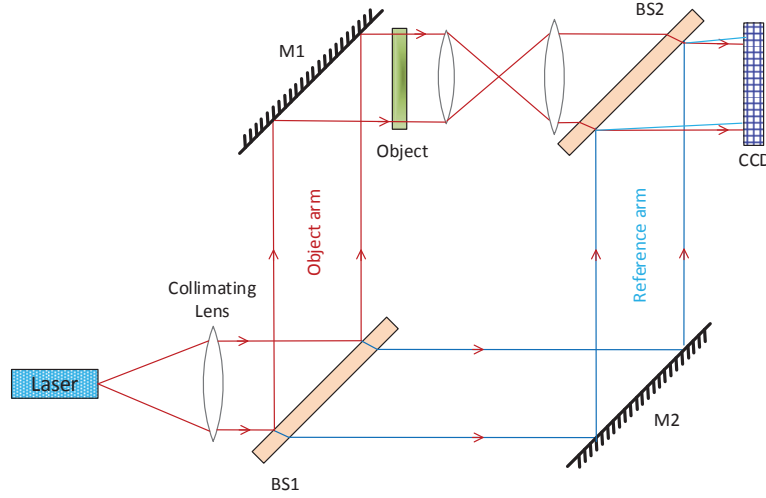


**Figure 1.16 :** Mach-Zehnder interferometer:  $M1$ ,  $M2$ , mirrors;  $BS1$ ,  $BS2$ , beam splitters. The interferometer consists of two arms reference arm and object arm. The beam passing through the object encodes the information about the object. The reference beam is interfered with the object beam from off-axis. The interference pattern is recorded on the CCD.

seen in Fig. 1.16). The beam splitter  $BS2$  helps in creating an off-axis angle on the reference beam. Both object arm and the reference arm are adjusted to have same path length from source to the detector. As the object beam and the reference beam arrive at the detector with an angle with respect to each other an interference pattern is formed. The intensity pattern which corresponds to the interference is recorded on the CCD as hologram. Let us consider a simpler interference in one dimension only, i.e. in  $\mathbf{x}$ . Then the interference pattern formed is given by the equation,

$$I_{intf} = I + I_R + e^{-i\alpha x} E + e^{i\alpha x} E^* \quad (1.34)$$

where  $I$  is the intensity of the total field or object beam,  $I_R$  is the intensity of the reference beam and  $E$  is the total field or the object field (incident field + scattered field) and  $E^*$  is its complex conjugate. The quantitative phase information of interest is recovered from this single intensity image by digital means.

The 2D Fourier transform of the recorded hologram (Eq. 1.34) is performed, resulting in,

$$\tilde{I}_{intf} = \tilde{I} + \tilde{I}_R + \delta_{-\alpha} * \tilde{E} + \delta_{\alpha} * \tilde{E}^*, \quad (1.35)$$

where  $\delta_{\alpha}$  is the Dirac function located at the spatial frequency  $(\alpha, 0)$ . We obtain  $\tilde{I}$  and  $\tilde{I}_R$  at the center of the spatial frequency origin, these terms will have a cut-off frequency of two times that of NA. Whereas the factors  $\delta_{-\alpha} * \tilde{E}$  and  $\delta_{\alpha} * \tilde{E}^*$  are confined to the NA in the Fourier space. Due to the convolution of the Dirac function with  $\delta_{-\alpha} * \tilde{E}$  and  $\delta_{\alpha} * \tilde{E}^*$ , these two terms are shifted from the center of the spatial frequency origin in the Fourier space and centered at  $(\alpha, 0)$  and  $(-\alpha, 0)$ . This shifting will depend on the off-axis angle introduced between the object beam and the reference beam. If the angle is big enough the terms  $\delta_{-\alpha} * \tilde{E}$  and  $\delta_{\alpha} * \tilde{E}^*$

will not overlap with the terms  $\tilde{I}$  and  $\tilde{I}_R$  which are located at the origin. Then, it is possible to have direct access to the complex total field of the object  $\tilde{E}$  knowing  $\tilde{E}_R$ .

Off-axis methods require only one single hologram to recover the phase information. This drastically decreases the sensitivity to external fluctuations. Temporal sampling is high in case of off-axis methods since one intensity image is sufficient. Hence, these methods can be employed in studying real-time changes of a phase object. On the other hand, the spatial frequency of sampling must be high enough to recover the fringe period and requirement of a reference wave are some of its disadvantages.

Digital holographic microscopy [80] and Hilbert phase microscopy [81] are some of the off-axis methods used in quantitative phase-contrast imaging microscope which employs the off-axis interferometry technique to recover the phase information.

### Other methods for phase imaging

Phase-shifting methods [82, 83] involves shifting of the phase relative to the object beam in steps and recording of holograms (interference between scattered field and reference beam) for each phase step. It is possible to calculate the phase from the three or more such phase steps.

In common-path methods [55, 68, 84], the reference beam and the object beam share the same propagation path. The principle can be explained with a simple lateral-shearing interferometer. The incoming beam is amplitude divided in to two or more beams propagating alongside each other. The interference between the beams is recorded and the phase of the wavefront is recovered digitally [85].

The white-light methods [86] a broadband white-light is used as a light source. The low coherence length of broadband sources results in a reduced point-to-point spatial phase noise. Utilizing monochromatic light sources will increase speckle and point-to-point spatial phase noise[87].

These are the main methods used to retrieve phase experimentally. The advantages of each method is as follows: off-axis methods provides fast acquisition rate, phase-shifting methods provide high transverse resolution, common-path methods provide temporal stability and white-light methods spatial uniformity [87] respectively. The disadvantages of each method is as follows: off-axis method require high resolution detector to well sample the interference fringes, phase-shifting methods require more measurements which affects the stability and it is time consuming, recovery of phase is not a straight forward step in common-path method, white-light method require precise adjustment of the object and reference arms. A combination of above methods can also be employed to retrieve the phase information combining the advantages and disadvantages.

A Shack-Hartmann wavefront sensor (SHWFS) [78, 88] can be used to estimate slow phase variations with less pixels on the detector, but microscopy applications require more pixels. So, a advanced wave front sensor called quadri-wave lateral shearing interferometry (QWLSI) [25, 26, 89–91] can also be employed to measure the amplitude and phase.

### 1.6.2 Description of the set-up

The tomographic microscope I have developed is presented on Fig. 1.17. The light source is a low coherence supercontinuum laser (NKT Photonics SuperK Extreme EXW-12), that can be filtered from 450 nm to 800 nm with a variable spectral width thanks to a variable bandpass filter (NKT Photonics SuperK Varia). The laser beam is linearly polarized and then divided into a reference beam and a beam directed towards the sample called sample beam or object beam. The object beam and the reference beam are interfered off-axially. Due to the low coherence any parasitic reflection from the optical components in the object beam path does not interfere with the measurement.

A fast steering mirror (M, Newport FSM-300) permits to control the deflection of the sample beam, while a beam expander and diaphragm D generate a wide collimated beam with near homogeneous power density. This beam illuminates the sample after transmission through the microscope objective (can be varied to have different NA) and the associated tube lens (L). It can be locally assimilated to a plane wave since the dimensions of the object are small compared to the width of the beam. The center of the mirror is conjugated with the center of the sample through the beam expander, the tube lens and the microscope objective. Thus, rotating the mirror varies the illumination angle without shifting laterally the beam on the object. The polar angle of the illumination can be varied over the whole NA of the objective. The field scattered by the object is collected by the microscope objective (Zeiss Epiplan-Apochromat 50 $\times$ , NA = 0.95 or Nikon Apo TIRF oil 100 $\times$ , NA = 1.49) and imaged on a sCMOS camera (Andor Zyla) after passing through relay lenses  $L_2$  and  $L_3$  to obtain a global magnification of about 300.

The magnified object image is detected in image space as it permits to adjust the position of the object directly and the signal to noise ratio is more adapted for small objects in the image space. In case of small objects the diffracted field will be spread over the NA in Fourier space measurement, in image space measurement it would focus at the location of the object. Along with that the specular reflection, the reflection of beam that corresponds to the substrate will have a stronger signal compared to the diffracted field of the sample, the camera dynamic range is not adapted to measure such variation in Fourier space measurement configuration. So, imaging in the image space is preferred compared to Fourier space measurement. The measurement of the reflection from the substrate is used for normalization of the TDM data, so it is also important to measure the specular reflection field. The normalization procedure employed is explained in the next chapter in detail.

After spatial filtering with a pinhole (P) and collimation, the reference beam is coherently superimposed on the image field with an off-axis arrangement thanks to beam splitter  $BS_3$ . Off-axis holography can then be performed to retrieve the amplitude and the phase of the image field. Retrieval of phase from the recorded holograms is described in section. 1.6.1.

The half-wave plates ( $HW_1$  and  $HW_2$ ) are used for full-vectorial field measurement. The use of them is explained as follows.

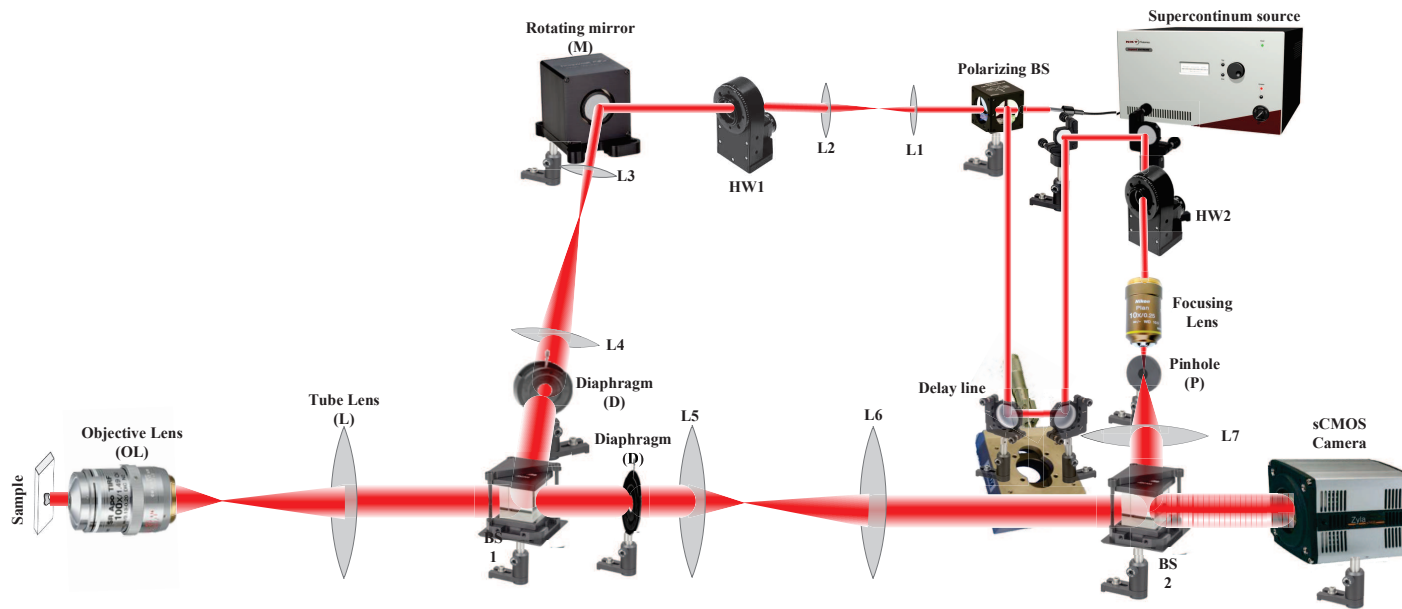


**Figure 1.17 :** Sketch of the experimental set-up : *M*, rotating mirror ; *D*, diaphragm ; *OL*, objective lens ; *L*, tube lens ;  $L_1, \dots, 7$ , lenses ;  $BS_1, \dots, 3$ , beam splitters;  $HW_{1,2}$ , half wave plates; *P*, pinhole.

### 1.6.2.1 Measurement of the full vectorial diffracted field

As pointed out in the previous section it is important to measure the full vectorial field and solve the equation,

$$\mathbf{E}_d(\mathbf{k}) = k_0 \mathbf{k} \times \left[ \mathbf{k} \times \int_{\Omega} \exp(-i\mathbf{k} \cdot \mathbf{r}) \chi(\mathbf{r}) \mathbf{E}(\mathbf{r}) d\mathbf{r} \right]. \quad (1.36)$$

The above equation for TDM at the image plane can be written as [92],

$$\mathbf{E}_d(\mathbf{r}_{\parallel}) = \int_{\mathbf{k}_{\parallel} < k_0 NA} \frac{1}{\sqrt{k_0^2 - \mathbf{k}_{\parallel}^2}} (e_s \hat{\mathbf{s}} + e_p \hat{\mathbf{p}}) \exp(i\mathbf{k}_{\parallel} \cdot \mathbf{r}_{\parallel}) d\mathbf{k}_{\parallel}. \quad (1.37)$$

where,  $k_0 = \frac{2\pi}{\lambda}$ ,  $\hat{\mathbf{s}} = \hat{\mathbf{z}} \times \hat{\mathbf{k}}$ ,  $\hat{\mathbf{p}} = \hat{\mathbf{s}} \times \hat{\mathbf{k}}$ ,  $\mathbf{k} = \mathbf{k}_{\parallel} + [1/\sqrt{k_0^2 - \mathbf{k}_{\parallel}^2}] \hat{\mathbf{z}}$ , and  $(e_s, e_p)$  are the diffracted fields complex amplitudes propagating along  $\mathbf{k}$  belonging to the polarizations  $\hat{\mathbf{s}}$  and  $\hat{\mathbf{p}}$ .

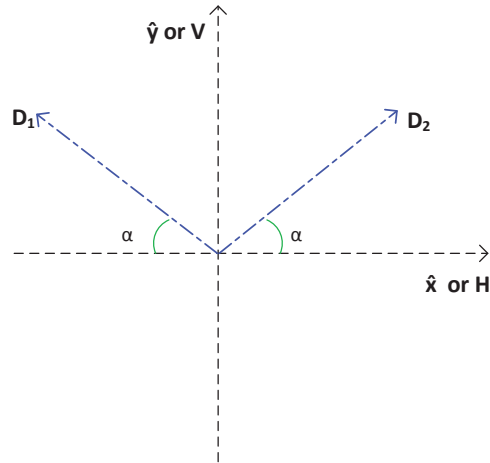


**Figure 1.18 :** Measurement of full vectorial field is performed along two bases. The illumination polarization is either along  $\hat{\mathbf{x}}$  or  $\hat{\mathbf{y}}$ . The detection polarization is either along  $\hat{\mathbf{D}}_1$  or  $\hat{\mathbf{D}}_2$ . This illumination and detection schema form a orthogonal bases. With  $\alpha = 45^\circ$ .

To carry out vectorial measurements of the diffracted field under full polarization, two half wave plates have been placed in the illumination and reference arms (HW<sub>1</sub> and HW<sub>2</sub>). They are used to generate two polarization basis : horizontal and vertical directions,  $\hat{\mathbf{x}}$  and  $\hat{\mathbf{y}}$  (shown in Fig. 1.18), for the illumination arm, and along the two diagonal directions,  $\hat{\mathbf{D}}_1 = (\hat{\mathbf{x}} + \hat{\mathbf{y}})/\sqrt{2}$  and  $\hat{\mathbf{D}}_2 = (\hat{\mathbf{x}} - \hat{\mathbf{y}})/\sqrt{2}$ , for the reference arm. These four directions are all orthogonal to  $\hat{\mathbf{z}}$ , which is the unit vector along the optical axis of the microscope. For an illumination polarized along  $\hat{\mathbf{x}}$ , detecting successively the scattered field polarized along  $\hat{\mathbf{D}}_1$  and  $\hat{\mathbf{D}}_2$  permits to retrieve the vectorial scattered field. Indeed, thanks to the microscope magnification,

the propagation angles of the Fourier components of the scattered field (or diffracted field) are so small in front of the camera (well below  $1^\circ$ ), that any polarization component along  $\hat{\mathbf{z}}$  can be neglected. Repeating this procedure for an illumination polarized along  $\hat{\mathbf{y}}$ , it is then possible to generate the vectorial scattered field for any linear polarization in the  $(\hat{\mathbf{x}}, \hat{\mathbf{y}})$  plane for the illumination.

The total field from object  $\mathbf{E} = \mathbf{E}_d + \mathbf{E}_{inc}$  is interfered with  $\mathbf{E}_R$  beam (not to be confused with reference field which is called  $\mathbf{E}_0$ !) experimentally. The usual procedure to obtain the full vectorial field is (see Fig. 1.18) by changing the polarization along the sample arm  $\mathbf{E}$  and reference beam  $\mathbf{E}_R$  and recovering phase from the holograms as: Illuminate *V* or  $\hat{\mathbf{y}}$  polarized light along sample arm and reference beam with light polarized along  $\hat{\mathbf{D}}_1$ , which form the illumination and detection schema as  $\hat{\mathbf{y}}\hat{\mathbf{D}}_1$ . Similarly,  $\hat{\mathbf{y}}\hat{\mathbf{D}}_2$ ,  $\hat{\mathbf{x}}\hat{\mathbf{D}}_1$  and  $\hat{\mathbf{x}}\hat{\mathbf{D}}_2$  are performed. From these data sets it is possible to compute the full-vectorial complex diffracted field data.

In a classical TDM set-up, the illumination and reference beams have the same polarization, and only a projection of the scattered field on this direction is measured. With our full-polarized set-up, getting the vectorial scattered field for any linear polarization of the illumination requires four times more data. The measurement procedure is therefore basically four times longer, but could be only twice longer using at once two orthogonally polarized reference beams [93].

In this thesis, I investigate samples deposited on a substrate. To improve the sensitivity of the reconstructions, I perform a reference measurement on the bare substrate. It permits to measure the specular reflected field for each illumination angle. By subtracting it to the field measured in the presence of the sample, only the diffracted field part remains, and the speckle noise generated by the illumination and the specular reflection is diminished.

### 1.6.3 Developments to the set-up

The Tomographic Diffractive Microscopy (TDM) setup has been upgraded with several new components, this section presents the developments. Before I started my thesis work, the setup had He-Ne ( $\lambda = 632.8nm$ ) laser with very high coherence length. This would contribute to the noise because of the reflection from the several optical components mixing with the diffracted field. It was desired to have low coherence length source and also to have a source which can be tuned to a desired wavelength. The camera used was CCD camera (Kappa PS4-1020) which had low sensitivity. The speed, sensitivity and the electronic noise can be reduced significantly by adapting a better camera. The rotating mirror to change the angle of illumination was driven by two stepper motors (Newport NSA12), which was slow and contributing to the time consumption in the measurement. As the setup operated at single wavelength until I started my thesis, the reference arm had fixed components, which cannot be tuned to change the path length of the reference beam. The half-wave plates positioned in the object and reference beams has to be tuned manually for each measurement. To recall, for a complete measurement four such adjustments ( $\hat{\mathbf{y}}\hat{\mathbf{D}}_1$ ,  $\hat{\mathbf{y}}\hat{\mathbf{D}}_2$ ,  $\hat{\mathbf{x}}\hat{\mathbf{D}}_1$  and  $\hat{\mathbf{x}}\hat{\mathbf{D}}_2$ , refer Sec. 1.6.2.1) of the half-wave

plates have to be performed to obtain full vectorial field. These were addressed and upgraded during my thesis for the betterment of the setup.

One of the significant improvement is the supercontinuum laser. This allows to tune the wavelength of interest from 450nm to 800nm and also a favorable bandwidth ranging from 4nm to several nanometers can be chosen. Due to its low coherence length (about 100  $\mu m$ ) there was a significant improvement in the reduction of the light reflecting from the optical components in the setup does not interfere, which significantly improved the measured data. But on the other hand the reference beam has to be tuned carefully to match the path length of the object arm path. Since it has a low coherence length of 100 $\mu m$ , it was challenging initially. After the introduction of delay line it is now familiar to tune the reference path length and get good contrasted fringes when object arm field and reference beam are interfered.

A sCMOS camera (Andor Zyla) was installed which is externally cooled with a coolant. This camera offers high speed, high sensitivity imaging performance with frame rates. Rolling and Global Shutter modes provide flexibility to adopt the imaging technique being performed. In Rolling shutter, different lines of the camera pixels array are exposed at different times. The read out of the camera reads those exposed pixels. In Global shutter, all the pixels are exposed simultaneously and captured at same instance. Because of cooling, read out noise decreased compared to a previous CCD camera. Also due to the interface of the camera with computer the acquisition is faster. It has to be noted that the sensor is protected by a transparent glass slide, the experiments performed on the camera showed there was no effect of this on the measured data due to the low coherence length of the supercontinuum laser (NKT Photonics SuperK Extreme EXW-12).

The setup was optimized to have a one-click acquisition schema. To realize this, two half-wave plates ( $HW_1$  and  $HW_2$  shown in fig. 1.17) were mounted on a rotating actuator. The camera, rotating mirror, and half-wave plates were controlled by the computer and can be programmed. The whole measurement process once the object to observe is fixed and the setup is tuned, the measurement can be performed with one-click on the computer. This takes into account the measurement procedure listed in the above section of changing polarization in both reference beam and sample beam arms.

## 1.7 Conclusion

This chapter explained the principles of tomographic Diffractive Microscopy (TDM) through wide-field microscope and phase microscope. The general principle is illuminating the sample with several varying incidence plane waves and detecting their complex diffracted field. Whereas in the classical wide-field microscope the Köhler illumination is used. Retrieval of phase is performed using the off-axis holography configuration in the context of phase microscopy. Phase microscopy is the first step towards understanding the link between the axial direction of the sample and the light propagating through it. Which is based on optical path difference measurement, though it is sensitive along optical axis does not provide 3D information or material

properties of the object. On the other hand, TDM depends on the measurement of diffracted field's amplitude and phase (complex field) of the sample for several incident angles. Measuring the complex diffracted field provides a link to retrieve linear susceptibility  $\chi$ . The Born and Rytov approximations provide quicker access to the sample permittivity considering approximations to the vectorial diffracted field, they establish a linear link between the sample permittivity contrast and the measured complex diffracted field. In general, the link between object and scattered field is non-linear. Approximative approaches provide rough estimate of the sample. So, non-linear reconstruction schema is needed to reconstruct the non-linearly linked diffracted field data. This non-linear inversion schema is presented in the third chapter.

The TDM provides better spatial frequency coverage and better sensitivity to high spatial frequencies compared to classical microscope due to the varying illumination angle and coherent detection schema. Various TDM configurations such as transmission, reflection and complete configurations provide access to various parts of the Optical Transfer Function (OTF) of the Ewald's sphere (synthetic 3D aperture). We noted that the resolution in transmission configuration along the axial direction is worse than the transverse direction due to the inaccessibility of high frequency components along the axial direction. It was stated that having access to both transmission and reflection would provide better resolution in combination with full-vectorial measurement. In the last chapter, I show how to obtain isotropic resolution combining the advantages from transmission and reflection configurations using a mirror.

Finally, the experimental setup utilized in this thesis work is presented in detail along with the significant upgrades in camera, wavelength tunable supercontinuum source, faster rotating mirror and the rotatable half-wave plates. The measurement setup is developed such that the measurement can be performed with one-click and faster compared to its state at the beginning of this thesis.

---

# Imaging with tomographic diffractive microscopy holograms under scalar approximations

---

“Your eyes can deceive you. Don’t trust them.”  
-Obi-Wan Kenobi, Star Wars

## 2.1 Introduction

In this chapter, we explore the different possibilities to utilize the tomographic diffractive microscope (TDM) complex field (amplitude and phase) data. In the TDM measurement, we illuminate the sample with different successive illuminations and the detection of diffracted field is performed (see Sec. 1.5). The TDM measurement is performed only once but the complex field data provides access to several imaging techniques by means of post numerical treatment. This is due to the fact that TDM measurement data provides complete complex scattered field information of the sample for varying illumination angles. This is a new approach, to numerically realize several imaging techniques from one single measurement. This chapter will focus on imaging under scalar approximations, neglecting the vectorial nature of the light; providing access to the reconstructed image rapidly.

Usually, the optical microscopes are built to perform specific imaging method such as bright-field microscopy, dark-field microscopy, phase-contrast microscopy or confocal microscopy. These microscopes provide images directly and require no post treatment. To realize other methods from the specific method the microscope is built for, the microscope system need changes in the optical components. For example, to perform dark-field imaging on a bright-field imaging microscope system the illumination and the detection schema has to be changed. However TDM has a fixed experimental setup and measurement is performed only once. Any of the imaging methods described in this chapter can be reconstructed later with post numerical treatment at our will. Along with the microscope methods specified above, TDM techniques such as two-dimensional synthetic aperture and three-dimensional synthetic aperture imaging can also be realized with TDM data.

It is known that combining two or more imaging techniques bring comprehensive information to better understand the sample [94]. For example, bright field

image and dark-field microscope image would provide information to determine the boundary of the substrate or the background and the sample. The combination of several imaging methods through numerical treatment is called multimodal numerical imaging. This is one of the advantage of TDM: one set of measurement can provide different comprehensive images of the sample and we expect these different imaging techniques provide better understanding about the sample in comparison to single imaging technique.

This chapter focused on TDM scalar imaging will present how TDM data set can be post processed numerically to obtain bright-field, dark-field, phase-contrast, confocal, two-dimensional synthetic aperture, and three-dimensional synthetic aperture microscopy. I performed the TDM measurement to obtain the measurement data. The algorithms used to realize the techniques described above with experimental data was developed by me during this thesis work. I will also present what are the additional advantages provided by the numerical modalities here.

Before we start with understanding numerical realization, let us understand the data set we have access to at the end of a TDM measurement.

## 2.2 TDM data set

To perform the scalar approximations based numerical imaging techniques, it is essential to understand the TDM measurement data set. This section will present the sample used throughout the chapter to perform different numerical imaging techniques, illumination strategy and the detected diffracted field.

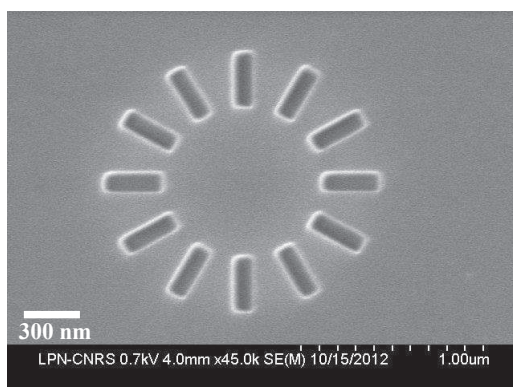


**Figure 2.1 :** *Scanning Electron Microscopy image of the fabricated sample used for demonstration of different numerical simulated imaging techniques in this chapter.*

Dr. Anne Talneau, Laboratoire de Photonique et de Nanostructures (LPN), Marcoussis, France fabricated a test sample as shown in Fig. 2.1. The sample was made up of resin rods (relative permittivity of 2) of width = 100nm, length = 300nm and height = 140nm deposited on the Si substrate. Twelve resin cylinders were placed radially at the summit of a dodecagon, let us call this reference star sample. Such a schema of sample is fabricated because it allows us to test the resolution. As

we observe from the outer edges to the inner edge the distance between the resin rods decreases, provides ideal configuration to test the resolution. I will reconstruct this sample numerically in this chapter using different imaging techniques.

The sample shown in Fig. 2.1 was placed in the TDM setup (shown in Fig. 1.17) to perform TDM measurement. The wavelength used for measurement is  $\lambda = 475nm$ . The objective used for illumination and detection has a NA=0.95. The sample was illuminated by eight directions of incidence, defined by a fixed polar angle of  $60^\circ$  and for every  $45^\circ$  of azimuthal angle inside the NA of objective. The sample used in this chapter is thinner in nature, for such a sample to improve the transverse resolution, high angles of incidence are important. High angles of incidences give rise to high spatial frequency components. Depending on the sample complexity the number of illumination angles required vary, for this sample we realized that 8 angles were sufficient. The diffracted field from the sample is interfered with a reference beam off-axially as explained in the previous chapter (Sec. 1.6). This results in obtaining 8 holograms corresponding to 8 angles of incidences. From these holograms the amplitude and the phase information are retrieved.

A full-vectorial measurement is performed, this means we illuminate and detect with known polarization as explained in section Sec. 1.6.2.1. To have the full-vectorial data set, I illuminate and detect as  $\hat{x}\hat{D}_1$ ,  $\hat{x}\hat{D}_2$ ,  $\hat{y}\hat{D}_1$  and  $\hat{y}\hat{D}_2$  (where first letter represent the illumination polarization and the other letter represents the detection polarization), see Fig. 1.18. That would result in 4 data sets. This chapter deals with non-polarized reconstruction (scalar approximation). To perform non-polarized imaging, I sum the intensity images obtained from  $\hat{x}\hat{D}_1$ ,  $\hat{x}\hat{D}_2$ ,  $\hat{y}\hat{D}_1$  and  $\hat{y}\hat{D}_2$ . For illumination case, by summing we create a non-polarized illumination. Because the illumination was either in  $\hat{x}$  or  $\hat{y}$  along orthogonal basis, a summation of intensities would yield non-polarized illumination. Also true for orthogonal detection basis  $\hat{D}_1$  and  $\hat{D}_2$  to obtain non-polarized detection data. So, non-polarized measurement =  $\hat{x}\hat{D}_1 + \hat{y}\hat{D}_1 + \hat{x}\hat{D}_2 + \hat{y}\hat{D}_2$ , sum of intensities of individual data set.

Now, I will show you the numerical reconstruction of different non-polarized imaging techniques from this data set. The experimental principle of each individual technique is explained. The numerical realization of the imaging technique with the TDM data will be presented. The difference between the experimental realization and the numerical realization with TDM data, its advantages are discussed.

## 2.3 Bright-field microscopy

Bright-field microscopy is the simplest of the microscopy techniques. This method was the first employed imaging technique to observe micro scaled objects. This technique is interesting because of simple experimental setup requirement and for imaging in real-time. It is based on the use of the intensity variation recorded on the camera to image the sample. The illumination light can either be white-light or monochromatic in nature.

The imaging can be performed in either transmission or reflection configuration. In both cases the illuminated light interacts with the sample. After interaction the light carries the information about the sample. Variation is caused in the intensity of light due to the absorbance of the sample variation and scattering. The absorbance and scattering varies at different locations of the sample due to the material properties (refractive index) and the thickness (geometrical) variations. Parts of the illuminated light does not undergo any variation. The interference between the unvaried illumination light and the scattered light produces the intensity variation. The reflected light from the substrate (in case of reflection) or illuminated light (in case of transmission) forms a bright background to provide contrast to the image. So, this technique is called bright-field imaging [9, 95]. The bright-field image as intensity variation is recorded on the camera. As noted in the previous chapter, cameras are capable of detecting only the intensity. This makes it possible to record the intensity in real time and observe the characteristics of the sample directly on the camera.

A simple representation of the bright-field imaging microscope is shown in Fig.1.1. The sample is illuminated with a single wide-field light source. As discussed in the previous chapter, the wide-field illumination can be decomposed into a set of plane waves propagating in different directions (discussed in last chapter, section.1.2). The condenser lens is used to illuminate the sample. The light propagates away after interacting with the sample, it is collected on the detector, thanks to the objective and the tube lens.

### Numerical TDM bright-field imaging

To numerically generate the TDM bright-field imaging, I use the sample described in this chapter and the illumination and detection schema is explained in the section Sec. 2.2. I have access to the complex diffracted field corresponding to each illumination. The amplitude information is sufficient for this method. How do we obtain the bright field image from this TDM data set?

The amplitude of the total field ( $E(\mathbf{r}) = E_0(\mathbf{r}) + E_d(\mathbf{r})$ ) is a sum of the amplitude of the scattered field  $E_d(\mathbf{r})$  and the reference field  $E_0(\mathbf{r})$  (field that would exist in the absence of a sample). We have access to 8 illumination angles amplitude data in this case. The bright field image is obtained by summing the intensities detected for each illumination angle,

$$|E_{\text{bright-field}}(\mathbf{r})|^2 = \sum_{q=1 \rightarrow n} |E_q(\mathbf{r})|^2, \quad (2.1)$$

where  $q$  represents the varying angle of incidence of the incident field and the corresponding total field. The TDM bright-field image for the sample shown in Fig. 2.1 is numerically obtained as shown in Fig. 2.2. It has to be noted that as I sum the intensities of 8 different angles of incidence, there is no interference between them. The contrast in the bright-field image is purely due to the interference between the scattered and the illuminated light.

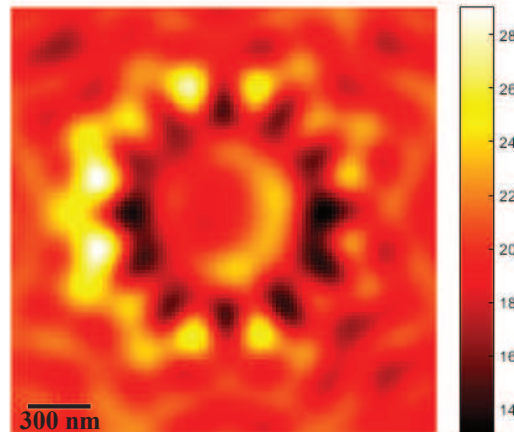


**Figure 2.2 :** *The TDM bright-field image of the sample at  $\lambda = 475\text{nm}$ . Scale bar represents the intensity.*

The Fig. 2.2 represents a non polarized TDM bright-field image. The previous section explained the method to obtain non-polarized data from the TDM data set. The Fig. 2.2 shows that we have resolution to separate the resin rods at the outer edge of the cylinders. But the resolution and contrast is not satisfactory to distinguish each individual rods towards the center of the sample.

#### Advantages and disadvantages:

The advantage of bright-field imaging technique is, it is easy to implement. It does not requires any extra optical components in a microscopy setup. The image is visualized in real-time. The limitations include low optical resolution, inability to observe low absorbance or weakly scattering objects, inability to image very low refractive index contrast or transparent samples. In biology, the sample is usually transparent in nature. So, they are stained to have good contrasted bright-field images, but staining might introduce some artifacts into the bright-field image [9, 74]. Bright-field imaging technique can be used as a technique which can provide initial insights into the sample. Later, a better imaging microscopy technique could be used to image a particular location or certain characteristics of the sample in detail.

The TDM bright-field method in comparison to the bright-field microscopy just requires numerical reconstruction and shares the same advantages as discussed above.

As the contrast is not sufficient enough to resolve individual resin rods in the sample, I explore other methods to image with improved contrast. One such method is dark-field imaging technique.

## 2.4 Dark-field imaging

Dark-field microscopy was conceived to increase the image contrast compared to the bright-field imaging technique. The general principle of the dark-field imaging is to collect only the diffracted light from the sample and block the illuminating light. The

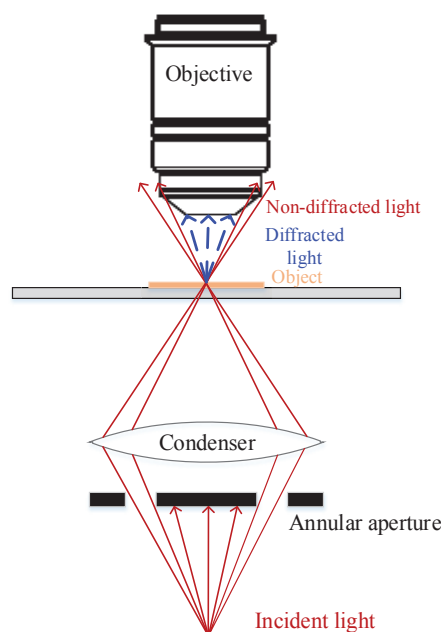


**Figure 2.3 :** *Dark field microscopy principle*

illuminating light (transmission case) or the light reflected from substrate (reflection case) form intense background signal and generally decreases the sample contrast in imaging. Sample in microscope is illuminated with a condenser lens, in wide-field microscope it forms a cone. To accomplish dark-field microscopy, instead of illuminating the sample with a full cone of wide-field light, it is illuminated with a hollow cone of wide-field light from a condenser lens. This hollow cone of light is formed by passing the illuminated light through a annular aperture before the condenser lens as shown in Fig. 2.3. The annular aperture blocks the center of the beam of the illuminated light. The hollow cone of light interacts with the sample.

In the absence of a sample the non-diffracted light does not enter the objective (see Fig. 2.3). So, the background appears dark in the absence of the object. In the presence of an object, the scattered light from the object enters the objective lens and is collected on the detector with help of tube lens. Scattered light enters the objective because of the change in the direction of propagation due to the refractive index change introduced by the sample and its geometrical thickness. The image formed on the detector appears bright (or contrasted) with dark background. Thus, it is called dark-field imaging [96].

It is possible to numerically realize the dark-field image from the TDM measurement data, the method is described as follows.

### Numerical TDM dark-field imaging

The principle of dark-field TDM is shown in Fig. 2.4, it represents the dark-field imaging for a single normal incidence illumination case. The idea is to stop the non-diffracted light from being detected as I stated in the principle of dark-field imaging.

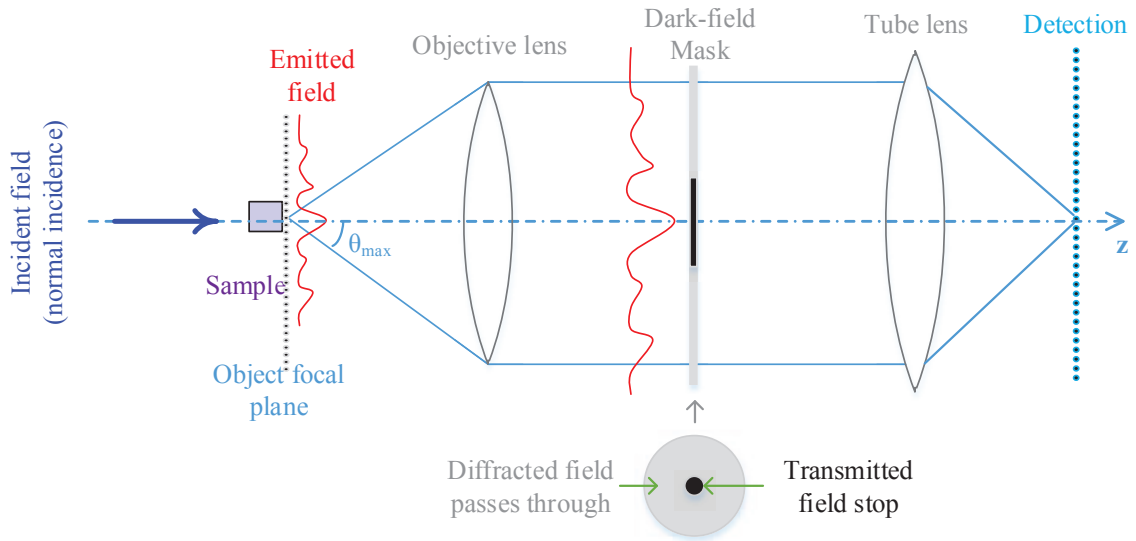


**Figure 2.4 :** *Dark field microscopy using TDM, only normal incidence illumination case is demonstrated here.*

For this purpose, a dark-field mask (blocker) is employed. This dark field mask is positioned in the back-focal plane of the objective in the Fourier domain. Ideally, the non-diffracted field or illuminated field in the Fourier domain forms a specular delta peak (generally broadened specular delta peak is observed in the case of experimental data). It is located at the center of the NA in the Fourier space for a perfect plane wave and normal incidence case (shown in Fig. 2.5). The location of the specular delta peak corresponding to the non-diffracted or illuminated field varies with varying angle of incidence inside the NA in the Fourier space. The dark-field mask blocks the non-diffracted field, shown in Fig. 2.5.B the black area of the Fourier domain. This is implemented numerically by multiplying data in Fourier space with a mask.

The sample, illumination schema and the detection schema utilized to collect the TDM data set is described in the section Sec. 2.2. From this, we already have access to the total field amplitude ( $E(\mathbf{r}) = E_0(\mathbf{r}) + E_d(\mathbf{r})$ ), which is a sum of the illuminated field amplitude and the diffracted field amplitude from the sample. To recall, the sample was illuminated with 8 varying angles of incidence. This varying angles of incidences produces specular delta peak of illumination at varying positions in the total field data. So to implement the TDM dark-field imaging principle stated before, we require a dynamic dark-field mask depending on the illumination angle.

It is important to note that as the measurement was performed in the image space to collect complex diffracted field, we can go to the Fourier space by performing Fourier transform. Once in the Fourier space, the location of the specular delta peaks are detected numerically in the Fourier domain for each illumination data set. For example, in Fig. 2.5.A, the specular delta peak is at the center of the NA in the Fourier domain data. For each angle of incidence, the specular delta peak is substituted by zeros. Fig. 2.5.B shows the example for the normal incidence illumination case. The diffracted field amplitude ( $E_d(\mathbf{r})$ ) is unaffected except in

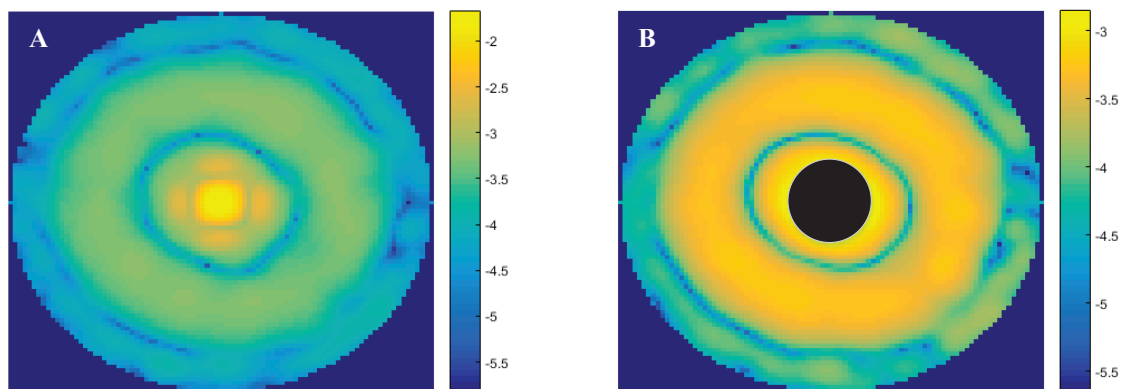


**Figure 2.5 :** *Suppression of the specular reflection in the Fourier space on the scattered field data. Fig.A: Total field in log10 scale inside the NA in the Fourier domain for normal incidence case. The bright spot corresponds to the non-diffracted field. Fig.B: The non-diffracted field is substituted by zeros numerically (black region), giving only the diffracted field ( $\mathbf{E}_d(\mathbf{r})$ ).*

the specular region, where we consider it does not carry useful information. This operation can be performed for field detected for every individual incidence angle. This means that we have access to only the diffracted field amplitude ( $E_d(\mathbf{r})$ ) of the sample for varying angles of incidence. From this data, the dark-field image can be obtained. The above operation can be represented as,

$$|E_{\text{dark-field}}(\mathbf{r})|^2 \approx \sum_{q=1 \rightarrow n} |E_{d_q}(\mathbf{r})|^2, \quad (2.2)$$

where  $q$  represents the varying angle of incidence. The diffracted field intensity from all the incidence angles are summed up to obtain the TDM dark-field image.

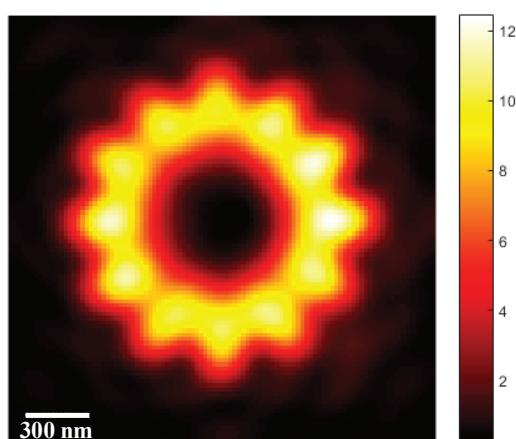


**Figure 2.6 :** *Dark field image of the sample Fig. 2.1 at  $\lambda = 475\text{nm}$*

The TDM dark field image of the sample seen in Fig. 2.1 is shown in Fig. 2.6. The image is also non-polarized in nature, similar to the case discussed in bright-field imaging section. Compared to the bright field image Fig. 2.2, the dark-field

image Fig. 2.6 is well contrasted with background being dark in nature. It has to be noted that the signal level in the dark field image is also lower compared to the bright-field image. The rods are not resolved towards the inner edge of the rods too.

### **Advantages and disadvantages:**

Dark field microscope imaging is preferred for viewing objects that are transparent and absorb very low light with low refractive index contrast. Because of the low refractive index contrast it is hard to identify the sample, this technique is useful for such cases. Dark-field imaging technique can provide an excellent tool to identify the boundaries and the location of the sample with sharp contrast with dark background. Presence of dust or other artifacts around the sample can also scatter light. Such scattered light can interfere with the detected field of the sample, this diminishes the accuracy of the dark-field image. So to avoid this, the sample has to be artifact or dust free, stressing the importance of sample preparation for dark-field imaging.

The position of condenser stop in classical dark-field microscope can produce artifacts and aberrations in imaging. Whereas, this disadvantage is overcome by means of numerical dark-field mask in numerical dark-field TDM. The size of the mask can also be varied depending on the spreading of the specular delta peak in the Fourier domain. In the classical dark-field imaging, the illumination is with wide-field hollow cone light with fixed dark-field mask. Whereas in the TDM dark-field imaging the sample is illuminated with varying coherent illumination angles, so the dark-field mask is dynamic and numerical. As the TDM dark-field mask is numerical in nature, it can be numerically constructed and applied to any illumination angle data. So, compared to the classical dark-field microscope where the illumination is limited within a cone, numerical dark-field TDM can be applied to all illumination angles inside NA. Thanks to the numerical mask, it is very advantageous to vary its size depending on the requirements on the sample to be imaged.

On the other hand, low signal level in the dark-field imaging is a disadvantage. This can be overcome by operating on the illuminated field instead of suppressing it, with such as phase contrast microscopy.

## **2.5 Phase contrast microscopy**

Phase contrast microscopy (PCM) provides contrast to the low contrasted samples and conserves the signal intensity. This is performed by transforming phase differences of light caused by refractive index variations at various locations of sample into differences in the intensity of light. As light propagates through the different regions of the sample with different optical path (refractive index and geometry of the sample) lengths the phase of the illuminated light is changed depending on the interaction location of the sample. But the intensity variation would be very small. As discussed in the previous chapter, the detectors and eye are insensitive to phase differences. If the change in the phase difference can be visualized as amplitude or intensity variation, that would provide a better contrasted image than just the

intensity variation image. Zernike understood this process and invented the phase contrast microscopy [11, 97].

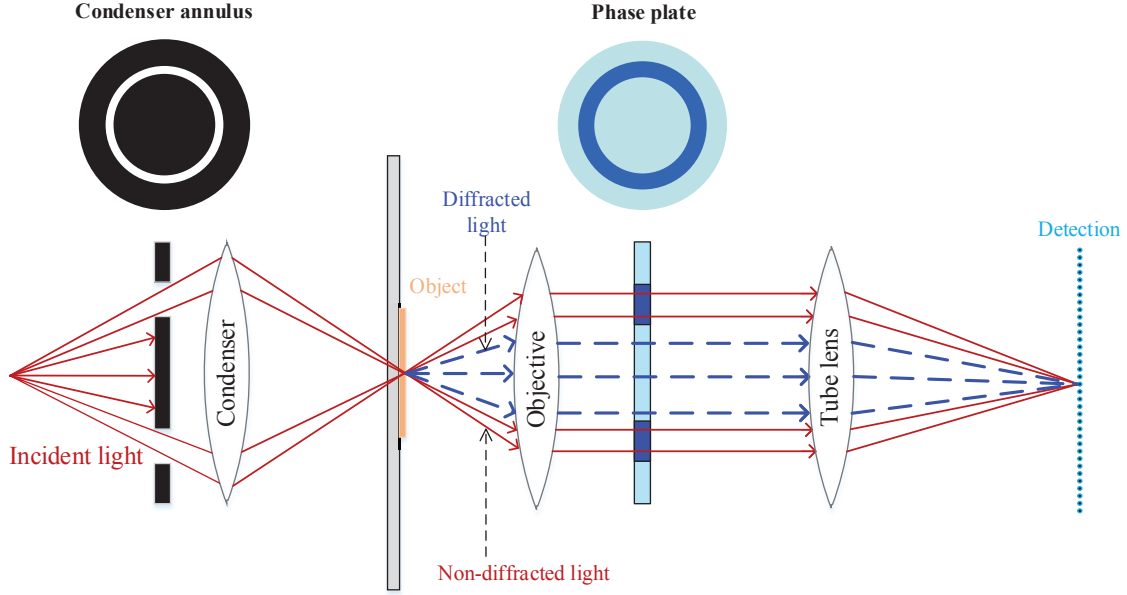


**Figure 2.7 :** *Phase contrast microscopy principle.*

To understand the principle of PCM, let us consider that we illuminate a sample with a plane wavefront light  $\mathbf{E}_{inc}(\mathbf{r})$ . The plane wavefront after interacting with the sample will consist of diffracted field ( $\mathbf{E}_d(\mathbf{r})$ ) and the non-diffracted field  $\mathbf{E}_0(\mathbf{r})$ . The detected light can be given by  $(\mathbf{E}(\mathbf{r}) = \mathbf{E}_0(\mathbf{r}) + \mathbf{E}_d(\mathbf{r}))$ . The intensity of the detected light is known by  $I = |\mathbf{E}_0 + \mathbf{E}_d|^2$ . This is interference between the diffracted and the non-diffracted field. The object will be poorly contrasted if  $\mathbf{E}_d \ll \mathbf{E}_0$ . In this case, the phase shift between  $\mathbf{E}_d$  and  $\mathbf{E}_0$  is equal to  $\pi/2$ , ie.,  $\mathbf{E}_d$  is in quadrature with  $\mathbf{E}_0$ . This results in poor interference between the diffracted and the non-diffracted field. This would lead to poorly contrasted image. On the other hand, if the phase difference between  $\mathbf{E}_d$  and  $\mathbf{E}_0$  is  $\pi$ , then we will have destructive interference, leading to highly contrasted image.

The phase difference of  $\mathbf{E}_d(\mathbf{r})$  and  $\mathbf{E}_0(\mathbf{r})$  is due to the optical path differences caused by refractive index and geometry of the sample at various locations of the sample. If the sample is of low refractive index compared to the surrounding then the optical path difference won't be sufficient enough to cause interference needed to contrast the sample. But the phase difference between  $\mathbf{E}_d(\mathbf{r})$  and  $\mathbf{E}_0(\mathbf{r})$  can be introduced artificially in the microscope to improve the contrast. This is the basic principle behind PCM.

The general implementation of phase contrast microscope (shown in Fig. 2.7) includes a condenser annulus and a phase plate in addition to the optical components of a wide-field microscope. The condenser annulus is placed in the front focal plane of the condenser lens, this lets hollow cone of light to pass through and blocking the light passing through the center of it. This hollow cone of light passes through the sample thanks to condenser lens. After passing through the sample the light has the

total field information, both the diffracted field and the non-diffracted field. The phase plate lying in the back focal plane of the objective consists of a phase ring which changes the phase of light passing through it by  $\pm\pi/2$ . Notice the geometry of the phase plate, only the light passing through the ring part of the phase plate undergo a phase shift compared to the center and periphery.

The illumination was with a hollow cone of light. So, the non-diffracted light (or illuminated light) passes through the ring of the phase plate undergoing additional  $\pm\pi/2$  phase shift with respect to the diffracted field. Between the diffracted and non-diffracted light there is a phase difference around  $\pi$  or  $0$  introduced artificially to form either constructive interference or destructive interference. Along with the artificially introduced phase shift the diffracted field can also possess phase shift from the refractive index variation and thickness. The intensity of the light is reduced or increased depending on the interference between the diffracted and non-diffracted light. So, the phase shift of the sample is transformed into intensity variation due to the interference.

The method can either be positive phase contrast or negative phase contrast depending on the  $\pm\pi/2$  phase ring used in the setup. In positive phase contrast ( $+\pi/2$  phase ring), the sample is contrasted against a bright background. On the other hand in negative phase contrast ( $-\pi/2$  phase ring), the sample appears brighter against a dark background. This can be numerically realized with the TDM data as follows.

### Numerical phase contrast TDM

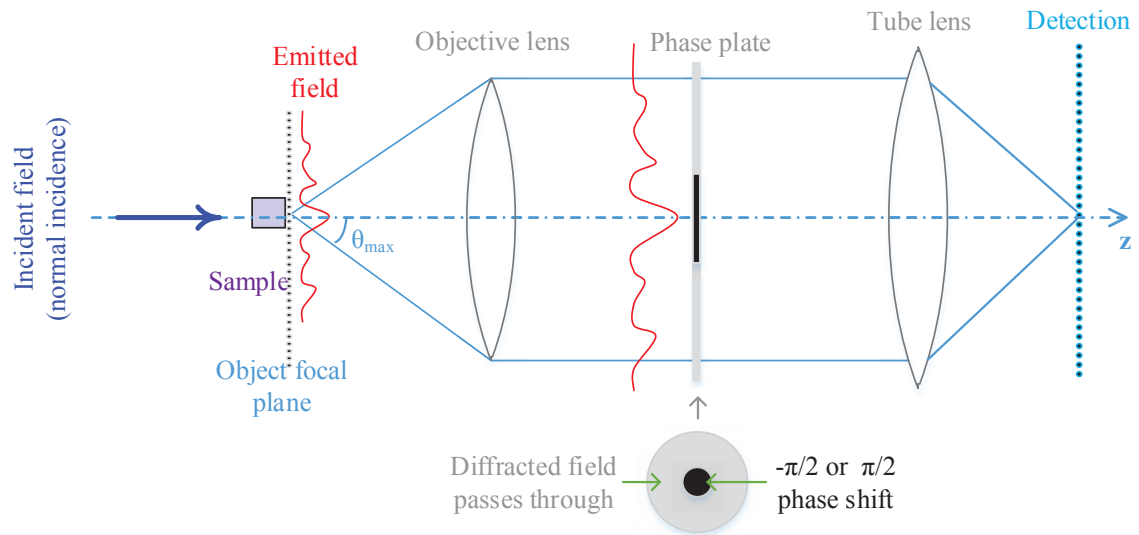


**Figure 2.8 :** Phase contrast microscopy with TDM

The phase contrast microscopy can be realized with the TDM data set by numerically generating a phase contrast TDM. The principle behind the numerical phase contrast TDM is shown in Fig. 2.8 for the normal incidence illumination case, in transmission TDM. The architecture and principle of the phase contrast TDM is

similar to the TDM dark-field imaging, except instead of a blocker in the back focal plane of the objective a phase plate is used. This phase plate introduces  $\pm\pi/2$  phase shift to the non-diffracted light (specular broadened delta peak) or illuminated light with respect to  $\mathbf{E}_d$ .

The TDM complex total field ( $\mathbf{E}(\mathbf{r}) = \mathbf{E}_0(\mathbf{r}) + \mathbf{E}_d(\mathbf{r})$ ) data was acquired as explained in the section Sec. 2.2. The location of the specular peak is determined in the Fourier domain for each illumination angle. A numerical phase plate is generated by introducing a  $\pm\pi/2$  values at the location of the non-diffracted field data or the specular broadened peak region. The intensities of all the detected fields are summed up to obtain the phase contrast TDM image. The mathematical representation is given by

$$|\mathbf{E}_{PCM}(\mathbf{r})|^2 \approx \sum_{q=1 \rightarrow n} |\mathbf{E}_q(\mathbf{r}) * \exp(i SPM)|^2, \quad (2.3)$$

where,  $\mathbf{E}$  is the total field, SPM is the specular phase mask with values zeros everywhere except  $\pm\pi/2$  at the specular non-diffracted light location and  $q$  represents the varying angle of incidence.

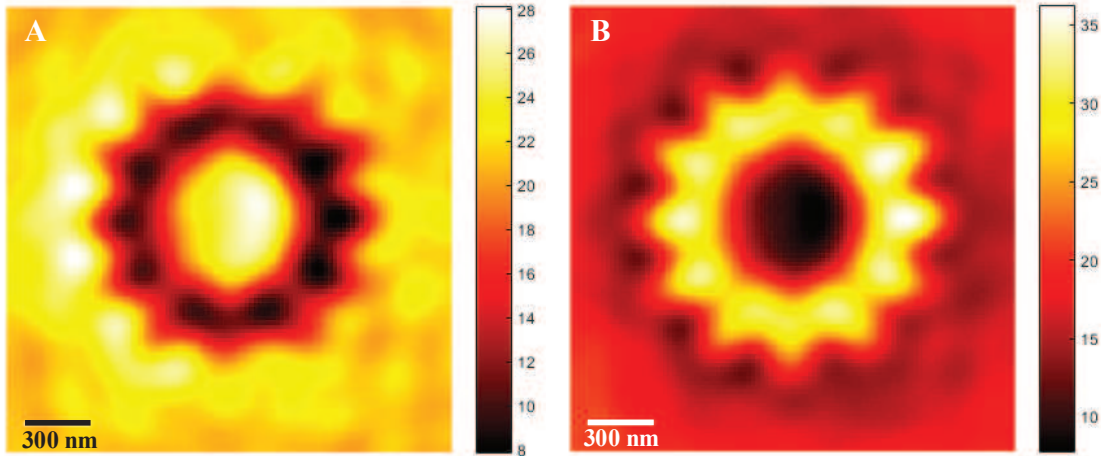


**Figure 2.9 :** Phase contrast TDM results of sample Fig. 2.2.A: Fig.A: Positive phase contrast TDM image. Fig.B: Negative phase contrast TDM image.

Phase contrast image of the sample, see Fig. 2.1 is shown in Fig. 2.9. The Fig. 2.9.A shows the phase contrast microscopy image generated with positive phase contrast TDM and Fig. 2.9.B represents the negative phase contrast TDM. Fig. 2.9.A shows destructive interference at the location of the resin rods on the sample, resulting in higher background signal and lower signal at the resin rods giving rise to positive phase contrast TDM. So, the sample is darker than the background. It is contrary in the case of negative phase contrast TDM, in this the sample is brighter than the background.

It is interesting to compare the signal level of the images obtained with methods already discussed in this chapter and the phase contrast TDM images. The bright field TDM image shown in Fig. 2.2 and the phase-contrast images seen in Fig. 2.9 have similar background signal. The background is brighter in bright-field TDM

and positive phase-contrast TDM image, except the phase contrast TDM is better contrasted because of the signal difference between the background and the resin rods being higher. The dark-field TDM image shown in Fig. 2.6 compared to the negative phase contrast TDM image seen in Fig. 2.9.B seem to be better contrasted. Phase-contrast does not seem to improve a lot the contrast here compared to dark-field, probably because the resin is partly absorbent. But, the total signal level of negative phase contrast TDM image is significantly higher than the dark-field TDM image. But the signal difference between the background and the resin rods are comparable.

### Advantages and disadvantages:

The main advantage is to obtain very high contrast images of the sample with out staining or introducing artifacts into the sample with high signal level. It is ideal for studying and analyzing very thin samples and low refractive index materials [97]. Phase contrast works if the phase delay induced by the sample is weak. In general phase contrast microscopy the phase plate limits the NA of the objective to an extent. Phase halo effect is a ring like artifact that surrounds the perimeter of the sample and the inner features, degrading the quality of PCM image. Shading off effect occurs when the sample's contrast reduces steadily as we move from the center of the sample towards its edges in PCM.

The limitations mentioned above can be overcome significantly by means of numerical phase contrast TDM. With numerical phase contrast TDM it is possible to use same NA for illumination and detection. This is possible thanks to the numerical phase of  $\pm\pi/2$  being applied on measured data for each illumination angle individually and numerically compared to experimental PCM phase mask reducing the size of the NA. Phase halo effect and the shading effects are avoided because of the use of numerical phase plate in the numerical phase contrast TDM. During the TDM experiment there is no phase plate to induce these effects. As numerical phase contrast TDM is a post experimental treatment, we have the possibility to apply either  $\pm\pi/2$  or other phase value differences to the non-diffracted field.

Numerical phase contrast TDM improved the signal intensity level and the contrast, but the resolution is still a concern. We explore the possibility to improve the resolution by performing numerical confocal microscopy on TDM data in the next section.

## 2.6 Confocal microscopy

Confocal microscopy is utilized to increase the image contrast of thick samples and also to improve resolution. Confocal microscopy is based on detecting the intensity variations. The principle is to restrict the light originating from overlying or nearby scattering objects located in the sample from being detected on the detector. To perform this, the light is detected from each point individually by observing a single diffraction limited spot along the transverse or the axial direction [98–100]. The light is restricted with help of a pinhole positioned in front of the detector. This

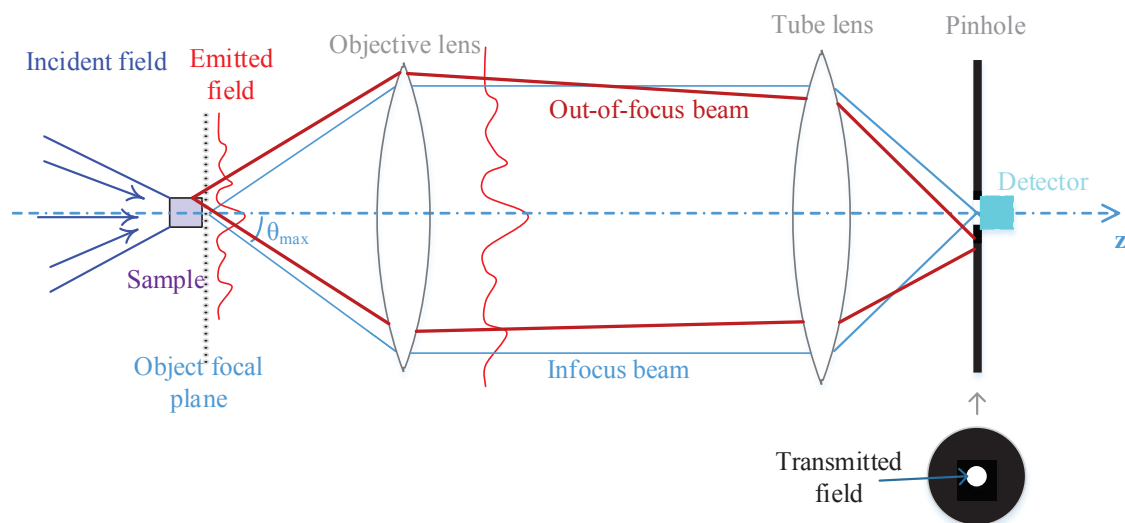


**Figure 2.10 :** *Confocal microscopy principle.*

pinhole blocks the out-of-focus scattered light and preserves the light at the point of focus, so the confocal images are free of defocus-blur and look sharper.

The principle of confocal microscopy is explained in the Fig. 2.10. The light is focused on the sample with help of a condenser lens, the in-focus diffracted field from the focus point propagates and reaches the detector (usually a photomultiplier tube). The out-of-focus diffracted light originating from the regions where light is not focused are cut-off by a pinhole positioned in front of the detector.

The pinhole positioned in front of the detector depends on the NA on the objective used, magnification of the optical system and wavelength used for the measurement. The diameter of the pinhole is usually optimized to fit the diameter of the Airy disk formed for a given microscope. The formation of Airy disk was explained in the section Sec. 1.2.2. Additional to the NA of the objective, wavelength used for measurement, the pinhole diameter determines the resolution of a confocal microscope. If the pinhole is larger than the airy disk, the out-focus light is collected and transverse resolution can be decreased. If a pinhole thinner than a Airy disk is used, the detected signal is weaker. A pinhole of size 1 airy unit (AU) gives the best signal to noise ratio.

The light is collected from a single focus point on a single point detector. To acquire a complete image, a scan has to be performed. The confocal scanning can be performed in 3D. In this section, I will concentrate only on the transverse resolution. The improvement in the axial resolution is discussed in detail elsewhere in this thesis.

The numerical means of producing better resolved confocal TDM image is described below.

### Confocal TDM

The complex diffracted field is obtained by illuminating the sample with 8 angles of incidences. Detailed description of the sample used, illumination schema and the

detection schema is described in the section Sec. 2.2. The sample is illuminated with 8 know wave vectors  $\mathbf{k}_{inc}$  and it diffracts in all possible directions. We collect certain components limited by the NA of the objective, the wave vector of the collected diffracted field is given by  $\mathbf{k}_d$ . Then, the accessible data set from the section Sec. 2.2 can be represented as  $\mathbf{E}_t(\mathbf{k}_d, \mathbf{k}_{inc}) = \mathbf{E}_d(\mathbf{k}_d, \mathbf{k}_{inc}) + \mathbf{E}_{inc}(\mathbf{k}_d, \mathbf{k}_{inc})$ , which is sum of diffracted and incident field) in the Fourier domain. The confocal image has to be obtained from this total field data.

To perform confocal scanning we have to focus light and collect the light from individual point numerically with a numerical pinhole. If 8 angles of incidence are sent together coherently it will create a focus point on the sample. The diffracted field from the focused spot has to be collected. This process is continued spot by spot (scan) over the whole sample to have the image.

The numerical realization of confocal TDM is presented here. We have the total field data from 8 angles of incidence. I sum the 8 total fields ( $\mathbf{E}_t(\mathbf{k}_d, \mathbf{k}_{inc})$ ). This results in getting total field from a focused spot,

$$\sum_{inc} \mathbf{E}_t = \mathbf{E}_t \left[ \sum_{inc} \mathbf{E}_{inc} \right], \quad (2.4)$$

where the term  $\sum_{inc} \mathbf{E}_{inc}$  corresponds to the confocal illumination spot. The above step is experimental equivalent of illuminating the sample with a confocal spot, it is done numerically. This is possible because diffraction is a linear process. As stated earlier, the confocal scanning will be performed in the transverse direction x and y. Let us focus on performing TDM confocal detection on a single point on the sample  $(x_0, y_0)$  step by step.

First step is to detect the light from the sample at a desired position  $(x_0, y_0)$ . To perform this, a phase factor has to be applied to each illumination total field data (of 8) to change the position of constructive interference (confocal spot detection). By this, the focus is shifted to the position  $(x_0, y_0)$  of the sample, which means we are illuminating at this point. The field obtained from this point in the Fourier domain is given by summing up all the total fields as,

$$\mathbf{E}_{dd}(\mathbf{k}_{dx}, \mathbf{k}_{dy}) = \sum_{\mathbf{k}_q} \mathbf{E}_t e^{-i\mathbf{k}_{qx} \cdot x_0 - i\mathbf{k}_{qy} \cdot y_0}, \quad (2.5)$$

where q represents the illumination angle. The  $\mathbf{E}_{dd}$  represents the sum of all the total field originating from the focused spot  $(x_0, y_0)$ . With  $k_{qx}$  and  $k_{qy}$  being the wave vectors components of the incident field in the x and y coordinates respectively. The  $k_{dx}$  and  $k_{dy}$  are the corresponding wave vectors components in detection.

Second step is to go to image space. The inverse Fourier transform of  $\mathbf{E}_{dd}$  would yield the image originating from the focused spot at illumination  $(x_0, y_0)$  on the sample.

Third step is to filter the image from the position  $(x_0, y_0)$  using a pinhole to perform confocal detection. For this purpose a numerical pinhole is constructed. The pinhole  $F(x_0, y_0)$  has ones at the location of the pinhole and zeros elsewhere. The

size of the pinhole can be one pixel or  $2 \times 2$  or  $3 \times 3$  or of user choice. For simplicity, let us consider only 1 pixel. The numerical multiplication of the numerical pinhole  $F(x_0, y_0)$  with the image from second step would provide the confocally detected information corresponding to the position  $(x_0, y_0)$  on the sample. But we so far has obtained information from only position  $(x_0, y_0)$  on the sample. To obtain the whole image of the sample, we have to perform a scan.

The final step is to perform the scan over the sample, the position  $(x_0, y_0)$  is changed over the sample. The above stated steps are repeated until the full scan of the sample is performed to obtain the full confocal image of the sample.

As stated in the section Sec. 2.2, we are under scalar approximations. The results from each polarization data sets are added together to obtain a non-polarized numerical confocal TDM image, for more details refer the final part of section Sec. 2.2.

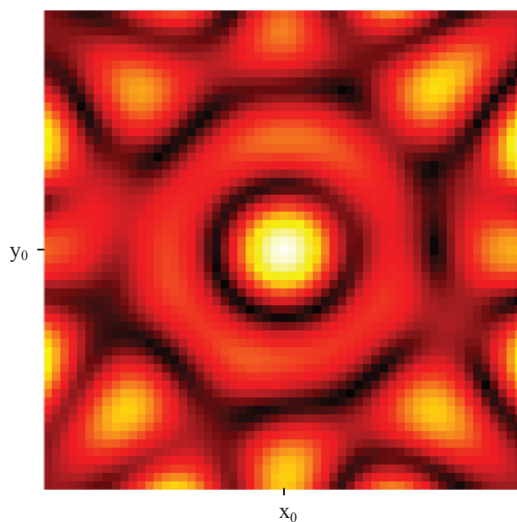


**Figure 2.11 :** For a focused point  $(x_0, y_0)$  on the sample, the detected intensity on a camera in the image space without a pinhole.

The above stated method is applied on the sample shown in Fig. 2.1 with 8 angles of incidences along the perimeter of the NA separated by 45 deg each. The detailed description of the data set used for confocal detection is explained in the section Sec. 2.2. The light is focused on the sample, point by point numerically, consider a point  $(x_0, y_0)$ . For  $(x_0, y_0)$ , the intensity detected on the detector by summing the 8 incidences and transforming to the image space will appear as a focus point at  $(x_0, y_0)$  (distorted Bessel beam) shown in Fig. 2.11 (i.e. after the second step explained in the numerical TDM confocal procedure above). The size of the central spot is about 400nm in diameter. The image Fig. 2.11 is without a pinhole detection. A numerical pinhole can be chosen to obtain the numerical confocal intensity of the point  $(x_0, y_0)$ , which would provide intensity for a single pixel.

To obtain the final full confocal image of the sample, the focus has to be scanned and detected with a pinhole all over the sample. The focus step size for illumination and the pinhole size for detection are critical for resolution and noise. They both can be chosen numerically. The numerical TDM confocal image obtained is shown

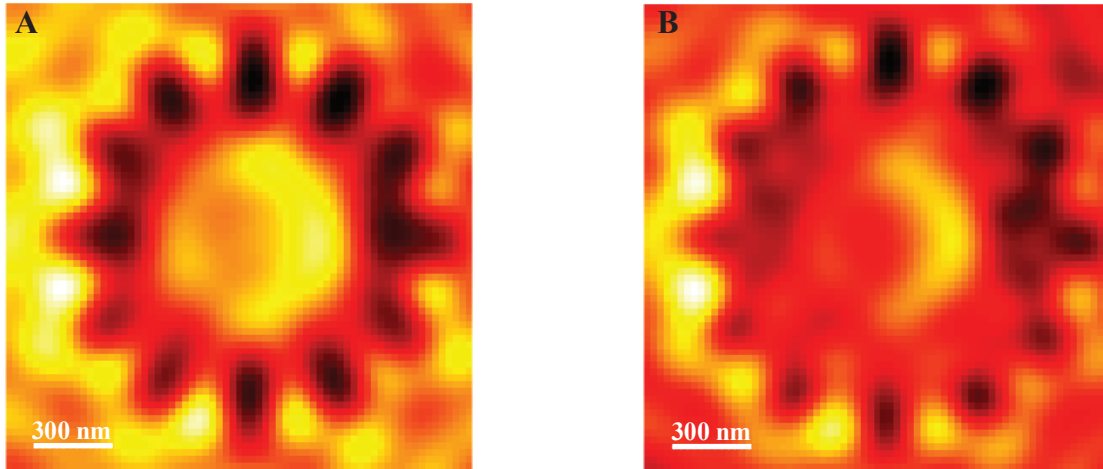


**Figure 2.12 :** *The confocal TDM image of the sample Fig. 2.1 generated numerically by utilizing the TDM hologram data and scanning digitally. Fig.A: The size of the confocal pinhole is 25nm. Fig.B: Size of the confocal pinhole is 425 nm, the size of central spot.*

in Fig. 2.12. Step size used for scan was 25nm, the size of the focusing beam would be a Airy disk limited by diffraction (for  $\lambda = 475nm$  and  $NA=0.95$ ), similar to Fig. 2.11. This Airy beam is used to illuminate the sample with a step size of 25nm.

For detection, a single pixel detection would result in a confocal image as shown in Fig. 2.12.A. The size of the pixel used for detection is 25nm. Numerical confocal TDM provides this ideal opportunity. Such a pinhole is difficult to implement in experimental confocal microscopy. If implemented one would obtain very low signal and impossible to detect the sample. As stated before, the size of the diameter of the Bessel beam is about 400nm. It is possible to increase the pinhole size to 425nm, the numerical TDM image obtained from such a pinhole is shown in Fig. 2.12.B. In this case, the intensity obtained from this 425nm pinhole is summed up and assigned to a single pixel on the confocal image.

A smaller pinhole provides better resolution as see in Fig. 2.12.A, but is sensitive to noise. As the pinhole size is increased Fig. 2.12.B, the resolution is not good enough to resolve the inner edges of the resin rods of the sample. The result obtained is better than the wide-field, dark-field or phase contrast microscopy image in terms of the resolution. The resin rods are better resolved in Fig. 2.12.A.

The numerical confocal TDM has several advantages compared to the generic confocal experimental setup, they are discussed below.

### Advantages and disadvantages:

The resolution is better than the generic wide-field methods because of the pinhole detection.

Many of the short comings of experimental confocal setup such as scanning rate, and dynamic pinhole with respect to the NA of the objective and wavelength used can be easily overcome by confocal TDM. Scanning is performed numerically, the

area of interest on the sample can be chosen with the confocal TDM, reducing time. The pinhole size can be varied numerically, importantly after the measurement and not during the measurement as in the case of generic confocal experimental setup. It is possible to extend this method to 3D. For 3D we would need more illumination angles, but a 3D position scan still be obtained from a 2D angular scan.

To further increase the resolution of the test sample and obtain a quantitative link between the object and detected field, we can then perform synthetic aperture techniques.

## 2.7 2D synthetic aperture microscopy

Two-dimensional synthetic aperture microscopy reconstructs the sample in 2D from the measured complex scattered field data of the TDM. In TDM, we illuminate the sample with various illumination angles and detect the scattered field data. Each illumination angle provides access to the detection of different regions of the spatial frequencies in Fourier domain. The amplitude and the phase information of the spatial frequencies are known. The principle of the 2D synthetic aperture is to recombine these different 2D complex spatial frequencies in the Fourier space to form single synthetic numerical aperture (NA). The diameter of such synthetic numerical aperture is twice larger than the diameter of the numerical aperture used for detection of single incidence in TDM. Inverse Fourier transform of the 2D synthetic aperture numerical aperture would yield the two-dimensional synthetic aperture reconstruction of the sample. The formation of 2D synthetic aperture is explained in detail below.

The formation of the synthetic 2D aperture is shown in Fig. 2.13. The object to be imaged is illuminated with coherent light, it diffracts the light in all possible directions. Objective lens collects the scattered light with a given NA. For normal incidence angle of illumination case, the scattered field detected in Fourier domain is shown in the Fig. 2.13 with red dotted circle. The red dotted circle specifies the limit of detected frequencies for a given NA of objective, given by radius  $k_0NA$ .

Now, let us consider that the object is illuminated with a coherent beam having wave vector  $\mathbf{k}_{inc1}$  as shown in Fig. 2.13.A. This would lead to the sample scattering different spatial frequencies compared to the normal incidence case, but the size of the numerical aperture used for detection remains  $k_0NA$  radius. The location of the detected spatial frequencies corresponding to  $\mathbf{k}_{inc1}$  illumination would depend on the  $\mathbf{k}_d - \mathbf{k}_{inc}$  in the Fourier domain, with  $\mathbf{k}_d$  being the detected diffracted field wave vector. Knowing this, the measured spatial frequencies can be positioned in the 2D synthetic aperture satisfying the condition  $\mathbf{k}_d - \mathbf{k}_{inc}$  as shown in Fig. 2.13.A.

Similarly, the angle of incidence is varied to  $\mathbf{k}_{inc2}$  (Fig. 2.13.B),  $\mathbf{k}_{inc3}$  (Fig. 2.13.C),  $\mathbf{k}_{inc4}$  (Fig. 2.13.D), etc., They provide access to different spatial frequencies in the Fourier domain. They are positioned in the synthetic numerical aperture satisfying the condition  $\mathbf{k}_d - \mathbf{k}_{inc}$  for each incidence and the diffracted field wave vector. The common spatial frequencies between different illumination angles when they are repositioned in the synthetic numerical aperture are averaged. The repositioning of

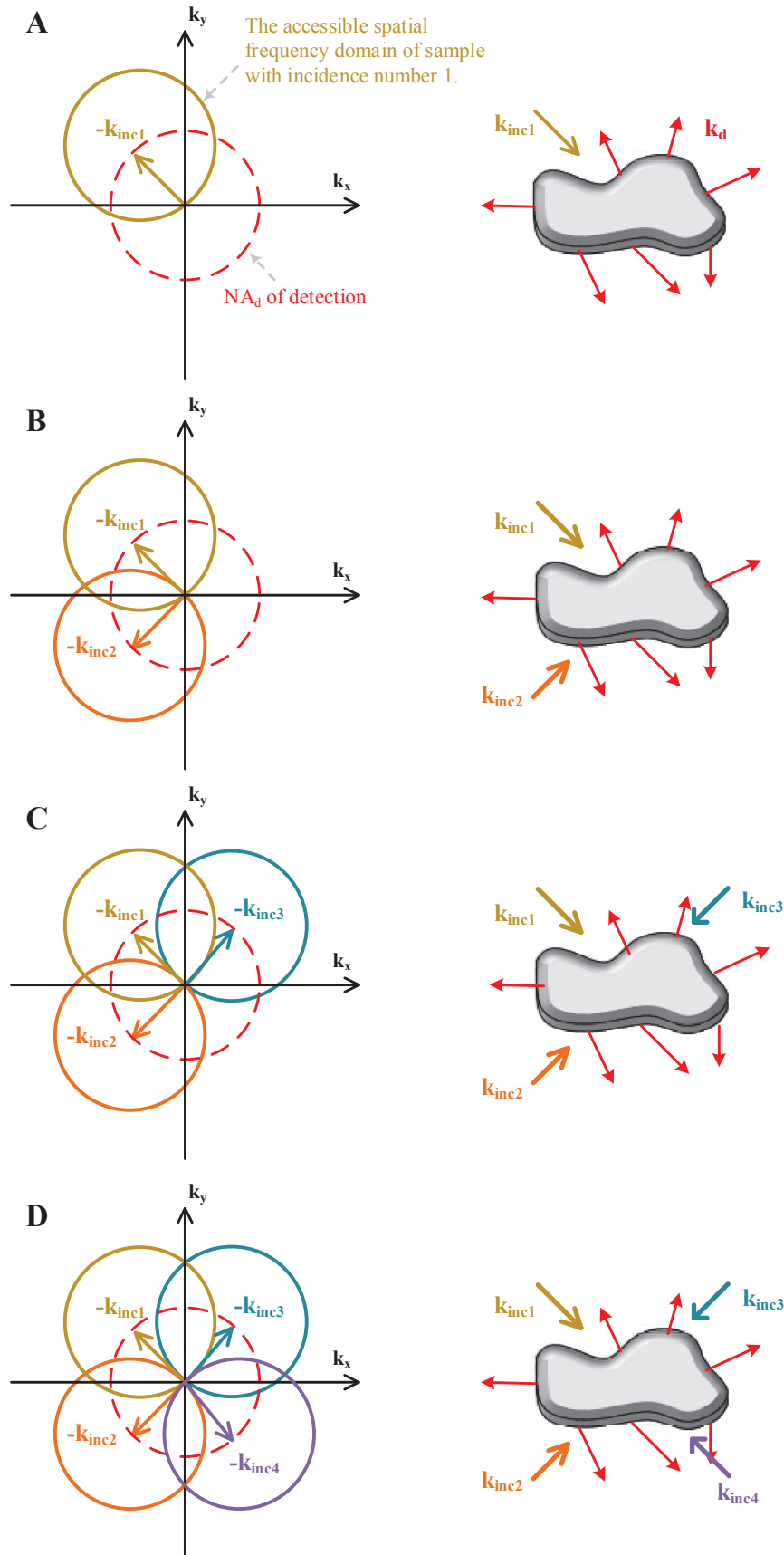
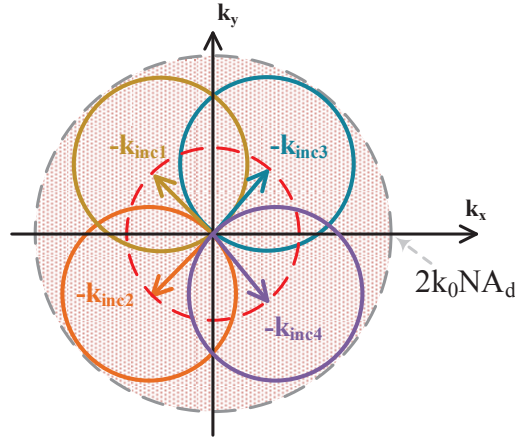


Figure 2.13 : Formation of 2D synthetic aperture in TDM.



**Figure 2.14 :** Final 2D synthetic aperture in TDM if all the possible angles of illumination are used compared to only 4 angles shown in Fig. 2.13.D.

the diffracted field data provides a 2D synthetic aperture whose numerical aperture is twice larger than the NA of the objective used for detection. The radius of the synthetic numerical aperture is  $2k_0NA$ . Combining many such illumination angles it is possible to fill the whole 2D synthetic aperture as shown in Fig. 2.14.

With 2D synthetic aperture microscopy we have increased the accessible spatial frequencies, which would mean increase in the resolution along the transverse direction. As the positioning of the spatial frequencies were performed in 2D space along transverse directions, the sample's 3D geometrical information cannot be reconstructed. But in the next section, the 2D spatial frequencies are positioned in 3D space to obtain the 3D geometry of the sample.

The reconstruction of the sample Fig. 2.1 can be demonstrated with the 2D synthetic aperture TDM. The measured data set used for 2D synthetic aperture reconstruction is explained in detail in the section Sec. 2.2 of this chapter. The measured complex scattered field data for each illumination angle were positioned in the Fourier domain as explained in this section above. This forms a nice 2D synthetic aperture as shown in Fig. 2.15.A. Notice that only 8 angles of incidence were used for this data set, we already have a good filling of the 2D synthetic aperture.

The Born approximation explained in the section Sec. 1.5.3 establishes a simple relationship between the measured scattered field and the sample. The Fourier transform of this 2D synthetic aperture complex data (Fig. 2.15.A) would yield the 2D reconstruction of the sample in the image space (Fig. 2.15.B) or equivalent reflectance of the sample [59]. We obtain a complex (amplitude and phase information) image. The image shown in Fig. 2.15.B represents the modulus of the reconstruction.

The reconstruction Fig. 2.15.B is a non-polarized reconstruction of the sample. But, the data set explained in the section Sec. 2.2 was performed with four polarization combinations ( $\hat{x}\hat{D}_1$ ,  $\hat{y}\hat{D}_1$ ,  $\hat{x}\hat{D}_2$  and  $\hat{y}\hat{D}_2$ ). To obtain the non-polarized reconstruction we sum the results obtained from all the above polarization combinations, resulting in Fig. 2.15.B.

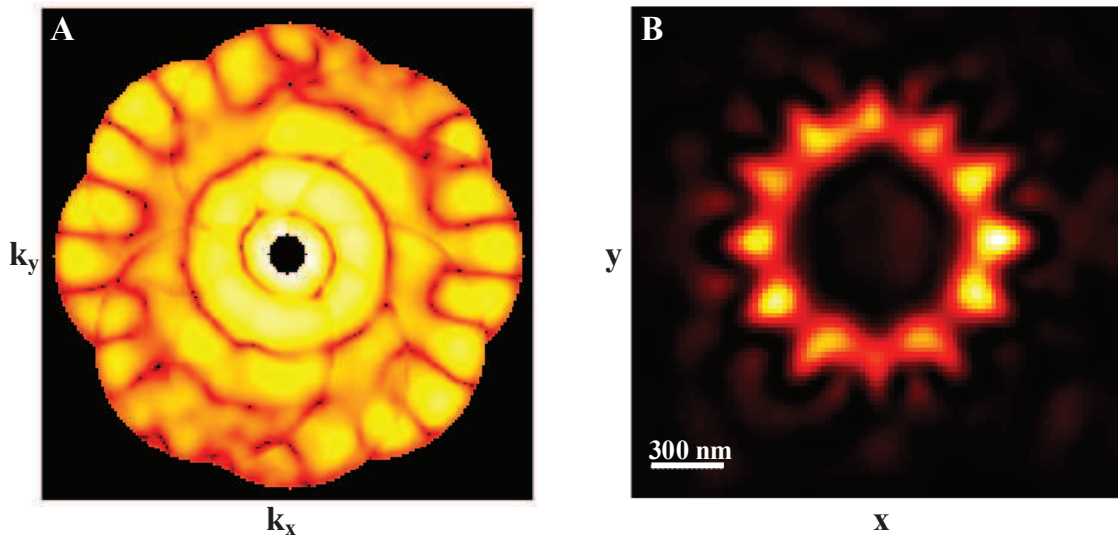


**Figure 2.15 :** *Fig.A: The modulus of 2D synthetic aperture in the Fourier domain shown in log scale for eight directions of incidences. The 8 incidences were defined by a fixed polar angle of  $60^\circ$  and an azimuthal angle regularly spaced within  $2\pi$ . Specular region (illumination modulus) is masked. Fig.B: 2D synthetic aperture reconstruction of sample (see Fig. 2.1 for the sample). Fourier transform of A would yield B. The Fig.B here displays the modulus of the complex reconstruction.*

The Fig. 2.15.B shows better reconstruction compared to the bright field, dark field, and phase contrast microscopy discussed in this chapter. The resolution is better than those techniques and slightly better than the confocal technique, observe the separation of the resin rods in Fig. 2.15.B. As we observe towards the interior of the rods, we fail to resolve the rods.

The 2D synthetic aperture TDM method provides only the 2D reconstruction of the sample. It fails to provide a link with the sample characteristics such as the relative permittivity or the 3D geometry of the object. Those information would help in understanding the sample further. On the other hand, this method is simple to implement, computationally less demanding and can be performed quickly.

The interest is to reconstruct the sample in 3D and calculate the permittivity map. So far we were able to perform only 2D reconstructions. Next step will be to use the measured complex field information to reconstruct the sample in 3D.

## 2.8 3D synthetic aperture microscopy

The real life samples are 3D in nature. The three-dimensional synthetic aperture microscopy provides the opportunity to reconstruct them in 3D. In the 3D synthetic aperture case, the image is related to the distribution of the permittivity inside the object and retrieves the geometrical information also. The 3D synthetic aperture microscopy is performed under Born approximation to reconstruct the 3D sample as explained in the previous chapter, section (Sec. 1.5.3). Under Born approximation, we know that there is a linear link between the complex scattered field data and the

relative permittivity of the object,  $E_d(\mathbf{k}_d, \mathbf{k}_{inc}) \propto 3D FT [\chi(\mathbf{k}_d - \mathbf{k}_{inc})]$ . Where,  $\chi$  is the relative permittivity contrast,  $E_d(\mathbf{k}_d, \mathbf{k}_{inc})$  is the diffracted field data.

Under the Born approximation the diffracted field data can be positioned in the Ewald's sphere as explained in the last chapter (Sec. 1.5.4). This establishes a link between the 3D sample and the 2D measured diffracted field data. The 2D diffracted field data is transformed into a cap of sphere and positioned in the 3D Ewald's sphere (see Fig. 1.8 for transmission configuration and Fig. 1.11 for reflection configuration). This 3D synthetic aperture (Ewald's sphere) can be inverse Fourier transformed in 3D to obtain the 3D reconstruction of the sample and the permittivity contrast distribution of the sample.

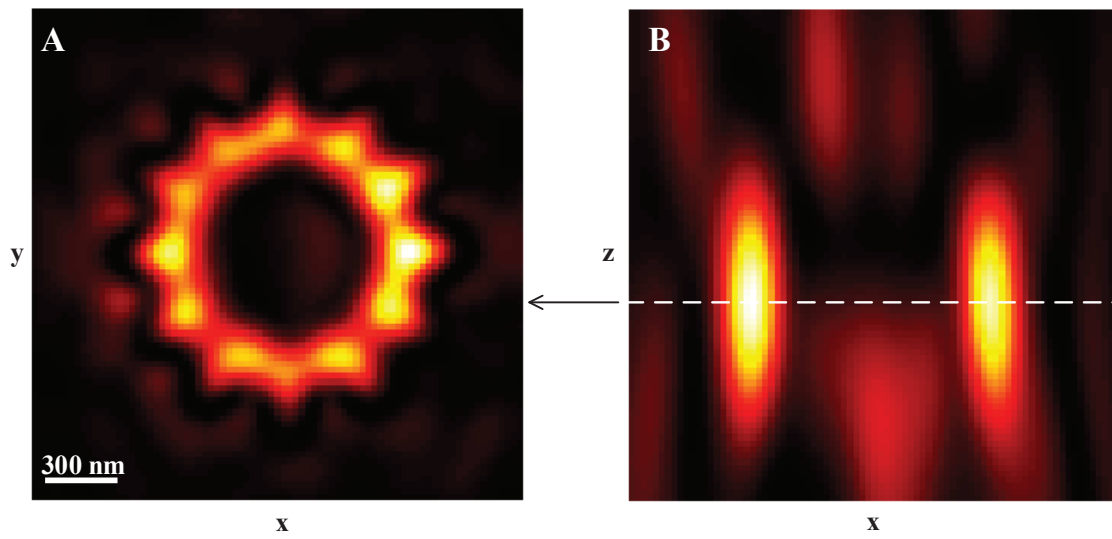


**Figure 2.16 :** *Fig.A: Modulus of 3D synthetic aperture reconstruction of sample Fig. 2.2.A in xy plane, a cut along z=0 plane. Fig.B: Modulus of reconstruction along the xz plane, a cut along the y=0 plane. Same scale in x, y and z.*

To demonstrate this method, we again use the data set used through this chapter, explained in section Sec. 2.2. To recall, the sample was illuminated with 8 angles of incidence. The diffracted field data corresponding to the 8 illumination angles were positioned in the Ewald's sphere and 3D inverse Fourier transformed to obtain the 3D result as shown in Fig. 2.16. The Fig. 2.16.A shows a transverse cut. The Fig. 2.16.B is to demonstrate the 3D capability, it shows a axial cut along y-axis ( $y=0$ ).

The reconstruction obtained with 3D synthetic aperture in transverse direction (xy, Fig. 2.16.A) is comparable to the reconstruction in the 2D synthetic aperture microscopy (Fig. 2.15.B). It has to be noted that one require lesser illumination angle of incidences for 2D synthetic aperture compared to the 3D synthetic aperture case. Because in 3D synthetic aperture 3D volume is filled with cap of spheres, whereas in 2D synthetic aperture case, we fill a circular area with 2D data. The axial direction reconstruction is therefore elongated, this also proves the point that the reconstruction in the axial direction in microscopes are worse than in the transverse direction.

Most of the groups researching on the TDM are oriented towards using this 3D synthetic aperture microscopy in the transmission configuration. Here we demonstrated with a sample deposited on a reflecting substrate and with very few angles of illumination to obtain initial 3D reconstruction of the sample. To recall the disadvantages of the Born approximation or 3D synthetic aperture microscopy, polarization effects are neglected, the medium is considered to be homogeneous, the sample is of low permittivity contrast etc., so it is not adapted here. But we have the initial 3D geometry of the sample reconstructed here.

The reconstruction obtained here has to be compared with the reconstruction that will be obtained using the accurate methods for inversion presented in the next chapter. Nevertheless, 3D synthetic aperture is a simple and rapid means of obtaining the 3D geometry of the sample. The sample that we imaged in this chapter had scatterers that are closer as we observed towards the inner edge of the sample. This implies that multiple scattering has to be taken into account [35]. The next chapter will utilize the same data set as here but will obtain better reconstruction in 3D with improved resolution and quantitative 3D permittivity map of the sample thanks to rigorous iterative inversion algorithm.

## 2.9 Conclusion

Tomographic diffractive microscope is seen by researchers as a new technique, different from other conventional microscope techniques. In this chapter, it is demonstrated to reproduce the conventional intensity based microscope techniques such as bright-field imaging, dark-field imaging, phase-contrast microscopy and confocal microscopy using the TDM measurement data. These techniques are numerically realized by utilizing the TDM measured data set. The advantage being the TDM measurement was performed only once on the sample. This is due to the fact that, TDM provides complete complex measured field data and includes all the stated methods for numerical reproduction later.

The conventional TDM reconstruction techniques results such as 2D and 3D synthetic aperture microscopy used by majority of the research groups in the world were also presented but adapted here with reflective substrate. But, the interest would be to reconstruct the sample with better resolution and 3D quantitative permittivity map than the methods discussed in this chapter. That would provide the best possible resolution and quantitative information about the sample. In the next chapter, we look for accurate methods to reconstruct the sample from the TDM data and compare the reconstructions obtained in this chapter.



---

# Imaging with tomographic diffractive microscopy holograms using accurate models

---

“Fast is fine, but accuracy is everything.”  
-Xenophon of Athens, Historian

## 3.1 Introduction

In this chapter, I numerically reconstruct objects using accurate modeling of the light (electromagnetic and polarization) matter (3D objects) interaction. In the previous chapter, I have presented the scalar approximation based reconstructions resulting in limited resolution and poor quality of reconstruction. The accurate modeling of light can improve the resolution and the quality of reconstruction compared to the scalar approximation techniques. The methods that will be explained in this chapter, go beyond the scalar techniques in utilization of the full-polarized nature of the incident light and measured complex diffracted field. For the reconstruction, no approximations are assumed. The link between the sample’s vectorial diffracted field and the material properties (permittivity contrast) are solved non-linearly by numerical means. This resulting in the 3D reconstruction of the sample permittivity map. We also developed a technique to handle the noisy optical tomography diffraction microscopy (TDM) measured data and reconstruct the sample from such a data set. Coupling of TDM data with accurate reconstruction techniques were tested on the samples with different orientations to test its viability.

Non-linear inversion approach is one of the specialization of our research group (SEMO, Institute Fresnel) compared to the other research groups working on optical tomography diffraction microscopy (TDM). Usual approach among the researchers working on TDM around the world is to reconstruct the sample under scalar approximations (Born or Rytov or other methods) with compromised resolution and the quality of the reconstruction[30, 52, 67]. We also specialize in reconstructing the samples deposited on a reflecting substrate and high permittivity contrast samples. The non-linear inversion algorithms were developed by the group, I adopted it to image the samples and achieve super-resolution images presented in this chapter.

I will present the full vectorial complex field TDM accurate reconstructions techniques to reconstruct the 3D permittivity of the probed sample with better resolution and quality compared to approximation approaches [93, 101]. Before the accurate non-linear inversion of the data, the data has to be processed.

## 3.2 Normalization of TDM data

The measurement of TDM data involves illumination of the sample with varying angles of incidence and collecting the complex diffracted field data from it. Due to varying incidence angles and the duration of measurement there can be fluctuations in the laser power or environmental perturbations etc. These fluctuations are compensated with the help of normalization. To have the same amplitude and phase for all illumination angles at a particular position on the sample, one has to normalize the TDM data. So, the normalization is performed on the amplitude and phase information of the data extracted from the TDM holograms.

### 3.2.1 Normalization procedure

The normalization procedure aims at setting the data set in agreement with the following assumptions. First, the sample is illuminated by plane waves with unity amplitudes. Second, the phase origin for the illuminating field and for the scattered field is placed on the surface of the substrate. The presence of the substrate is indeed taken into account. Because for varying angles of incidence, the Fresnel reflection coefficients changes and it is accounted for during the normalization procedure.

The phase origin is not known during the measurement. It is nevertheless possible to correct the phase of the data set to become in agreement with the assumption that phase origin is located on the substrate. We have developed two methods to correct this phase origin mismatch, which are detailed in Ref. [76]. Two important points then remain in the procedure. First, normalize the modulus of the scattered field to compensate the possible laser power fluctuations from one illumination angle to another. Second, normalize the phase of this field, to correct the different phase delays introduced on the illuminating beam from one illumination angle to another. These two steps use as reference signal the specular reflection on the substrate. This approach is valid if in the specular direction the scattered field is negligible compared to the specular reflection coming from the sample, which is true for small objects that are studied in this thesis.

In the full polarized measurements, the polarization of the illuminating beam can be initially along  $\hat{\mathbf{x}}$  or  $\hat{\mathbf{y}}$  (see Fig. 1.17 and Fig. 1.18). In the general case, once the beam has been deflected by the fast steering mirror to an arbitrary direction, the polarization of the incident field  $\mathbf{E}_{\text{inc}}$  on the object can be decomposed into its S (TE) and P (TM) components :

$$\mathbf{E}_{\text{inc}} = -\cos(\phi_i)E_{\text{inc}}\hat{\mathbf{s}} + \sin(\phi_i)E_{\text{inc}}\hat{\mathbf{p}}, \quad (3.1)$$

where  $E_{\text{inc}}$  is the complex amplitude of  $\mathbf{E}_{\text{inc}}$  and  $\phi_i$  is the azimuthal angle of the illumination. The specularly reflected field  $\mathbf{E}_r$  then becomes :

$$\mathbf{E}_r = -\cos(\phi_i)r_S E_{\text{inc}}\hat{\mathbf{s}} + \sin(\phi_i)r_P E_{\text{inc}}\hat{\mathbf{p}}, \quad (3.2)$$

with  $r_S$  and  $r_P$  the Fresnel reflection coefficients for S and P polarizations.

### 3.2.2 Normalization factor

The field  $\mathbf{E}_{\text{im}}$  imaged on the camera is measured along the two polarization directions  $\hat{\mathbf{D}}_1$  and  $\hat{\mathbf{D}}_2$  (shown in Sec. 1.6.2.1).  $\mathbf{E}_{\text{im}}$  is the sum of the field scattered by the object and the field  $\mathbf{E}_r$  reflected by the substrate. For any illumination angle, it is possible to calculate theoretically the value  $\mathbf{E}_r^{\text{th}} \cdot \hat{\mathbf{D}}_p$  ( $p = 1$  or  $2$ ) for the case  $|E_i| = 1$ , as supposed in the inversion procedure. Note that in the image space of the camera, thanks to the high magnification,  $\hat{\mathbf{s}}$  and  $\hat{\mathbf{p}}$  can be considered in the  $(\hat{\mathbf{x}}, \hat{\mathbf{y}})$  plane.

To normalize both the modulus and the phase of the data set  $\mathbf{E}_{\text{im},l} \cdot \hat{\mathbf{D}}_p$ , it has to be multiplied for each illumination  $l$  by the factor  $M_l$  :

$$M_l = \frac{|\gamma_l|S \mathbf{E}_{r,l}^{\text{th}} \cdot \hat{\mathbf{D}}_p e^{-j\varphi_l}}{2\pi \langle |\mathbf{E}_{\text{im},l} \cdot \hat{\mathbf{D}}_p| \rangle_S}, \quad (3.3)$$

where  $\gamma_l$  is the projection of  $\mathbf{k}_l$  on the optical axis of the microscope, and  $S$  the surface of the field of view that can be imaged on the camera.  $\varphi_l$  is the phase that is measured in the specular reflection direction.  $\langle |\mathbf{E}_{\text{im},l} \cdot \hat{\mathbf{D}}_p| \rangle_S$  is the mean modulus, averaged over the field of view, of the signal detected on the camera for the  $l$ -th illumination. As the object is small on the image, it can be considered as the experimental value of  $\langle |\mathbf{E}_{r,l} \cdot \hat{\mathbf{D}}_p| \rangle_S$ .

The multiplication by  $M_l$  ensures that the maximal value of  $|\mathbf{E}_{\text{im},l} \cdot \hat{\mathbf{D}}_p|$  in far field, which corresponds to the specular reflection, is equal to that scattered by a portion of substrate of surface  $S$  when illuminated by a plane wave with unity amplitude. This is the amplitude normalization part.

The phase normalization must guarantee that all the illuminating plane waves have a common phase origin placed on the substrate, as in the inversion algorithm. To fulfill experimentally this condition, the phase of the detected field  $\mathbf{E}_{\text{im},l} \cdot \hat{\mathbf{D}}_p$  has to be shifted by a constant, so that the phase in the specular reflection direction matches the argument of the theoretical Fresnel reflection coefficient. This is exactly what is performed through the multiplication by  $M_l$ .

Once this normalization has been carried out for each polarization combination in the data set  $(\hat{\mathbf{x}}\hat{\mathbf{D}}_1, \hat{\mathbf{y}}\hat{\mathbf{D}}_1, \hat{\mathbf{x}}\hat{\mathbf{D}}_2$  and  $\hat{\mathbf{y}}\hat{\mathbf{D}}_2)$ , it is possible to combine them to generate the vectorial scattered field  $\mathbf{f}_l$ , for any linear polarization of the illumination in the  $(\hat{\mathbf{x}}, \hat{\mathbf{y}})$  plane.

Such normalized data can further be used to perform accurate reconstruction of the sample.

### 3.3 Non linear inversion method

In classical TDM, the inversion consists in applying a 3D inverse Fourier transform to the data set. This simplified approach is valid only if the following conditions are met. First, the single scattering approximation is verified. Second, the scalar approximation is valid, ignoring the polarized nature of light. Third, the sample is illuminated by a plane wave and surrounded by a homogeneous medium. We have developed an inversion algorithm that breaks all these limitations by taking into account the full-vectorial (polarization) nature of the scattered field and the non-linear link between the sample and the measured field.

First, we will understand the role of polarization and the requirement to perform four measurements to obtain the full-vectorial data set.

#### 3.3.1 Polarization and transverse isotropic resolution

In this section, I will present the importance of the polarization for illumination and detection with respect to the resolution. In the section Sec. 1.6.2.1, we demonstrated the measurement of the full-vectorial field for both illumination and the detection. To recall, the polarization of illumination and the detection are controlled by means of the half-wave plates positioned in the experimental setup. It is controlled in both illumination path and the detection path. Four data sets with either vertical or horizontal polarization along the illumination directions and  $\hat{D}_1$  or  $\hat{D}_2$  ( $\pm 45^\circ$  with respect to vertical direction, see Fig. 1.18) along the reference beam direction are measured. From these four data sets, it is possible to obtain a full-polarized data set for any polarization using Jones operator. To be precise, the four data sets measured during the measurements are  $\hat{x}\hat{D}_1$ ,  $\hat{x}\hat{D}_2$ ,  $\hat{y}\hat{D}_1$ , and  $\hat{y}\hat{D}_2$ ; with the first letter indicating the illumination polarization and the other letter indicating the detection polarization.

To demonstrate the requirement of full-polarized measurement and its influence, we consider the four individual data sets measured during the measurement using TDM. We use the same reference sample we used in the previous chapter with 12 resin rods placed radially at the summit of a dodecagon Fig. 2.1. The illumination angles and the detection are also conserved. Let us consider the case of  $\hat{x}\hat{D}_1$ , we observe the dark-field image obtained for only this polarization combination. The dark-field image corresponding to  $\hat{x}\hat{D}_1$  is shown in Fig. 3.1.A, obtained with the method described in the section Sec. 2.4. The Fig. 3.1.A shows incomplete information about the object. Instead of 12 resin rods, we image only 10 spots in the dark-field image at the location of the resin rods. This is due to the incident and detection polarization combination being  $\hat{x}\hat{D}_1$ .

Yet the different polarization combinations  $\hat{x}\hat{D}_2$  (Fig. 3.1.B),  $\hat{y}\hat{D}_1$  (Fig. 3.1.C), and  $\hat{y}\hat{D}_2$  (Fig. 3.1.D) yield complementary information about the sample. Each case illuminates and detects with different polarization, so we obtain the complimentary information. This emphasizes the importance of the full-polarized measurements in the TDM for achieving isotropic super-resolution along the transverse direction. It

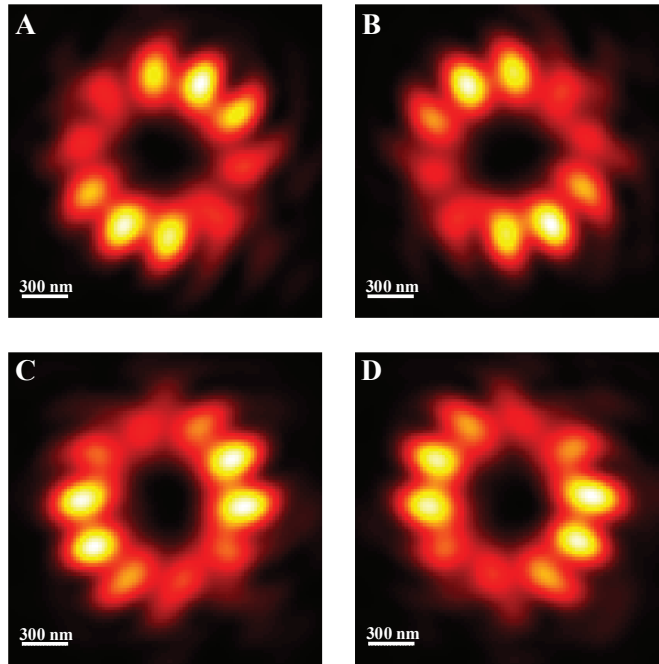


**Figure 3.1 :** Dark field images corresponding to, Fig.A:  $\hat{x}\hat{D}_1$ , Fig.B:  $\hat{x}\hat{D}_2$ , Fig.C:  $\hat{y}\hat{D}_1$ , and Fig.D:  $\hat{y}\hat{D}_2$ .

has to be noted that relying on single polarization or scalar measurements would fail to provide isotropic transverse resolution.

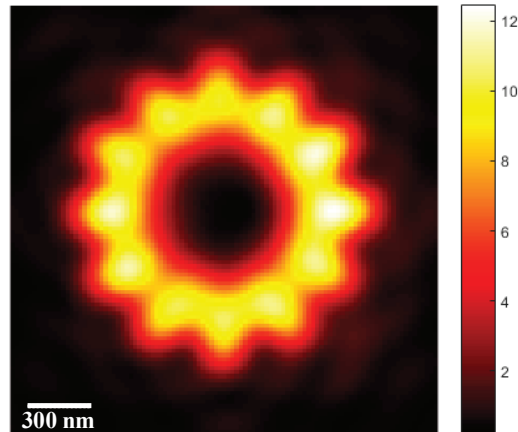


**Figure 3.2 :** Unpolarized dark-field image of the sample at  $\lambda = 475\text{nm}$ , resulting from the summation of Figs. 3.1.A, B, C, and D, in the transverse direction ( $xy$ ).

The unpolarized dark-field image of the sample is displayed in Fig. 3.2, it shows a transverse cut along the  $xy$  direction. The image is obtained by summing the four  $\hat{x}\hat{D}_1$ ,  $\hat{x}\hat{D}_2$ ,  $\hat{y}\hat{D}_1$ , and  $\hat{y}\hat{D}_2$  different polarization (Figs. 3.1.A, B, C, and D) dark-field images and averaging. The image Fig. 3.2 shows all the 12 branches of the

imaged sample, highlighting the importance of taking into account all polarization cases.

We understood that for isotropic resolution all the polarization cases have to be taken into account or unpolarized light has to be used. However unpolarized light produces limited resolution images as shown on Fig. 3.2 or in the previous chapter. So, we perform 4 different measurements ( $\hat{x}\hat{D}_1$ ,  $\hat{x}\hat{D}_2$ ,  $\hat{y}\hat{D}_1$ , and  $\hat{y}\hat{D}_2$ ) and combine them to obtain full-vectorial field, this will permit to improve the resolution. To seek better resolution and 3D reconstruction we progress towards the utilization of full-vectorial field without approximations for TDM imaging starting from now in this thesis.

Before we understand our inversion approach on the measured data, it is important to understand the forward scattering problem. This helps in understanding the way we estimate the sample, the forward estimation is used in the inversion procedure.

### 3.3.2 Forward problem

Forward scattering problem is modeling the interaction of the electromagnetic fields with an object of interest. In simple terms, we know size, shape and constituent material of an object along with it's surrounding medium. We illuminate the know electromagnetic field ( $\mathbf{E}_{inc}$ ) and we calculate the unknown scattered field ( $\mathbf{E}_d$ ) from the object (shown in Fig. 3.3). Generally, the forward scattering problem is solved by numerical means. Analytical solution exists only for simple objects (e.g. homogeneous spheres, cylindrical objects etc.) [102]. Though there exists many methods to perform forward scattering problem, we use the coupled dipole method (CDM) or discrete dipole method [92, 103, 104] to compute the forward problem. The CDM has the advantage of restricting the computational domain to the size the object, the calculation precision can be optimized by the size of the discretization units (seen in Fig. 3.3 as cubes).

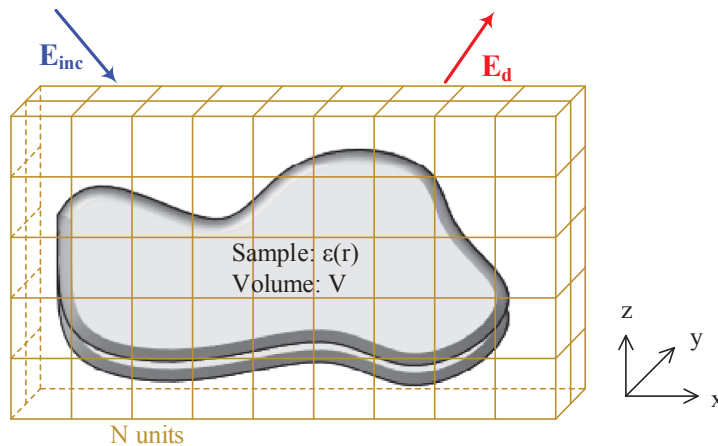


**Figure 3.3 :** The coupled dipole method discretization of arbitrary 3D object into  $N$  cubical units. The  $\mathbf{E}_{inc}$  is the incident field and  $\mathbf{E}_d$  scattered field.

Purcell and Pennypacker [103] introduced the CDM method in 1973 to study the scattering of light. From the chapter 1 we recall the relation we derived between the scattered field and incident field,

$$\mathbf{E}_d(\mathbf{k}, \mathbf{k}_l) = \int_V \mathbf{g}(\mathbf{k}, \mathbf{r}') \chi(\mathbf{r}') \mathbf{E}(\mathbf{r}', \mathbf{k}_l) d\mathbf{r}', \quad (3.4)$$

$$\mathbf{E}(\mathbf{r}, \mathbf{k}_l) = \mathbf{E}_0(\mathbf{r}, \mathbf{k}_l) + \int_V \mathbf{G}(\mathbf{r}, \mathbf{r}') \chi(\mathbf{r}') \mathbf{E}(\mathbf{r}', \mathbf{k}_l) d\mathbf{r}'. \quad (3.5)$$

$\mathbf{k}_l$  is the wave vector of the  $l^{\text{th}}$  illuminating plane wave, and  $\mathbf{k}$  is the wave vector along which the scattered field is detected in far field. The object is represented by its permittivity contrast  $\chi = \varepsilon - \varepsilon_b$ , where  $\varepsilon$  is the relative permittivity of the object and  $\varepsilon_b$  that of the surrounding medium, equal to 1 for the samples placed in the air and equal to 1.515 for the samples in oil environment.  $\mathbf{E}_0$  is the reference field, the one existing in the absence of the object.  $\mathbf{E}$  is the total field, the sum of  $\mathbf{E}_0$  and  $\mathbf{E}_d$ .  $\mathbf{g}$  and  $\mathbf{G}$  are respectively the near field and the far field Green tensors.  $\mathbf{g}(\mathbf{k}, \mathbf{r}')\mathbf{p}$  is the near field emitted in the  $\mathbf{k}$  direction by a dipole  $\mathbf{p}$  placed at  $\mathbf{r}'$  in the reference medium.  $\mathbf{G}(\mathbf{r}, \mathbf{r}')\mathbf{p}$  is the electric field at  $\mathbf{r}$  emitted by a dipole placed at  $\mathbf{r}'$  in the reference medium.  $V$  is the volume of the sample. Note that when all approximations used in classical TDM are met, Eq. 3.5 becomes a simple 3D Fourier transform of  $\chi$  (discussed in chapter 1 under Born and Rytov approximations).

Now, let us calculate the scattered field that we would obtain on a measurement surface by illuminating a known sample. The distance between the measurement surface and the sample decides whether calculations are near-field or far-field. As TDM is far-field measurement technique, we stick to the far-field calculation of the forward problem with CDM in this thesis. To calculate the sample's forward scattered field the sample is discretized in a bounded cube shaped box with  $N$  units as shown in Fig. 3.3. Using cubic discretization the Eqn. 3.5 can be written as,

$$\mathbf{E}(\mathbf{r}, \mathbf{k}_l) = \mathbf{E}_0(\mathbf{r}, \mathbf{k}_l) + \sum_{j=1}^N \int_{V_j} \mathbf{G}(\mathbf{r}, \mathbf{r}') \chi(\mathbf{r}') \mathbf{E}(\mathbf{r}', \mathbf{k}_l) d\mathbf{r}'. \quad (3.6)$$

with  $V_j$  the volume of the  $j$ -th cube used for discretization. We use the hypothesis that the field and the permittivity are uniform inside each sub cubic discretization. Then,

$$\mathbf{E}(\mathbf{r}, \mathbf{k}_l) = \mathbf{E}_0(\mathbf{r}, \mathbf{k}_l) + \sum_{j=1}^N \left[ \int_{V_j} \mathbf{G}(\mathbf{r}, \mathbf{r}') d\mathbf{r}' \right] \chi(\mathbf{r}') \mathbf{E}(\mathbf{r}', \mathbf{k}_l). \quad (3.7)$$

The above equation can be transformed into a system of linear equations to perform volume integration numerically as,

$$\begin{aligned} \mathbf{E}(\mathbf{r}_m, \mathbf{k}_l) = & \mathbf{E}_0(\mathbf{r}_m, \mathbf{k}_l) + \sum_{j=1, j \neq m}^N \left[ \int_{V_j} \mathbf{G}(\mathbf{r}_m, \mathbf{r}') d\mathbf{r}' \right] \chi(\mathbf{r}_j) \mathbf{E}(\mathbf{r}_j, \mathbf{k}_l) \\ & + \left[ \int_{V_m} \mathbf{G}(\mathbf{r}_m, \mathbf{r}') d\mathbf{r}' \right] \chi(\mathbf{r}_m) \mathbf{E}(\mathbf{r}_m, \mathbf{k}_l). \end{aligned} \quad (3.8)$$

with  $m=1, \dots, N$ .

We make an approximation that the Green's function is constant over any cubic cell when  $m \neq j$ . For a particular case when  $m = j$ , the Green's function presents a singularity as  $\mathbf{G}(\mathbf{r}_m, \mathbf{r}')$  goes to infinity,  $|\mathbf{r}_m - \mathbf{r}'| \rightarrow 0$ . In literature there are various approaches to solve this, we use a approach that  $V_m$  approaches zero, i.e. as  $V_m$  shrinks down around the point  $\mathbf{r}_m$  [105].

$$\lim_{V_m \rightarrow 0} \int_{W_m} \mathbf{G}(\mathbf{r}_i, \mathbf{r}') d\mathbf{r}' = \mathbf{L}, \quad (3.9)$$

where  $\mathbf{L}$  depends on the shape of  $V_m$  [105]. For a spherical or cubic shape we can write [105]

$$\mathbf{L} = -\frac{\mathbf{I}}{3}, \quad (3.10)$$

with  $\mathbf{I}$  being the identity matrix.

Then the Eq. (3.8) can be expressed as

$$\mathbf{E}(\mathbf{r}_m) = \mathbf{E}_0(\mathbf{r}_m) + \sum_{j=1, j \neq m}^N \mathbf{G}(\mathbf{r}_m, \mathbf{r}_j) \chi(\mathbf{r}_j) \mathbf{E}(\mathbf{r}_j) V_j - \frac{\chi(\mathbf{r}_m)}{3} \mathbf{E}(\mathbf{r}_m). \quad (3.11)$$

When we have large number of discretization cells, the linear system is solved iteratively [106]. We usually begin with an initial estimate, at the end of the iterative procedure one obtains the exact result [92]. If one solves the above equation, we would obtain the total field inside the object. The accuracy of the field can be varied by changing the discretization size of the cubic unit. From the total field it is possible to calculate the scattered field, in the far-field it can be expressed as,

$$\mathbf{E}_d(\mathbf{r}) = \sum_{j=1}^N \mathbf{G}(\mathbf{r}, \mathbf{r}_j) \chi(\mathbf{r}_j) \mathbf{E}(\mathbf{r}_j) V_j - \frac{\chi(\mathbf{r}_m)}{3} \mathbf{E}(\mathbf{r}_m). \quad (3.12)$$

Which means that the scattered field can be calculated for any arbitrary position  $\mathbf{r}$  from the above equation. So, for a known object with known illumination electromagnetic field the diffracted field in the far-field can be calculated.

The forward problem is useful to compare it with the measured scattered field and make sure that the measurement was performed under best possible means. But the interest is to calculate the sample permittivity from the measured diffracted field. The forward problem helps to estimate the sample in the inversion procedure, described in the following section.

### 3.3.3 Inverse problem

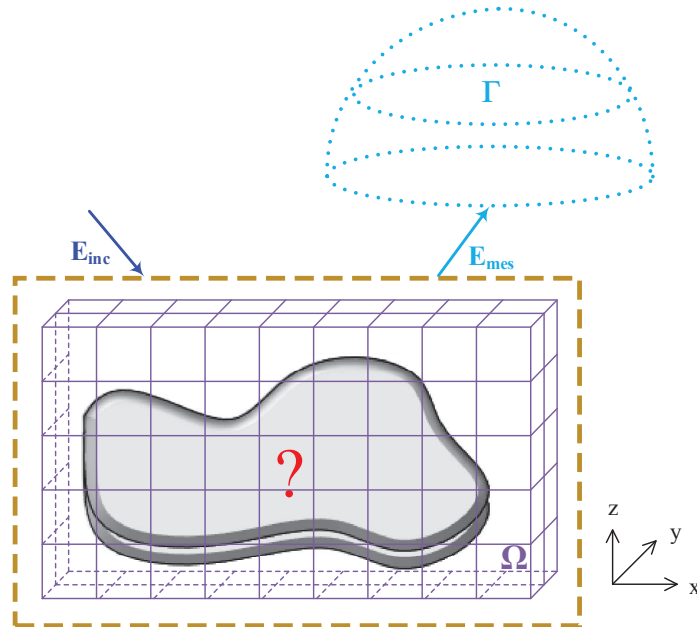


**Figure 3.4 :** *Geometry of the inverse problem: the investigation domain in inversion procedure  $\Omega$ .  $\Gamma$  is the measurement data. The unknown object is reconstructed from the measured data within an inversion box discretized by cubic units of desired size.*

The inverse problem is to reconstruct the shape, constitutive material (namely the spatial permittivity distribution) and the position of the object from the measured full-vectorial complex scattered field (Fig. 3.4). We know the illuminated electromagnetic field, and the measurement of the scattered field is performed experimentally. We calculate the unknown object in this section. For TDM data most methods in the literature solve the 3D inverse problems under Born or Rytov approximations [46, 50] under scalar considerations. These methods do not take into account the polarization and the vectorial nature of the electromagnetic field. In our group we developed an inversion algorithm to take those into consideration during the reconstruction. This is important because the samples are 3D in nature and the light interacts electromagnetically. The importance of polarization was emphasized in section Sec. 3.3.1.

Our inversion method is an iterative inversion procedure. It is based on combination of linearized methods [107–110] and modified gradient method [111, 112] to determine the permittivity of an unknown object inside an investigating domain  $\Omega$ . The inversion method retrieves simultaneously the sample permittivity contrast  $\chi$  and the total field  $\mathbf{E}_l$  in a bounded investigation domain  $\Omega$  (outside  $\Omega$ ,  $\chi$  is assumed to be null) from the set of scattered far field measured data  $\mathbf{f}_l$ , for  $l = 1, \dots, L$  illumination angles. The method has been already successfully applied to reconstruct and retrieve the permittivity of several 3D objects [25, 113–115].

We illuminate by plane waves on an object and collect the scattered light from it on a camera. We know the angles used for illumination and we calculate the angles of the scattered field for each pixel. The calculation is possible thanks to the known NA of the objective, wavelength of light used for measurement, pixel size of the camera and the overall magnification of the TDM experimental setup. Thus, the illumination angles, normalized measured diffracted field data with their corresponding collected angles, wavelength used for measurement and the substrate on which samples are deposited (recall, samples used in this thesis are reflective in nature and deposited on a substrate) are known. With these parameters the process of reconstruction of the object begins by numerical means. The volume integrals of Eqs. 3.4 and 3.5 are performed over  $\Omega$  and numerically solved by discretization  $\Omega$  into  $N$  subunits on a cubic lattice with period much smaller than the wavelength of illumination. Similar to the discretization performed in the forward problem. For the sake of simplicity, symbolic notations are used for Eqs. 3.4 and 3.5, which are restated as :

$$\mathbf{E}_{d,l} = \underline{\underline{B}}\chi\mathbf{E}_l, \quad (3.13)$$

$$\mathbf{E}_l = \mathbf{E}_{\text{ref},l} + \underline{\underline{A}}\chi\mathbf{E}_l, \quad (3.14)$$

where  $\underline{\underline{B}}$  and  $\underline{\underline{A}}$  are the operators for the far field and near field Green tensors, respectively <sup>i</sup>.

Starting from an initial guess provided by the back-propagation of the data set [116],  $\chi$  and  $\mathbf{E}_l$  are gradually estimated as shown in forward problem and adjusted at each iteration so as to minimize a cost functional involving the measured data. The basic idea underlying the Hybride inversion method is to build up two sequences related to the permittivity contrast and the total field within the scattering domain according to

$$\mathbf{E}_{l,n} = \mathbf{E}_{l,n-1} + \kappa_{l,n;\nu}\boldsymbol{\nu}_{l,n} + \kappa_{l,n;\omega}\boldsymbol{\omega}_{l,n}, \quad (3.15)$$

$$\chi_n = \chi_{n-1} + \beta_n d_n, \quad (3.16)$$

where the  $\boldsymbol{\nu}_{l,n}$ ,  $\boldsymbol{\omega}_{l,n}$  and  $d_n$  are updating direction in the research domain for the total field  $\mathbf{E}_{l,n}$  and the contrast  $\chi_n$ , respectively. The  $\kappa_{l,n}$ ,  $\beta_n$  are scalar coefficients. For more details about the updating and detailed description of the variables, please refer to thesis of Ting Zhang [92]. So, for iteration number  $n$ , the cost functional reads :

$$\mathcal{F}_n(\chi_n, \mathbf{E}_{l,n}) = W_\Gamma \sum_{l=1}^L \|\mathbf{h}_{l,n}^{(1)}\|_\Gamma^2 + W_\Omega \sum_{l=1}^L \|\mathbf{h}_{l,n}^{(2)}\|_\Omega^2, \quad (3.17)$$

where  $W_\Gamma$  weighting coefficient and  $W_\Omega$  is normalization coefficients respectively, defined by

$$W_\Gamma = \frac{1}{\sum_{l=1}^N \|\mathbf{f}_l^{\text{mes}}\|_\Gamma^2}. \quad (3.18)$$

<sup>i</sup>The presence of the substrate is taken into through these tensors

$$W_{\Omega} = \frac{1}{\sum_{l=1}^N \|\mathbf{E}_l^{\text{inc}}\|_{\Omega}^2}. \quad (3.19)$$

The  $\mathbf{h}_{l,n}^{(1)}$  and  $\mathbf{h}_{l,n}^{(2)}$  are residual errors computed from Eqs. (3.13) and (3.14), respectively :

$$\mathbf{h}_{l,n}^{(1)} = \mathbf{f}_l - \underline{\underline{B}}\chi_n \mathbf{E}_{l,n}, \quad (3.20)$$

$$\mathbf{h}_{l,n}^{(2)} = \mathbf{E}_{\text{ref},l} - \mathbf{E}_{l,n} + \underline{\underline{A}}\chi_n \mathbf{E}_{l,n}. \quad (3.21)$$

The minimization is performed with the hybrid gradient procedure described in Ref. [113].

By providing the illumination angles used to illuminate the unknown object and the measured scattered field data to the inversion algorithm, it computes the 3D object permittivity map. This algorithm has been widely used during this PhD thesis to reconstruct various objects. The next section will present one such result obtained from the measurement performed on the sample shown in Fig. 2.1.

### 3.3.4 Experimental results

#### a) Test sample

The TDM data used for non-linear inversion in this section is presented in detail in section Sec. 2.2. To recall, the sample (Fig. 2.1) was illuminated with eight directions of incidences, defined by a fixed polar angle of  $60^\circ$  and an azimuthal angle regularly spaced with  $45^\circ$  and scattered field is measured. The data set is processed for different polarization combination measurements performed for full-vectorial measurement (described in Sec. 1.6.2.1). The data is phase and amplitude normalized as explained in the Sec. 3.2 and Sec. 3.3. The complex diffracted field data can now be inverted as described in this section above to obtain 3D permittivity map of the sample.

The results obtained using the measured data on the test sample is shown in Fig. 3.5. The Fig. 3.5.A shows a transverse image obtained using the dark-field TDM explained in the previous chapter, Sec. 2.4. The Fig. 3.5.B is obtained by the application of the 3D synthetic aperture approach on the same measured data explained in Sec. 2.8, its axial image is shown in Fig. 3.6.A. The 3D-FFT (Fig. 3.5.B) resolution is slightly better than the dark-field image (Fig. 3.5.A).

As stated above, once the scattered field is measured, it can be projected to have any vectorial combination for illumination and detection. Using this, we transformed the data as  $\hat{\mathbf{x}}\hat{\mathbf{x}}$  (illumination polarization is along  $\hat{\mathbf{x}}$  and detection polarization is also along  $\hat{\mathbf{x}}$ ) and  $\hat{\mathbf{y}}\hat{\mathbf{y}}$  (illumination polarization is along  $\hat{\mathbf{y}}$  and detection polarization is also along  $\hat{\mathbf{y}}$ ). Such polarization combination data was provided to the inversion

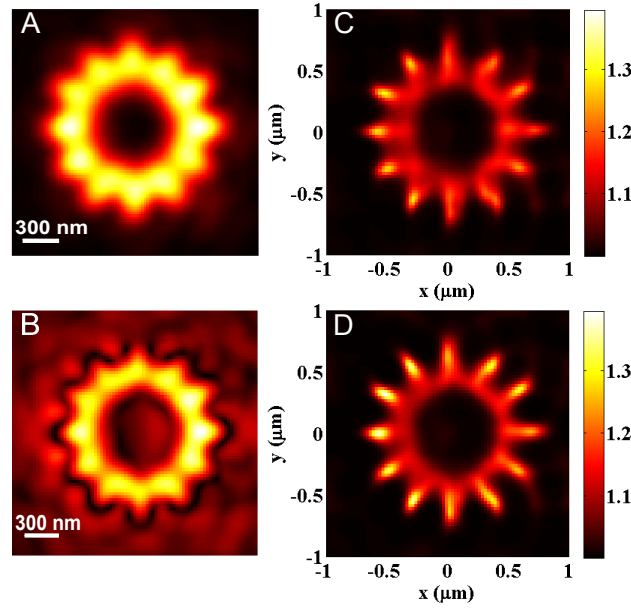


**Figure 3.5 :** Reference sample: Fig.A: Full-polarized dark-field image. Fig.B: Transverse cut along the center of the full-polarized 3D-FFT reconstruction. Fig.C: Reconstructed permittivity averaged over the sample's height using  $\hat{x}\hat{x} + \hat{y}\hat{y}$  TDM. Fig.D: Reconstructed permittivity averaged over the sample's height using the full-polarized TDM.

algorithm. The result obtained with such an inversion data set is shown in Fig. 3.5.C. From the inversion procedure we also obtain 3D reconstruction of the sample, the axial cut corresponding to Fig. 3.5.C is shown in Fig. 3.6.B. This reconstruction is better than both 3D-FFT and dark-field image. But the inner edges of the rods along the diagonal directions of the sample are not well resolved because the polarization being  $\hat{x}\hat{x}$  and  $\hat{y}\hat{y}$ . This further emphasizes the importance of full-polarized TDM and non-linear inversion.

So, we perform the full-vectorial inversion. The result obtained with full-polarized TDM and non-linear inversion explained in the above section is shown in Fig. 3.5.D, it shows a transverse cut along the  $xy$  direction. The corresponding axial cut is shown in Fig. 3.6.C. This provides the best transverse isotropic resolution.

The results of Fig. 3.5 and Fig. 3.6 shows that the vectorial inversion provides a significantly better transverse resolution, axial sensitivity, and overall 3D permittivity map than the other methods discussed in the previous chapter. In particular, it resolves the inter distance between the branches at its smallest (100 nm) which is not the case for the 3D synthetic aperture microscopy, dark-field images, phase-contrast microscopy and confocal microscopy. Polarization of the illumination and the scattered field is taken into account. The individual rods are well separated and the resolution is beyond the Rayleigh criterion limit discussed in the Sec. 1.2.2.

The time required to perform a non-linear inversion depends on the size of the object being reconstructed, number of illumination angles used during the measurement, the discretization size of the scattered field data in Fourier space, the dis-

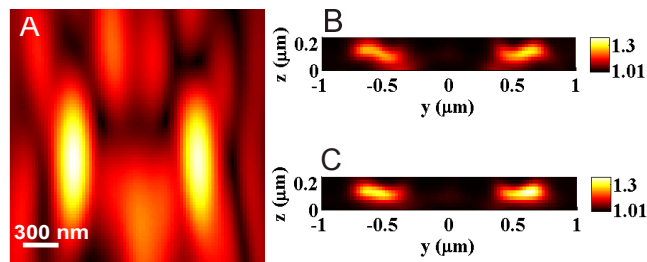


**Figure 3.6 :** Reference sample. Fig.A: Axial cut along the center of the full-polarized 3D-FFT reconstruction. Fig.B: Reconstructed permittivity along the center of  $yz$ -plane using  $\hat{x}\hat{x} + \hat{y}\hat{y}$  TDM. Fig.C: Reconstructed permittivity along the center  $yz$ -plane using the full-polarized TDM at  $\lambda = 475\text{nm}$ .

cretization size used for the numerical reconstruction (size of the pixel), the speed of the computer used for the inversion, the model used for inversion (Born [110] or Hybride method [111] or Conjugate gradient method [117]) and the algorithm optimization. The above stated parameters can be fine tuned to achieve results depending on the requirements. For the result presented for the above sample, shown in Fig. 3.5.C in 3D, it took about 8 hours to perform non-linear inversion.

On the other hand the inversion procedure is computationally demanding and time-consuming compared to the other methods, but efforts are being made in our group to decrease the inversion time significantly. The inversion time and computational speed of course depends on the amount of illumination incident angles used, the resolution and the accuracy that one would like to reconstruct etc. In the world, not many research groups have coupled the TDM to an inversion algorithm that takes into account multiple scattering and the polarization effects and provides such a super-resolution image. Also, working in reflection configuration with TDM is challenging. These were some of the specializations of our group (SEMO, Institute Fresnel, Marseille).

To demonstrate further the robustness of coupling the TDM with non-linear inversion algorithm we tested further complicated samples than the one presented in this section.

### b) Sample with one missing branch

To demonstrate the efficacy of our method and in-dependency of the symmetric nature of samples, we fabricated a sample with a resin branch missing [Fig. 3.7]. The dark-field image [Fig.3.8.A], 3D-FFT [Fig.3.8.B],  $\hat{x}\hat{x} + \hat{y}\hat{y}$  polarized TDM [Fig.3.8.C] and full-polarized TDM [Fig.3.8.D] results corresponding to the sample are presented.

The missing branch is very evident from all the techniques from the above images. The resolution and discussions for the reference star sample are also applicable to this particular sample. The inability of  $\hat{x}\hat{x} + \hat{y}\hat{y}$  TDM to resolve diagonal branches is clearly seen in this sample by comparing Fig. 3.8.C and 3.8.D. Though the sample is asymmetric the reconstruction algorithms provide similar permittivity estimate and resolution.

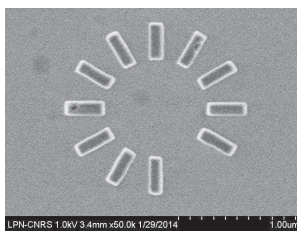


**Figure 3.7 :** SEM image of sample with one missing branch compared to the sample shown in Fig. 3.6.

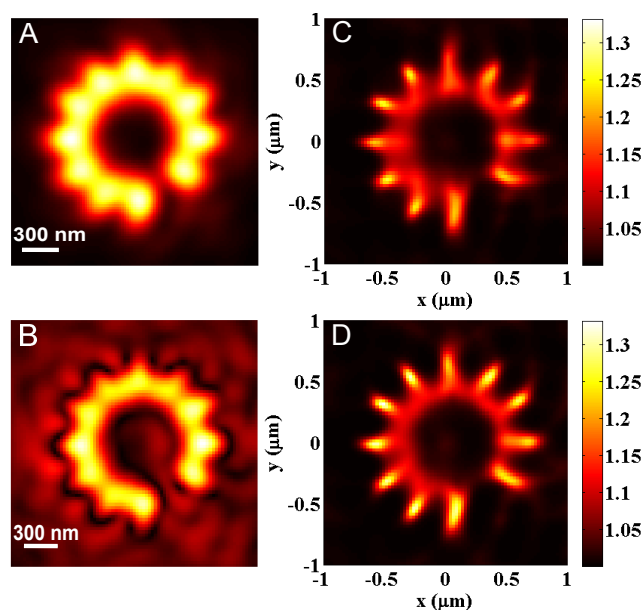


**Figure 3.8 :** Results of star sample with one missing branch. Fig.A: Full-polarized dark-field image. Fig.B: Transverse cut along the center of the full-polarized 3D-FFT reconstruction. Fig.C: Reconstructed permittivity averaged over the sample's height using  $\hat{x}\hat{x} + \hat{y}\hat{y}$  TDM. Fig.D: Reconstructed permittivity averaged over the sample's height using the full-polarized TDM at  $\lambda = 475\text{nm}$ .

### c) Sample with misaligned branches

To further demonstrate the efficiency of our technique in retrieving the alignment of sample branches we fabricated a sample as shown in Fig.3.9, two of the sample branches were misaligned in comparison to the reference sample.

Again, the full-polarized TDM provides best results with better resolution compared to other methods. The misaligned branch at the bottom is not very well resolved with  $\hat{x}\hat{x} + \hat{y}\hat{y}$  TDM, whereas full-polarized TDM resolves better. The other methods; 3D-FFT and dark-field image fail to provide conclusive evidence on the misaligned branches.

The resolution we obtained with the non-linear inversion method is one of the best considering marker-free nature of the sample. We explored the possibilities to extend the resolution beyond what is obtained in this section, but experimental noise was one of the issue preventing the inversion procedure from converging. It would

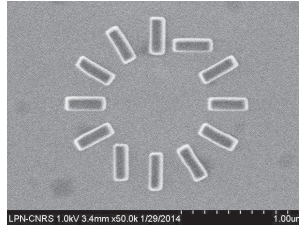


**Figure 3.9 :** (SEM image of sample with one branch misaligned compared to sample Fig. 3.6.

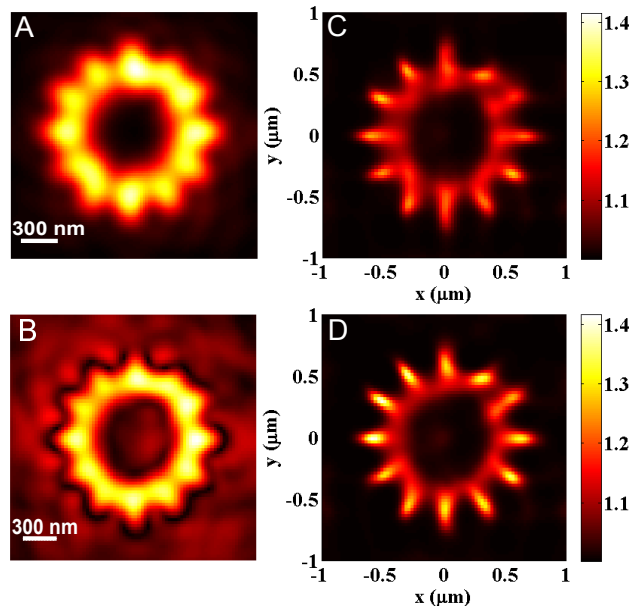


**Figure 3.10 :** Results of star sample with misaligned branches. Fig.A: Full-polarized dark-field image. Fig.B: Transverse cut along the center of the full-polarized 3D-FFT reconstruction. Fig.C: Reconstructed permittivity averaged over the sample's height using  $\hat{x}\hat{x} + \hat{y}\hat{y}$  TDM. Fig.D: Reconstructed permittivity averaged over the sample's height using the full-polarized TDM at  $\lambda = 475\text{nm}$ .

be advantageous to have a procedure to handle noisy TDM experimental data. I will now explain such a method to locate and reconstruct the samples when the TDM data is corrupted by experimental noise.

### 3.4 TDM imaging in noisy environment

In this section, we study the detection and the localization of objects in a noisy environment. It is a major issue because all the imaging applications have some level of noise or we are interested in a particular features of a sample in a very noisy data. Usually, the features of a sample maybe buried in the heterogeneous noise due to experimental noise, heterogeneities of the host medium etc. It is also of interest to localize a particular area of the sample and reconstruct, this would mean smaller area of reconstruction. The above discussed topics has been widely

researched in acoustics and electromagnetic domains and lead to development of several numerical treatments to obtain meaningful image from noisy data[118–120]. The time reversal technique or its monochromatic counterpart, DORT procedure (for the French acronym *décomposition de l'opérateur de retournement temporel*, Time Reversal Operator Decomposition) has emerged has the powerful technique to identify the sample features from noisy environment.

### 3.4.1 Principle of DORT

Let us understand the time reversal concept first. It is based on the idea that the wave propagation does not vary in a lossless non-magnetic media. We will take the help of wave equation to understand this, given by

$$\nabla^2 \mathbf{E}(\mathbf{r}, t) - \mu_0 \varepsilon(\mathbf{r}) \frac{\partial^2}{\partial t^2} \mathbf{E}(\mathbf{r}, t) = 0. \quad (3.22)$$

The solution to the above equation is  $\mathbf{E}(\mathbf{r}, t)$ , the vectorial electric field in the 3D. With  $\mu_0$  and  $\varepsilon(\mathbf{r})$  are the magnetic permeability and electric permittivity of the medium, respectively. In the above equation we have a second order time-derivative operator which depends on time  $t$ . For any scattered field  $\mathbf{E}(\mathbf{r}, t)$ , there is  $\mathbf{E}(\mathbf{r}, -t)$ , which is also a solution to the Eqn. 3.22. This is called time reversal invariance. The solution  $\mathbf{E}(\mathbf{r}, -t)$  means we have a wave which converges coherently to the emitting sources. So far we were in the time domain.

We will now understand the building of the scattering matrix in Fourier space. Let us assume, we have several scatterers in a sample. We illuminate the scatterers successively by electromagnetic excitation  $l=1, \dots, N_s$ . For each illumination  $l$ , we measure the scattered field at the detector pixels called receivers,  $m=1, \dots, N_r$ . From this we build a complex scattering matrix  $\mathbf{K}_{lm}$ , with  $l$  being the illumination field and  $m$  being the detection pixel. Observe the similarities between the TDM illumination and detection schema with the construction of scattering matrix  $\mathbf{K}$ .

In case of lossless medium, the time reversal and the complex conjugation are equivalent operations. So, the illumination becomes detection pixel and detection becomes illumination pixel  $\mathbf{K}_{lm} = \mathbf{K}_{ml}$ . The conjugate transpose matrix of  $\mathbf{K}$  is described by  $\mathbf{K}^\dagger$ . The time reversal operator (TRO) can then be described by  $\mathbf{L} = \mathbf{K}^\dagger \mathbf{K}$ .  $\mathbf{L}$  is a Hermitian operator with eigenvalues being positive real valued and its eigenvectors are orthogonal in nature [121].

The DORT is time reversal's counterpart in frequency domain. DORT consists in analyzing the eigenvalues and eigenvectors of the Time Reversal Operator (TRO), in order to synthesize incident fields that focus selectively on targets of interest. We have two important properties of  $\mathbf{L}$ . First, the number of dominant eigenvalues depends on the number of scatters present in the sample. The eigenvector associated with the eigen value permits us to localize and focus selectively. This procedure requires to record the complex field (amplitude and phase) scattered by the sample for various illuminations in order to build the scattering matrix  $\mathbf{K}$  of the target ( $\mathbf{K}$  relates the incoming field to the outgoing one).

### Relation between DORT and SVD

As explained above time reversal operator can be represented by  $\mathbf{L} = \mathbf{K}^\dagger \mathbf{K}$ . It can be shown that  $(\mathbf{K}^\dagger \mathbf{K})^\dagger = (\mathbf{K}^\dagger \mathbf{K})$ . Which means that  $\mathbf{L}^\dagger = \mathbf{L}$ . The eigenvalues and the eigenvectors of the matrix  $\mathbf{L}$  can be calculated. Which can be represented as  $\mathbf{L} = \mathbf{v} \Lambda \mathbf{v}^\dagger$ , with  $\Lambda$  being singular values and  $\mathbf{u}$  &  $\mathbf{v}$  representing unitary matrices.

Now, the Singular Value Decomposition (SVD) can be performed on the scattering matrix  $\mathbf{K}$  directly. Which would yield,  $\mathbf{K} = \mathbf{v} \Lambda \mathbf{u}^\dagger$ . It can be shown that  $\mathbf{K}^\dagger \mathbf{K} = \mathbf{v} \Lambda \mathbf{v}^\dagger$ .

This means that DORT utilizes the intensity of the field and SVD utilizes the complex field itself. Using SVD, it can be shown that for point-like scatterers in the single scattering regime, a few singular vectors of  $\mathbf{K}$  (or equivalently, the eigenvectors of the time reversal operator  $\mathbf{K}^\dagger \mathbf{K}$  where  $\dagger$  denotes the conjugate transpose), hereafter called the DORT vectors, correspond to incident fields that focus selectively on the targets [122, 123]. This method has been recently applied in optical domain to perform focusing on gold nanoparticles placed under an aberrating layer [124].

### DORT inversion

The DORT or time reversal technique permits to identify and localize the scatters located in the sample. This is done by generating agile incident fields that focus on targets embedded in a randomly inhomogeneous medium. But this method does not provide images of the sample that we would like to reconstruct [124]. To obtain quantitative information about the samples (geometrical size and permittivity) additional data processing and inversion is required [120, 125].

DORT has to be combined with an inversion procedure to obtain quantitative information. The inversion procedure can be the procedure explained in the section Sec. 3.3.3. Recently, it was proposed to apply an inversion procedure on data obtained with DORT illuminations [124, 126]. It was shown on simulated data that this combined DORT-inversion approach was significantly better than standard inversion techniques for estimating targets buried in an inhomogeneous soil. The DORT illuminations dimmed the influence of the clutter and allowed the restriction of the investigation domain to small regions surrounding the targets [126]. We localize and we construct only around a small region around the target that we are willing to reconstruct. In this section, we adapt this procedure to optical microscopy and show experimentally its interest for imaging objects of various sizes in a noisy background [121].

Since we have access to the complex scattered field data from the TDM measurement, we can perform the DORT to localize and SVD to reconstruct the sample. We demonstrate the powerfulness of this method by demonstrating it on experimental TDM data set in this section to reconstruct the samples.

## 3.4.2 Application of DORT to TDM

We have seen that the full-polarized TDM enables to reconstruct the sample 3D permittivity map with a resolution about one-fourth of the wavelength whatever the

direction in the transverse plane. In this section, we apply the DORT and inversion procedures to reconstruct the samples on TDM data corrupted with experimental noise.

With the classical TDM inversion procedure, the sample is reconstructed with a domain larger than sample. If we have a sample with small interesting features, reconstructing the whole sample is time consuming. To avoid this we can perform selective reconstruction by knowing the location of the targets beforehand inside the sample. DORT can help in localization of the targets. We can take a small domain for reconstruction around the target and reconstruct the target quantitatively.

To apply DORT inversion to the TDM data, we will process it and construct a scattering matrix as follows.

In TDM, the sample is illuminated with a collimated beam under various incident angles and polarization states and its scattered field (phase and amplitude) is recorded for a large number of observation directions within the Numerical Aperture (NA) of the microscope objective. We have seen the reconstruction of the sample in scalar approximations in the previous chapter and the non-linear inversion techniques in this chapter. The interest of TDM is that it provides directly the scattering matrix of the sample and it is thus perfectly adapted to the implementation of the DORT-inversion procedure.

A full-polarized measurement has to be performed to obtain the scattering matrix  $\mathbf{K}$ . The illumination and the detection schema for the full-polarized measurement was discussed in section Sec. 1.6.2.1. To recall, the illumination and detection is performed as  $\hat{\mathbf{x}}\hat{\mathbf{D}}_1$ ,  $\hat{\mathbf{y}}\hat{\mathbf{D}}_1$ ,  $\hat{\mathbf{x}}\hat{\mathbf{D}}_2$  and  $\hat{\mathbf{y}}\hat{\mathbf{D}}_2$ , with first letter representing the illumination polarization and the other representing the detection polarization.

There are three steps involved in applying DORT-inversion. First is to build suitable scattering matrix from measured TDM data. Second step is to perform eigenvalue decomposition of the time reversal operator. The final step to perform inversion.

For first step, let us say, I illuminate the sample with incidences  $m=1,2,\dots,M$ . To build a scattering matrix suitable for DORT-inversion, I need to project the incident field  $\hat{\mathbf{x}}$  and  $\hat{\mathbf{y}}$  to obtain  $\hat{\mathbf{s}}$  and  $\hat{\mathbf{p}}$  respectively. Where,  $\hat{\mathbf{s}}$  is polarization P or TM and  $\hat{\mathbf{p}}$  is polarization S or TE.

$$\begin{pmatrix} \hat{\mathbf{p}} \\ \hat{\mathbf{s}} \end{pmatrix} = \begin{pmatrix} \cos \phi_{\text{inc}} & \sin \phi_{\text{inc}} \\ -\sin \phi_{\text{inc}} & \cos \phi_{\text{inc}} \end{pmatrix} \begin{pmatrix} \hat{\mathbf{x}} \\ \hat{\mathbf{y}} \end{pmatrix}, \quad (3.23)$$

By this way, we obtain the scattered field corresponding to different incident angles  $l$  and two incident polarization states S and P, for  $N$  observation directions. Here,  $N$  is the number of pixels on the camera used for detection. Similarly, the measured scattered field ( $\hat{\mathbf{D}}_1$  and  $\hat{\mathbf{D}}_2$ ) can be decomposed in to S and P polarizations respectively. So, for each incident angle  $m$ , at the detection pixel on the camera  $n$ , four different groups of data can be observed, as  $K_{mn}^{pp}$ ,  $K_{mn}^{ps}$ ,  $K_{mn}^{sp}$  and  $K_{mn}^{ss}$ . The first letter of the superscript indicates the polarization state of the illumination (TM or TE), and the second letter indicates the projection of the vectorial scattered field on the polarization state TM or TE. Then we can construct a scattering matrix  $\mathbf{K}$

of dimension  $2M \times 2N$ .

$$\mathbf{K} = \begin{pmatrix} K_{11}^{pp} & K_{12}^{pp} & \dots & K_{1N}^{pp} & K_{11}^{ps} & K_{12}^{ps} & \dots & K_{1N}^{ps} \\ K_{21}^{pp} & K_{22}^{pp} & \dots & K_{2N}^{pp} & K_{21}^{ps} & K_{22}^{ps} & \dots & K_{2N}^{ps} \\ \vdots & \vdots & \ddots & \vdots & \vdots & \vdots & \ddots & \vdots \\ K_{N1}^{pp} & K_{N2}^{pp} & \dots & K_{NN}^{pp} & K_{N1}^{ps} & K_{N2}^{ps} & \dots & K_{NN}^{ps} \\ K_{11}^{sp} & K_{12}^{sp} & \dots & K_{1N}^{sp} & K_{11}^{ss} & K_{12}^{ss} & \dots & K_{1N}^{ss} \\ K_{21}^{sp} & K_{22}^{sp} & \dots & K_{2N}^{sp} & K_{21}^{ss} & K_{22}^{ss} & \dots & K_{2N}^{ss} \\ \vdots & \vdots & \ddots & \vdots & \vdots & \vdots & \ddots & \vdots \\ K_{M1}^{sp} & K_{M2}^{sp} & \dots & K_{MN}^{sp} & K_{M1}^{ss} & K_{M2}^{ss} & \dots & K_{MN}^{ss} \end{pmatrix}. \quad (3.24)$$

In theory, the scattering matrix  $\mathbf{K}$  is strictly symmetrical (due to the reciprocity theorem), see the thesis of T.Zhang [92]. In the experimental configuration, we illuminate with few angles compared to the number of detection points on the detector. The non-symmetrical behavior can be corrected by replacing each element  $\mathbf{K}_{mn}$ , by  $\frac{1}{2}(\mathbf{K}_{mn} + \mathbf{K}_{nm})$  [127]. But the singular value decomposition (SVD) can be directly performed on the matrix  $K$ , without symmetrizing the scattering matrix [128].

The second step is to calculate the singular value decomposition and observe them being focused on the scatters. We calculate the SVD of the scattering matrix  $\mathbf{K}$ ,  $\mathbf{K} = \sum_{j=1}^{2M} \mathbf{v}_j \sigma_j \mathbf{u}_j^\dagger$ , where  $\sigma_j$  is the singular value of  $\mathbf{K}$ , which is real and non-negative. In this expression, the  $2N$  vector  $\mathbf{v}_j$  gives the vectorial field diffracted by the sample when the illumination is a sum of plane waves with directions  $\mathbf{k}_m = 1 \dots M$  with  $\hat{\mathbf{p}}$  and  $\hat{\mathbf{s}}$  amplitudes fixed by the  $2M$  vector  $\mathbf{u}_j$ . Due to the reciprocity theorem, the  $2M$  vector  $\mathbf{u}_j$  can also be interpreted as the vectorial field diffracted along the  $-\mathbf{k}_m = 1 \dots M$  direction when the illumination is a sum of plane waves with directions  $\mathbf{k}_N = 1 \dots N$  and  $\hat{\mathbf{p}}$  and  $\hat{\mathbf{s}}$  amplitudes fixed by the  $2M$  vector  $\mathbf{v}_j$ . For forming the DORT agile illuminations, it is preferable to consider the reciprocal configuration as the beam given by  $\mathbf{v}_j$  contains many more plane wave directions than that given by  $\mathbf{u}_j$ .

To get an insight on the focusing property of  $\mathbf{v}_j = 1, \dots, 2M$  beams, its field  $\mathbf{E}_j^{SV}(\mathbf{r})$  in the sample domain is generated by propagating each plane wave component in a simplified medium made of a bare air-silicon interface. One gets,

$$\mathbf{E}_j^{SV}(\mathbf{r}) = \sum_{q=1}^N \mathbf{v}_j^p(n) \mathbf{E}^p(\mathbf{r}, -\mathbf{k}_m) + \mathbf{v}_j^s(n) \mathbf{E}^s(\mathbf{r}, -\mathbf{k}_m), \quad (3.25)$$

where  $\mathbf{E}^{p,s}(\mathbf{r}, -\mathbf{k}_m)$  is the field at  $\mathbf{r}$  obtained when the silicon interface is illuminated by a s or p polarized plane wave with direction  $-\mathbf{k}_m$  and  $\mathbf{v}_j^p(n)$  or  $\mathbf{v}_j^s(n)$  is the p or s polarized component of  $\mathbf{v}_j$  for the  $n$ -th direction.

For each single point-like scatterer, there exists one significant singular value in case of a scalar illumination and detection [92]. Since we are illuminating and detecting with two polarizations (s and p), we will have two dominant singular values for each scatterer. However it has to be noted that the number of singular values corresponding to a scatterer will depend on the background medium, size of the scatterer, illumination polarization etc..

The third step is the improvement of the sample characterization using an iterative inversion method explained in Sec. 3.3.3 on a area or a feature of the sample of interest. This takes advantage of the DORT focusing properties to identify the area or the feature of interest. Instead of running the inversion procedure on the  $2M \times 2N$  scattered field of the scattering matrix  $\mathbf{K}$  that are obtained for the  $2M$  plane wave illuminations, we consider the  $2M \times 2M$  scattered field given by  $\mathbf{u}_j=1,\dots,2M$  obtained for the  $2M$  agile illuminations  $\mathbf{v}_j=1,\dots,2M$ . This means selecting only a small region of interest inside the full focused field. Note that, as long as all the singular vectors are kept in the reconstruction procedure, the DORT preprocessing corresponds to a simple rearrangement of the data and not to a data reduction technique. The diminished size of the data and the smaller area of reconstruction helps in obtaining the 3D result faster, resulting in gain in the non-linear inversion time. The diminution of the scattered field data is entirely compensated by the information carried out by the complex illumination patterns.

The above stated DORT or SVD inversion can be applied to TDM experimental data for reconstruction.

### 3.4.2.1 Experimental result

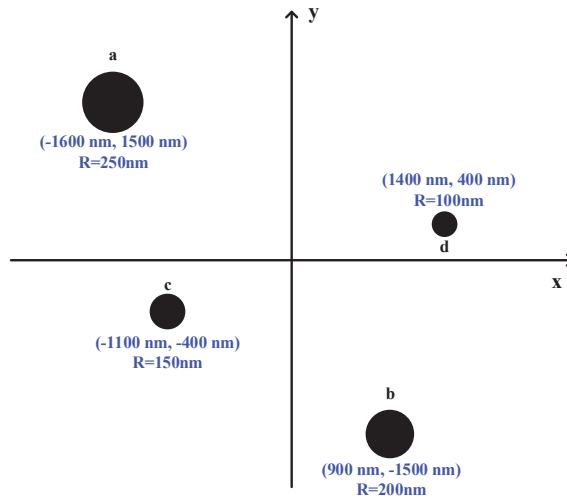


**Figure 3.11 :** *Sample geometry in the transverse cut plane. It is composed of four resin cylinders with permittivity 2, height 170 nm and different radii deposited on a silicon substrate with permittivity  $15.07+0.148i$  at the illumination wavelength 632.8 nm.*

The experimental setup of the TDM is discussed in detail in chapter Chap. 1 and section Sec. 1.6. For the DORT-inversion, I illuminate a sample with  $\lambda = 632.8nm$  light and an air objective with  $NA=0.95$  (Zeiss Epiplan-Apochromat  $\times 50$ ). The sample used for the demonstration is shown in Fig. 3.11. The sample under study is made of four resin cylinders with permittivity 2, height 170 nm and radii 250 nm,

200 nm, 150 nm and 100 nm, deposited on a reflective silicon substrate, as shown in Fig. 3.11. For estimating such a thin sample with global transverse width about 7 wavelengths,  $M = 5 \times 5$  directions of illumination and  $N = 60 \times 60$  directions of observation regularly spaced within the NA of the objective have been taken. The number of observation points ensures that the scattered field is correctly sampled while the number of illuminations ensures an appropriate data over unknown ratio in the reconstruction process as will be shown below. The experiment is conducted with 25 illuminations, with  $\theta_{\text{inc}}^{\text{max}} = 61^\circ$ , and  $\phi_{\text{inc}}$  is evenly distributed between 0 and  $360^\circ$ . To retrieve the components of  $\mathbf{K}$  which are close to the specular region, we conducted two measurements, one with the sample and one without the sample (sole the silicon substrate). By subtracting these two fields we were able to partially recover the scattered field in the specular region.

First, the experiment was performed on the sample (Fig. 3.11) without any noisy medium. The bright field image of the sample is obtained by summing up all the total field intensities as discussed in detail in the previous chapter, section Sec. 2.3. It is shown in Fig. 3.12.A. The four cylinders are clearly visible with varying width.

Now, we test the focusing property of the SVD. Fig. 3.12.B displays the sum of the intensities of singular vectors back propagated following Eqn. 3.25 at  $z = 100\text{nm}$  above the substrate. The four bright patterns that are visible over a null background demonstrate the focusing properties of these agile illuminations. Yet, the three-dimensional intensity distribution remains significantly different from that of simple focusing beams, see Fig. 3.12.G as it reflects the complexity of the DORT vectors behavior when the scatterers size is comparable to the wavelength and the imaging configuration is not free-space. In particular, the rather small axial width of the focused fields is due to the interference between the incident plane waves and their reflection by the silicon substrate [129].

The DORT processing permits, thanks to its focusing properties, Fig. 3.12.B, the restriction of the investigation domain  $\Omega$  to the most illuminated regions. As a result, the computation time required by the inversion is drastically reduced and the reconstruction is more accurate. The sample is reconstructed by running the inversion process on a  $2 \times 2 \times 0.25\mu\text{m}^3$  investigation box centered about each cylinder successively. Note that when the targets exhibit very different scattering power, a successive selective inversion is more efficient than a global reconstruction.

Fig. 3.12.C-F display the transverse cut of the permittivity map of each cylinder and an axial cut of the permittivity of the biggest cylinder is seen in Fig. 3.12.H. We observe that the quantitative inversion improves significantly the characterization of the targets as compared to the DORT image especially in the axial plane, compare Fig. 3.12.G and Fig. 3.12.H. The reconstructions are in satisfactory agreement with the actual permittivity profile and the expected resolution of about  $\lambda/4$  [6, 130]. The permittivity underestimation (especially for the smallest cylinder) is linked to the overestimation of the transverse footprint due to the limited resolution.

We now consider the much more difficult configuration in which the sample is placed behind an aberrating layer. To realize this, a piece of transparent plastic foil is placed through the illumination and collection paths in the experiment, see Fig. 1.17. The plastic foil is placed between the tube lens  $L_1$  and beam splitter

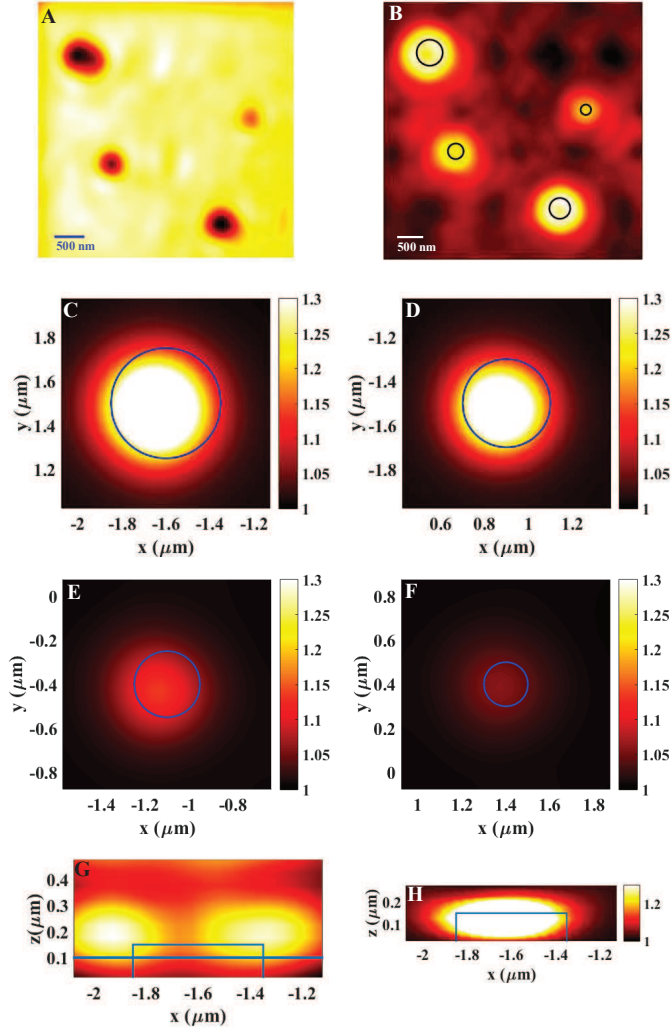


**Figure 3.12 :** *Noise free configuration. Fig.A–B: Qualitative images of the sample in the  $(x, y)$  plane. Fig.A: Bright field conventional microscope image generated by summing the experimental intensity recorded at the image plane of the TDM for the  $2L = 50$  illuminations. Fig.B: DORT image obtained by summing the intensities of the fields generated by all the singular vectors  $v_j=1, \dots, 2L$  of the scattering matrix at  $z = 100$  nm above the substrate. Fig.C–F: Selective quantitative reconstructions of the four cylinders. The quantitative inversion procedure is run on the scattered fields  $u_j=1, \dots, 2L$  obtained for the agile illuminations  $v_j=1, \dots, 2L$ . The investigation domain is restricted to a  $2 \times 2 \times 0.25 \mu\text{m}^3$  box surrounding one scatterer at a time. The reconstructed permittivity map is displayed in the  $(x, y)$  plane at  $z = 100$  nm. Figs.G–H: Image of the sample in the  $(x, z)$  plane along the line passing through the middle of the largest cylinder indicated in subplot Fig.B. Fig.G: qualitative DORT image [as in subplot Fig.B]. The bright torus observed above the cylinder reflects the complexity of the DORT focusing behavior when the scatterer size is comparable to the wavelength. Fig.H: Selective quantitative reconstruction of the largest cylinder. The scatterer shape is significantly improved compared to Fig.G.*

$BS_2$ , so it perturbs the incident and scattered fields. In this noisy configuration,

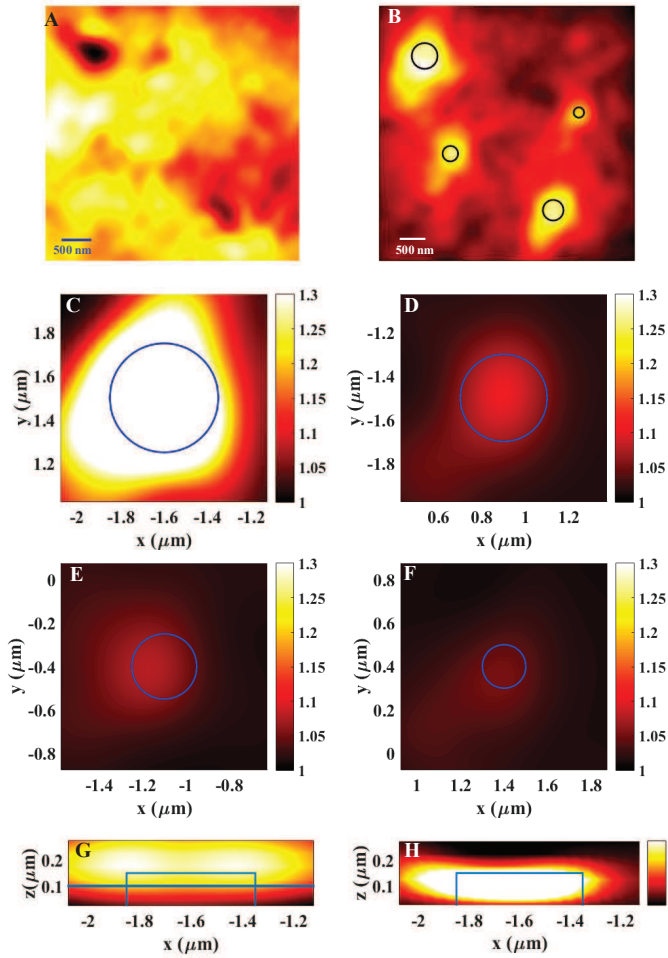


**Figure 3.13 :** Same as Fig. 3.12 but in the noisy configuration.

the conventional bright field microscopy image of the sample is so deteriorated that only the largest cylinder is visible, see Fig. 3.13.A. On the other hand, the DORT focusing image obtained by summing all the  $v_j=1, \dots, 2M$  field intensities in the sample domain calculated with Eq. (1) (thus neglecting the influence of the aberrating layer) permits to distinguish the four cylinders, see Fig. 3.13 [121]. The relative size of the targets can even be roughly guessed and the axial width of the focused beams is similar to that obtained in the noiseless configuration about one half of the wavelength Fig. 3.13.G. Note that the multiple scattering between the cylinders and the aberrating layer is negligible in this experiment. Hence, the image of the smallest scatterer in this linear regime gives a good approximation of the resolution one can expect with this noise level.

The selective inversion procedure improves further the characterization of the cylinders by retrieving their round shape and axial dimensions, see Figs. 3.13.C-F, Fig. 3.13.H, albeit with a significant underestimation of the permittivity. Note that, in this noisy configuration, the inversion procedure applied to the data without the DORT preprocessing failed in retrieving the two smallest cylinders.

### 3.4.3 SVD in image space

The treatment performed above was done in the Fourier domain. The single value decomposition (SVD) can also be performed in the image space on a constructed imaging matrix  $\mathbf{T}$ . To construct the imaging matrix  $\mathbf{T}$ , we use the four measurement data sets ( $\hat{\mathbf{x}}\hat{\mathbf{D}}_1$ ,  $\hat{\mathbf{y}}\hat{\mathbf{D}}_1$ ,  $\hat{\mathbf{x}}\hat{\mathbf{D}}_2$  and  $\hat{\mathbf{y}}\hat{\mathbf{D}}_2$ ) explained in the previous section. To recall, the measurement was obtained by illumination the sample (Fig. 3.11) with 25 illuminations and collecting the complex field data for different polarization cases. For image space SVD, I used dark-field data, i.e. the specular reflection substituted with zeros in the Fourier space (like dark-field imaging explained in Sec. 2.4). Now, the four data sets with respect to each illumination and detection can be placed in a imaging matrix  $\mathbf{T}$  as shown below:

$$\mathbf{T} = \begin{pmatrix} T_{11}^{\hat{\mathbf{x}}\hat{\mathbf{D}}_1} & T_{12}^{\hat{\mathbf{x}}\hat{\mathbf{D}}_1} & \dots & T_{1N}^{\hat{\mathbf{x}}\hat{\mathbf{D}}_1} & T_{11}^{\hat{\mathbf{x}}\hat{\mathbf{D}}_2} & T_{12}^{\hat{\mathbf{x}}\hat{\mathbf{D}}_2} & \dots & T_{1N}^{\hat{\mathbf{x}}\hat{\mathbf{D}}_2} \\ T_{21}^{\hat{\mathbf{x}}\hat{\mathbf{D}}_1} & T_{22}^{\hat{\mathbf{x}}\hat{\mathbf{D}}_1} & \dots & T_{2N}^{\hat{\mathbf{x}}\hat{\mathbf{D}}_1} & T_{21}^{\hat{\mathbf{x}}\hat{\mathbf{D}}_2} & T_{22}^{\hat{\mathbf{x}}\hat{\mathbf{D}}_2} & \dots & T_{2N}^{\hat{\mathbf{x}}\hat{\mathbf{D}}_2} \\ \vdots & \vdots & \ddots & \vdots & \vdots & \vdots & \ddots & \vdots \\ T_{M1}^{\hat{\mathbf{x}}\hat{\mathbf{D}}_1} & T_{M2}^{\hat{\mathbf{x}}\hat{\mathbf{D}}_1} & \dots & T_{MN}^{\hat{\mathbf{x}}\hat{\mathbf{D}}_1} & T_{M1}^{\hat{\mathbf{x}}\hat{\mathbf{D}}_2} & T_{M2}^{\hat{\mathbf{x}}\hat{\mathbf{D}}_2} & \dots & T_{MN}^{\hat{\mathbf{x}}\hat{\mathbf{D}}_2} \\ T_{11}^{\hat{\mathbf{y}}\hat{\mathbf{D}}_1} & T_{12}^{\hat{\mathbf{y}}\hat{\mathbf{D}}_1} & \dots & T_{1N}^{\hat{\mathbf{y}}\hat{\mathbf{D}}_1} & T_{11}^{\hat{\mathbf{y}}\hat{\mathbf{D}}_2} & T_{12}^{\hat{\mathbf{y}}\hat{\mathbf{D}}_2} & \dots & T_{1N}^{\hat{\mathbf{y}}\hat{\mathbf{D}}_2} \\ T_{21}^{\hat{\mathbf{y}}\hat{\mathbf{D}}_1} & T_{22}^{\hat{\mathbf{y}}\hat{\mathbf{D}}_1} & \dots & T_{2N}^{\hat{\mathbf{y}}\hat{\mathbf{D}}_1} & T_{21}^{\hat{\mathbf{y}}\hat{\mathbf{D}}_2} & T_{22}^{\hat{\mathbf{y}}\hat{\mathbf{D}}_2} & \dots & T_{2N}^{\hat{\mathbf{y}}\hat{\mathbf{D}}_2} \\ \vdots & \vdots & \ddots & \vdots & \vdots & \vdots & \ddots & \vdots \\ T_{M1}^{\hat{\mathbf{y}}\hat{\mathbf{D}}_1} & T_{M2}^{\hat{\mathbf{y}}\hat{\mathbf{D}}_1} & \dots & T_{MN}^{\hat{\mathbf{y}}\hat{\mathbf{D}}_1} & T_{M1}^{\hat{\mathbf{y}}\hat{\mathbf{D}}_2} & T_{M2}^{\hat{\mathbf{y}}\hat{\mathbf{D}}_2} & \dots & T_{MN}^{\hat{\mathbf{y}}\hat{\mathbf{D}}_2} \end{pmatrix}. \quad (3.26)$$

The first block in the imaging matrix  $T_{mn}$  corresponds to the polarization  $\hat{\mathbf{x}}\hat{\mathbf{D}}_1$ , with  $m$  being the incident angle going from 1 to  $M$  and  $n$  being the detection pixels ranging from 1 to  $N$ . Similarly, the blocks  $\hat{\mathbf{y}}\hat{\mathbf{D}}_1$ ,  $\hat{\mathbf{x}}\hat{\mathbf{D}}_2$  and  $\hat{\mathbf{y}}\hat{\mathbf{D}}_2$  are positioned in the imaging matrix.

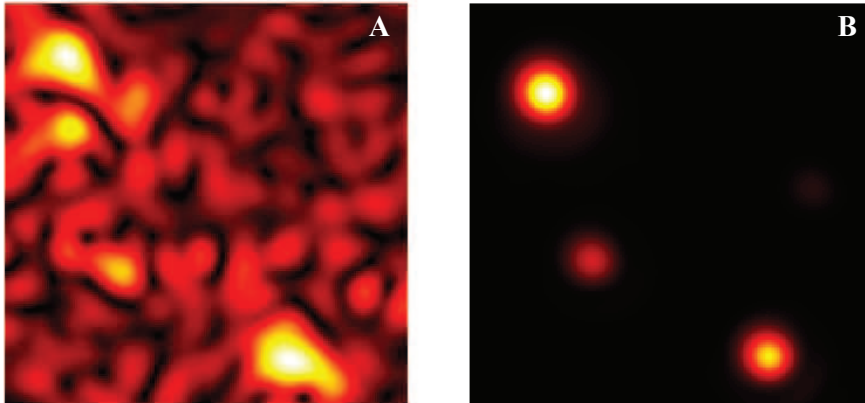


**Figure 3.14 :** *DORT inversion in the image space. A. The dark-field image of the noisy data with cylinders being distorted. B. The SVD focusing property at the location of the cylinders, obtained by summing the singular vectors.*

The singular value decomposition (SVD) can be performed directly on the  $\mathbf{T}$  matrix using Matlab inbuilt function. We would obtain the corresponding singular values and the singular vectors. From here, the approach remains the same as explained for scattering matrix  $\mathbf{K}$  in the section Sec. 3.4.2. Using equation Eqn. 3.25, it is possible to compute the focusing of the agile illuminations on the scattering objects (cylinders of different size).

The SVD was performed on the data set described before (same data set used in Fourier space  $\mathbf{K}$ ) but in the image space for the noisy data set with the specular reflection being suppressed during the processing. The Fig. 3.14.A represents the dark-field image, where it is difficult to identify the scatterers or the cylinders. By summing agile illuminations obtained by SVD we were able to focus and detect the scatterers. The result of this operation is shown in Fig. 3.14.B, in the image space. The four cylinders are seen without any clutter and revealing their location. Now, each individual cylinder can be selected and corresponding data can be extracted in the image space. This data can be further processed with non-linear algorithm described previously in this chapter to obtain the 3D reconstruction with better resolution.

The interest of performing SVD in image space is its simplicity. The SVD is performed directly in the image space and direct extraction of the location of the cylinders is performed. In case of the Fourier space SVD, the treatment is performed in the Fourier space and its focusing property is observed in the image space. The cylinder of interest is selected for the reconstruction in the image space and inverse Fourier transformed back to perform selective non-linear inversion. Comparing the result in the Fourier space SVD shown in Fig. 3.13.B and the image space SVD shown in Fig. 3.14.B, they both reveal the location of the cylinders, with later providing better focusing without distortion of cylinders. This is mainly due to the fact that Fourier space SVD was performed with usual data treatment and image space SVD with dark-field data. To recall, the usual data treatment being performing two measurements, one with sample on the substrate called total field measurement and other without the sample (on bare substrate) called reference field measurement. After normalization, I subtract reference measurement from the total field measurement I suppress the specular reflection to obtain scattered field from sample only. But the specular reflection is not completely suppressed. Whereas the image space SVD was performed with the specular reflection substituted with zeros (like dark-field imaging explained in Sec. 2.4) along with the data treatment performed on Fourier space SVD. The smallest cylinder in the image space SVD is faintly visible compared to the Fourier space SVD. Both methods provide equivalent results, any of these methods can be adapted to locate the scatterers in noisy data set.

I have demonstrated the usefulness of SVD in dealing with noisy TDM data. In the previous section (Sec. 3.3), I have shown that a transverse resolution of 100nm can be achieved with non-linear inversion procedure. Now, we would like to combine these two procedures (non-linear inversion + SVD treatment) in addition with an approximate knowledge about the sample to further improve the transverse resolution, presented in next section.

### 3.5 Bounded inversion method for $\lambda/10$ resolution

In this section, we present a sophisticated inversion technique which takes advantage of the imposition of binary behavior to the permittivity distribution in the non-linear inversion procedure and noise reduction procedure using SVD explained in the previous section for the improvement of the data. With those we obtain an unprecedented  $\lambda/10$  resolution on complex objects, experimentally.

Thanks to the non-linear inversion algorithm, it gives us the possibility to add a priori information about the object under reconstruction. Usually we poses minimal information about the objects that we would like to reconstruct. This minimal information can be introduced in the non-linear inversion program, helping it to converge faster and better. The minimal information that we will introduce in this section is the permittivity bound. We don't specify the exact permittivity value of the object that we are trying to reconstruct in 3D, but minimum and maximum bound of the permittivity value is provided to the algorithm.

Along with a priori information, we also calculate the singular vectors and Eigen values corresponding to the data. Summing of the singular explained in Sec. 3.4.2 provides focusing on the sample and helps the inversion procedure to better converge iteratively. In other words, the DORT or SVD procedure bring the noise reduction in the data.

Both the above steps helps in achieving  $\lambda/10$  resolution, demonstrated here experimentally. This development should find general applications each time the target is made of a known material, particularly in the nanotechnology or solid-state domains.

The permittivity distribution  $\varepsilon(\mathbf{r})$  within a bounded investigation domain  $\Omega$  was reconstructed from the scattered far-field data using non-linear inversion reconstruction algorithm, hereafter called Bounded Inversion Method (BIM). This took advantage of the knowledge of the object and background permittivity values,  $\varepsilon_{ref}$  and  $\varepsilon_{background}$  respectively. Several techniques can be used for implementing this a priori information in inversion schemes. Some of them impose strictly two values to the permittivity distribution [131, 132], others are less constraining and use an auxiliary function to bound  $\varepsilon(\mathbf{r})$  between  $\varepsilon_{ref}$  and  $\varepsilon_{background}$  [132]. We have implemented the latter option as it can be readily implemented in a standard gradient minimization method. More precisely, the permittivity contrast  $\chi(\mathbf{r}) = \varepsilon(\mathbf{r}) - \varepsilon_{background}$  in  $\Omega$  was estimated iteratively by minimizing a cost functional  $\mathbf{F}(\chi)$  [126] representing the distance between the experimental data  $f_{l,m}^{mes}(\chi)$  and the field  $f_{l,m}^{sim}(\chi)$  that would be scattered by the permittivity estimate:

$$\mathbf{F}(\chi) = = \frac{\sum_{l=1}^L \sum_{m=1}^M \|\mathbf{f}_{l,m}^{mes} - \mathbf{f}_{l,m}^{sim}\|^2}{\sum_{l=1}^L \sum_{m=1}^M \|\mathbf{f}_{l,m}^{mes}\|^2}, \quad (3.27)$$

The  $f_{l,m}^{sim}$  was simulated rigorously, thus accounting for multiple scattering if any, by solving Maxwell equations (see the previous two sections for a description of the forward and inverse problems). To constrain the permittivity, the contrast  $\chi$  was

written in the form,

$$\chi = (\varepsilon_{ref} - \varepsilon_{background}) [1 - \exp(-\xi^2)] \quad (3.28)$$

where  $\xi$  became the novel parameter of the inversion algorithm. Using this formulation, least  $\xi$  corresponds to the background medium and maximum  $\xi$  corresponds to the object. At each iteration,  $\xi$  was modified along a descent direction which depended on the gradient of the cost function with respect to  $\chi$  times the derivative of  $\chi$  with respect to  $\xi$ . By construction, the descent direction tends towards 0 for small and large  $\xi$  and thus promotes the extreme values  $\xi_{background}$  or  $\xi_{ref}$  for the estimated permittivity.

### Experimental result

We now try to demonstrate the feasibility of this method on several samples from the experimental data. We considered a sample made of 12 resin rods ( $\varepsilon_{ref}=2$ ), of length 520nm, width about 97nm and height 140nm touching each other at the center of the star, see Fig. 3.15.A. Note that the spacing between the rods is always inferior to the Rayleigh limit, even at the external border where it reaches 320nm. The sample was illuminated with 44 incidence angles with a NA=0.95 and the scattered field data is measured for four different polarization combination with  $\lambda = 475nm$ . The full-vectorial data set is built and normalized and non-linear inversion can now be performed on this data.

Despite a moderate contrast and small 140nm height, we observed with rigorous simulations that the sample (Fig. 3.15.A) supports multiple scattering and that the noise on the experimental data is about 55%. The noise was estimated by replacing  $f_{l,m}^{sim}(\chi)$  in Eqn. 3.27 with the  $f_{l,m}^{sim}(\chi_{true})$ , with the later being the field calculated using the forward problem for the sample shown in Fig. 3.15.A. Such a numerical forward calculation provides the scattered field one would obtain from the sample without noise.

We first examined the sample using classical microscopy. As expected, the dark-field microscope image, Fig. 3.15.B, obtained by summing the diffracted intensities recorded at the image plane for all the illuminations, retrieved a doughnut without any hint about the rods. The standard tomographic reconstruction (using a Fourier transform technique for processing the data), did not show any improvement either (not shown in figure). In contrast, the rods were visible up to mid-length on the non-linear reconstruction Fig. 3.15.C and were spectacularly retrieved on the BIM reconstruction Fig. 3.15.D. The axial-cut along the axial z direction versus the curvilinear abscissa of the reconstructed rods are shown in Fig. 3.15.E, it shows the rods separately with accurate estimation of height of the rods. More precisely, the air wedge between the resin branches could be retrieved by non-linear inversion down to 150nm 3.15.C and by BIM down to 50nm 3.15.D [133].

To push further the investigation on the limits of our imaging technique, we considered in a second example a star-sample made of rods of width 76 nm, length about 490 nm and height 140 nm Fig. 3.16.A. With this smaller and less scattering sample, the experimental noise was estimated to 85%. Unsurprisingly, classical

microscopy and standard tomography failed to image the sample, see Fig. 3.16.B. On the other hand, the rods started to be visible in the HM reconstruction Fig. 3.16.C and were retrieved up to their contact point by BIM, Fig. 3.16.D. More precisely, in

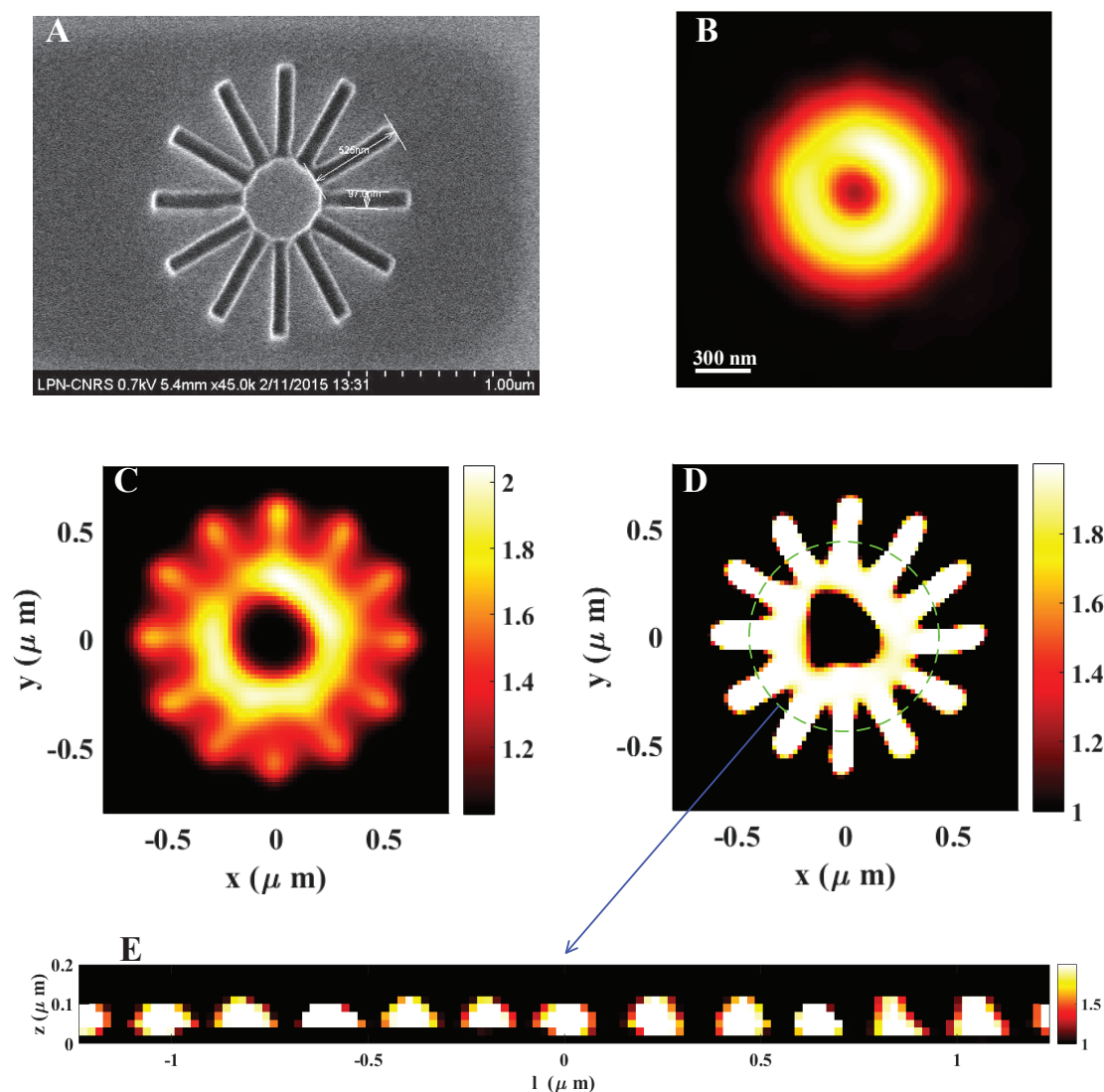


**Figure 3.15 :** Images of a resin star-sample of 97 nm wide rods of length 520 nm on a Si substrate. Fig.A: Scanning electronic microscope image. Fig.B: Dark field microscopy with  $NA=0.95$ . Fig.C: Reconstruction obtained with non-linear inversion method from Tomographic Diffraction Microscopy data with  $NA=0.95$ . Fig.D: Permittivity reconstruction obtained with BIM using the knowledge of the resin permittivity from the same data as Fig.C. Fig.E: Permittivity distribution in the axial  $z$  direction versus the curvilinear abscissa of the dashed circle in Fig.D. The mesh size taken for all the reconstructions is 20 nm. BIM is able to distinguish the rods down to an inter spacing about 50 nm. The width of the rods is estimated to 117 nm in average (between 5 and 6 pixels). The color code indicates the level of relative permittivity in Figs.C and D at  $\lambda = 632.8\text{nm}$ .

this noisier experiment, the air wedge between the branches could be retrieved by non-linear inversion down to 200 nm and by BIM down to 50 nm.

Most impressively, BIM was able to tell the difference between rods of width 97 nm and rods of width 76 nm, compare Fig. 3.15.D and Fig. 3.16.D. The average values of the reconstructed rods width, measured at mid-length over all the branches, was 117 nm for the first sample and 87 nm for the second one. This result is in agreement with the air wedge retrieval and suggests that, on these examples, the resolution of BIM was about 50 nm if not better.

In case of non-linear inversion the reconstruction was better than the Rayleigh limit of 330 nm. In addition, introducing a priori information on the target, as

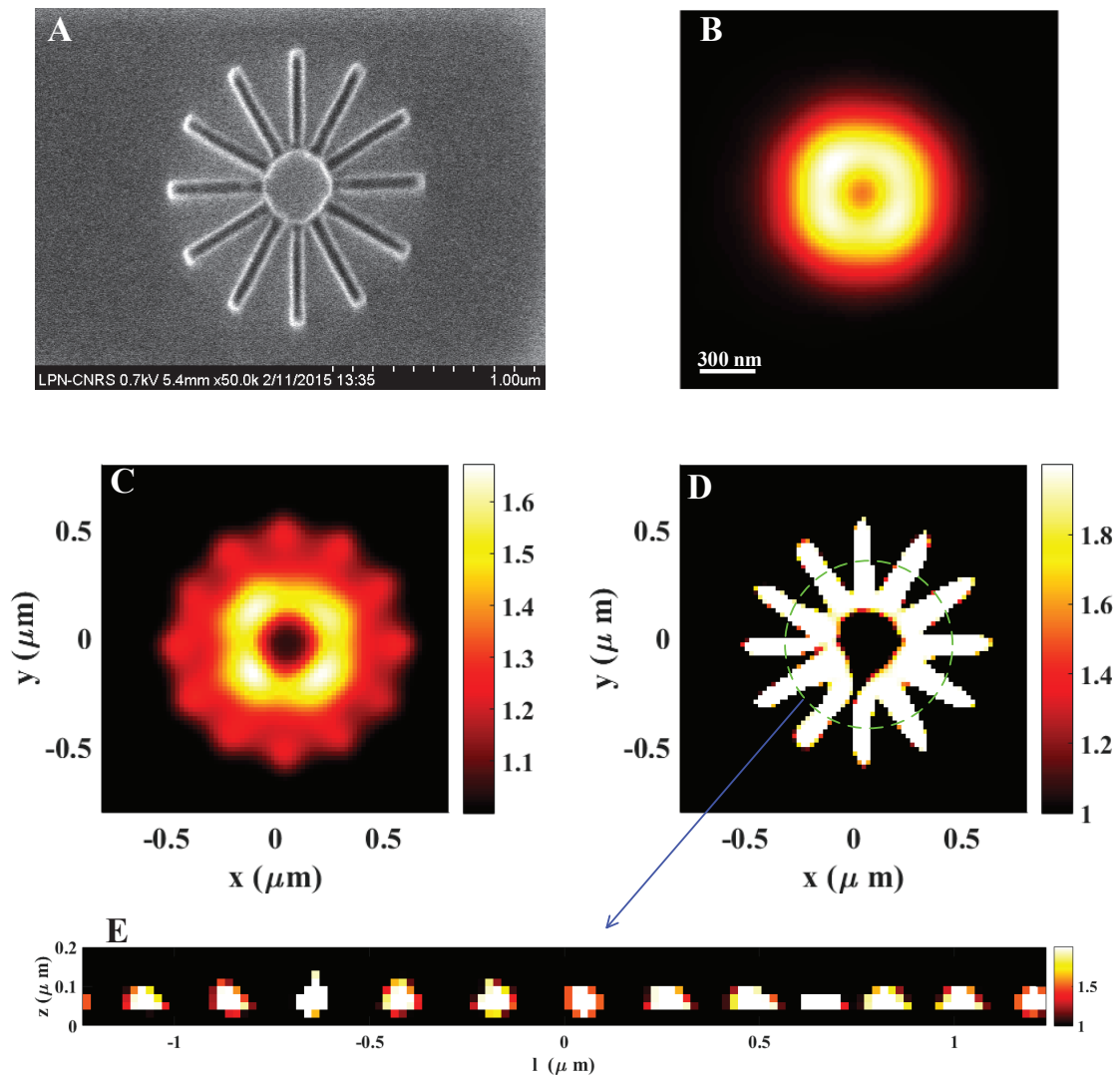


**Figure 3.16 :** Same as Fig. 3.15, but the rods width is 76 nm and their length is 490 nm. Similarly to Fig. 3.15, BIM is able to distinguish the rods down to an inter spacing about 50 nm. The rods width is estimated to 87 nm in average (between 4 and 5 pixels) at  $\lambda = 632.8\text{nm}$ .

in BIM, had a strong effect on the accurate recovery of the object high spatial frequencies. The resolution of the BIM images reached about 50 nm. To point out the interest of the binary constraint on the permittivity retrieval, we compared the BIM reconstructions to that given by an iterative inversion algorithm presented in the previous section, that assumes only the positivity of the sought permittivity.

We have demonstrated the best transverse resolution with the TDM and in marker-free microscopy of about 50nm at  $\lambda = 632.8nm$ .

## 3.6 Conclusion

Tomographic diffractive microscope (TDM) images reconstructed by the most of the research teams around the world are performed under Born approximation for low permittivity contrast objects. Though this approach limits the resolution, it is twice better than the Rayleigh criterion resolution. On the other hand, the TDM had not been applied to samples deposited on a substrate and for samples with high permittivity contrast. In this chapter, it was demonstrated by applying accurate inversion techniques the possibility to achieve even better transverse resolution and 3D geometrical quantitative reconstruction of sample with the permittivity map. This was possible due to the accurate modeling of the scattering of light and taking into account the polarization of the light. The polarization is important to achieve isotropic transverse resolution. Using non-linear inversion algorithms on complex measured TDM data a transverse resolution of 100 nm was achieved at  $\lambda = 475nm$ .

The application of singular value decomposition (SVD) or Decomposition of Time Reversal Operator (DORT) to identify scattering objects in noisy TDM data was demonstrated experimentally. This will help in identifying individual objects and reconstructing them better in noisy TDM measurements. Combination of SVD noise reduction technique and if the permittivity bound of the sample is known, the transverse resolution can further be improved to 50 nm ( $\lambda/10$ ) at  $\lambda = 632.8nm$ , best ever transverse resolution achieved in the marker-free optical microscopes.

The TDM reconstruction techniques under Born approximation in chapter 2 provided quick reconstruction of sample with reduced transverse resolution. This chapter demonstrated the need and the power of accurate techniques to improve transverse resolution and obtain 3D quantitative material properties map. The axial-resolution still remains a problem with the best possible axial-resolution being about  $\lambda$ . We will try to improve the axial resolution of optical microscopes in the next chapter.

---

# Mirror-assisted tomography: axial resolution improvement

---

“There are two ways of spreading light: to be the candle or the mirror that reflects it.”

-Edith Wharton, Writer

## 4.1 Introduction

The axial resolution of optical microscopy and optical diffractive tomography microscopy is several times worse than the transverse resolution in transmission configuration. This is due to the inability to illuminate and detect the light from all possible directions on an object under observation. The illumination and observation is usually performed in one side of the object. If an object is illuminated from all possible directions, the object scatters the light in  $4\pi$  steradians, but we usually detect with an objective with a fixed NA. The scattered field within the reach of the NA of the objective is only collected, the remaining field goes undetected. The remaining scattered field is important for the isotropic resolution. Similarly to collecting the scattered field in all directions it is also crucial to illuminate in all possible directions. The illumination and detection both are essential for isotropic resolution.

In this context, several ideas had been proposed to overcome the asymmetry and to improve the angular coverage of a microscope. One of the widely explored idea is to illuminate and detect with 2 objectives which are positioned at opposite directions to each other with object between them, called 4Pi microscope [134]. This needs precise positioning of the two objectives. In the similar context of two objectives, *theta* microscope has also been proposed [135]. In this, one of the objective for collection is positioned at an angle to the illumination axis. This objective helps to collect the scattered field that is not collected with single objective setup. On the other hand, the idea of sample rotation is being explored as an alternative too. The principle is to rotate the sample, which facilitates to illuminate and detect along a particular axis of rotation [28, 61, 136], this was further extended by performing tomography on the rotating sample to have better angular coverage for illumination and detection [137]. The idea has been successful but are limited to certain objects

that are rotatable. The rotation can be performed with optical tweezers while observing with TDM as well [138]. But rotating a sample needs precise maintenance of the center of rotation. In spite of these methods, the image resolution remains below the resolution one would obtain with an isotropic configuration, when the sample is illuminated and detected in all possible directions.

To overcome these challenges, we explore the idea to illuminate and detect in all possible directions, the idea of mirror-assisted tomography was proposed by Mudry et al. [3] to address this problem. This method involves deposition of sample on top of a mirror and perform tomography. A mirror-assisted tomographic microscope includes the advantages of both transmission microscope and reflection microscope configurations. Thanks to the reflection of the mirror, the sample is illuminated and observed in both directions. The sample then has to be numerically reconstructed by taking in to account the presence of the mirror.

In this chapter, we will understand the need of mirror-assisted tomography, its advantages, the sample fabrication and the experimental results and challenges in details. I studied the sample requirements for the experimental demonstration of the axial-resolution improvement with non-linear inversion program. The fabrication was performed in LPN, Marcoussis. I took part in optimizing the fabrication steps. I performed measurements with the samples, treated the data and used non-linear inversion algorithms to show the first results on mirror-assisted tomography. The preliminary results show spectacular improvement brought about by the mirror-assisted tomography for axial-resolution.

## 4.2 Problem statement

Let us understand the axial resolution problem in optical microscopy. As stated in the section 1.5.4, if we place ourselves in the context of the Born approximation, using the angles of illumination and detection in all possible directions, with  $4\pi$  steradians, provides a perfectly isotropic resolution to reconstruct the object: it is called the complete configuration (Fig. 1.14). To achieve such a configuration one has to illuminate and detect in the all possible directions on a objects as shown in Fig. 4.1.A. It is however difficult to achieve in practice because of the need to use several objectives to illuminate and detect in several directions.

With the tomography approach, it is possible to illuminate and detect in several directions beyond just one illumination angle. But even the tomography approach does not provide a complete configuration. Tomographic microscope is either used in transmission configuration or reflection configuration. Almost all the tomographic microscopy research groups adopt a configuration in transmission (shown in Fig. 4.1.B). In this configuration, object is illuminated with one objective and detected with another objective placed in the opposite side to each other. This transmission tomography microscopy configuration should enable to do better than the Rayleigh criterion in transverse resolution, but the axial resolution is significantly worse, and that of at least a factor of 3 ([19], p. 491). This is due to the fact that the field scattered by the object is collected with a limited NA of the objective

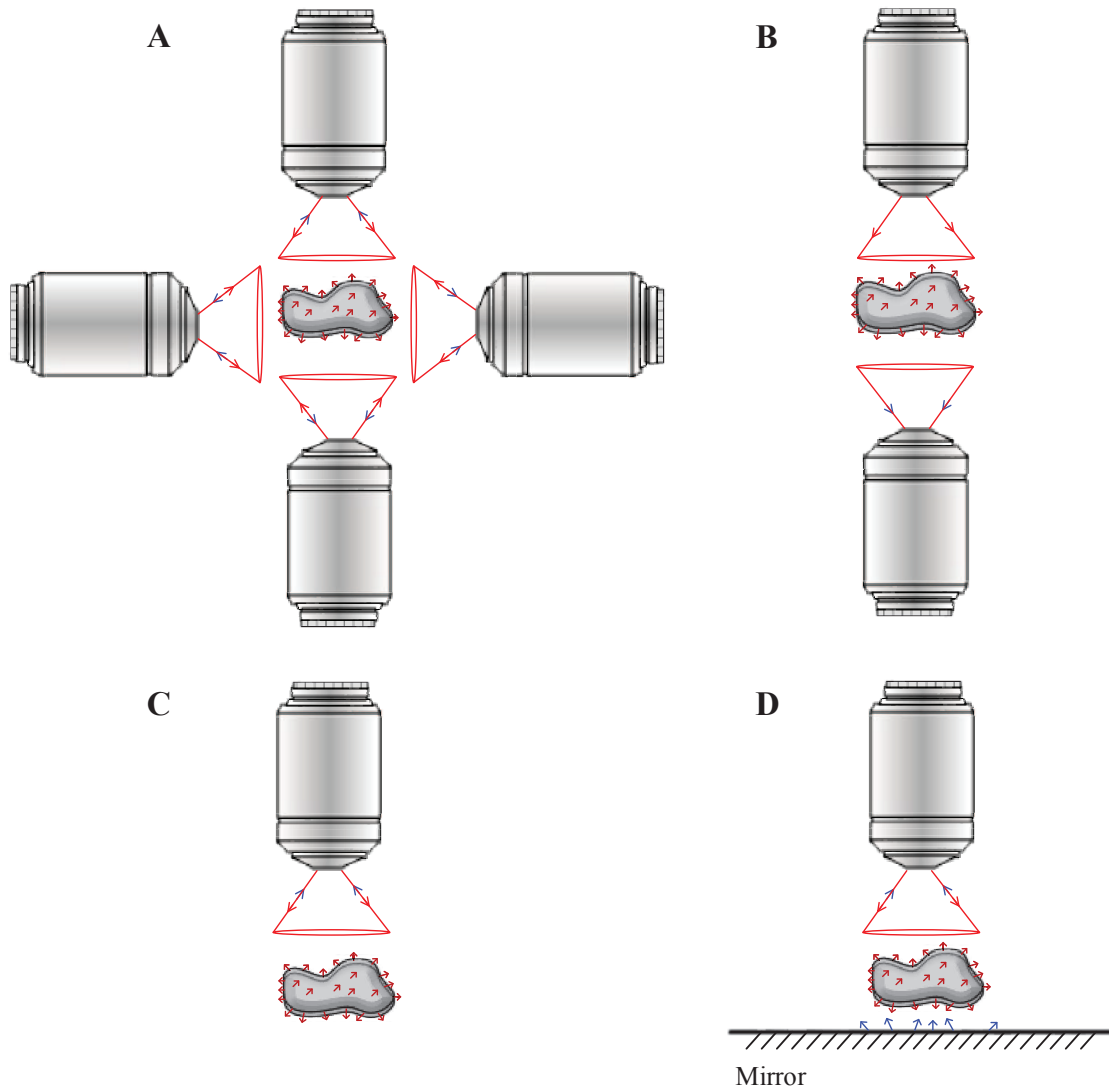


**Figure 4.1 :** *Different possible configurations used for imaging in microscopy. Fig.A: Isotropic or complete configuration (hypothetical configuration). Fig.B: Transmission configuration. Fig.C: Reflection configuration. Fig.D: Mirror-assisted configuration*

used for detection and only in a single direction. The OTF of the transmission configuration is shown in Fig. 1.8. The PSF corresponding to it is shown in Fig. 1.9. The PSF is elongated in the axial direction, also explains the poor axial resolution with transmission configuration.

However, in the reflection configuration (shown in Fig. 4.1.C), the sample is illuminated and detected with single objective from the same side of the object. Compared to the transmission configuration, in the reflection configuration we detect different scattered field components. This can be understood with help of OTF shown in Fig. 1.12. The detected spatial frequency components are different and

the range of detected frequencies also vary. To recall, the reflection PSF is complex in nature (shown in Fig. 1.13).

By putting together the transmission tomography OTF (Fig. 1.8) and reflection tomography OTF (Fig. 1.13), we fill OTF with more spatial frequencies in the axial direction for one-half of the OTF as shown in Fig. 4.2.

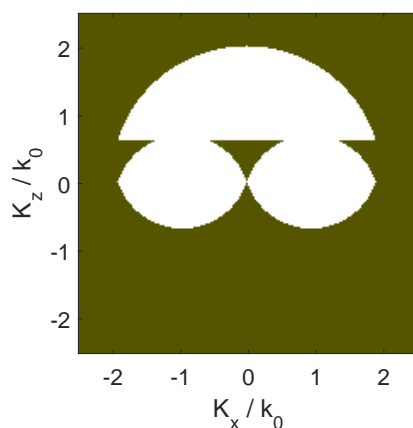


**Figure 4.2 :** *Combination of transmission configuration and reflection configuration OTF, which is Fig. 1.8 + Fig. 1.12 for NA= 0.95. This yields better axial OTF support.*

But the disadvantage is that we have to perform two measurements on the same sample, once in transmission and once in reflection with same illumination and detection tomography schema just to fill better the one-half of the OTF. It would be advantageous to perform single tomographic measurement to have both transmission and reflection spatial frequencies and fill better the OTF close to isotropic configuration. This leads us to the mirror-assisted tomography.

### 4.3 Solution: Mirror assisted tomography using non-linear inversion

As transmission and reflection configurations provide different spatial frequency components in the OTF, combining both these would be an ideal case to better fill the OTF and improve the PSF. Assuming a numerical aperture of 0.95, this combined configuration that can be approximated by breaking it successively in to two transmission measurements and two measurements in reflection, according to the two possible orientations of the optical axis. We will understand this with help of the Fig. 4.3. The transmission measurements are represented in Fig. 4.3.A with 1 and 2 from two opposite sides of object for illumination. The respective transmission components are detected along the directions 4 and 3 in Fig. 4.3.A. Similarly, for reflection measurement one has to perform two measurements, represented by 1 for illumination with 3 for detection and 2 for illumination with 4 for detection in

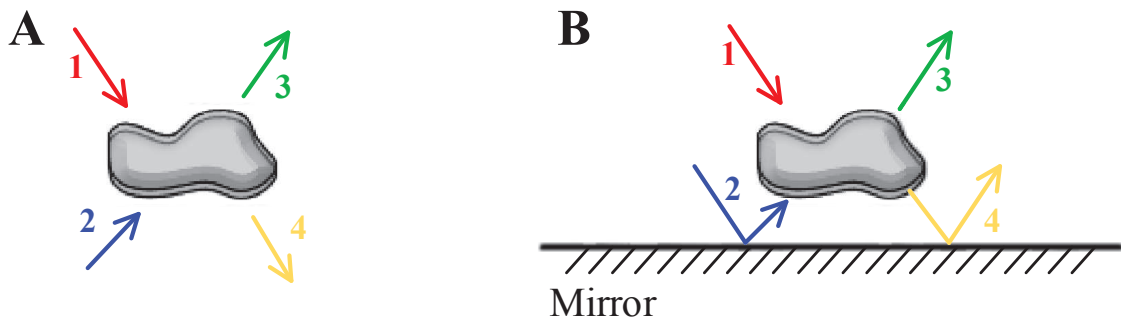


**Figure 4.3 :** *Fig.A: General microscopy configurations, **first transmission measurement:** illuminated along 1 and detected along 4, **second transmission measurement:** illuminated along 2 and detected along 3, **first reflection measurement:** illuminated along 1 and detected along 3 and **second reflection measurement:** illuminated along 2 and detected along 4. Fig.B: Mirror-assisted tomography: this configuration includes **two transmission measurements** (illuminated along 1, mirror with its reflection helps in detecting transmission components 4 and illumination along 2 with detection along 3) and **two reflection measurements** (illuminated along 1, detection of reflection components along 3 and mirror illuminates the sample 2 with detection along 4). Note that all these components are mixed.*

Fig. 4.3.A. One can be convinced by considering support for spatial frequencies accessible in Fourier space for combination of the 4 measurements, we better fill the OTF.

To combine these steps and get as close as possible to the full configuration, the approach that I have initiated is to place the object to reconstruct on top of a mirror and use a tomographic reflection configuration [3]. This is shown in Fig. 4.1.D and Fig. 4.3.B. The mirror is perpendicular to the optical axis of the microscope and the sample is between the mirror and the objective (see Fig. 4.1.D). The diffracted field is the coherent superposition of the fields that would be obtained from both sides of the object in reflection and transmission. The Fig. 4.3.B helps us to understand how we can obtain the coherent superposition of transmitted and reflected components in single measurement.

In Fig. 4.1.D the sample on top of mirror is illuminated once but it involves various configurations as shown in Fig. 4.3.B. The light can be transmitted directly through the object and reflected from the mirror to the detector surface as shown in Fig. 4.3.B by 1 and 4. Or it can be reflected from the mirror directly and transmits though the object shown by 2 and 3 in Fig. 4.3.B. The other possibility is, it can directly reflect from the object and detected on the detector surface represented by 1 and 3 in Fig. 4.3.B. One more reflection possibility is by light reflecting on the mirror and reflected by the object and reaching the detector, shown by 2 and 4 in Fig. 4.3.B. So, a single mirror-assisted tomography yielding 4 measurements, but they are mixed and has to be unmixed into respective components.

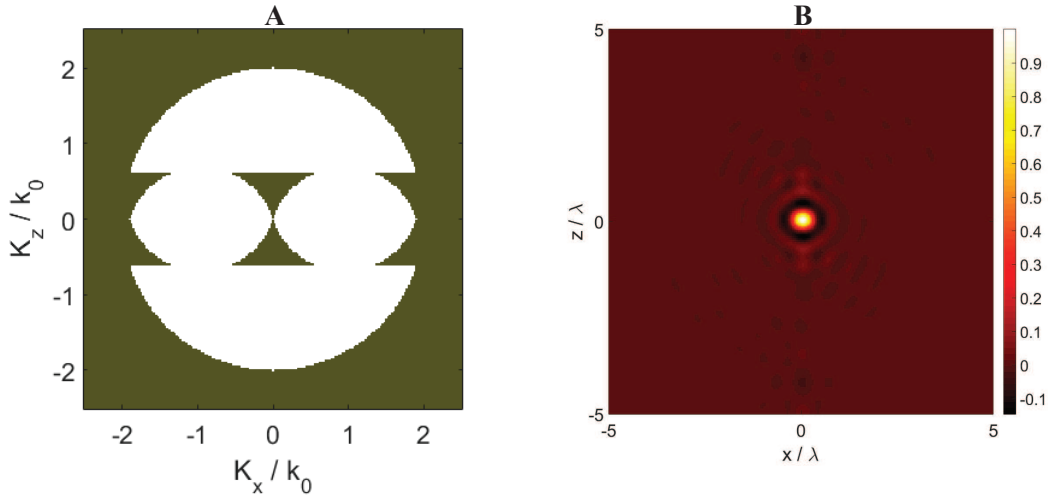


**Figure 4.4 :** *Mirror-assisted tomography OTF and PSF. Fig.A: axial cut ( $\mathbf{K}_x \mathbf{K}_z$ ) of the 3D synthetic aperture along the center of the  $\mathbf{K}_y$  axis in the Fig. 4.5.C. Fig.B: Intensity of the PSF along the axial direction.*

The mirror-assisted tomography measurement would contain all the spatial frequency components but they are mixed. These components can be positioned in the 3D synthetic aperture, this is demonstrated with its formation shown in Fig. 4.5. The final axial cut of OTF obtained by mirror-assisted TDM is shown in Fig. 4.4.A. It is better filled in comparison to transmission or reflection OTF, though there are certain void positions still present. The PSF of mirror-assisted TDM is partially isotropic (in both transverse and axial direction) in nature, shown in Fig. 4.4.B.

Even if the Born approximation is valid, it is impossible to reconstruct the object by a single inverse Fourier transform from the 3D synthetic aperture because transmission and reflection components are mixed. Using nonlinear inversion procedure explicitly taking into account the presence of the mirror in the modelling then overcomes this difficulty.

In this mirror-assisted configuration, it is necessary, not to place the object too close to the mirror. Because, the intensity resulting from the interference between the incident wave and specular reflection is low on average close to the mirror over all angles of illumination, and therefore not conducive to effectively illuminate the object.

The concept of mirror-assisted tomography has been theoretically validated by Mudry et.al [3]. I will discuss briefly about that here.

## 4.4 Validation on synthetic data

The theory of mirror-assisted tomography is presented in detail in the thesis work of E. Mudry [139]. He discusses the role of polarization, modeling of the electromagnetic field in the presence of a mirror and the reconstruction of the object. He also

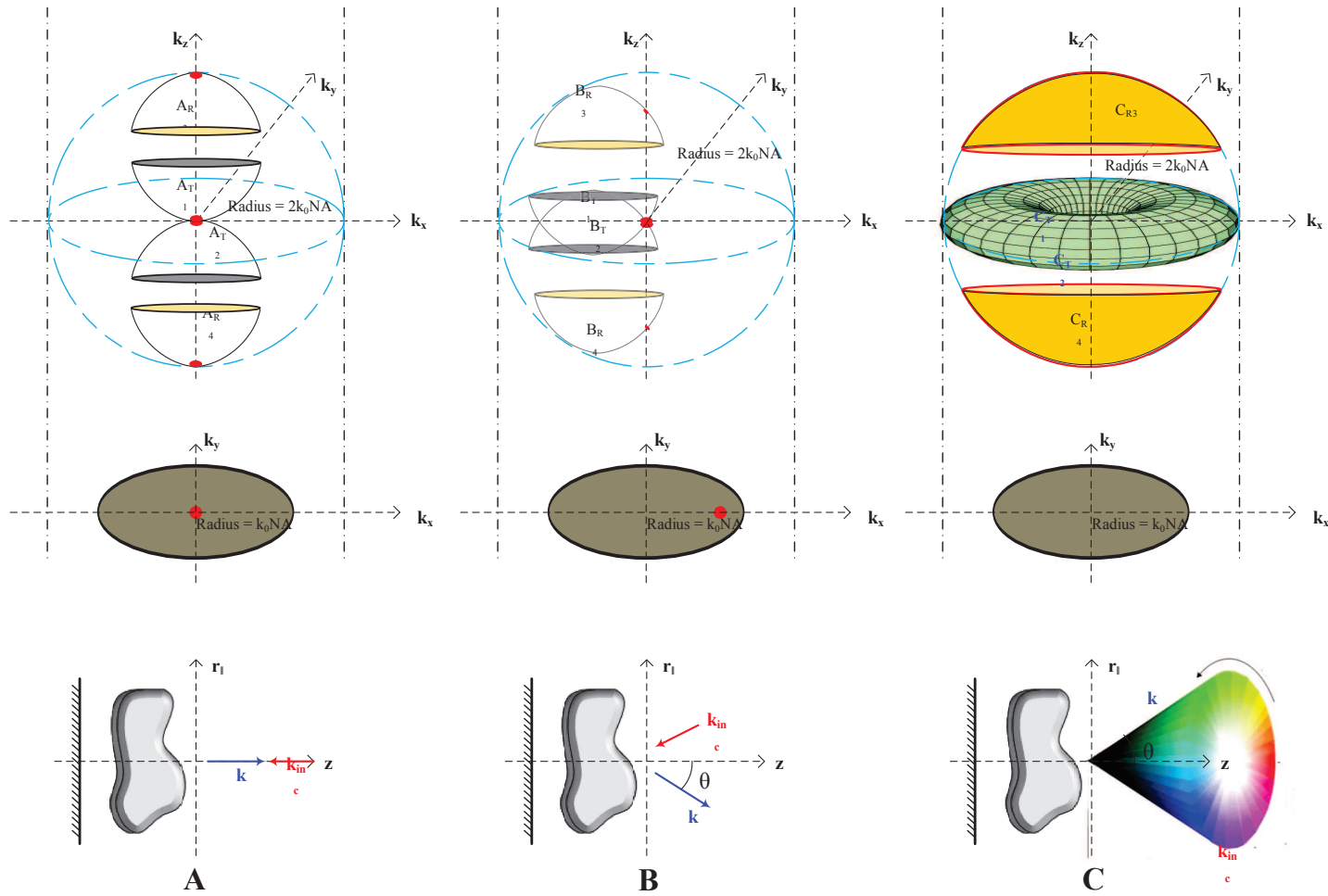


**Figure 4.5 :** Synthetic numerical aperture formation in mirror-assisted TDM configuration. In Fig.A, object is illuminated by normal incidence, the diffracted field is shown in Fourier domain with red dot being the specular focus of the incident field. This is decomposed into two transmission and two reflection measurements. They are projected to form a cap of spheres and positioned on the synthetic Ewald's sphere satisfying the condition  $\mathbf{K} = \mathbf{k} - \mathbf{k}_{inc}$ . There are 4 cap of spheres corresponding to transmission ( $A_{T1}$  &  $A_{T2}$ ) and reflection ( $A_{R3}$  &  $A_{R4}$ ) respectively. Similarly for Fig.B, object is illuminated with extreme angle along positive  $r_{\parallel}$  direction and cap of spheres is positioned according to  $\mathbf{K} = \mathbf{k} - \mathbf{k}_{inc}$ . For Fig.C, object is illuminated with many varying angles in  $r_{\parallel}$  direction and diffracted field is collected. Then they are positioned in the 3D synthetic aperture, transmission components form a torus at the center, and the reflection components form hemispheres at the bottom and top of the 3D synthetic aperture.

performed numerical experiments to validate the idea of mirror-assisted tomography, which was published in 2010 [3].

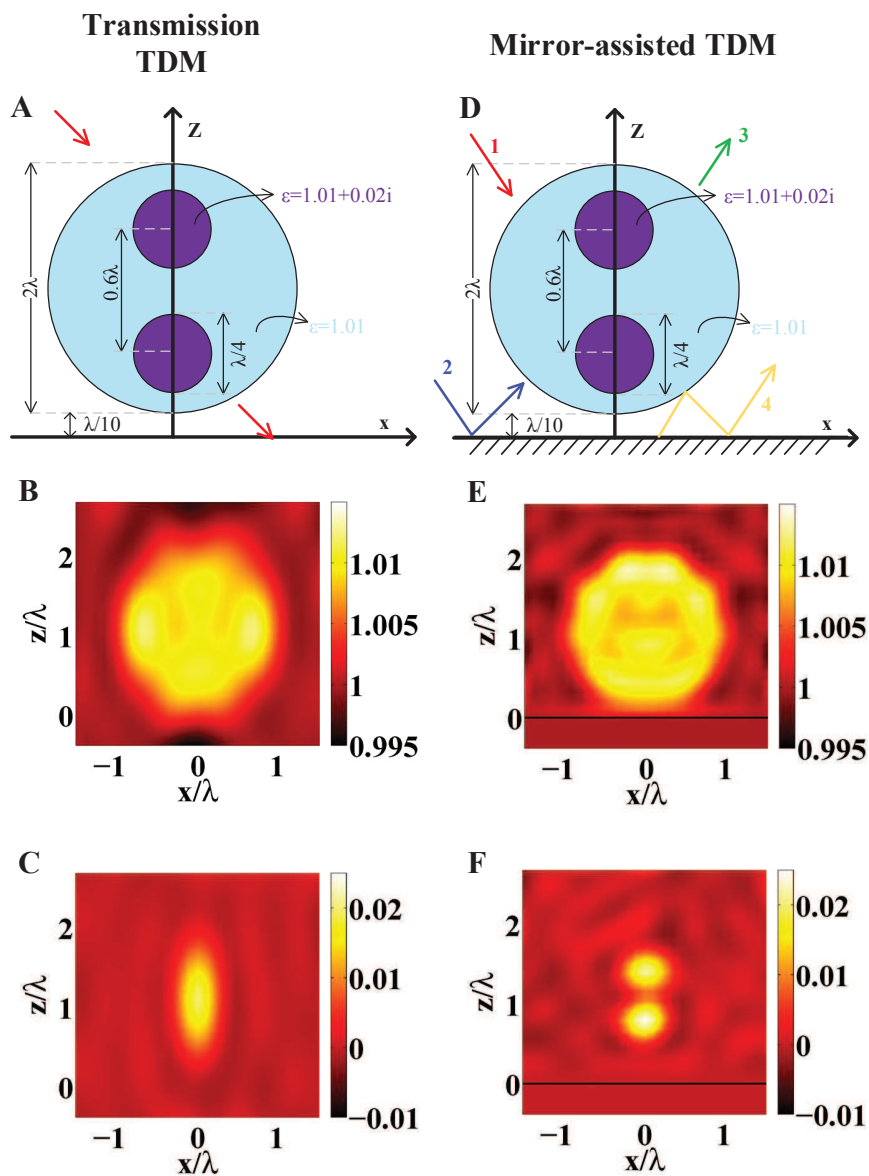


**Figure 4.6 :** Numerical Validation of the mirror-assisted tomography on a test object in transmission and mirror-assisted tomography configurations [3]. **Transmission:** Fig.A: Sphere (diameter =  $2\lambda$ ) of dielectric permittivity  $\epsilon = 1.01$  containing two absorbent spherical inclusions (diameter =  $\lambda/4$ ) of permittivity,  $\epsilon = 1.01 + 0.02i$ . The distance between the two absorbent spherical objects was  $0.6\lambda$ . Fig.B: Reconstruction of Fig.A, real part. Fig.C: Reconstruction of Fig.A, imaginary part. **Mirror-assisted tomography:** Fig.D: Same as Fig.A with a mirror positioned along the  $x$  axis. Reconstruction of Fig.D, real part shown in Fig.E, imaginary part shown in Fig.F [3].

Inversions performed on numerical data show the interest of mirror-assisted tomography (see Fig. 4.1.D). The test object (shown in Fig. 4.6.A) taken was a sphere (diameter =  $2\lambda$ ) of dielectric permittivity  $\varepsilon = 1.01$  containing two absorbent spherical inclusions (diameter =  $\lambda/4$ ) of *permittivity*,  $\varepsilon = 1.01 + 0.02i$ . The distance between the two absorbent spherical objects was  $0.6\lambda$ . The simulated diffracted field was corrupted with noise signal of 5%. A 0.95 numerical aperture is used, inside which 64 angles of incidence in 121 detection angles regularly spaced were used. The nonlinear inversion procedure used to perform this synthetic inversion was presented in the previous chapter, Sec. 3.3.3.

The results from E. Mudry shows that the transmission configuration fail to return the two inclusion cylinders due to its low axial resolution power (shown in Fig. 4.6.B&C). On the other hand, the mirror-aided configuration provides almost identical to those reconstructions of the full configuration (shown in Fig. 4.6.E&F).

This provided a solid foundation for us to examine mirror-assisted tomography and demonstrate it experimentally, this can be used to improve axial resolution in optical microscopy.

## 4.5 Sample requirements and fabrication

As we had the numerical and theoretical understanding of the method from E. Mudry [3], we wanted to design and test the samples that are feasible to be imaged under the TDM before fabrication by synthetic reconstruction. Then the samples were fabricated. This section explains these two steps in detail.

### 4.5.1 Sample requirements and synthetic reconstructions

We performed some numerical experiments to understand the material (permittivity) requirements and the dimensions of the sample of interest to perform mirror-assisted tomography. I will present the numerical studies here.

For the numerical experiments and experimental results in this chapter a very high numerical aperture objective was desired, this was understood from the theoretical work. The higher NA objective permits to fill the OTF better compared to a smaller NA objective. For this we choose an objective with  $NA = 1.49$ , to be used with oil.

To better test the axial resolution of mirror-assisted tomography we convinced to position two cylinders in the axial direction on top of a reflective mirror (eg., shown in Fig. 4.7). Two  $TiO_2$  (refractive index= 2.3922 or relative dielectric permittivity  $[\varepsilon(r)] = 5.7226$ ) cylinders of 100nm height and 300nm in diameter were placed on top of a aluminum(Al) mirror. The configuration is shown in Fig. 4.7.A. The first cylinder is located at a distance “ $d$ ” from the Al mirror and the two  $TiO_2$  cylinders are separated by a distance “ $s$ ”. The variables “ $d$ ” and “ $s$ ” are varied during the numerical experiment. Though I performed various numerical experiments, for simplicity, I present results for only one configuration with “ $d$ ” = 200nm and “ $s$ ” = 200nm sample, shown in Fig. 4.7.B.

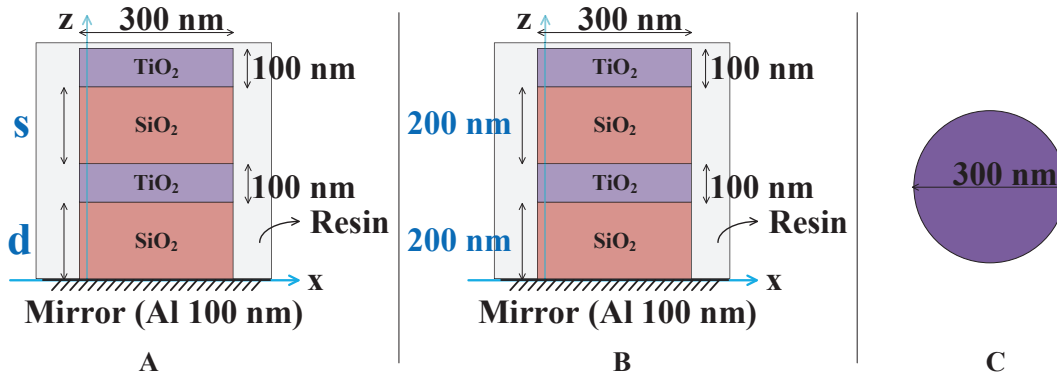


**Figure 4.7 :** *Test samples. Fig.A: General specifications of the test samples, with  $s$  being the separation distance between the two  $\text{TiO}_2$  cylinders and  $d$  being the distance between the Al mirror layer and the first  $\text{TiO}_2$  cylinder. Fig.B: Specifications of the sample used for the numerical experiment of the mirror-assisted tomography presented in this section. Fig.C: Top view of  $\text{TiO}_2$  cylinder, it shows the diameter of 300 nm.*

To test the axial resolution we need this two  $\text{TiO}_2$  cylinders to be “levitating” on the top of the mirror. This can be achieved in optics by using the material properties of the medium in which the cylinders are located. For this we choose  $\text{SiO}_2$  whose refractive index is 1.5 (or  $\varepsilon(r) = 2.25$ ) and a resin also with 1.5 refractive index (or  $\varepsilon(r) = 2.25$ ). The  $\text{SiO}_2$  occupies between the two  $\text{TiO}_2$  cylinders to cause the 3D positioning effect. Later, resin is coated over the cylinders. Oil also has a refractive index of 1.5 (or  $\varepsilon(r) = 2.25$ ), which will be used along with the objective. Oil, resin and the  $\text{SiO}_2$  have a refractive index of 1.5, as we observe the two  $\text{TiO}_2$  cylinders from the oil objective, we would have the two cylinders providing levitating feeling due to uniformity of the refractive index. This provides an ideal way to test the axial resolution.

So, a configuration as shown in Fig. 4.7.B was numerically simulated. With the help of the forward problem discussed in the previous chapter (see Sec. 3.3.2). I calculated the field that would be diffracted by the sample and then non-linear inversion was performed on this numerically calculated field (one would obtain this field in the experimental case if there is zero experimental or measured noise). The mirror was taken into account and the sample (Fig. 4.7.B) was numerically illuminated with coherent plane waves at  $\lambda = 632.8\text{nm}$  with  $\text{NA}=1.49$  in the presence of oil. The illumination angles used for the illumination is explained in the Fig. 4.8, 24 angles of incidence, 12 each along the  $\mathbf{K}_x$  and  $\mathbf{K}_y$  directions were used. There was no noise introduced in the numerical experiment. For each illumination angle forward problem provides the complex diffracted field data in the Fourier space. The data is accumulated for all illumination angles and it is numerically inverted with the help of non-linear inversion algorithm (see Sec. 3.3.3).

I numerically placed the two  $\text{TiO}_2$  cylinders, so the size and location of the inversion box (the box with volume  $\Omega$  shown in Fig. 3.4) required for non-linear inversion procedure was defined by me. The box is located 100nm from the Al layer

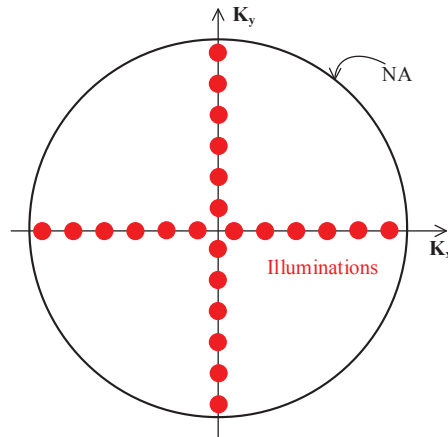


**Figure 4.8 :** *Illumination schema used for mirror-assisted tomography. The NA of the objective is shown in Fourier space with illumination angles (red dots). The samples were illuminated with 24 angles of incidence, 12 each along the  $K_x$  and  $K_y$  directions within the NA of the objective.*

and extended to  $1\mu\text{m}$  in  $z$  direction, along  $x$  and  $y$  it is  $500\text{nm}$ . Each voxel in the inversion box was discretized to be  $50\text{nm}$  in size.

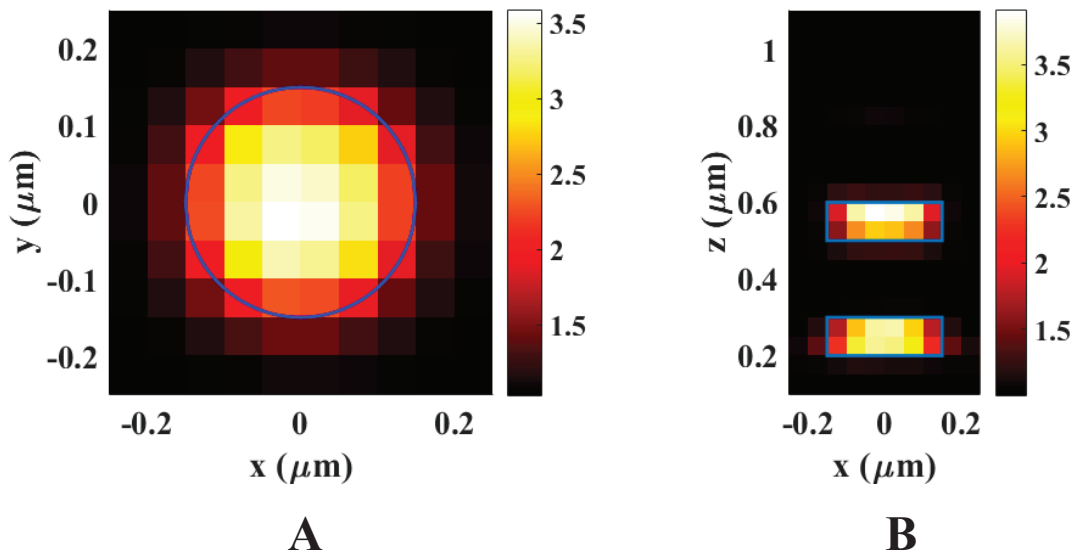


**Figure 4.9 :** *Result of numerical experimental reconstruction. Fig.A: Transverse cut ( $xy$  direction) along center of the bottom of the  $\text{TiO}_2$  shown in Fig.B. Fig.B: Axial cut ( $xz$  direction) along  $y=0$  in (A).*

The numerical results obtained from the synthetic inversion is shown in fig. 4.9. The transverse cut along the axial center of the bottom cylinder provided a good estimate of the diameter ( $300\text{nm}$ ) of the cylinder (shown in Fig. 4.9.A). The axial cut along the  $xz$  axis along the center of the axis is shown in Fig. 4.9.B. The color bars represent the permittivity values which are normalized with respect to the

medium. The medium being  $\text{SiO}_2$ , resin and oil; their permittivity is normalized to 1. After normalization the permittivity value of  $\text{TiO}_2$  should have been 2.3922, but it is overestimated here. This can be optimized in the inversion program. From the results the two cylinders are well retrieved without any artifacts and are well separated.

Along with this 200nm separation distance between the two  $\text{TiO}_2$  cylinders, various separations distances such as “ $s$ ” = 100nm, 300nm were tested and numerical reconstruction was satisfactory. So, we decided to fabricate the samples as shown in Fig. 4.7 with “ $s$ ” = 100nm, 200nm and 300nm separation distance between the  $\text{TiO}_2$  cylinders and “ $d$ ” with 200nm and 600nm.

I will now show how the fabrication of such samples is performed in the clean room of a fabrication facility step by step.

### 4.5.2 Sample fabrication

The samples required to test the improvement brought by the mirror-assisted tomography were fabricated in Laboratoire de Photonique et de Nanostructures (LPN), Marcoussis, France by Anne Talneau. One of the methods used to fabricate the samples required for measurement is by means of depositing different layers of materials on a Silicon (Si) substrate and then etch them to the required shapes by suitable etching process. Finally, a resin coat is deposited on top of the fabricated cylinders.

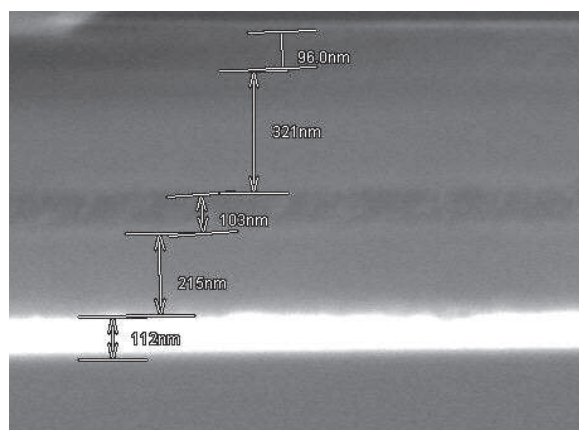


**Figure 4.10 :** SEM image of the layers deposited on the Si substrate of  $100\mu\text{m}$ . The layers and their thickness shown are Al (112nm),  $\text{SiO}_2$  (215nm),  $\text{TiO}_2$  (103nm),  $\text{SiO}_2$  (321nm) and  $\text{TiO}_2$  (96nm) respectively.

The first step in this process is to deposit different layers required for the sample. In our case, as the sample is made up of several layers such as Al,  $\text{SiO}_2$  and  $\text{TiO}_2$  we have to deposit them one after another in the order. For this, we start with a silicon (Si) wafer and deposit Al layer of 100nm thickness, then the  $\text{SiO}_2$  of 200nm is deposited with help of electron beam and ion gun deposition technique on top of the Al layer. Similarly  $\text{TiO}_2$  (100nm),  $\text{SiO}_2$  (200nm) and  $\text{TiO}_2$  (100nm) are deposited using electron gun and ion gun within the same vacuum chamber respectively. After

deposition of several layers, the final SEM image of the layers would look as shown in the Fig. 4.10.

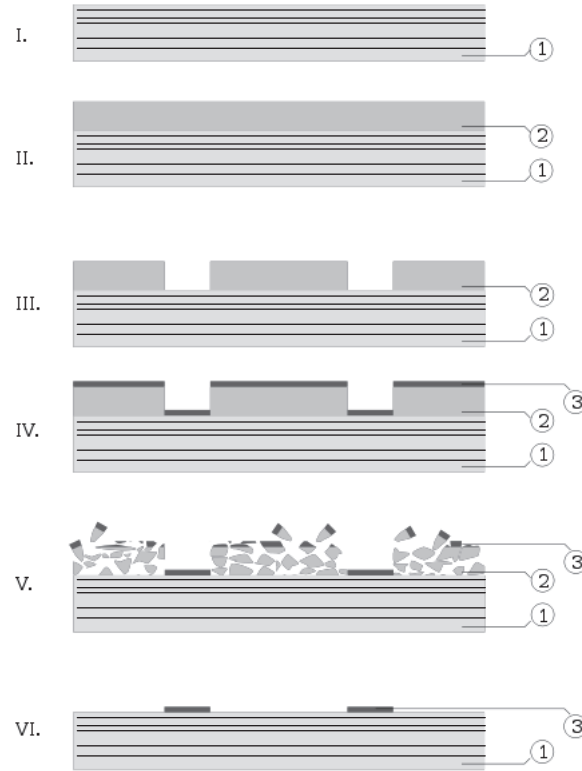


**Figure 4.11 :** *Lift-off procedure: I. Preparation of the substrate (1) with layers deposited on it. II. Deposition of the PMMA stencil layer (2). III. Patterning the PMMA layer using e-beam lithography, creating an inverse pattern. IV. Deposition of the target material, Al (3). V. Washing out the PMMA layer together with the Al material on its surface VI. Final pattern Layers: (1) substrate with different layers and (3) Al pattern.*

The second step is to deposit a mask on top of the layers to perform etching. For this depending on the diameter of the cylinders the mask has to be patterned. This is performed using Al mask by lift-off on PMMA (Poly(methyl methacrylate)). The steps involved in this procedure are explained in the Fig. 4.11.

The third step is to perform etching. Etching can be performed by reactive-ion etching (RIE) or inductively coupled plasma (ICP) or by other means. The areas where the Al resist is present will be unaffected and the other regions are etched away by the ions or plasma used during the process. Ions react and knock-off the material to be etched. Since we require well calibrated structures for quantifying the axial resolution, it is challenging to obtain well etched cylinders with perfect vertical walls. This is due to the fact that several parameters such as temperature, pressure, time, and the gasses ( $\text{SF}_6$ , Ar,  $\text{O}_2$ , etc..) are involved in the process of RIE or ICP

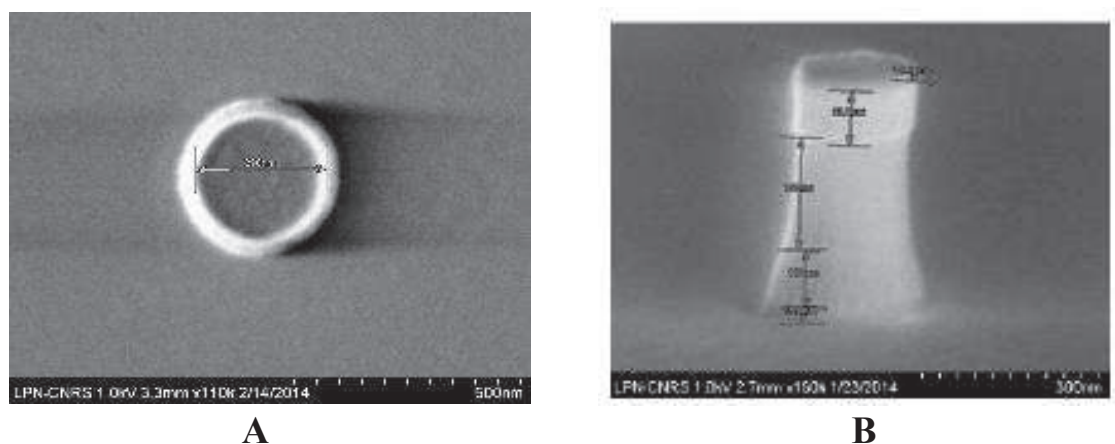


**Figure 4.12 :** *Fabricated sample under SEM. Fig.A: Top view of the cylinder. Fig.B: The axial view of the cylinder.*

etching. These parameters are different for different materials such as  $\text{TiO}_2$ ,  $\text{SiO}_2$ , etc.

The parameters mentioned above have to be fine tuned to obtain vertical cylinders depending on the material composition of the layers. Because, the ions are vertically delivered from ICP or RIE, the knock-off of material does not occur very isotropically. There are various layers to be etched requiring different kinetic energies. If the process is not optimized that would result in anisotropic etch profiles of the required cylinders. For this, the parameters has to be fine tuned by trial & error and by characterizing at each step with help of SEM (scanning electron microscope). The parameters and the process were optimized by Anne Talneau at LPN clean room facilities.

Once the layers are etched, we already have the required structures with the Al mask on the top. This Al mask can be selectively removed. Then the resin with refractive index value 1.5 is deposited on the top of the cylinders to have the final required sample. The SEM image of final fabricated sample is shown in Fig. 4.12.

Several such samples with different variations (parameters “ $s$ ” and “ $d$ ” shown in Fig. 4.7.A are modified) were fabricated with Al layer acting as the mirror. These samples were used to experimentally test the mirror-assisted tomography for axial-resolution improvement.

## 4.6 Experimental results

In a preliminary study, we have validated on synthetic data the ability of our approach to retrieve accurate reconstructions of the sample along the axial direction [3]. Here, I will present its first experimental validation on calibrated multi-layered nano-objects requiring isotropic super-resolution which were designed and fabricated in the previous section. Fig. 4.12.A shows the case of a nano-pillar embedded in resin, where only the two layers of  $\text{TiO}_2$  produce the scattering signal. This sample is

placed in the TDM experimental setup explained in the section Sec. 1.6.2 to perform mirror-assisted tomography.

First, I will present the general requirements in performing mirror-assisted tomography, then particular samples are discussed in detail. The wavelength used for the measurements was  $\lambda = 632.8nm$ , NA of the objective is 1.49 (CFI Apo TIRF 100x: Nikon) in the presence of oil with refractive index 1.5. The illuminations were performed along the  $\mathbf{K}_x$  and  $\mathbf{K}_y$  directions as shown in Fig. 4.8. Twelve angles were used along the  $\mathbf{K}_x$  and  $\mathbf{K}_y$  each, totally 24 angles (between  $5-51^\circ$  for illumination) of incidence was used to illuminate the sample with plane coherent beams of light. The full-vectorial scattered field was measured as explained in the section Sec. 1.6.2.1.

Before the non-linear inversion is performed on the measured data, I perform data-preconditioning to improve it.

### 4.6.1 Data pre-conditioning

The measured data quality has to be enhanced by performing a reference measurement and aberration correction to have better reconstruction results.

#### a) Reference measurement

To improve the sensitivity of the reconstructions, we perform a reference measurement on the bare substrate (location where there is no sample present). It permits us to measure the specular reflected field for each illumination angle. By subtracting it from the field measured in the presence of the sample, only the scattered field part remains, and the speckle noise generated by the illumination and the specular reflection is suppressed.

#### b) Aberration correction

The optical components in the optical tomographic diffractive microscopy setup has to be adjusted precisely to perform a high quality measurement. Even though I adjust these components, there can be aberrations from the high NA objective used in the measurements. It is important to quantify such aberration and apply it on the measured data to improve it. For this purpose, I used a well calibrated sample to obtain the aberration profile. The calibrated sample used for measurement are groves extended along y axis. Along the x-axis, there were two groves with dimensions of  $1\mu m$  and  $0.5\mu m$  width respectively, they were separated by  $0.5\mu m$  spacing. The sample was illuminated with 20 angles of incidence and the scattered field was measured with the TDM setup. Its corresponding theoretical field was also calculated (thanks to Gabriel Soriano, SEMO, Institute Fresnel). The aberration profile profile is computed by subtracting the theoretical phase from the measured phase of the scattered field. Such a 1D aberration profile is extended to 2D considering the rotational invariance of the obtained profile within the NA. The final aberration profile ( $\mathbf{E}_{ab}$ ) obtained is shown in Fig. 4.13.

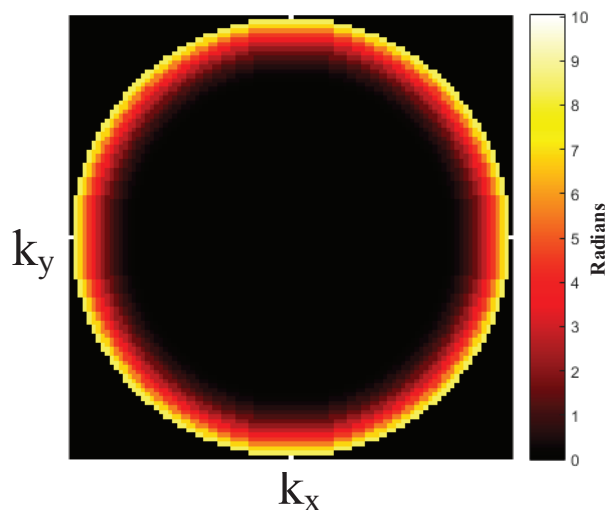


**Figure 4.13 :** *Aberration profile of the experimental setup obtained using a calibrated sample for  $NA=1.49$ , CFI Apo TIRF 100 $\times$ : Nikon.*

This aberration profile has to be subtracted from the phase of the complex scattered field data to obtain the aberration free measurement. Since the TDM measurement provides the complex scattered field, the aberration can be directly subtracted from it. Now, the non-linear inversion algorithm can perform its task of 3D reconstruction to show the axial-resolution improvement.

We noticed that the direct Born approximation or the inverse Fourier transform approach (without separating the transmission and reflection components) fail to resolve the two  $TiO_2$  cylinders that are located 200nm separated from each other. We expect by taking into account the presence of mirror using non-linear inversion, we should be able to resolve the two  $TiO_2$  cylinders experimentally.

#### 4.6.2 Mirror-assisted tomography using non-linear inversion: results

The experimental validation of the mirror-assisted tomography is shown in this section on the fabricated  $TiO_2$  nano cylinders. Ideal case to demonstrate the improvement in the axial resolution would be to fabricate several variations of the nano cylinders with varying distances and show the experimental results for each variation. Variations means changing the distance between the first cylinder and the Al mirror layer (shown by “ $d$ ” in the Fig. 4.7.A) or changing the distance between the two  $TiO_2$  cylinders (shown by “ $s$ ” in the Fig. 4.7.A). I will show the results obtained for several such variations here. It has to be noted that the height of the  $TiO_2$  cylinders always remain as 100nm with 300nm diameter. The diameter of 300nm for cylinders was chosen to obtain significant scattered field from the sample in terms of signal to noise ratio. The focus here is to show the improvement in axial-resolution, this justifies the thickness of 100nm compared to 300nm diameter for cylinders.

### Sample 1: 100nm side-by-side axial separation

We fabricated a sample as shown in the Fig. 4.14.A. The two TiO<sub>2</sub> cylinders that we would like to resolve are separated by 100nm side-by-side axially using SiO<sub>2</sub> layer. The first TiO<sub>2</sub> cylinder is separated from the aluminum mirror by 200nm using a SiO<sub>2</sub> layer as well. The sample is covered with a resin layer of refractive index 1.5.

A fabricated sample as described above is positioned in the TDM experimental setup (consult section Sec. 1.6.2 for the details of the experimental setup). The objective used for the measurement is oil objective (NA=1.49, CFI Apo TIRF 100x: Nikon) with oil of refractive index 1.515. The sample was illuminated with 24 illuminations of wavelength  $\lambda = 632.8nm$ , 12 along the vertical direction and 12 along the horizontal direction at the center of the NA of the objective as explained earlier and shown in Fig. 4.8. The measurement was performed to obtain the complex scattered field along with illumination and detection polarization. Of course, off-axis interferometry was used to obtain the complex scattered field (amplitude and phase). The measured scattered field is processed by correcting the aberration as explained earlier. The amplitude and the phase normalization as explained in the previous chapter (section Sec. 3.2) was also performed to have the same phase for each illumination. Most importantly, the phase origin is located on the Al mirror.

The scattered field data obtained from the above steps is numerically inverted with the help of non-linear inversion algorithm explained in the previous chapter (refer section Sec. 3.3). The presence of the Al mirror below the TiO<sub>2</sub> cylinders was taken into consideration during the inversion procedure. I know the thickness of the SiO<sub>2</sub> layer on top of the Al layer, which is 200nm,. So, the inversion box (the box with volume  $\Omega$  shown in Fig. 3.4) starts at 100nm from the Al mirror layer. The size of the pixels used for the inversion is 25nm, i.e. the length of the sides of the cube in Fig. 3.4. The result obtained from the inversion procedure is presented in Fig. 4.14.B&C.

The result (Fig. 4.14.B) shows the ability of the mirror-assisted tomography along with non-linear inversion to resolve the two TiO<sub>2</sub> cylinders located 100nm side-by-side in the axial direction ( $z$ ). The permittivity value is also retrieved, shown in the color bar of Fig. 4.14.B. The color bar shows a normalized permittivity value with the surrounding SiO<sub>2</sub> and resin coating taken to be 1. The ideal permittivity value on the TiO<sub>2</sub> cylinders must have been 2.3922 but we obtain about 1.8 in the Fig. 4.14.B and C, this is due to the experimental noise. The second TiO<sub>2</sub> cylinder is of lower permittivity value, this can be due to a fabrication defect. Or it can also be due to the illumination pattern formed during the illumination on a mirror, this issue is discussed in detail later.

The transverse-cut along the  $xy$  direction is presented in Fig. 4.14.C. The diameter of 300nm is well reconstructed.

The result presented here is the best result obtained with marker-free microscopy to my knowledge to resolve axially. The axial resolution at best for optical microscopy is in the region of  $\lambda$ , in this experimental case it should be about 420nm ( $632.8nm/1.5$ , wavelength used divided by the refractive index of oil). I have experimentally shown the ability to resolve 200nm center to center separated TiO<sub>2</sub>

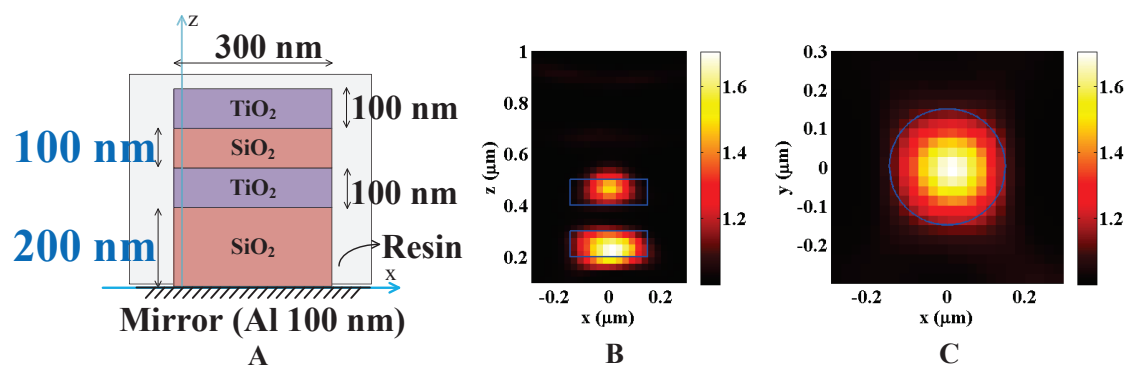


**Figure 4.14 :** Mirror-assisted tomography experimental result. *Fig.A:* Fabrication schema of the sample,  $\text{TiO}_2$  (refractive index = 2.32) cylinders of 300nm in diameter separated by 100nm side-by-side axial distance filled with  $\text{SiO}_2$  (refractive index = 1.5). The mirror and the first cylinder are separated by a distance of 200nm with  $\text{SiO}_2$ . The sample is covered by a resin layer (refractive index = 1.5). *Fig.B:* The experimental non-linear reconstruction of the sample shown in Fig.A.  $\text{TiO}_2$  cylinders are well resolved along the axial direction ( $z$ ). *Fig.C:* Transverse cut ( $xy$ ) along the center of the first cylinder from the mirror, diameter of 300nm is well reconstructed at  $\lambda = 632.8\text{nm}$  and 1.49 NA objective.

cylinders thanks to mirror-assisted tomography. The axial resolution that I have shown here is better than  $\lambda/2$ , much better than conventional optical microscopes.

#### Sample 2: 200nm side-by-side axial separation

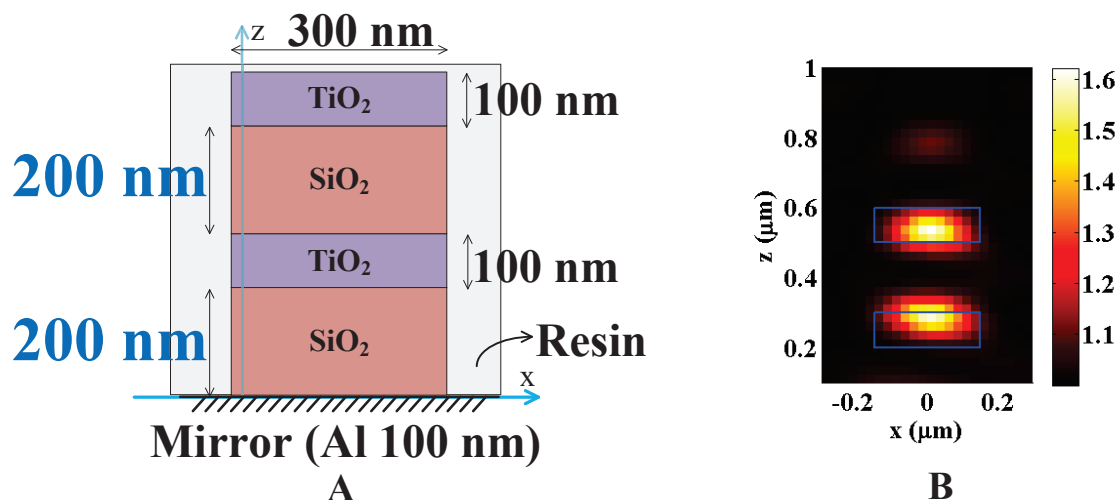


**Figure 4.15 :** Mirror-assisted tomography experimental result. *Fig.A:* Fabrication schema of the sample: similar to Fig. 4.14.A, except the distance between the two  $\text{TiO}_2$  cylinders is 200nm. *Fig.B:* The experimental non-linear reconstruction of the sample shown in Fig.A.  $\text{TiO}_2$  cylinders are well resolved along the axial direction  $z$ .

To further demonstrate the possibility to reconstruct the TiO<sub>2</sub> cylinders at different locations on top of an Al mirror, we fabricated a sample as shown in Fig. 4.15.A. The distance between the first TiO<sub>2</sub> cylinder and the mirror is 200nm (distance “*d*” in the Fig. 4.7.A). The two TiO<sub>2</sub> cylinders are separated by 200nm edge-to-edge axially (distance “*s*” in the Fig. 4.7.A). The diameter of 300nm and the other properties are conserved from the previous sample described earlier in this section. The TDM measurement with the same illumination and detection schema as explained for the previous sample was performed to obtain the polarization resolved complex scattered field data. The data was processed to perform the non-linear inversion.

The result of the 200nm side-by-side separated TiO<sub>2</sub> cylinders is presented in the Fig. 4.15.B. It shows the axial reconstruction along *xz* direction. The two TiO<sub>2</sub> cylinders are well separated and they share similar permittivity distribution with noise hindering in reconstructing the correct value. The height of each cylinders is 100nm, they are well reconstructed.

### Sample 3: 300nm side-by-side axial separation

As we experimentally reconstructed more challenging samples with 100nm side-by-side and 200nm side-by-side axially separation (distance “*s*” in the Fig. 4.7.A) between TiO<sub>2</sub> cylinders, we expected to reconstruct samples with higher separation distance with ease. To confirm this we fabricated a sample with 300nm side-by-side axial separation between the TiO<sub>2</sub> cylinders and 600nm mirror to the first cylinder. To note, the mirror to the first cylinder distance is not a decisive parameter until the sample to be imaged is located below 1 $\mu$ m from the mirror and above 100nm.

For this sample with 300nm side-by-side axial separation, we faced challenges in experimental reconstruction. The experimental reconstruction had a rebound located between the 300nm side-by-side separated TiO<sub>2</sub> cylinders. The possible causes and the challenges are described in detail here.

To demonstrate the above described challenge and to show the ability of the mirror-assisted tomography to non-linearly reconstruct the samples irrespective of their distance from the Al mirror layer, we fabricated a sample as shown in the Fig. 4.16.A. The distance between the mirror to the first TiO<sub>2</sub> cylinder along the axial direction is 600nm, the two TiO<sub>2</sub> cylinders are separated by 300nm side-by-side axially.

The TDM measurement was performed with the above described sample. The wavelength, illumination and other experimental parameters are preserved from the measurement performed on the previous sample ( $\lambda = 632.8nm$ , 24 illumination angles forming a cross and NA=1.49 with oil of refractive index 1.515). The measured complex field data is processed by applying aberration correction as usual. The data is inverted using the non-linear inversion algorithm by taking into account the presence of mirror to obtain a result as shown in Fig. 4.16.B.

The result in the Fig. 4.16.B reconstructs the two TiO<sub>2</sub> cylinders between 600-700 nm and 1000-1100nm from the mirror. The reconstruction box is positioned at 500nm from the Al mirror layer. In the reconstruction box, along with the two TiO<sub>2</sub> cylinders there are two rebounds located. One of the rebound is located between

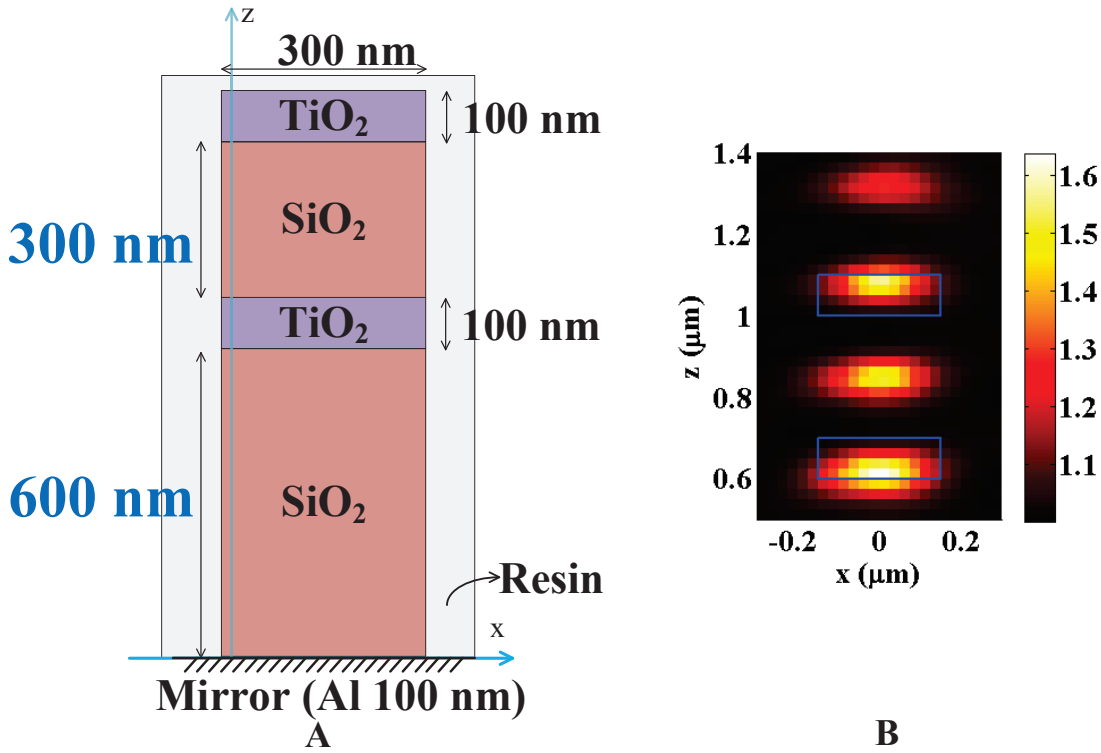


**Figure 4.16 :** Mirror-assisted tomography experimental result. *Fig.A:* Fabrication schema of the sample: similar to Fig. 4.14.A, except the distance between the two TiO<sub>2</sub> cylinders is 300nm and Al mirror layer to first cylinder is 600nm. *Fig.B:* The experimental non-linear reconstruction of the sample shown in Fig.A along  $xz$  direction.

(800-900nm) the two TiO<sub>2</sub> cylinders and the other rebound is at the top (1300-1400nm) of the second TiO<sub>2</sub> cylinder respectively. We will understand the origin of these rebounds.

To understand the problem of rebounds I performed synthetic inversion (more details about the synthetic inversion are presented in Sec. 4.5.1 for the sample configuration shown in Fig. 4.16.A. To recall, synthetic inversion numerically calculates the scattered field data and performs inversion on it. It provided a perfect reconstruction with the same illumination angles and the NA used for measurement, the result is shown in Fig. 4.17. But this result is obtained in the absence of noise, considering perfect measurement conditions, which is not possible to obtain in the experimental measurement case.

Now I will compare the differences between the synthetic inversion data (Fig. 4.17) and experimental measurement data (Fig. 4.16.B.) to explain the rebounds. Of course experimental data has noise originating from several sources (e.g. camera, optical components, speckle noise etc.). I will quantify the level of noise as well. As we employ a high NA objective, it introduces aberrations into the measured data. The quantity of the noise is different for different illumination angles and for different pixels located at varies positions of the NA in the Fourier space.

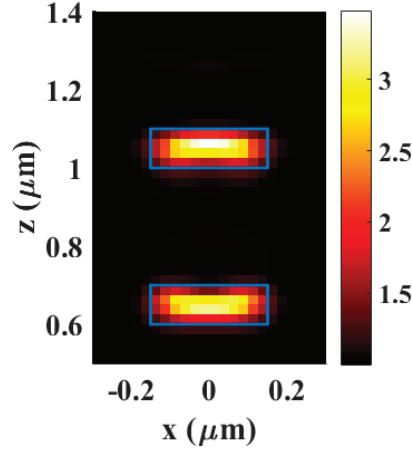


**Figure 4.17 :** *Mirror-assisted tomography inversion result applied on theoretical data. Fabrication schema of the sample shown in Fig. 4.16.A. The numerical non-linear reconstruction, the cylinders are well resolved along the axial direction  $xz$  separated by 300nm side-by-side.*

To quantify the noise and aberrations, we solved the forward problem (explained in section Sec. 3.3.2) and numerically calculated the scattered field for the sample with the illumination angles used during the measurement. For each illumination angle of incidence, represented by  $l=1 \rightarrow L$ ,  $L$  being the last illumination angle, we calculated the scattered field with  $q$  scattering angles, with  $q=1 \rightarrow Q$ . Then I calculated the error ( $R$ ) between the numerically calculated scattered field data ( $\mathbf{E}_T$ ) and measured scattered field data ( $\mathbf{E}_M$ ) using the formula below for the scattered field measured for each illumination angle of incidence,

$$R_l = \frac{\sum_{q=1}^Q \|\mathbf{E}_{T,l} - \mathbf{E}_{M,l}\|^2}{\sum_{q=1}^Q \|\mathbf{E}_{T,l}\|^2}, \quad (4.1)$$

We found that the  $R_l$  is more than 100% for the scattered field measured with angles of incidences close to the normal incidence. The angles away from the normal incidence had noise error of less than 100%. So we discarded the angles which had higher error, i.e. angles close to normal incidence angles. From the calculations we realized that phase is more noisy and plays a major role in reconstruction. So we further investigated phase of  $\mathbf{E}_T$  and  $\mathbf{E}_M$ .

We realized also that the phase at the edge of the NA in Fourier space was more noisy compared to the data in the center of the NA. But high spatial frequencies are important for the axial resolution. So, we replaced the phase at the edge of the NA in Fourier space of  $\mathbf{E}_M$  (measured scattered field data) with  $\mathbf{E}_T$  (numerically calculated scattered field data) for each illumination angle of incidence. The reconstruction worked better, which is shown in Fig. 4.18

Though the aberration correction improved the measurement to an extent but it was not sufficient enough to obtain a satisfactory reconstruction. Due to the

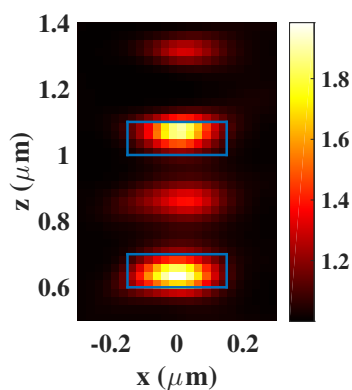


**Figure 4.18 :** *Reconstruction of sample with configuration shown in Fig. 4.16.A with the scattered field data corresponding to the angles of incidence close to the normal incidence suppressed and the phase at the edge of the NA in Fourier replaced by numerically calculated phase. This is better than the experimental result presented in Fig. 4.16.B, this gives insights into the importance of noise and aberrations.*

noise, the non-linear reconstruction algorithm could not converge. As we perform cost minimization to perform numerical inversion, the inversion stops at a certain iteration though the reconstruction is not satisfactory. For better resolution, in general the high frequency components (components located at the extreme edge of the NA in Fourier space) are important. But these are corrupted by aberrations and are not sufficiently improved by the data-conditioning aberration correction performed in section, Sec. 4.6.1. We corrected to a certain extent, it is not good enough to provide optimal reconstruction result.

In conclusion, the aberrations and the noise has to be minimized to obtain a better reconstruction and improvement in axial resolution of the sample presented in this section.

Important observation is that irrespective of the mirror to the first cylinder distance, the rebounds were always observed for the the 300nm side-by-side separation of two  $\text{TiO}_2$  cylinders case. I observed this when I performed experimental reconstruction of  $\text{TiO}_2$  cylinders side-by-side separated by 300nm axially and the first  $\text{TiO}_2$  located at 200nm from the Al mirror layer. The experimental result is not presented here as it looks similar to the result presented in Fig. 4.16.B. But in future, we would like to examine more and reconstruct this challenging sample, some of the perspectives for reconstruction are presented later in this chapter.

In this section, so far I demonstrated the axial resolution improvement with two cylinders deposited on top of a Al mirror. We would like to demonstrate the axial resolution improvement brought about by the TDM mirror-assisted tomography and the transverse resolution improvement with usual TDM with a single sample, this is performed as follows.

### Transverse and axial resolution improvement demonstration with single sample

A sample as shown in Fig. 4.19 was fabricated. It contains four  $\text{TiO}_2$  cylinders, two of them are positioned at 200nm from the Al mirror, separated along the x-axis by 100nm. Another two more of the  $\text{TiO}_2$  cylinders are positioned at 500nm from the mirror also separated by 100nm along the x-axis. The separation distance between the  $\text{TiO}_2$  cylinders along the z-axis is 200nm. Such a sample was positioned for imaging under the TDM microscope to perform mirror-assisted tomography to demonstrate the transverse and axial resolution improvement along x and z axis respectively.

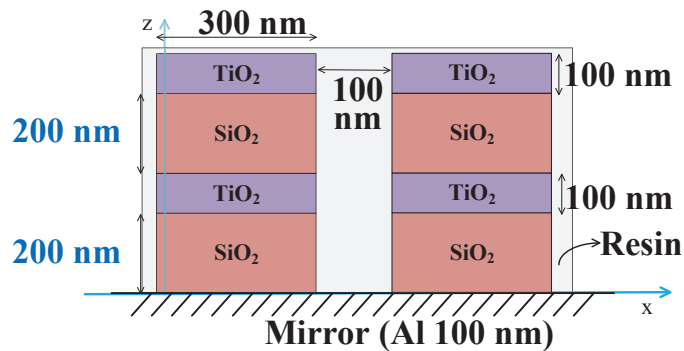


**Figure 4.19 :** *Sample schema to demonstrate both axial and transverse resolution: the schema is similar to the schema shown in Fig. 4.15.A, additional to that, two more  $\text{TiO}_2$  cylinders are positioned along the x-axis separated by 100nm. This forms four  $\text{TiO}_2$  cylinders to be resolved in both transverse and axial direction.*

The experimental measurement was processed to correct the aberrations and normalization to perform non-linear inversion. The result of the non-linear inversion by taking into account the Al mirror is shown in the Fig. 4.20. The transverse resolution (xy direction) is demonstrated with the cylinder diameters of 300nm and separation of 100nm side-by-side. The axial resolution (xz or yz direction) of 200nm side-by-side separation between the two  $\text{TiO}_2$  cylinders can be seen. The  $\text{TiO}_2$  cylinder close to the Al mirror seems to be slightly shifted away from its actual location, we believe this is at the correct location. The shift in the location could be due to the fabrication of cylinder at slightly shifted location.

There are rebounds located close to the Al mirror and at 800nm. The problems discussed in the previous section about the rebounds are applicable to this experimental result too.

Here, I have demonstrated the axial resolution improvement brought about by the mirror-assisted tomography. The challenges in using mirror-assisted tomography has also been discussed. The next section will explain the outlook to improve the mirror-assisted tomography.

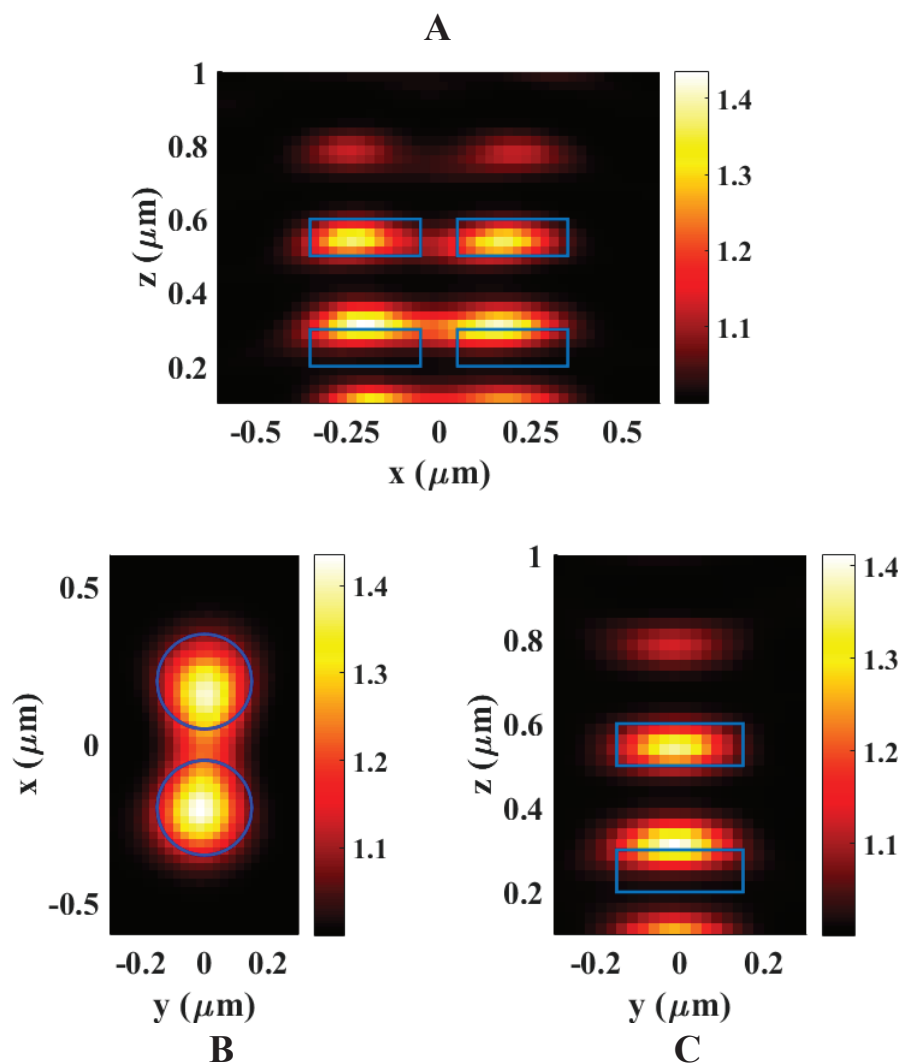


**Figure 4.20 :** Result to demonstrate both axial and transverse resolution using mirror-assisted tomography on sample shown in Fig. 4.19. Fig.A: The axial-cut ( $xz$  direction) showing four  $\text{TiO}_2$  cylinders along with few rebounds. Fig.B: The transverse-cut ( $xy$  direction) along the center of  $\text{TiO}_2$  cylinders located close to the mirror, each cylinder is of diameter 300nm. The two cylinders are transversely separated by 100nm side-by-side. Fig.C: Axial-cut ( $yz$  direction) along the center of  $x$ -axis with faint rebound.

## 4.7 Future perspectives

We have been exploring many ideas to improve the mirror-assisted tomography and apply it to bigger objects and biological cells in future. Though we obtained axial resolution of 100nm and 200nm for  $\text{TiO}_2$  cylinders deposited on the Al Mirror, we have rebounds in the case of 300nm separation case. We retrieve the cylinders with rebounds. We understand that the experimental data is noisy at the edge of the NA and causing the non-linear inversion program problems to converge. Ideal case

would be to optimize the aberrations or phase of the measured data as much as possible with the help of well calibrated samples in the future.

Optimization of the illumination is also important in mirror-assisted tomography. To understand the problem with illumination, observe the Fig. 4.21. A sample positioned on the top of mirror is illuminated with a plane wave (see Fig. 4.21.A) illumination. The light is reflected back from the mirror. The reflected light and the illuminated light interfere with each other causing the variation in the intensity with which we illuminate the sample at different locations along the axial direction (see Fig. 4.21.B). This variation in illumination does not illuminate the sample uniformly. This could be one of the reasons for the rebounds. It is more difficult for the inversion algorithm to deconvolute the field and the object when the field is highly inhomogeneous. To recall, in the inversion procedure we consider we illuminate the sample uniformly with coherent plane waves. When this is significantly different, it causes problem in inverting the experimental data.

We have been trying to optimize the illumination pattern to illuminate the sample uniformly. As we illuminate with different illumination angles of incidence to perform mirror-assisted tomography, the interference pattern formed from each of them is different. These illumination angles has to be selected in such a way that, the summation of the interference patterns yield a uniform illumination on the sample.

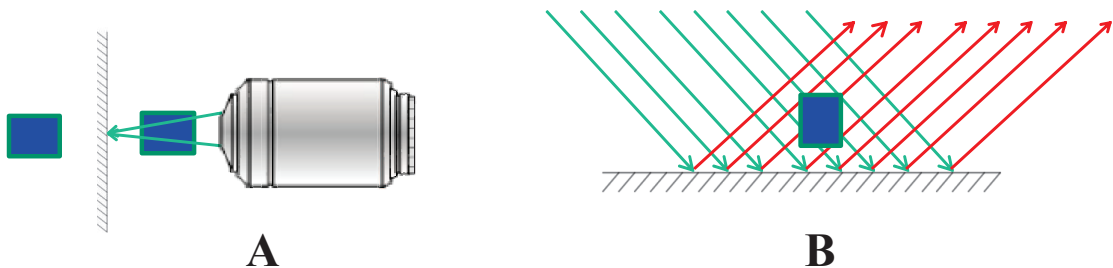


**Figure 4.21 :** *Illumination in mirror-assisted tomography: Fig.A: A sample positioned on top of a mirror is illuminated with an objective, we observe real object and the mirror-image. Fig.A: The sum of the illuminations forms a interference pattern due to the illuminated and the reflected beams.*

The TDM was applied to image biological cells with low resolution [140]. The ideal extension would be to image biological samples and apply mirror-assisted tomography on them to increase the isotropic resolution. In this thesis, I demonstrated the resolution in transverse and axial direction improvement due to the TDM, mirror-assisted tomography and the non-linear inversion on known samples which are deposited on the reflective substrate. We performed initial measurements to image biological samples. The biological cells are bigger in nature (in the range of few micrometers). This demands higher computer memory to perform non-linear inversion on such bigger samples to obtain higher resolution images. It is necessary to obtain more data, so more illumination angles is one of the ways to obtain it.

Another method to obtain more experimental data is to perform multi-wavelength measurement. On a sample, we perform mirror-assisted tomography with different wavelengths. Then the non-linear inversion algorithm can be used on this data to obtain the result by taking into account the illumination with various wavelengths. In terms of 3D synthetic aperture inversion, we fill the 3D synthetic aperture with more data due to the multi-wavelength measurement.

The non-linear inversion algorithm is time consuming, the inversion time depends on the resolution with which we would like to reconstruct the object and the size of the object, the model used to perform inversion (Born or rigorous inversion techniques) etc. So, the non-linear inversion has to be optimized to perform inversions faster, this is already been looked into by Patrick Chaumet and Kamal Belkebir from our group SEMO, Institute Fresnel, Marseille. Provided these improvements, mirror-assisted tomography presents a powerful case to improve axial resolution in optical microscopes in future.

## 4.8 Conclusion

The axial resolution of optical microscopes is generally three times worse than the transverse resolution. The previous chapters detailed the transverse resolution improvement due to the TDM and non-linear inversion. The axial resolution is worse due to the illumination and detection configurations employed to collect the scattered field from the sample in microscopes. To improve this and to combine the advantages of both transmission and reflection configuration, a mirror-assisted tomography was proposed [3] and the experimental results and challenges were presented in this chapter.

To demonstrate the axial resolution improvement, two  $\text{TiO}_2$  cylinders with 300nm diameter, 100nm height and varying axial separation distance were fabricated in LPN, Marcoussis, France. Axial separation of 100nm and 200nm side-by-side were experimentally resolved using mirror-assisted tomography. The axial-resolution improvement presented in this chapter is best-ever with a marker-free microscopy achieved using a single objective to our knowledge. A sample to demonstrate both transverse and axial-resolution of the TDM with single sample was also fabricated and result was presented. The mirror-assisted tomography has some challenges to overcome such as rebounds. The challenges were explained with a sample containing two  $\text{TiO}_2$  cylinders separated by 300nm.

In the end, high illumination and high scattering angle data was shown to be very important for axial resolution improvement. To have quality high scattering angle data we need to perform careful correction of aberrations, this has to be optimized in the future. To extend mirror-assisted tomography to biological samples, the perspectives to increase the amount of data collected by means of multi-wavelength and increase in the speed of the non-linear inversion algorithm were proposed.

---

# Conclusion

---

“Because a fact seems strange to you, you conclude that it is not one. ... All science, however, commences by being strange. Science is successive. It goes from one wonder to another. It mounts by a ladder. The science of to-day would seem extravagant to the science of a former time. Ptolemy would believe Newton mad.”

-Victor Hugo, Writer

This PhD thesis is devoted to the optical tomographic diffractive microscopy (TDM) for three-dimensional isotropic resolution improvement. We illuminated the objects with varying angles of plane waves and measured the complex diffracted field from them using a TDM experimental setup and performed numerical inversions. The incident field was known, the diffracted field was measured and the unknown objects were three-dimensionally reconstructed beyond the optical diffraction limit resolution. Thanks to the multiple scattering at the unknown object and the accurate models I used to reconstruct the measured diffracted field with computers. This is originality of our approach in reaching label-free super-resolution compared to the fluorescence based techniques which rely on the fluorescent markers.

The measured data from the experimental setup was significantly enhanced due to the implementation of low-coherence supercontinuum source, externally cooled high sensitive camera, high sensitive mirror for varying the illumination and a delay line for off-axis interferometry during this thesis. The measured complex diffracted field was numerically inverted to reconstruct the object with linear inversion (Born, Rytov etc.) and accurate non-linear inversion (iterative) algorithms.

The linear inversion algorithms can be used to reconstruct resolution limited images from the measured data. These algorithms consider there is a linear link between the object and field measured from it. We shown the numerical imaging of various microscope techniques such as bright-field microscope, dark-field microscope, phase-contrast microscope, confocal microscope, 2D synthetic aperture microscope and 3D synthetic aperture microscope from the experimentally measured complex diffracted field TDM data under linear approximations. The advantage being the TDM measurement was performed once with several angles on the sample. Thanks to the single measurement, TDM provides complete complex measured field data to realize various microscopy techniques. I discussed in detail the advantages and disadvantages of each numerical microscopy technique. We believe that numerical realization of several such microscopy techniques provide complementary information about the object, leading to better understanding. We realized these techniques to demonstrate the rapid and simple means of getting first understanding of the object under observation. The main disadvantage is the resolution being limited.

We have shown that using rigorous non-linear inversion algorithm by taking into account the illumination and the detection polarization and the non-linear link between the object with its diffracted complex field the resolution can be improved. It was demonstrated that polarization plays a role in obtaining isotropic transverse resolution. We have achieved transverse resolution of 100nm without any labeling (marker-free) of the samples by this approach. The coupling of TDM full-polarized complex field data with the inversions algorithm makes it possible to reconstruct any irregularities in the sample too. Using singular value decomposition as a tool along with non-linear inversion algorithm to reconstruct the samples in a noisy environment was demonstrated spectacularly. We have shown that it is possible to achieve even higher resolution of 50nm ( $\lambda/10$ ) by providing a priori information (sample permittivity range with in a bound) about the sample and taking advantage of SVD treatment.

Along with the transverse resolution improvement, axial resolution is equally important to perform 3D isotropic super-resolution. Poor axial resolution is due to the fundamental asymmetry of illumination and detection in microscopes. Illumination and detection are performed only on one side of the sample. To obtain 3D isotopic resolution the illumination and detection have to be performed in all possible angles in 3D, which is very hard to realize in practice. To overcome this, a mirror-assisted TDM set-up was proposed: the main idea is to deposit the sample on a mirror, so that it is illuminated and observed simultaneously from both sides thanks to the mirror.

We have validated on synthetic data to resolve two cylinders located at various positions on top of a mirror. To experimentally demonstrate the axial-resolution improvement, we fabricated two cylinders on top of a mirror at various locations. We performed TDM measurement and applied non-linear inversion algorithm by taking into account the presence of mirror. This permits to resolve two cylinders that are separated by 100nm and 200nm side-by-side positioned along the axial direction. This demonstrates the experimental applicability of our mirror-assisted tomography approach to retrieve accurate reconstructions of the sample along the axial direction. For the sample with 300nm side-by-side axial separation, the experimental result presents rebounds and is challenging to reconstruct. For the global improvement of the axial resolution and to overcome the challenges accurate quantification of the aberrations coming from the use high NA objectives, optimization of the illumination, multi-wavelength measurement were presented as perspectives. The extension of the mirror-assisted tomography to bigger objects and biological objects require optimization of algorithms and faster computers, which is already being looked into.

In conclusion, I believe that optical tomographic diffraction microscopy coupled with non-linear inversion algorithm is one of the futuristic methods that will be employed to reconstruct objects in three-dimensions with their optical material properties at resolution far superior to the conventional microscopes. With the improved non-linear inversion algorithms, computational time and advancements in mirror-assisted tomography, hopefully it would turn into a industrial product used by physicist and biologist with ease.

---

# Bibliography

---

- [1] E. Betzig, S. W. Hell, and W. E. Moerner. The nobel prize in chemistry 2014, "for the development of super-resolved fluorescence microscopy". The Royal Swedish Academy of Sciences, 2014.
- [2] H. von Helmholtz and H. Fripp. On the limits of the optical capacity of the microscope. *The Monthly Microscopical Journal*, 16(1):15–39, 1876.
- [3] E. Mudry, P. C. Chaumet, K. Belkebir, G. Maire, and A. Sentenac. Mirror-assisted tomographic diffractive microscopy with isotropic resolution. *Opt. Lett.*, 35(11):1857–1859, 2010.
- [4] E. Wolf. Three-dimensional structure determination of semi-transparent objects from holographic data. *Opt. Commun.*, 1:153–156, 1969.
- [5] V. Lauer. New approach to optical diffraction tomography yielding a vector equation of diffraction tomography and a novel tomographic microscope. *J. Microsc.*, 205:165–176, 2002.
- [6] G. Maire, F. Drsek, J. Girard, H. Giovannini, A. Talneau, D. Konan, K. Belkebir, P. C. Chaumet, and A. Sentenac. Experimental Demonstration of Quantitative Imaging beyond Abbe’s Limit with Optical Diffraction Tomography. *Phys. Rev. Lett.*, 102:213905–4, 2009.
- [7] B. Simon, M. Debailleul, A. Beghin, Y. Tourneur, and O. Haeberlé. High-resolution tomographic diffractive microscopy of biological samples. *J. Biophoton.*, 3:462–467, 2010.
- [8] S. Arhab, G. Soriano, K. Belkebir, A. Sentenac, and H. Giovannini. Full wave optical profilometry. *J. Opt. Soc. Am. A*, 28(4):576–580, 2011.
- [9] C. C. Reyes-Aldasoro. *Bright Field Microscopy*, chapter 6, pages 215–289. John Wiley & Sons, Ltd, 2015.
- [10] S. Patskovsky, E. Bergeron, D. Rioux, and M. Meunier. Wide-field hyperspectral 3d imaging of functionalized gold nanoparticles targeting cancer cells by reflected light microscopy. *Journal of Biophotonics*, 8(5):401–407, 2015.

- [11] F. Zernike. Phase contrast, a new method for the microscopic observation of transparent objects. *Physica*, 9(7):686 – 698, 1942.
- [12] D. Fu, S. Oh, W. Choi, T. Yamauchi, A. Dorn, Z. Yaqoob, R. R. Dasari, and M. S. Feld. Quantitative dic microscopy using an off-axis self-interference approach. *Opt. Lett.*, 35(14):2370–2372, 2010.
- [13] J. W. Lichtman and J.-A. Conchello. Fluorescence microscopy. *Nature Methods*, 2:910–919, 2005.
- [14] T. Wilson. Confocal microscopy. *Academic Press: London, etc*, 426:1–64, 1990.
- [15] P. J. Keller, A. D. Schmidt, J. Wittbrodt, and E. H. Stelzer. Reconstruction of zebrafish early embryonic development by scanned light sheet microscopy. *science*, 322(5904):1065–1069, 2008.
- [16] M. Gustafsson. Surpassing the lateral resolution limit by a factor of two using structured illumination microscopy. *J. Microsc.*, 198:82–87, 2000.
- [17] F. Helmchen and W. Denk. Deep tissue two-photon microscopy. *Nature methods*, 2(12):932–940, 2005.
- [18] W. Denk, J. H. Strickler, and W. W. Webb. Two-photon laser scanning fluorescence microscopy. *Science*, 248(4951):73–76, 1990.
- [19] M. Born and E. Wolf. *Principles of Optics*. Cambridge University Press, 1999.
- [20] E. Abbe. Beiträge zur theorie des mikroskops und der mikroskopischen wahrnehmung. *Beiträge zur Theorie des Mikroskops und der mikroskopischen Wahrnehmung*, 9:413–468, 1873.
- [21] A. J. den Dekker and A. van den Bos. Resolution: a survey. *J. Opt. Soc. Am. A*, 14(3):547–557, Mar 1997.
- [22] D. Gabor. A new microscopic principle. *Nature*, 161(4098):777–778, 1948.
- [23] J. Girard, G. Maire, H. Giovannini, A. Talneau, K. Belkebir, P. C. Chaumet, and A. Sentenac. Nanometric resolution using far-field optical tomographic microscopy in the multiple scattering regime. *Phys. Rev. A*, 82(6):061801, 2010.
- [24] I. Yamaguchi and T. Zhang. Phase-shifting digital holography. *Opt. Lett.*, 22(16):1268–1270, 1997.
- [25] Y. Ruan, P. Bon, E. Mudry, G. Maire, P. C. Chaumet, H. Giovannini, K. Belkebir, A. Talneau, B. Wattellier, S. Monneret, and A. Sentenac. Tomographic diffractive microscopy with a wavefront sensor. *Opt. Lett.*, 37(10):1631–1633, 2012.

- [26] P. Bon, G. Maucort, and B. W. ad S. Monneret. Quadriwave lateral shearing interferometry for quantitative phase microscopy of living cells. *Opt. Express*, 17:13080–13094, 2009.
- [27] A. C. Kak and M. Slaney. *Principles of computerized tomographic imaging*. IEEE Press, 1999.
- [28] F. Charrière, A. Marian, F. Montfort, J. Kuehn, T. Colomb, E. Cuche, P. Marquet, and C. Depeursinge. Cell refractive index tomography by digital holographic microscopy. *Opt. Lett.*, 31(2):178–180, 2006.
- [29] F. Charrière, N. Pavillon, T. Colomb, C. Depeursinge, T. J. Heger, E. A. D. Mitchell, P. Marquet, and B. Rappaz. Living specimen tomography by digital holographic microscopy: morphometry of testate amoeba. *Opt. Express*, 14(16):7005–7013, 2006.
- [30] W. Choi, C. Fang-Yen, K. Badizadegan, S. Oh, N. Lue, R. R. Dasari, and M. S. Feld. Tomographic phase microscopy. *Nat. Methods*, 4:717–719, 2007.
- [31] R. Dändliker and K. Weiss. Reconstruction of the three-dimensional refractive index from scattered waves. *Optics Communications*, 1(7):323 – 328, 1970.
- [32] D. W. Sweeney and C. M. Vest. Reconstruction of three-dimensional refractive index fields from multidirectional interferometric data. *Appl. Opt.*, 12(11):2649–2664, 1973.
- [33] C. Godavarthi, T. Zhang, G. Maire, P. C. Chaumet, H. Giovannini, A. Talneau, K. Belkebir, and A. Sentenac. Superresolution with full-polarized tomographic diffractive microscopy. *J. Opt. Soc. Am. A*, 32(2):287–292, 2015.
- [34] A. J. Devaney. Inversion formula for inverse scattering within the born approximation. *Opt. Lett.*, 7(3):111–112, 1982.
- [35] S. Lecler, Y. Takakura, and P. Meyrueis. Interpretation of light scattering by a bisphere in the electrodynamic regime based on apertures interference and cavity resonance. *Journal of Optics A: Pure and Applied Optics*, 9(10):802, 2007.
- [36] B. Chen and J. J. Stamnes. Validity of diffraction tomography based on the first born and the first rytov approximations. *Appl. Opt.*, 37(14):2996–3006, 1998.
- [37] K. Iwata and R. Nagata. Calculation of refractive index distribution from interferograms using the born and rytov’s approximation. *Japanese Journal of Applied Physics*, 14(S1):379, 1975.
- [38] L. Zapalowski, M. Fiddy, and S. Leeman. On the born rytov controversy. In *1983 Ultrasonics Symposium*, pages 928–930, 1983.

- [39] A. C. Kak and M. Slaney. *Principles of computerized tomographic imaging*. Philadelphia: Society for Industrial and Applied Mathematics. Philadelphia : Society for Industrial and Applied Mathematics, 2001.
- [40] D. Mintzer. Wave propagation in a randomly inhomogeneous medium. ii. *The Journal of the Acoustical Society of America*, 25(6):1107–1111, 1953.
- [41] F. Natterer and F. Wubbeling. *Mathematical methods in image reconstruction*. Philadelphia, PA: Society for Industrial and Applied Mathematics, 2001.
- [42] S. Trattner, M. Feigin, H. Greenspan, and N. Sochen. Validity criterion for the born approximation convergence in microscopy imaging. *J. Opt. Soc. Am. A*, 26(5):1147–1156, 2009.
- [43] B. Simon, M. Debailleul, V. Georges, V. Lauer, and O. Haeberlé. Tomographic diffractive microscopy of transparent samples. *Eur. Phys. J. Appl. Phys.*, 44:29–35, 2008.
- [44] M. Debailleul, B. Simon, V. Georges, O. Haeberlé, and V. Lauer. Holographic microscopy and diffractive microtomography of transparent samples. *Meas. Sci. Technol.*, 19(7):074009, 2008.
- [45] M. Debailleul, V. Georges, B. Simon, R. Morin, and O. Haeberlé. High-resolution three-dimensional tomographic diffractive microscopy of transparent inorganic and biological samples. *Opt. Lett.*, 34(1):79–81, 2009.
- [46] R. Fiolka, K. Wicker, R. Heintzmann, and A. Stemmer. Simplified approach to diffraction tomography in optical microscopy. *Opt. Express*, 17(15):12407–12417, 2009.
- [47] M. Kim, Y. Choi, C. Fang-Yen, Y. Sung, R. R. Dasari, M. S. Feld, and W. Choi. High-speed synthetic aperture microscopy for live cell imaging. *Opt. Lett.*, 36(2):148–150, 2011.
- [48] Z. Wang, D. L. Marks, P. S. Carney, L. J. Millet, M. U. Gillette, A. Mihi, P. V. Braun, Z. Shen, S. G. Prasanth, and G. Popescu. Spatial light interference tomography (slit). *Opt. Express*, 19:19907–19918, 2011.
- [49] M. Kim, Y. Choi, C. Fang-Yen, Y. Sung, K. Kim, R. R. Dasari, M. S. Feld, and W. Choi. Three-dimensional differential interference contrast microscopy using synthetic aperture imaging. *J. Biomed. Opt.*, 17:026003, 2012.
- [50] Y. Sung, W. Choi, N. Lue, R. R. Dasari, and Z. Yaqoob. Stain-free quantification of chromosomes in live cells using regularized tomographic phase microscopy. *PLoS ONE*, 7:e49502, 2012.
- [51] M. Mir, S. D. Babacan, M. Bednarz, M. N. Do, I. Golding, and G. Popescu. Visualizing Escherichia coli sub-cellular structure using sparse deconvolution spatial light interference tomography. *PLoS ONE*, 7:e39816, 2012.

- [52] Y. Cotte, F. Toy, P. Jourdain, N. Pavillon, D. Boss, P. Magistretti, P. Marquet, and C. Depeursinge. Marker-free phase nanoscopy. *Nature Photonics*, 7(3):113–117, 2013.
- [53] K. Kim, K. S. Kim, H. Park, J. C. Ye, and Y. Park. Real-time visualization of 3-d dynamic microscopic objects using optical diffraction tomography. *Opt. Express*, 21(26):32269–32278, 2013.
- [54] T. Kim, R. Zhou, M. Mir, S. D. Babacan, P. S. Carney, L. L. Goddard, and G. Popescu. White-light diffraction tomography of unlabelled live cells. *Nature Photonics*, 8:256–263, 2014.
- [55] W.-C. Hsu, J.-W. Su, T.-Y. Tseng, and K.-B. Sung. Tomographic diffractive microscopy of living cells based on a common-path configuration. *Opt. Lett.*, 39:2210–2213, 2014.
- [56] H. Dupoisot, A. Polettaeff, G. Daury, and P. de Vernejoul. Off-axis recording and synthetic aperture imaging in light microscopy. *Optics Communications*, 72(1-2):42 – 46, 1989.
- [57] S. Vertu, J.-J. Delaunay, I. Yamada, and O. Haeberlé. Diffraction microtomography with sample rotation: influence of a missing apple core in the recorded frequency space. *Centr. Eur. J. of Phys.*, 7:22–31, 2009.
- [58] J. Sharpe, U. Ahlgren, P. Perry, B. Hill, A. Ross, J. Hecksher-Sørensen, R. Baldock, and D. Davidson. Optical projection tomography as a tool for 3d microscopy and gene expression studies. *Science*, 296(5567):541–545, 2002.
- [59] S. A. Alexandrov, T. R. Hillman, T. Gutzler, and D. D. Sampson. Synthetic aperture fourier holographic optical microscopy. *Phys. Rev. Lett.*, 97(16):168102, 2006.
- [60] Y. Choi, M. Kim, C. Yoon, T. D. Yang, K. J. Lee, and W. Choi. Synthetic aperture microscopy for high resolution imaging through a turbid medium. *Opt. Lett.*, 36(21):4263–4265, 2011.
- [61] S. S. Kou and C. J. R. Sheppard. Image formation in holographic tomography. *Opt. Lett.*, 33(20):2362–2364, 2008.
- [62] S. S. Kou and C. J. R. Sheppard. Image formation in holographic tomography: high-aperture imaging conditions. *Appl. Opt.*, 48(34):H168–H175, 2009.
- [63] O. Haeberlé, K. Belkebir, H. Giovaninni, and A. Sentenac. Tomographic diffractive microscopy: basics, techniques and perspectives. *Journal of Modern Optics*, 57(9):686–699, 2010.
- [64] S. Vertu, J. Flügge, J.-J. Delaunay, and O. Haeberlé. Improved and isotropic resolution in tomographic diffractive microscopy combining sample and illumination rotation. *Central European Journal of Physics*, 9(4):969–974, 2011.

- [65] A. J. Devaney. Inverse-scattering theory within the Rytov approximation. *Opt. Lett.*, 6:374–376, 1981.
- [66] R. Carminati. Phase properties of the optical near field. *Phys. Rev. E*, 55:4901–4904, 1997.
- [67] Y. Sung, W. Choi, C. Fang-Yen, K. B. zadegan, R. R. Dasari, and M. S. Feld. Optical diffraction tomography for high resolution live cell imaging. *Opt. Express*, 17(1):266–277, 2009.
- [68] Y. Kim, H. Shim, K. Kim, H. Park, J. H. Heo, J. Yoon, C. Choi, S. Jang, and Y. Park. Common-path diffraction optical tomography for investigation of three-dimensional structures and dynamics of biological cells. *Opt. Express*, 22(9):10398–10407, 2014.
- [69] G. Maire, J. Girard, F. Drsek, H. Giovannini, A. Talneau, K. Belkebir, P. C. Chaumet, and A. Sentenac. Experimental inversion of optical diffraction tomography data with a nonlinear algorithm in the multiple scattering regime. *J. Mod. Opt.*, 57:746–755, 2010.
- [70] K. Belkebir, P. C. Chaumet, and A. Sentenac. Influence of multiple scattering on three-dimensional imaging with optical diffraction tomography. *J. Opt. Soc. Am. A*, 23:586–595, 2006.
- [71] J. D. Rosny and C. Prada. Multiple scattering: The key to unravel the sub-wavelength world from the far-field pattern of a scattered wave. *Phys. Rev. E*, 75:048601–1, 2007.
- [72] A. Sentenac, C.-A. Guérin, P. C. Chaumet, F. Drsek, H. Giovannini, N. Bertaux, and M. Holschneider. Influence of multiple scattering on the resolution of an imaging system: a Cramer-Rao analysis. *Opt. Express*, 15:1340–1347, 2007.
- [73] F. Simonetti. Multiple scattering: The key to unravel the subwavelength world from the far-field pattern of a scattered wave. *Phys. Rev. E*, 73:036619–13, 2006.
- [74] A. B. Sarah M Wilson. Preparation of plant cells for transmission electron microscopy to optimize immunogold labeling of carbohydrate and protein epitopes. *Nature Protocols*, 7:1716–1727, 2012.
- [75] J. Jung, K. Kim, J. Yoon, and Y. Park. Hyperspectral optical diffraction tomography. *Opt. Express*, 24(3):2006–2012, 2016.
- [76] G. Maire, Y. Ruan, T. Zhang, P. C. Chaumet, H. Giovannini, D. Sentenac, A. Talneau, K. Belkebir, and A. Sentenac. High-resolution tomographic diffractive microscopy in reflection configuration. *J. Opt. Soc. Am. A*, 30:2133–2139, 2013.

- [77] P. Godard, M. Allain, and V. Chamard. Imaging of highly inhomogeneous strain field in nanocrystals using x-ray bragg ptychography : a numerical study. *Phys. Rev. B.*, 84:144109, 2011.
- [78] B. Platt and R. Shack. History and principles of shack-hartmann wavefront sensing. *Journal of refractive surgery (Thorofare, N.J. : 1995)*, 17(5):573 – 577, 2001.
- [79] D. Malacara, editor. *Optical Shop Testing*. Wiley-Interscience, 2007.
- [80] E. Cuhe, F. Bevilacqua, and C. Depeursinge. Digital holography for quantitative phase-contrast imaging. *Opt. Lett.*, 24(5):291–293, 1999.
- [81] T. Ikeda, G. Popescu, R. R. Dasari, and M. S. Feld. Hilbert phase microscopy for investigating fast dynamics in transparent systems. *Opt. Lett.*, 30(10):1165–1167, 2005.
- [82] S. V. King and C. J. Cogswell. A phase-shifting dic technique for measuring 3d phase objects: experimental verification. In J.-A. Conchello, Cogswell, C. J, and T. Wilson, editors, *Three-Dimensional and Multidimensional Microscopy: Image Acquisition and Processing XI*, volume 5324, pages 191–196, 2004.
- [83] D. O. Hogenboom, C. A. DiMarzio, T. J. Gaudette, A. J. Devaney, and S. C. Lindberg. Three-dimensional images generated by quadrature interferometry. *Opt. Lett.*, 23(10):783–785, 1998.
- [84] G. Popescu, L. P. Deflores, J. C. Vaughan, K. Badizadegan, H. Iwai, R. R. Dasari, and M. S. Feld. Fourier phase microscopy for investigation of biological structures and dynamics. *Opt. Lett.*, 29(21):2503–2505, 2004.
- [85] J.-M. Desse, P. Picart, and F. Olchewsky. Quantitative phase imaging in flows with high resolution holographic diffraction grating. *Opt. Express*, 23(18):23726–23737, 2015.
- [86] B. Bhaduri, H. Pham, M. Mir, and G. Popescu. Diffraction phase microscopy with white light. *Opt. Lett.*, 37(6):1094–1096, 2012.
- [87] M. Mir, B. Bhaduri, R. Wang, R. Zhu, and G. Popescu. Chapter 3 - quantitative phase imaging. In E. Wolf, editor, *Progress in Optics*, volume Volume 57, pages 133–217. Elsevier, 2012.
- [88] R. V. Shack and B. C. Platt. Production and use of a lenticular Hartmann screen. *J. Opt. Soc. Am. A*, 61:656, 1971.
- [89] J. Primot and L. Sogno. Achromatic three-wave (or more) lateral shearing interferometer. *J. Opt. Soc. Am. A*, 12(12):2679–2685, 1995.
- [90] J. Primot. Three-wave lateral shearing interferometer. *Appl. Opt.*, 32(31):6242–6249, 1993.

- [91] J.-C. Chanteloup. Multiple-wave lateral shearing interferometry for wave-front sensing. *Appl. Opt.*, 44(9):1559–1571, 2005.
- [92] T. Zhang. *Electromagnetic wave imaging of targets buried in a cluttered medium using an hybrid Inversion-DORT method*. PhD thesis, École Doctorale - ED 352, Institut Fresnel UMR 7249, Team SEMOX, 2014.
- [93] T. Colomb, F. Dürr, E. Cuche, P. Marquet, H. G. Limberger, R.-P. Salathé, and C. Depeursinge. Polarization microscopy by use of digital holography: application to optical-fiber birefringence measurements. *Appl. Opt.*, 44(21):4461–4469, 2005.
- [94] E. Beaurepaire, L. Moreaux, F. Amblard, and J. Mertz. Combined scanning optical coherence and two-photon-excited fluorescence microscopy. *Opt. Lett.*, 24(14):969–971, 1999.
- [95] A. Valdecasas, D. Marshall, J. Becerra, and J. Terrero. On the extended depth of focus algorithms for bright field microscopy. *Micron*, 32(6):559 – 569, 2001.
- [96] S. H. Gage. Modern dark-field microscopy and the history of its development. *Transactions of the American Microscopical Society*, 39(2):95–141, 1920.
- [97] D. B. Murphy. *Fundamentals of Light Microscopy and Electronic Imaging*. Wiley-Liss, 2001.
- [98] R. H. Webb. Confocal optical microscopy. *Reports on Progress in Physics*, 59(3):427, 1996.
- [99] S. W. Paddock. Principles and practices of laser scanning confocal microscopy. *Molecular Biotechnology*, 16(2):127–149, 2000.
- [100] C. L. Smith. *Basic Confocal Microscopy*. John Wiley & Sons, Inc., 2001.
- [101] R. C. Jones. A new calculus for the treatment of optical systems. *J. Opt. Soc. Am.*, 31(7):488–493, 1941.
- [102] F. Kleinermann, N. J. Avis, and F. A. Alhargan. Analytical solution to the three-dimensional electrical forward problem for a circular cylinder. *Inverse Problems*, 16(2):461, 2000.
- [103] E. M. Purcell and C. R. Pennypacker. Scattering and absorption of light by nonspherical dielectric grains. *Astrophys. J.*, 186:705–714, 1973.
- [104] A. Lakhtakia. Strong and weak forms of the method of moments and the coupled dipole method for scattering of time-harmonic electromagnetics fields. *Int. J. Mod. Phys. C*, 3:583–603, 1992.
- [105] A. D. Yaghjian. Electric dyadic green’s functions in the source region. *Proceedings of the IEEE*, 68(2):248–263, 1980.

- [106] P. C. Chaumet and A. Rahmani. Electromagnetic force and torque on magnetic and negative-index scatterers. *Opt. Exp.*, 17:2224–2234, 2009.
- [107] W. C. Chew and Y. M. Wang. Reconstruction of two-dimensional permittivity distribution using distorted Born iterative method. *IEEE Trans. Med. Imaging*, 9:218–225, 1990.
- [108] N. Joachimowicz, C. Pichot, and J.-P. Hugonin. Inverse scattering: an iterative numerical method for electromagnetic imaging. *IEEE Trans. Antennas Propagat.*, 39:1742–1753, 1991.
- [109] A. G. Tijhuis. Born-type reconstruction of material parameters of an inhomogeneous lossy dielectric slab from reflected-field data. *Wave Motion*, 11:151–173, 1989.
- [110] A. G. Tijhuis, K. Belkebir, A. C. S. Litman, and B. P. de Hon. Theoretical and Computational Aspects of 2-D Inverse Profiling. *IEEE Trans. Geosci. Remote Sensing*, 39(6):1316–1330, 2001.
- [111] R. E. Kleinman and P. M. van den Berg. A modified gradient method for two-dimensional problems in tomography. *J. Comput. Appl. Math.*, 42:17–35, 1992.
- [112] R. E. Kleinman and P. M. van den Berg. An extended range-modified gradient technique for profile inversion. *Radio Sci.*, 28(5):877–884, 1993.
- [113] E. Mudry, P. C. Chaumet, K. Belkebir, and A. Sentenac. Electromagnetic wave imaging of three-dimensional targets using a hybrid iterative inversion method. *Inverse Probl.*, 28(6):065007, 2012.
- [114] K. Belkebir, S. Bonnard, F. Pezin, P. Sabouroux, and M. Saillard. Validation of 2D inverse scattering algorithms from multi-frequency experimental data. *J. Electromag. Waves Appl.*, 14:1637–1667, 2000.
- [115] K. Belkebir and A. G. Tijhuis. Modified<sup>2</sup> gradient method and modified Born method for solving a two-dimensional inverse scattering problem. *Inverse Probl.*, 17(6):1671–1688, 2001.
- [116] K. Belkebir, P. C. Chaumet, and A. Sentenac. Superresolution in total internal reflection tomography. *J. Opt. Soc. Am. A*, 22:1889–1897, 2005.
- [117] P. C. Chaumet and K. Belkebir. Three-dimensional reconstruction from real data using a conjugate gradient-coupled dipole method. *Inverse Probl.*, 25:024003–17, 2009.
- [118] C. Prada and M. Fink. Eigenmodes of the time reversal operator: a solution to selective focusing in multiple-target media. *Wave Motion*, 20:151–163, 1994.

- [119] H. Tortel, G. Micolau, and M. Saillard. Decomposition of the time reversal operator for electromagnetic scattering. *J. Electromag. Waves Appl.*, 13:687–719, 1999.
- [120] A. Dubois, K. Belkebir, and M. Saillard. Localization and characterization of two-dimensional targets buried in a cluttered environment. *Inverse Probl.*, 20(6):S63–S79, 2004.
- [121] T. Zhang, C. Godavarthi, P. C. Chaumet, G. Maire, H. Giovannini, A. Talneau, C. Prada, A. Sentenac, and K. Belkebir. Tomographic diffractive microscopy with agile illuminations for imaging targets in a noisy background. *Opt. Lett.*, 40(4):573–576, 2015.
- [122] M. Fink, C. Prada, F. Wu, and D. Cassereau. Self focusing with time reversal mirror in inhomogeneous media. *Proc. IEEE Ultrason. Symp.*, 2:681–686, 1989.
- [123] R. Carminati, R. Pierrat, J. de Rosny, and M. Fink. Theory of the time reversal cavity for electromagnetic fields. *Opt. Lett.*, 32:3107–3109, 2007.
- [124] S. M. Popoff, A. Aubry, G. Lerosey, M. Fink, A. C. Boccara, and S. Gigan. Exploiting the time-reversal operator for adaptive optics, selective focusing, and scattering pattern analysis. *Phys. Rev. Lett.*, 107:263901, 2011.
- [125] G. Micolau and M. Saillard. D.O.R.T. method as applied to electromagnetic sensing of buried objects. *Radio Sci.*, 38(3):1038, 2003.
- [126] T. Zhang, P. C. Chaumet, E. Mudry, A. Sentenac, and K. Belkebir. Electromagnetic wave imaging of targets buried in a cluttered medium using a hybrid inversion-dort method. *Inverse Probl.*, 28(12):125008, 2012.
- [127] C. Prada, S. Manneville, D. Spoliansky, and M. Fink. Decomposition of the time reversal operator: detection and selective focusing on two scatterers. *J. Acoust. Soc. Am.*, 9:2067–2076, 1996.
- [128] M. Davy, J.-G. Minonzio, J. de Rosny, C. Prada, and M. Fink. Influence of noise on subwavelength imaging of two close scatterers using time reversal method: theory and experiments. *Progress In Electromagnetics Research*, 98:333–358, 2009.
- [129] E. Mudry, E. L. Moal, P. Ferrand, P. C. Chaumet, and A. Sentenac. Isotropic diffraction-limited focusing using a single objective lens. *Phys. Rev. Lett.*, 105(20):203903, 2010.
- [130] T. Zhang, Y. Ruan, G. Maire, D. Sentenac, A. Talneau, K. Belkebir, P. C. Chaumet, and A. Sentenac. Full-polarized tomographic diffraction microscopy achieves a resolution about one-fourth of the wavelength. *Phys. Rev. Lett.*, 111:243904, 2013.

- [131] A. Litman, D. Lesselier, and F. Santosa. Reconstruction of two-dimensional binary obstacle by controlled evolution of a level-set. *Inverse Probl.*, 14:685–705, 1998.
- [132] P. C. Chaumet, K. Belkebir, and A. Sentenac. Experimental microwave imaging of three-dimensional targets with different inversion procedures. *J. Appl. Phys.*, 106:034901–8, 2009.
- [133] T. Zhang, C. Godavarthi, P. C. Chaumet, G. Maire, H. Giovannini, A. Talneau, M. Allain, K. Belkebir, and A. Sentenac. Far-field diffraction microscopy at  $\frac{\lambda}{10}$  resolution. *Optica*, 3(6):609–612, 2016.
- [134] S. W. Hell, S. Lindek, C. Cremer, and E. H. K. Stelzer. Confocal microscopy with an increased detection aperture: type-b 4pi confocal microscopy. *Opt. Lett.*, 19(3):222–224, 1994.
- [135] E. H. K. Stelzer and S. Lindek. Fundamental reduction of the observation volume in far-field light microscopy by detection orthogonal to the illumination axis: confocal theta microscopy. *Optics Communications*, 111(5-6):536–547, 1994.
- [136] S. Vertu, J. Flügge, J.-J. Delaunay, and O. Haeberlé. Diffraction microtomography with sample rotation: influence of a missing apple core in the recorded frequency space. *Centr. Eur. J. of Phys.*, 9:969–974, 2011.
- [137] J. Bailleul, B. Simon, B. Colicchio, M. Debailleul, and O. Haeberlé. 3d high- and isotropic resolution in tomographic diffractive microscopy by illumination angular scanning, specimen rotation and improved data recombination. *Proc. SPIE*, 9896:98960M–98960M–9, 2016.
- [138] K. Kim, J. Yoon, and Y. Park. Simultaneous 3d visualization and position tracking of optically trapped particles using optical diffraction tomography. *Optica*, 2(4):343–346, 2015.
- [139] E. Mudry. *Resolution improvement in fluorescence and phase optical microscopy*. PhD thesis, École Doctorale - ED 352, Institut Fresnel UMR 7249, Team SEMOX, 2012.
- [140] F. Momey, A. Berdeu, T. Bordy, J.-M. Dinten, F. K. Marcel, N. Picollet-D’ahan, X. Gidrol, and C. Allier. Lensfree diffractive tomography for the imaging of 3d cell cultures. *Biomed. Opt. Express*, 7(3):949–962, 2016.

# Résumé

La microscopie optique est classiquement limitée par la diffraction à une résolution transverse d'environ  $\lambda/2$  et une résolution axiale de  $\lambda$  ( $\lambda$  étant la longueur d'onde). De nombreux domaines, tels que les nanotechnologies, les sciences des matériaux ou la biologie, nécessitent de résoudre les objets à de plus petites échelles. Cette thèse vise à améliorer la résolution en trois dimensions grâce à une technique récente d'imagerie : la microscopie tomographique diffractive (MTD). Son principe est d'éclairer l'objet successivement sous différents angles en lumière cohérente, de détecter le champ diffracté en phase et en amplitude, et de reconstruire la carte 3D de permittivité de l'objet par un algorithme d'inversion. La MTD s'est avérée capable de combiner plusieurs modalités utiles d'imagerie sans marquage, telles que la microscopie plein champ, la microscopie champ sombre, la microscopie à contraste de phase, la microscopie confocale, ou encore la microscopie à synthèse d'ouverture 2D ou 3D. Toutes sont basées sur des approximations scalaires et linéaires qui supposent un lien linéaire entre l'objet et le champ mesuré, ce qui restreint leur domaine d'application pour restituer l'objet de manière quantitative. A l'aide d'une inversion numérique rigoureuse prenant en compte la polarisation du champ et le phénomène de diffusion multiple, nous sommes parvenus à reconstruire la carte 3D de permittivité d'objets avec une résolution de  $\lambda/4$ . Une amélioration supplémentaire la portant à  $\lambda/10$  a été rendue possible par l'insertion d'information a priori sur l'objet dans l'algorithme d'inversion. Enfin, l'amélioration de la résolution axiale a été étudiée. Celle-ci est fondamentalement moins bonne que la résolution transverse du fait de l'asymétrie des schémas d'illumination et de détection dans les microscopes. Pour s'affranchir de cette limitation, une configuration de tomographie assistée par miroir a été implémentée et a mis en évidence un pouvoir de séparation axial meilleur que  $\lambda/2$ . Au final, la MTD s'est illustrée comme un outil de caractérisation puissant pour reconstruire en 3D les objets ainsi que leurs indices optiques, à des résolutions bien supérieures à celles des microscopes conventionnels.

**Key words:** Microscopie optique; super-résolution; tomographie; inversion numérique; microscopie de phase; imagerie 3D; tomographie assistée par miroir.



# Abstract

Classical optical microscopy is limited in resolution by the wavelength of light (diffraction limit) restricting lateral resolution to about  $\lambda/2$ , and axial resolution to about  $\lambda$  (the wavelength). Various domains, such as nanotechnology, material science or biology, require tools to resolve smaller objects at best possible resolution with optics. This PhD thesis is devoted to the three-dimensional isotropic resolution improvement using optical tomographic diffraction microscopy (TDM), an emerging optical microscope technique. The principle is to illuminate the sample successively with various angles of coherent light, collect the complex (amplitude and phase) diffracted field and reconstruct the sample 3D permittivity map through an inversion algorithm. A single TDM measurement was shown to combine several popular microscopy techniques such as bright-field microscope, dark-field microscope, phase-contrast microscope, confocal microscope, 2D and 3D synthetic aperture microscopes. All rely on scalar and linear approximations that assume a linear link between the object and the field diffracted by it, which limit their applicability to retrieve the object quantitatively. Thanks to a rigorous numerical inversion of the TDM diffracted field data which takes into account the polarization of the field and the multiple scattering process, we were able to reconstruct the 3D permittivity map of the object with a  $\lambda/4$  transverse resolution. A further improvement to  $\lambda/10$  transverse resolution was achieved by providing a priori information about the sample to the non-linear inversion algorithm. Lastly, the axial resolution improvement was studied. Poor axial resolution is due to the fundamental asymmetry of illumination and detection in microscopes. To overcome this, a mirror-assisted tomography configuration was implemented, and has demonstrated a sub- $\lambda/2$  axial resolution capability. As a result, TDM can be seen as a powerful tool to reconstruct objects in three-dimensions with their optical material properties at resolution far superior to conventional microscopes.

**Key words:** Optical microscopy; super-resolution; tomography; numerical inversion; phase microscopy; 3D imaging; mirror-assisted tomography.